Department of Physics and Astronomy

Heidelberg University

Master thesis

in Physics

submitted by

Stefanie Czischek

born in Lauterbach

2016

Discrete Truncated Wigner Approximation of Sudden Quenches in the Transverse Field Ising Chain

This Master thesis has been carried out by Stefanie Czischek

at the

Kirchhoff-Institute for Physics

under the supervision of

Prof. Dr. Thomas Gasenzer

(Diskrete trunkierte Wigner Approximation von plötzlichen Quenches in der Ising Kette in einem transversen Feld):

In der folgenden Masterarbeit wurde die kürzlich eingeführte diskrete trunkierte Wigner Approximation verwendet, um quantenmechanische Spinketten zu simulieren. Während Simulationsmethoden für diskrete Quantenmodelle vor allem in höheren Dimensionen und großen Systemen rar sind, soll die neue Methode auch in diesen Bereichen gute Näherungen ergeben. Rey et al. führten diese Approximation basierend auf einer klassischen Näherung der Quantendynamik in [27] ein und zeigten die Stärke in der Simulation von Spinsystemen mit langreichweitigen Wechselwirkungen. In der folgenden Arbeit wurde die Methode auf das Ising Modell im transversalen Feld mit Nächste-Nachbar-Wechselwirkungen angewendet, um Quenches in die Nähe des Quanten-Phasenüberganges zu simulieren. Hierbei wurde deutlich, dass die Methode für Quenches nah zum kritischen Punkt und weit weg davon gute Ergebnisse liefert, bei mittleren Abständen jedoch Abweichungen auftreten. Kastner et al. führten in [16] weiterhin verschiedene Möglichkeiten zum Aufbau der Methode sowie Näherungen höherer Ordnung der Quantendynamik ein. In der folgenden Arbeit wurden weitere Möglichkeiten hergeleitet, um die Simulationsmethode aufzubauen. Dabei wurde festgestellt, dass die Qualität der verschiedenen Arten von dem simulierten Modell abhängt. Auch die Näherung höherer Ordnung der Dynamik wurde in dieser Arbeit analysiert. Hierbei wurde beobachtet, dass diese im Vergleich zur klassischen Näherung nur für kurze Zeiten funktioniert, in diesem Bereich aber vielversprechende Ergebnisse liefert.

(Discrete Truncated Wigner Approximation of Sudden Quenches in the Transverse Field Ising Chain):

In the following thesis, a recently developed method, the discrete truncated Wigner approximation, was used to simulate quantum spin chains. While simulation methods for discrete quantum systems are scarce, especially for large systems and higher dimensions, this new method is expected to simulate even such systems. Rey et al. introduced the method, which is based on a classical approximation, in [27] and proved its strength in the simulation of spin systems with long-range interactions. In the following thesis, the approximation was applied on a transverse field Ising chain with nearest-neighbour interactions to simulate sudden quenches into the vicinity of a quantum phase transition. While the approximation was shown to work well for quenches close to the critical point and far away from it, deviations were found at intermediate distances. Kastner et al. further introduced various setups of the simulation method, as well as higher order approximations of the quantum dynamics in [16]. In the following thesis, more possible setups of the method were introduced and analysed. It was concluded that the quality of the various setups depends on the simulated model. Additionally, the higher order approximations of the quantum dynamics were analysed. It was observed that this method only works for short times compared to the classical approximation, but gives promising results within this region.

Contents

1 Introduction

Recent experimental advances use quantum simulators to enable the observation of spin dynamics out of equilibrium [1, 2, 10, 15, 19, 28]. Such systems can not be analysed directly, since they are hard to realise in the laboratory or to model on a supercomputer. Hence, for further analysations quantum simulators are necessary, which are based on a quantum system simulating the not realisable model in a controllable way.

With these quantum simulators, spin lattices can be experimentally realised in a state far from equilibrium by applying sudden changes, so called quenches, in the Hamiltonian describing the dynamics of the system. Since the complex time evolutions in such quantum mechanical systems out of equilibrium can not be calculated analytically in most cases, many main aspects, like the build-up of correlations, are not well understood.

An experimental realisation of systems out of equilibrium is given in [31], where ultracold Bosons are considered in a three-dimensional lattice potential with an additional harmonic trap. The authers produced a rubidium condensate in a cigar-shaped magnetic trap by evaporative cooling. After an initial temperature has been set, the magnetic trap has been decompressed adiabatically towards an almost spherical trap and the lattice, as well as the trap have been switched off simultaneously. This way, the condensate has been released and the dynamics have been analysed. It has been shown that ultracold atoms in optical lattices can be used to experimentally study quantum critical phenomena.

In [19], also a rubidium condensate in a cigar-shaped trap has been realised. The transversal excitations are suppressed in this configuration, so that the condensate only shows excitations in a longitudinal direction and hence can be considered as an effective one-dimensional system. The atoms can then be found in two hyperfine states of the magnetic quantum number, namely $|F = 2, m_F = -1\rangle$ and $|F = 1, m_F = 1\rangle$. The condensate can be effectively considered as a spin-$\frac{1}{2}$ system and hence is a quantum simulator. Other possible quantum simulators for spin systems can be realised using polar molecules [10], Rydberg atoms [28] or trapped ions [15].

These quantum simulators are very important, since the efficient numerical simulation of the dynamics in spin systems out of equilibrium is still an outstanding problem. In [31], a Quantum Monte Carlo simulation has been compared with the quantum simulations and it has been found that both simulation methods show equal results for small interaction strengths. For larger interaction strengths, for which the considered system is closer to a quantum critical point, the computational simulation has been found to get worse, while the quantum simulation still shows

good results. For a theoretical consideration it would be helpful to have a better possibility to computationally simulate quantum spin systems out of equilibrium.

Existing computational simulation methods for quantum spin systems out of equilibrium are, for example, the time-dependent density matrix renormalisation group methods [33], which have been proven to give very good results. However, these methods can only be used in one dimension and simulating dynamics is already hard in one dimension. These methods also fail in the vicinity of quantum phase transitions. Other possibilities are cluster expansions [10], which only show good results for dilute samples and short-range interactions, or phase space methods [23], which do not give good results at strong interactions and long times. Dynamics in the vicinity of a quantum phase transition are not captured well in all these methods.

Apart from that, phase space methods, like the truncated Wigner approximation, are very strong at short times and weak interactions. They are based on sampling a large number of initial states from a Wigner function, which is a quasi-probability-distribution on the phase space in the sense that it shows properties of a probability distribution, but is not positive definite. All sampled initial states are then classically evolved in time and the resulting expectation value is calculated using a combination of the time evolved observables. This basic idea of the method includes quantum fluctuations into the approximation by the combination of the several time evolved observables. Due to this, the approximation is in good agreement with the exact solution. Spontaneous quenches can also be approximated with this method, so that it is very powerful in the computational simulation of spin systems out of equilibrium. Hence, it is used very often, as for example in [19].

While the truncated Wigner approximation is limited to short times and it has been proven to miss revivals in the dynamics of the modelled system, it has been expanded into the discrete truncated Wigner approximation in [27, 26, 16]. This expanded method is based on a discrete phase space and is more efficient in simulating discrete quantum mechanical models, like spin systems. The initial states are then sampled from a Wigner function on a discrete phase space, so that only a finite number of possible initial states exists. This is in contradiction to the truncated Wigner approximation, which is defined on a continuous phase space and is thus more efficient for simulations of continuous quantum systems. The discrete truncated Wigner approximation is expected to catch revivals in the dynamics of the spin system due to the discrete initial states, which are classically evolved in time. Hence, it is expected to be more powerful in the points where the truncated Wigner approximation breaks down.

It has been shown in [27, 26, 16] that the discrete truncated Wigner approximation gives very good results in simulations of spin-$\frac{1}{2}$ systems. There it has been observed that this method even works at longer time scales and with strong interactions. It has also been found to show revivals in the dynamics of the system, which are not captured by the truncated Wigner approximation. Hence, this expansion shows very promising results in regions where existing simulation methods are scarce.

In this thesis, the discrete truncated Wigner approximation will be applied on the transverse field Ising model with nearest-neighbour interactions. While in [27, 26, 16]

only non-interacting systems with long-range interactions have been considered, it will be analysed within this work whether the method also shows good results in an interacting system. Especially, it will be analysed how the method behaves in the vicinity of a quantum phase transition, which is also given in the transverse field Ising model. Also the behaviour of the simulation method within this region has not been analysed in [27, 26, 16]. To get the system into the vicinity of the quantum critical point, sudden quenches will be considered, which can be included into the discrete truncated Wigner approximation.

In [18, 22], this transverse field Ising model has been diagonalised exactly and dynamics after sudden quenches have been calculated analytically, for example, in [6, 7]. By comparison with these exact solutions, it will be analysed within this thesis whether the quantum mechanical system can be approximated semi-classically by the discrete truncated Wigner approximation and, especially, it will be considered how this property depends on the distance from the quantum critical point. Finding a simulation method which shows good results in the vicinity of a quantum phase transition would be a great acchievement, because it has already been mentioned that especially in this region computational simulation methods are scarce.

This thesis is organised as follows. In chapter 2, the discrete phase space, as defined in [35, 36], will be introduced and the time evolution of the sampled initial states will be derived. While the quantum mechanical equations of motion can not be solved explicitly, they are truncated in the discrete truncated Wigner approximation. In [27, 26], a truncation at first order is derived, which results in classical equations of motion. A second order truncation based on a Bogoliubov-Born-Green-Kirkwood-Yvon (BBGKY) hierarchy is introduced in [16]. Both truncation schemes will be reviewed here. This gives all ingredients to generally introduce the discrete truncated Wigner approximation.

In chapter 3, a spin-$\frac{1}{2}$ system will be considered and the general discrete truncated Wigner approximation will be adapted to this special system. In [16], several schemes how to sample the initial states from the phase space have been derived. Since the quality of these sampling schemes will be found to depend on the approximated system, further new schemes will be introduced within this work. This way, it will become possible to analyse in more detail how the qualities of the various sampling schemes depend on the simulated system. The method will then be benchmarked for all sampling schemes and both time evolution approximations on an Ising chain.

Sudden quenches of the transverse field Ising model will be considered in chapter 4, where first the model and the analytical solution will be explained further. Afterwards, the system will be simulated by the discrete truncated Wigner approximation with the various introduced sampling schemes. The results will be compared to the exact calculations. It will be found that in this model, the sampling schemes introduced within this thesis will show better agreement with the exact solution, while it will be the other way around in the Ising chain. In studying sudden quenches into the vicinity of the quantum critical point, it will be observed that the quality of the simulation depends on the distance from the critical point. This dependence shows

an interesting behaviour, good agreement with the exact solutions will be found in the approximations of quenches close to the critical point and far away from it. In the region in between, at intermediate distances from the critical point, differences between the approximation and the exact solution will be observed. This result is very peculiar, since one would not expect the simulation to be in good agreement with the exact solution close to the critical point. Additionally, if the simulation works well close to the critical point, one would not expect it to show worse results at intermediate distances. There is no trivial explanation for these deviations. This surprising result might be a hint for quantum effects, which can not be captured by the semi-classical approximation, appearing for quenches to intermediate distances from the critical point. In the same way it might be promising that the method works in the vicinity of the quantum critical point.

2 The Discrete Truncated Wigner Approximation

The discrete truncated Wigner approximation is a semi-classical simulation method for dynamics of a discrete quantum mechanical system, which are often hard to solve exactly. It is based on sampling an initial state from a Wigner function on a discrete phase space and evolving it in time, while the full quantum mechanical time evolution is truncated. This way many classical trajectories are calculated and the time-evolved observables are averaged to include quantum uncertainties into the semi-classical approximation.

In section 2.1 a continuous quantum mechanical phase space analogous to the classical phase space will be derived according to [11, 23]. For discrete quantum mechanical systems, a discrete phase space is needed, which will be derived in section 2.2 according to [35, 36]. On this discrete phase space a Wigner function can be defined from which an initial state can be sampled. Two ways to truncate the full quantum mechanical time evolution at different orders will be derived in sections 2.3 and 2.4 according to [16, 26, 27]. At this point all ingredients of the discrete truncated Wigner approximation are introduced and the whole procedure will be summarised in section 2.5.

2.1 The Continuous Quantum Mechanical Phase Space

The continuous quantum mechanical phase space can be built up analogously to the classical phase space. One two-dimensional, continuous phase space is needed to describe the state of each particle in the system containing all possible states of the particle. Each axis of the phase space then denotes an infinite set of parallel horizontal or vertical lines, which in the classical case are associated with different values for position and momentum. In the quantum mechanical phase space, each set of parallel lines is associated with an operator, where the position and momentum operators $\hat{\boldsymbol{q}}$ and $\hat{\boldsymbol{p}}$ are chosen. Each line is then associated with an eigenstate of the corresponding operator. Since position and momentum eigenstates $\boldsymbol{q}$ and $\boldsymbol{p}$ have continuous eigenvalues, these can be associated with an infinite number of horizontal and vertical lines respectively.

Given the principles of the continuous quantum mechanical phase space, a transformation of the quantum operators into the phase space is needed. One possibility, and the one which will be used here, is to define Weyl symbols $\Omega_{\mathrm{W}}(\boldsymbol{q}, \boldsymbol{p})$ of the quantum mechanical operators $\hat{\Omega}(\hat{\boldsymbol{q}}, \hat{\boldsymbol{p}})$, where the hats indicate operators. The

Weyl symbols are denoted with a subscript W and are defined in phase space. The mapping between an operator and its Weyl symbol can be written down in the position and the momentum basis, respectively [11, 23],

$$\Omega_{\mathrm{W}}(\boldsymbol{q},\boldsymbol{p}) = \frac{1}{\pi\hbar}\int \langle \boldsymbol{q}-\boldsymbol{x}|\,\hat{\Omega}(\hat{\boldsymbol{q}},\hat{\boldsymbol{p}})\,|\boldsymbol{q}+\boldsymbol{x}\rangle \exp\left(\frac{2i\boldsymbol{p}\boldsymbol{x}}{\hbar}\right)\mathrm{d}\boldsymbol{x}, \tag{2.1}$$

$$\Omega_{\mathrm{W}}(\boldsymbol{q},\boldsymbol{p}) = \frac{1}{\pi\hbar}\int \langle \boldsymbol{p}-\boldsymbol{x}|\,\hat{\Omega}(\hat{\boldsymbol{q}},\hat{\boldsymbol{p}})\,|\boldsymbol{p}+\boldsymbol{x}\rangle \exp\left(\frac{2i\boldsymbol{q}\boldsymbol{x}}{\hbar}\right)\mathrm{d}\boldsymbol{x}. \tag{2.2}$$

To make the mapping between operators and functions on the phase space unique, several conditions on the transformation need to be introduced, as stated in [20]. There, the authors derived a unique mapping with the needed properties, which is also the mapping used here.

A quantum state can be fully described in its Hilbert space by the density operator $\hat{\rho}$. The Weyl symbol corresponding to the density operator is called the Wigner function $W(\boldsymbol{q},\boldsymbol{p})$ and can also be written in the position and the momentum basis, respectively [11, 23, 34, 35],

$$W(\boldsymbol{q},\boldsymbol{p}) = \frac{1}{\pi\hbar}\int \langle \boldsymbol{q}-\boldsymbol{x}|\,\hat{\rho}(\hat{\boldsymbol{q}},\hat{\boldsymbol{p}})\,|\boldsymbol{q}+\boldsymbol{x}\rangle \exp\left(\frac{2i\boldsymbol{p}\boldsymbol{x}}{\hbar}\right)\mathrm{d}\boldsymbol{x}, \tag{2.3}$$

$$W(\boldsymbol{q},\boldsymbol{p}) = \frac{1}{\pi\hbar}\int \langle \boldsymbol{p}-\boldsymbol{x}|\,\hat{\rho}(\hat{\boldsymbol{q}},\hat{\boldsymbol{p}})\,|\boldsymbol{p}+\boldsymbol{x}\rangle \exp\left(\frac{2i\boldsymbol{q}\boldsymbol{x}}{\hbar}\right)\mathrm{d}\boldsymbol{x}. \tag{2.4}$$

Given the Wigner function, one can express quantum mechanical averages analogously to classical ones,

$$\langle\Omega\rangle_{\mathrm{classical}} = \iint \Omega(\boldsymbol{q},\boldsymbol{p})\,P(\boldsymbol{q},\boldsymbol{p})\,\mathrm{d}\boldsymbol{q}\mathrm{d}\boldsymbol{p}, \tag{2.5}$$

$$\begin{aligned}\left\langle\hat{\Omega}\right\rangle_{\mathrm{quant}} &= \mathrm{Tr}\left(\hat{\Omega}(\hat{\boldsymbol{q}},\hat{\boldsymbol{p}})\,\hat{\rho}(\hat{\boldsymbol{q}},\hat{\boldsymbol{p}})\right)\\ &= \iint \Omega_W(\boldsymbol{q},\boldsymbol{p})\,W(\boldsymbol{q},\boldsymbol{p})\,\mathrm{d}\boldsymbol{q}\mathrm{d}\boldsymbol{p}.\end{aligned} \tag{2.6}$$

Here $P(\boldsymbol{q},\boldsymbol{p})$ is the classical phase space probability distribution which translates into the Wigner function in the quantum mechanical phase space.

One property of the Wigner function is that its integral over one variable gives the probability of the second variable, as follows directly from equations (2.3) and (2.4),

$$\int W(\boldsymbol{q},\boldsymbol{p})\,\mathrm{d}\boldsymbol{q} = \langle\boldsymbol{p}|\,\hat{\rho}\,|\boldsymbol{p}\rangle\,, \tag{2.7}$$

$$\int W(\boldsymbol{q},\boldsymbol{p})\,\mathrm{d}\boldsymbol{p} = \langle\boldsymbol{q}|\,\hat{\rho}\,|\boldsymbol{q}\rangle\,. \tag{2.8}$$

Given this, one can easily see that the integral of the Wigner function over the whole phase space is unity,

$$\begin{aligned}\iint W(\boldsymbol{q},\boldsymbol{p})\,\mathrm{d}\boldsymbol{q}\mathrm{d}\boldsymbol{p} &= \int \langle\boldsymbol{p}|\,\hat{\rho}\,|\boldsymbol{p}\rangle\,\mathrm{d}\boldsymbol{p},\\ &= \mathrm{Tr}(\hat{\rho}) = 1.\end{aligned} \tag{2.9}$$

Hence, the Wigner function is normalized and shows some properties of a probability distribution over the phase space. Because there is no condition on it to be positive definite, it can also have negative entries and is thus called a quasi-probability-distribution [11, 23, 34, 35]. If a projection of the Wigner function along a direction of the phase space is considered, the probability distribution of the observable associated with this direction is found, as can be directly seen from equation (2.7). Although the Wigner function is a quasi-probability-distribution for states, it integrates to a probability for observables.

Considering the integral of the Wigner function over a region of the phase space bounded by two lines $\boldsymbol{c}_1 = a\boldsymbol{q} + b\boldsymbol{p}$ and $\boldsymbol{c}_2 = a\boldsymbol{q} + b\boldsymbol{p}$ with $a, b \,\epsilon\, \mathbb{R}$ and $\boldsymbol{c}_1, \boldsymbol{c}_2 \,\epsilon\, \mathbb{R}^D$, one can see that the probability of the observable $a\hat{\boldsymbol{q}} + b\hat{\boldsymbol{p}}$ has a value between $\boldsymbol{c}_1$ and $\boldsymbol{c}_2$. Analogously to the integral over one direction of phase space in equations (2.7) and (2.8), this is a non-negative probability [35].

For two density operators $\hat{\rho}$ and $\hat{\rho}'$ of two arbitrary states, the inner product of the corresponding Wigner functions $W(\boldsymbol{q}, \boldsymbol{p})$ and $W'(\boldsymbol{q}, \boldsymbol{p})$ gives the trace of the product of the density operators as can be shown by simply plugging the definition of the Wigner function into equation (2.3),

$$2\pi\hbar \int\int W(\boldsymbol{q}, \boldsymbol{p})\, W'(\boldsymbol{q}, \boldsymbol{p})\, \mathrm{d}\boldsymbol{q}\mathrm{d}\boldsymbol{p} = \mathrm{Tr}\left(\hat{\rho}\hat{\rho}'\right). \tag{2.10}$$

The detailed derivation of this relation is explained in appendix A.1.

As will become clear in section 2.2, a different way to describe the mapping between the Hilbert space and the phase space will be needed to define the discrete quantum mechanical phase space. One possibility for this is to use phase-point operators $\hat{A}(\boldsymbol{q}, \boldsymbol{p})$. These are Hermitian operators acting on the Hilbert space which project each point in Hilbert space onto a point in phase space. Hence one operator exists for each point in phase space. In terms of the phase-point operators, the mapping of the density operator onto the Wigner function takes the form [35]

$$\hat{\rho} = \int W(\boldsymbol{q}, \boldsymbol{p})\, \hat{A}(\boldsymbol{q}, \boldsymbol{p})\, \mathrm{d}\boldsymbol{q}\mathrm{d}\boldsymbol{p}. \tag{2.11}$$

Combining this mapping with equation (2.3), one can calculate the phase-point operator in the position basis,

$$\begin{aligned} W(\boldsymbol{q}, \boldsymbol{p}) &\overset{!}{=} \frac{1}{\pi\hbar} \int\int\int \langle \boldsymbol{q} - \boldsymbol{x}|\, W(\boldsymbol{q}', \boldsymbol{p}')\, \hat{A}(\boldsymbol{q}', \boldsymbol{p}')\, |\boldsymbol{q} + \boldsymbol{x}\rangle \exp\left(\frac{2i\boldsymbol{p}\boldsymbol{x}}{\hbar}\right) \mathrm{d}\boldsymbol{x}\mathrm{d}\boldsymbol{q}'\mathrm{d}\boldsymbol{p}' \\ \Leftrightarrow \langle \tilde{\boldsymbol{q}}'|\, \hat{A}(\boldsymbol{q}', \boldsymbol{p}')\, |\tilde{\boldsymbol{q}}''\rangle &= \delta\left(\boldsymbol{q}' - \frac{\tilde{\boldsymbol{q}}' + \tilde{\boldsymbol{q}}''}{2}\right) \exp\left(-\frac{i\boldsymbol{p}'\left(\tilde{\boldsymbol{q}}'' - \tilde{\boldsymbol{q}}'\right)}{\hbar}\right). \end{aligned} \tag{2.12}$$

The detailed derivation is given in appendix A.2.

An analogous expression can be derived in the momentum basis [27, 35],

$$\langle \tilde{\boldsymbol{p}}'|\, \hat{A}(\boldsymbol{q}', \boldsymbol{p}')\, |\tilde{\boldsymbol{p}}''\rangle = \delta\left(\boldsymbol{p}' - \frac{\tilde{\boldsymbol{p}}' + \tilde{\boldsymbol{p}}''}{2}\right) \exp\left(-\frac{i\boldsymbol{q}'\left(\tilde{\boldsymbol{p}}'' - \tilde{\boldsymbol{p}}'\right)}{\hbar}\right). \tag{2.13}$$

Given these expressions, the phase-point operator can be written explicitly in the position and momentum basis, respectively,

$$\hat{A}(\boldsymbol{q},\boldsymbol{p}) = 2\int\int\int |\tilde{\boldsymbol{q}}'\rangle \langle\tilde{\boldsymbol{q}}'|\,\boldsymbol{p}\rangle \langle\boldsymbol{p}|\,\tilde{\boldsymbol{q}}''\rangle \langle\tilde{\boldsymbol{q}}'-\tilde{\boldsymbol{q}}|\,\boldsymbol{q}\rangle \langle\boldsymbol{q}|\,\tilde{\boldsymbol{q}}''+\tilde{\boldsymbol{q}}\rangle \langle\tilde{\boldsymbol{q}}''|\,\mathrm{d}\tilde{\boldsymbol{q}}\mathrm{d}\tilde{\boldsymbol{q}}'\mathrm{d}\tilde{\boldsymbol{q}}'', \quad (2.14)$$

$$\hat{A}(\boldsymbol{q},\boldsymbol{p}) = 2\int\int\int |\tilde{\boldsymbol{p}}'\rangle \langle\tilde{\boldsymbol{p}}'|\,\boldsymbol{q}\rangle \langle\boldsymbol{q}|\,\tilde{\boldsymbol{p}}''\rangle \langle\tilde{\boldsymbol{p}}'-\tilde{\boldsymbol{p}}|\,\boldsymbol{p}\rangle \langle\boldsymbol{p}|\,\tilde{\boldsymbol{p}}''+\tilde{\boldsymbol{p}}\rangle \langle\tilde{\boldsymbol{p}}''|\,\mathrm{d}\tilde{\boldsymbol{p}}\mathrm{d}\tilde{\boldsymbol{p}}'\mathrm{d}\tilde{\boldsymbol{p}}''. \quad (2.15)$$

The properties of the Wigner function described earlier follow from properties of the phase-point operators, as shown in [35]. The normalisation of the Wigner function in equation (2.9) follows from the normalised trace of the phase-point operator at each point $(\boldsymbol{q},\boldsymbol{p})$ in phase space,

$$\begin{aligned}
\mathrm{Tr}\left(\hat{A}(\boldsymbol{q},\boldsymbol{p})\right) &= \int \langle\boldsymbol{q}'|\,\hat{A}(\boldsymbol{q},\boldsymbol{p})\,|\boldsymbol{q}'\rangle\,\mathrm{d}\boldsymbol{q}' \\
&= \int \delta(\boldsymbol{q}-\boldsymbol{q}')\exp\left(-\frac{i\boldsymbol{p}'(\boldsymbol{q}'-\boldsymbol{q}')}{\hbar}\right)\mathrm{d}\boldsymbol{q}' \\
&= \int \delta(\boldsymbol{q}-\boldsymbol{q}')\,\mathrm{d}\boldsymbol{q}' \\
&= 1. \qquad (2.16)
\end{aligned}$$

Using this and equation (2.11), one can show the normalization of $W(\boldsymbol{q},\boldsymbol{p})$ using $\mathrm{Tr}(\hat{\rho}) = 1$ [35],

$$\begin{aligned}
\mathrm{Tr}(\hat{\rho}) &= \mathrm{Tr}\left(\int\int W(\boldsymbol{q},\boldsymbol{p})\,\hat{A}(\boldsymbol{q},\boldsymbol{p})\,\mathrm{d}\boldsymbol{q}\mathrm{d}\boldsymbol{p}\right) \\
&= \int\int W(\boldsymbol{q},\boldsymbol{p})\,\mathrm{Tr}\left(\hat{A}(\boldsymbol{q},\boldsymbol{p})\right)\mathrm{d}\boldsymbol{q}\mathrm{d}\boldsymbol{p} \\
&= \int\int W(\boldsymbol{q},\boldsymbol{p})\,\mathrm{d}\boldsymbol{q}\mathrm{d}\boldsymbol{p} \\
&= 1. \qquad (2.17)
\end{aligned}$$

Considering the trace of the phase-point operator product $\hat{A}(\boldsymbol{q}_1,\boldsymbol{p}_1)\,\hat{A}(\boldsymbol{q}_2,\boldsymbol{p}_2)$, one finds [35]

$$\mathrm{Tr}\left(\hat{A}(\boldsymbol{q}_1,\boldsymbol{p}_1)\,\hat{A}(\boldsymbol{q}_2,\boldsymbol{p}_2)\right) = 2\pi\hbar\delta(\boldsymbol{q}_1-\boldsymbol{q}_2)\,\delta(\boldsymbol{p}_1-\boldsymbol{p}_2). \quad (2.18)$$

The detailed calculation is shown in appendix A.3.

This shows that the phase-point operators are orthogonal operators with the inner product defined by the trace of the operator product. Thus, any Hermitian operator can be written as a linear combination of the phase-point operators [27, 35]. Using equations (2.11) and (2.18), an expression for the Wigner function $W(\boldsymbol{q},\boldsymbol{p})$ in terms

of the phase-point operators can be given,

$$\hat{\rho}\hat{A}\left(\boldsymbol{q}',\boldsymbol{p}'\right) = \int\int W\left(\boldsymbol{q},\boldsymbol{p}\right)\hat{A}\left(\boldsymbol{q},\boldsymbol{p}\right)\hat{A}\left(\boldsymbol{q}',\boldsymbol{p}'\right)\mathrm{d}\boldsymbol{q}\mathrm{d}\boldsymbol{p} \tag{2.19}$$

$$\begin{aligned}\Rightarrow \mathrm{Tr}\left(\hat{\rho}\hat{A}\left(\boldsymbol{q}',\boldsymbol{p}'\right)\right) &= \mathrm{Tr}\left(\int\int W\left(\boldsymbol{q},\boldsymbol{p}\right)\hat{A}\left(\boldsymbol{q},\boldsymbol{p}\right)\hat{A}\left(\boldsymbol{q}',\boldsymbol{p}'\right)\mathrm{d}\boldsymbol{q}\mathrm{d}\boldsymbol{p}\right)\\ &= \int\int W\left(\boldsymbol{q},\boldsymbol{p}\right)\mathrm{Tr}\left(\hat{A}\left(\boldsymbol{q},\boldsymbol{p}\right)\hat{A}\left(\boldsymbol{q}',\boldsymbol{p}'\right)\right)\mathrm{d}\boldsymbol{q}\mathrm{d}\boldsymbol{p}\\ &= 2\pi\hbar\int\int W\left(\boldsymbol{q},\boldsymbol{p}\right)\delta\left(\boldsymbol{q}-\boldsymbol{q}'\right)\delta\left(\boldsymbol{p}-\boldsymbol{p}'\right)\mathrm{d}\boldsymbol{q}\mathrm{d}\boldsymbol{p}\\ &= 2\pi\hbar W\left(\boldsymbol{q}',\boldsymbol{p}'\right)\end{aligned} \tag{2.20}$$

$$\Rightarrow W\left(\boldsymbol{q},\boldsymbol{p}\right) = \frac{1}{2\pi\hbar}\mathrm{Tr}\left(\hat{\rho}\hat{A}\left(\boldsymbol{q},\boldsymbol{p}\right)\right). \tag{2.21}$$

As for the Wigner function, one can examine the integral of the phase-point operators over the phase space. It defines a projection operator $\hat{P}$,

$$\hat{P} = \frac{1}{2\pi\hbar}\int\int\hat{A}\left(\boldsymbol{q},\boldsymbol{p}\right)\mathrm{d}\boldsymbol{q}\mathrm{d}\boldsymbol{p}. \tag{2.22}$$

If the integral is taken over a region of the phase space spanned by $a\boldsymbol{q}+b\boldsymbol{p}=\boldsymbol{c}_1$ and $a\boldsymbol{q}+b\boldsymbol{p}=\boldsymbol{c}_2$ with $a,b\,\epsilon\,\mathbb{R}$ and $\boldsymbol{c}_1,\boldsymbol{c}_2\,\epsilon\,\mathbb{R}^D$, this operator $\hat{P}$ describes a projection onto a subspace of the phase space spanned by the eigenstates of the operator $a\hat{\boldsymbol{q}}+b\hat{\boldsymbol{p}}$ with eigenvalues lying between $\boldsymbol{c}_1$ and $\boldsymbol{c}_2$ [35].

In summary, the continuous quantum mechanical phase space is defined based on Weyl symbols and the Wigner quasi-probability-distribution. There are two ways to transform operators into Weyl symbols, where the translation with phase-point operators can be used to define an analogous translation into the discrete phase space using discrete phase-point operators, as will be shown in the following section 2.2.

2.2 The Discrete Quantum Mechanical Phase Space

After the continuous quantum mechanical phase space has been defined in section 2.1, a discrete quantum mechanical phase space can be derived in an analogous way. Therefore, a system of N orthogonal states is considered and the discrete phase space is set up on a finite mathematical field of dimension $N\times N$. Such a mathematical field can only be created if N is a prime number. There exist different possibilities to define a discrete phase space for non prime N, but since no other cases are considered in this thesis, N will be defined as a prime number in the following [35, 36].

A finite mathematical field is defined by the numbers $0,\ldots,N-1$ if all additions and multiplications are treated as calculations modulo N [35]. Analogous to the continuous phase space, the discrete phase space is a two-dimensional vector space over a finite field which is given by an $N\times N$ array of points. The two directions of the array will be labelled a_1 and a_2 as shown in figure 2.1.

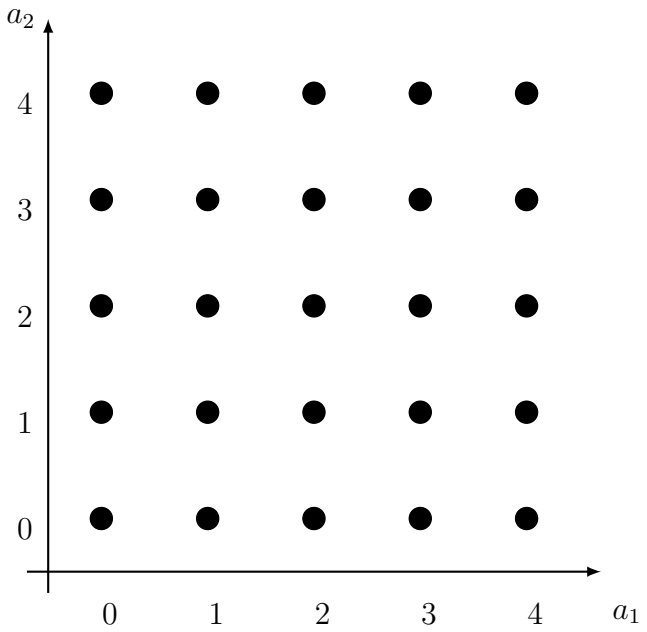

Figure 2.1: Illustration of a phase space for a system of $N = 5$ orthogonal states. Each dot stands for a point in the discrete phase space [35, 36].

On such a finite mathematical field, lines are defined by the equation $ma_1+na_2 = p$ where m, n and p are elements of the field, thus they are also treated modulo N. Two lines are parallel if their equations only differ in the value of p. For example, $ma_1 + na_2 = q$ is parallel to the $ma_1 + na_2 = p$ if $p \neq q$. One can then show that there are exactly $N(N + 1)$ lines with $N + 1$ sets of parallel lines in a phase space of a system with N orthogonal states [35].

In the two-dimensional continuous phase space there are only two sets of parallel lines, namely the vertical lines and the horizontal lines. There, each set of parallel lines is associated with an observable and the lines are identified with the eigenvalues of the corresponding operators. As explained in section 2.1, the horizontal lines are associated with the momentum operator and the vertical lines are associated with the position operator. The continuous eigenvalues of these operators are then assigned to the infinite number of horizontal and vertical lines. Analogously to the continuous phase space, an observable can be identified with each set of parallel lines in the discrete phase space and each line is identified with an eigenvalue of the corresponding operator. There is only one condition on the observables associated with the sets of parallel lines. They need to be mutually unbiased to form a basis. In formulas this means that $|\langle v_i \,|\, w_j\rangle|^2$ needs to be independent of i and j when $\{|v_i\rangle\}$ is the set of eigenstates of the operator associated with one set of parallel lines and $\{|w_i\rangle\}$ is the set of eigenstates of the operator associated with a different set of parallel lines [35].

With the discrete phase space defined as an array of $N \times N$ points for a system of N orthogonal states, the next step is to define the phase-point operators to project

each point in Hilbert space onto one point in phase space. This then defines the Weyl symbols and the Wigner function analogously to the continuous case. For each point $\boldsymbol{\alpha} = (a_1, a_2)$ in phase space, there exists one phase-point operator $\hat{A}_{\boldsymbol{\alpha}}$ which is defined so that its properties are analogous to the continuous case. Hence, the operators act on the state-space, which forces them to be $N \times N$ matrices. As in the continuous case in equation (2.16), the trace of each operator should be unity,

$$\mathrm{Tr}\left(\hat{A}_{\boldsymbol{\alpha}}\right) = 1. \tag{2.23}$$

The trace of the product of two operators in the continuous case is given by equation (2.18). In the discrete case, this translates into

$$\mathrm{Tr}\left(\hat{A}_{\boldsymbol{\alpha}}\hat{A}_{\boldsymbol{\beta}}\right) = N\delta_{\boldsymbol{\alpha},\boldsymbol{\beta}}. \tag{2.24}$$

The continuous Dirac delta functions are replaced by discrete Kronecker deltas δ_{ij} and the factor $2\pi\hbar$ is replaced by N. This replacement of the factor $2\pi\hbar$ can be loosely understood by considering an area $\mathcal{A}$ in the continuous phase space. This area contains $\frac{\mathcal{A}}{2\pi\hbar}$ orthogonal states. The translation from the continuous to the discrete phase space replaces integrals by sums. Therefore, the area $\mathcal{A}$ is replaced by a number of points. Considering the whole discrete phase space, it consists of N^2 points for a system with N orthogonal states. Thus, to get the number of orthogonal states, the number of points is divided by N, which is analogously to the continuous phase space, where the area $\mathcal{A}$ is divided by $2\pi\hbar$ to get the number of orthogonal states. For this reason, the factor $2\pi\hbar$ is replaced by N in the translation from the continuous to the discrete phase space [35].

Equation (2.22) defines a projection operator onto the continuous phase space. An analogous projection operator onto a line λ can be defined in the discrete phase space by replacing the integral by a sum and the factor $2\pi\hbar$ by N [35],

$$\hat{P}_\lambda = \frac{1}{N}\sum_{\boldsymbol{\alpha}\epsilon\lambda}\hat{A}_{\boldsymbol{\alpha}}. \tag{2.25}$$

This operator describes a projection onto the line λ of the phase space and is the average of all phase-point operators on this line.

Given these properties, there are multiple ways to define the phase-point operators. One possibility, which will later be found useful, is given by [35]

$$\begin{aligned} \hat{A}_{\boldsymbol{\alpha}} &= \frac{1}{2}\left[(-1)^{a_1}\,\hat{\sigma}_x + (-1)^{a_1+a_2}\,\hat{\sigma}_y + (-1)^{a_2}\,\hat{\sigma}_z + \hat{\mathrm{I}}\right] && \text{for } N = 2, \\ \left(\hat{A}_{\boldsymbol{\alpha}}\right)_{kl} &= \delta_{2a_1,k+l}\exp\left(\left(\frac{2\pi i}{N}\right)a_2\,(k-l)\right) && \text{for prime } N \neq 2, \end{aligned} \tag{2.26}$$

with k, l being the matrix indices which take values $0, \ldots, N-1$ and $\hat{\sigma}_x$, $\hat{\sigma}_y$, $\hat{\sigma}_z$ being the Pauli matrices.

While this is only one possible representation of the phase-point operators, other representations $\hat{A}'_{\boldsymbol{\alpha}}$ are given by unitary transformations $\hat{A}'_{\boldsymbol{\alpha}} = \hat{U}\hat{A}_{\boldsymbol{\alpha}}\hat{U}^\dagger$, since unitary transformations conserve the needed properties.

With these phase-point operators, the Wigner function $W_{\boldsymbol{\alpha}}$ can be defined in the discrete phase space analogously to the continuous phase space. Since integrals in the continuous case are translated into sums in the discrete case, equation (2.11) can be translated into

$$\hat{\rho} = \sum_{\boldsymbol{\alpha}} W_{\boldsymbol{\alpha}} \hat{A}_{\boldsymbol{\alpha}}. \tag{2.27}$$

The phase-point operators $\hat{A}_{\boldsymbol{\alpha}}$ are chosen to have properties analogous to the continuous case, so they can also be inverted to give an equation for the discrete Wigner function,

$$W_{\boldsymbol{\alpha}} = \frac{1}{N} \mathrm{Tr}\left(\hat{\rho} \hat{A}_{\boldsymbol{\alpha}}\right), \tag{2.28}$$

which can be shown to have properties analogous to the continuous Wigner function. As in equation (2.9), the discrete Wigner function is normalized,

$$\sum_{\boldsymbol{\alpha}} W_{\boldsymbol{\alpha}} = 1. \tag{2.29}$$

Hence it also is a quasi-probability-distribution. Analogously to the continuous case, the sum p_λ of the Wigner function along a line λ of the phase space describes the probability distribution of the observable associated with the line,

$$p_\lambda = \sum_{\boldsymbol{\alpha} \epsilon \lambda} W_{\boldsymbol{\alpha}}. \tag{2.30}$$

Also the inner product of two Wigner functions $W_{\boldsymbol{\alpha}}$ and $W'_{\boldsymbol{\alpha}}$ corresponding to two different density operators $\hat{\rho}$ and $\hat{\rho}'$ is given analogously to equation (2.10), where again $2\pi\hbar$ is replaced by N,

$$N \sum_{\boldsymbol{\alpha}} W_{\boldsymbol{\alpha}} W'_{\boldsymbol{\alpha}} = \mathrm{Tr}\left(\hat{\rho}\hat{\rho}'\right). \tag{2.31}$$

This way, a discrete quantum mechanical phase space is defined analogously to the continuous quantum mechanical phase space. While systems with continuous states should be studied in the continuous phase space, the discrete phase space is more useful for systems with a finite number of orthogonal states, like spin systems.

2.3 The First Order Truncated Wigner Approach

After the quantum mechanical phase space is defined, dynamics of a quantum system can be calculated using the phase space variables. Therefore, the time evolution of a Weyl symbol $\Omega_{\mathrm{W}}(\boldsymbol{q}, \boldsymbol{p})$ of an arbitrary quantum mechanical operator $\hat{\Omega}(\hat{\boldsymbol{q}}, \hat{\boldsymbol{p}})$ needs to be calculated. The time evolution of the operator in the Hilbert space is given by the von Neumann equation [11, 23],

$$i\hbar \dot{\hat{\Omega}} = \left[\hat{H}, \hat{\Omega}\right], \tag{2.32}$$

with the dot describing the time derivative, $\hat{H}$ being the Hamiltonian operator and the square brackets describing the commutator. Both operators $\hat{\Omega}$ and $\hat{H}$ depend on the operators $\hat{\boldsymbol{q}}$ and $\hat{\boldsymbol{p}}$, but for convenience the arguments are left out here and in the following.

To get the time evolution of Ω_W, the Weyl symbol of both sides of equation (2.32) needs to be calculated. Then the left hand side gives $i\hbar\dot{\Omega}_\mathrm{W}$. The right hand side is harder to calculate, since the Weyl symbol of a commutator is needed. To derive this, one can consider the Weyl symbol of a general commutator of two arbitrary operators $\hat{\Omega}_1$ and $\hat{\Omega}_2$ [11, 23],

$$\begin{aligned}
[\Omega_1, \Omega_2]_\mathrm{W} &= (\Omega_1\Omega_2)_\mathrm{W} - (\Omega_2\Omega_1)_\mathrm{W} \\
&= \Omega_{1,\mathrm{W}} \left[\exp\left(\frac{-i\hbar\Lambda}{2}\right) - \exp\left(\frac{i\hbar\Lambda}{2}\right)\right] \Omega_{2,\mathrm{W}} \qquad (2.33)\\
&= \Omega_{1,\mathrm{W}} \left(-2i\sin\left(\frac{\hbar\Lambda}{2}\right)\right) \Omega_{2,\mathrm{W}}. \qquad (2.34)
\end{aligned}$$

Using $\Lambda = \frac{\overleftarrow{\partial}}{\partial \boldsymbol{p}}\frac{\overrightarrow{\partial}}{\partial \boldsymbol{q}} - \frac{\overleftarrow{\partial}}{\partial \boldsymbol{q}}\frac{\overrightarrow{\partial}}{\partial \boldsymbol{p}}$. The derivation of this time evolution is explained in detail in appendix A.4.

With this, the time evolution of a Weyl symbol on the quantum mechanical phase space can be calculated [23],

$$i\hbar\dot{\hat{\Omega}} = \left[\hat{H}, \hat{\Omega}\right] \qquad (2.35)$$

$$\Rightarrow i\hbar\dot{\Omega}_\mathrm{W} = -2iH_\mathrm{W}\sin\left(\frac{\hbar\Lambda}{2}\right)\Omega_\mathrm{W} \qquad (2.36)$$

$$\Rightarrow \dot{\Omega}_\mathrm{W} = -\frac{2}{\hbar}H_\mathrm{W}\sin\left(\frac{\hbar\Lambda}{2}\right)\Omega_\mathrm{W}. \qquad (2.37)$$

Using the definition of Λ, this equation can be written in terms of the Moyal bracket $\{\dots\}_\mathrm{MB} = \frac{2}{\hbar}\sin\left(\frac{\hbar}{2}\{\dots\}\right)$ with the Poisson brackets $\{\dots\} = \frac{\overleftarrow{\partial}}{\partial \boldsymbol{p}}\frac{\overrightarrow{\partial}}{\partial \boldsymbol{q}} - \frac{\overleftarrow{\partial}}{\partial \boldsymbol{q}}\frac{\overrightarrow{\partial}}{\partial \boldsymbol{p}}$ [23],

$$\dot{\Omega}_\mathrm{W}(\boldsymbol{q}, \boldsymbol{p}) = -\left\{H_\mathrm{W}(\boldsymbol{q}, \boldsymbol{p}), \Omega_\mathrm{W}(\boldsymbol{q}, \boldsymbol{p})\right\}_\mathrm{MB}. \qquad (2.38)$$

Given the equation of motion of the Weyl symbol $\dot{\Omega}_\mathrm{W}$, also the equation of motion of the Wigner function W as the Weyl symbol of the density operator $\hat{\rho}$ is defined and thus the dynamics of the spin system in phase space can be calculated. The differential equation (2.38) is impossible to write down in a closed expression and more of symbolic nature. To get an approximation of the solution, one can Taylor expand the Moyal bracket in terms of $\hbar$ around $\hbar = 0$, where the Moyal bracket turns into the Poisson bracket. So, up to first order in $\hbar$, the quantum fluctuations

do not effect the equations of motion [23],

$$\begin{aligned}\dot{\Omega}_{\mathrm{W}}(\boldsymbol{q},\boldsymbol{p}) &= -\frac{2}{\hbar}H_{\mathrm{W}}(\boldsymbol{q},\boldsymbol{p})\left[\frac{\hbar}{2}\Lambda+\mathcal{O}\left(\hbar^3\right)\right]\Omega_{\mathrm{W}}(\boldsymbol{q},\boldsymbol{p})\\ &= -\left\{H_{\mathrm{W}}(\boldsymbol{q},\boldsymbol{p}),\Omega_{\mathrm{W}}(\boldsymbol{q},\boldsymbol{p})\right\}+\mathcal{O}\left(\hbar^2\right)\\ &= \left\{\Omega_{\mathrm{W}}(\boldsymbol{q},\boldsymbol{p}),H_{\mathrm{W}}(\boldsymbol{q},\boldsymbol{p})\right\}+\mathcal{O}\left(\hbar^2\right). \end{aligned} \tag{2.39}$$

Equation (2.39) is the Liouville equation which describes classical time evolutions.

The expectation value of an arbitrary operator is given by the average of its Weyl symbol weighted with the Wigner function, as stated in equation (2.6). Thus, the time evolution of the expectation value can be approximated in the Heisenberg picture using the average of the classical time evolution of the Weyl symbol weighted with a Wigner function which is fixed at the initial state. The classical time evolution of the Weyl symbol can be calculated using the classical equations of motion for $\boldsymbol{q}(t)$ and $\boldsymbol{p}(t)$ and putting $\Omega_{\mathrm{W}}(\boldsymbol{q},\boldsymbol{p})(t) \to \Omega_{\mathrm{W}}(\boldsymbol{q}_{\mathrm{cl}}(t),\boldsymbol{p}_{\mathrm{cl}}(t))$, where $\boldsymbol{q}_{\mathrm{cl}}(t)$ and $\boldsymbol{p}_{\mathrm{cl}}(t)$ are the classical time evolutions of the initial values $\boldsymbol{q}_0$ and $\boldsymbol{p}_0$ [23, 27],

$$\left\langle\hat{\Omega}\right\rangle(t) \approx \int\!\!\int \Omega_{\mathrm{W}}(\boldsymbol{q}_{\mathrm{cl}}(t),\boldsymbol{p}_{\mathrm{cl}}(t))\,W(\boldsymbol{q}_0,\boldsymbol{p}_0)\,\mathrm{d}\boldsymbol{q}_0\mathrm{d}\boldsymbol{p}_0 \tag{2.40}$$

With the same approximation also the time evolution of the Wigner function can be easily calculated and since the Wigner function is the Weyl symbol of the density operator, this gives the dynamics of the quantum mechanical system.

Analogously to the continuous phase space, the time evolution can be calculated for systems with discrete states on the discrete phase space. The time evolution of a Weyl symbol is not influenced by the form of the phase space, so also in the discrete case the time evolution of a Weyl symbol can be approximated by a classical time evolution. Thus, the equations of motion of an arbitrary operator $\Omega(\boldsymbol{\alpha})$ in the discrete phase space are given analogously to equation (2.39),

$$\dot{\Omega}_{\mathrm{W}}(\boldsymbol{\alpha}) = \left\{\Omega_{\mathrm{W}}(\boldsymbol{\alpha}),H_{\mathrm{W}}(\boldsymbol{\alpha})\right\}+\mathcal{O}\left(\hbar^2\right). \tag{2.41}$$

The time evolution of the expectation value of an operator $\hat{\Omega}$ can now be calculated analogously to equation (2.40) in the continuous case. The system is again considered in the Heisenberg picture, so that the Wigner function is fixed, while the Weyl symbols are evolved in time. By putting, analogously to the continuous case, $\Omega_{\mathrm{W}}(\boldsymbol{\alpha})$ to $\Omega_{\mathrm{W}}(\boldsymbol{\alpha}_{\mathrm{cl}}(t))$ with the classical time evolution $\boldsymbol{\alpha}_{\mathrm{cl}}(t)$ of the initial value $\boldsymbol{\alpha}_0$ and by translating the integrals into sums, one gets [26, 27]

$$\left\langle\hat{\Omega}\right\rangle(t) \approx \sum_{\boldsymbol{\alpha}} \Omega_{\mathrm{W}}(\boldsymbol{\alpha}_{\mathrm{cl}}(t))\,W(\boldsymbol{\alpha}_0), \tag{2.42}$$

which is analogous to equation (2.40).

The dynamics of the expectation value of an operator $\left\langle\hat{\Omega}\right\rangle$ can now be calculated numerically using equation (2.42). Since this time evolution is truncated at first order in $\hbar$, the dynamics of the quantum mechanical system are approximated semi-classically.

2.4 The Second Order Truncated Wigner Approach

In section 2.3, the time evolution of the expectation value of an operator in the quantum mechanical phase space was calculated in the Heisenberg picture, where the Weyl symbols are evolved in time while the Wigner function is time independent. It is also possible to consider the time evolution of the expectation value of an operator in phase space in the Schrödinger picture, where the Weyl symbols $\Omega_{\mathrm{W}}(\boldsymbol{q}_0, \boldsymbol{p}_0)$ are time independent and the phase-point operators $\hat{A}(\boldsymbol{q}(t), \boldsymbol{p}(t))$ are evolved in time. In the Hilbert space this means that the density matrix $\rho(t)$ depends on time. Thus, the Wigner function is still time independent, while the time evolution is defined in phase-point operators [16],

$$\hat{A}(\boldsymbol{q}(t), \boldsymbol{p}(t)) = \exp(-iHt)\,\hat{A}(\boldsymbol{q}, \boldsymbol{p})\exp(iHt) \tag{2.43}$$

$$\Rightarrow \hat{\rho}(t) = \int\int W(\boldsymbol{q}_0, \boldsymbol{p}_0)\,\hat{A}(\boldsymbol{q}(t), \boldsymbol{p}(t)). \tag{2.44}$$

The same time evolution of the density operator can be calculated using discrete time evolved phase-point operators,

$$\begin{aligned}\hat{A}_{\boldsymbol{\alpha}}(t) &= \hat{A}(\boldsymbol{\alpha}(t)) \\ &= \exp(-iHt)\,\hat{A}_{\boldsymbol{\alpha}}\exp(iHt) \qquad (2.45)\end{aligned}$$

$$\Rightarrow \hat{\rho}(t) = \sum_{\boldsymbol{\alpha}} W(\boldsymbol{\alpha}_0)\,\hat{A}_{\boldsymbol{\alpha}}(t). \tag{2.46}$$

While the time evolutions derived in the Heisenberg picture in section 2.3 were purely classical approximations, quantum effects can be included by calculating the time evolution of the phase-point operators using the Bogoliubov-Born-Green-Kirkwood-Yvon (BBGKY) hierarchy and the reduced density operators [16]. This way, an approximation of the equations of motion to higher orders is possible, while the approximation was only to first order in $\hbar$ in section 2.3. Thus, the correlations between the spins in the simulated model can be calculated to higher accuracy, as will be analysed in chapter 4.

Since the phase-point operators fulfil the same properties as the density operators except for the positive definiteness, the time evolution of reduced density operators using a BBGKY hierarchy can analogously be defined for reduced phase-point operators [16]. Therefore, the equations of motion will be derived generally for reduced density operators and after this the analogous expressions will be given for the phase-point operators.

Reduced density operators $\hat{\varrho}_{1\ldots s}$ are defined as the partial trace of the N-particle density operator $\hat{\rho}_{1\ldots N} = \hat{\rho}_1 \otimes \hat{\rho}_2 \otimes \cdots \otimes \hat{\rho}_N$ [3, 21],

$$\hat{\varrho}_{1\ldots s} = \mathrm{Tr}_{s+1\ldots N}(\hat{\rho}_{1\ldots N}). \tag{2.47}$$

The normalisation condition of the density operator still holds,

$$\mathrm{Tr}_{1\ldots s}(\hat{\varrho}_{1\ldots s}) = 1. \tag{2.48}$$

The properties of the reduced density operators follow directly from the properties of the full density operator, which can be directly seen from the definition in equation (2.47). From this it can also be seen that all reduced density operators of different orders are directly connected to each other [3],

$$\hat{\varrho}_{1\ldots s} = \mathrm{Tr}_{s+1\ldots s+k}\left(\hat{\varrho}_{1\ldots s+k}\right). \tag{2.49}$$

Plugging the definition of the reduced density operators into the von Neumann equation (2.32), the time evolution of the reduced density operators of general order can be calculated for a general N-particle Hamiltonian $\hat{H}_{1\ldots N}$ with a term for on-site interactions and another term for pair interactions [3, 21],

$$\hat{H}_{1\ldots N} = \sum_{i=1}^{N} \hat{H}_i + \sum_{\substack{i,j=1 \\ i\neq j}}^{N} \hat{H}_{ij}, \tag{2.50}$$

$$i\hbar\dot{\hat{\rho}}_{1\ldots N} = \left[\hat{H}_{1\ldots N}, \hat{\rho}_{1\ldots N}\right] \tag{2.51}$$

$$\Rightarrow i\hbar\mathrm{Tr}_{s+1\ldots N}\left(\dot{\hat{\rho}}_{1\ldots N}\right) = \left[\hat{H}_{1\ldots N}, \mathrm{Tr}_{s+1\ldots N}\hat{\rho}_{1\ldots N}\right] \tag{2.52}$$

$$\begin{aligned}\Rightarrow i\hbar\dot{\hat{\varrho}}_{1\ldots s} &= \sum_{i=1}^{N}\left[\hat{H}_i, \hat{\varrho}_{1\ldots s}\right] + \sum_{\substack{i,j=1 \\ i\neq j}}^{N}\mathrm{Tr}_j\left(\left[\hat{H}_{ij}, \hat{\varrho}_{1\ldots s,j}\right]\right) \\ &= \sum_{i=1}^{s}\left[\hat{H}_i, \hat{\varrho}_{1\ldots s}\right] + \sum_{i=1}^{s}\sum_{\substack{j=1 \\ j\neq i}}^{N}\mathrm{Tr}_j\left(\left[\hat{H}_{ij}, \hat{\varrho}_{1\ldots s,j}\right]\right).\end{aligned} \tag{2.53}$$

The reduced density operators of first and second order $\hat{\varrho}_i$ and $\hat{\varrho}_{ij}$ are defined as [3, 16, 21]

$$\hat{\rho}_i = \mathrm{Tr}_{\not{i}}\left(\hat{\rho}_{1\ldots N}\right), \tag{2.54}$$

$$\hat{\rho}_{ij} = \mathrm{Tr}_{\not{i}\not{j}}\left(\hat{\rho}_{1\ldots N}\right), \tag{2.55}$$

where $\mathrm{Tr}_{\not{i}}$ and $\mathrm{Tr}_{\not{i}\not{j}}$ denote the partial trace over the whole Hilbert space except for the factor associated with particle i or particles i and j respectively.

From equation (2.53), the equations of motion for the reduced density operators of first and second order can be written down explicitly as further derived in [3, 16],

$$i\hbar\dot{\hat{\varrho}}_i = \left[\hat{H}_i, \hat{\varrho}_i\right] + \sum_{\substack{k=1 \\ k\neq i}}^{N}\mathrm{Tr}_k\left(\left[\hat{H}_{ik}, \hat{\varrho}_{ik}\right]\right), \tag{2.56}$$

$$i\hbar\dot{\hat{\varrho}}_{ij} = \left[\hat{H}_i + \hat{H}_j + \hat{H}_{ij}, \hat{\varrho}_{ij}\right] + \sum_{\substack{k=1 \\ k\neq i,j}}^{N}\mathrm{Tr}_k\left(\left[\hat{H}_{ik} + \hat{H}_{jk}, \hat{\varrho}_{ijk}\right]\right). \tag{2.57}$$

For most physical N-particle systems, the dynamics are mostly influenced by the lower order reduced density operators. Thus, the equations of motion can be approximated by decoupling lower orders of the hierarchy and neglecting higher orders. In most cases the approximation already works well if only the first four orders are considered [3, 21]. With this approximation it is possible to write down closed expressions for the differential equations resulting from (2.51). The full hierarchy then has the same properties as the exact von Neumann equation, while the properties of the lower order approximations depend on the decoupling and may need to be corrected for each approximation [3].

The time evolution of the density operator can be expressed as a function of the time evolved discrete phase-point operators using equation (2.27) [16],

$$\begin{aligned}\hat{\rho}_{1\ldots N}(t) &= \sum_{\boldsymbol{\alpha}} W_{\boldsymbol{\alpha}} \hat{A}_{\boldsymbol{\alpha}}(t) \\ &= \sum_{\alpha_1\ldots\alpha_N} W_{\alpha_1\ldots\alpha_N} \hat{A}_{1\ldots N}^{\alpha_1\ldots\alpha_N}(t) \\ &= \sum_{\alpha_1\ldots\alpha_N} W_{\alpha_1} \otimes \cdots \otimes W_{\alpha_N} \hat{A}_{\alpha_1}(t) \otimes \cdots \otimes \hat{A}_{\alpha_N}(t) . \end{aligned} \tag{2.58}$$

Thus, also the time evolution of the phase-point operators is given by the von Neumann equation,

$$i\hbar \dot{\hat{A}}_{\boldsymbol{\alpha}} = \left[\hat{H}_{1\ldots N}, \hat{A}_{\boldsymbol{\alpha}}\right] . \tag{2.59}$$

As already mentioned earlier, the phase-point operators have the same properties as the density operators, except for the positive definiteness. Therefore, reduced phase-point operators $\hat{\mathscr{A}}_{\boldsymbol{\alpha}}$ can be defined analogously to the reduced density operators [16],

$$\hat{\mathscr{A}}_{1\ldots s}^{\alpha_1\ldots\alpha_N} = \mathrm{Tr}_{s+1\ldots N}\left(\hat{A}_{1\ldots N}^{\alpha_1\ldots\alpha_N}\right) . \tag{2.60}$$

Given the reduced phase-point operators, their time evolution, given by the von Neumann equation, can be approximated analogously to the time evolution of the density operators using a BBGKY hierarchy [16].

The first and second order reduced phase-point operators $\hat{\mathscr{A}}_i$ and $\hat{\mathscr{A}}_{ij}$ can be defined analogously to the first and second order reduced density operators in equations (2.54) and (2.55) [16],

$$\hat{\mathscr{A}}_i = \mathrm{Tr}_{\not{\imath}}\left(\hat{\mathscr{A}}_{1\ldots N}\right) , \tag{2.61}$$

$$\hat{\mathscr{A}}_{ij} = \mathrm{Tr}_{\not{\imath}\not{\jmath}}\left(\hat{\mathscr{A}}_{1\ldots N}\right) . \tag{2.62}$$

For a general Hamiltonian $\hat{H}_{1\ldots N}$ with on-site interactions $\hat{H}_i$ and pair interactions $\hat{H}_{ij}$, the time evolution of the first and second order phase-point operators is then given analogously to equations (2.56) and (2.57) for the first and second order re-

duced density operators [16],

$$\hat{H}_{1\ldots N} = \sum_{i=1}^{N} \hat{H}_i + \sum_{\substack{i,j=1 \\ i\neq j}}^{N} \hat{H}_{ij},$$

$$i\hbar\dot{\hat{\mathscr{A}}}_i = \left[\hat{H}_i, \hat{\mathscr{A}}_i\right] + \sum_{\substack{k=1 \\ k\neq i}}^{N} \mathrm{Tr}_k\left(\left[\hat{H}_{ik}, \hat{\mathscr{A}}_{ik}\right]\right), \tag{2.63}$$

$$i\hbar\dot{\hat{\mathscr{A}}}_{ij} = \left[\hat{H}_i + \hat{H}_j + \hat{H}_{ij}, \hat{\mathscr{A}}_{ij}\right] + \sum_{\substack{k=1 \\ k\neq i,j}}^{N} \mathrm{Tr}_k\left(\left[\hat{H}_{ik} + \hat{H}_{jk}, \hat{\mathscr{A}}_{ijk}\right]\right). \tag{2.64}$$

To get an expression for the second and third order reduced phase-point operators $\hat{\mathscr{A}}_{ij}$ and $\hat{\mathscr{A}}_{ijk}$ which occur in the time evolution, correlation operators $\hat{\mathscr{C}}_{ij}$ and $\hat{\mathscr{C}}_{ijk}$ are defined. With these, a cluster expansion for the second and third order reduced density operators can be used to separate them into product parts of first order reduced density operators and correlated parts expressed by the correlation operators [16],

$$\hat{\mathscr{A}}_{ij} = \hat{\mathscr{A}}_i\hat{\mathscr{A}}_j + \hat{\mathscr{C}}_{ij}, \tag{2.65}$$

$$\hat{\mathscr{A}}_{ijk} = \hat{\mathscr{A}}_i\hat{\mathscr{A}}_j\hat{\mathscr{A}}_k + \hat{\mathscr{A}}_i\hat{\mathscr{C}}_{jk} + \hat{\mathscr{A}}_j\hat{\mathscr{C}}_{ik} + \hat{\mathscr{A}}_k\hat{\mathscr{C}}_{ij} + \hat{\mathscr{C}}_{ijk}. \tag{2.66}$$

Using these cluster expansions, the time evolution of the first order phase-point operator in equation (2.63) can be written as

$$i\hbar\dot{\hat{\mathscr{A}}}_i = \left[\hat{H}_i, \hat{\mathscr{A}}_i\right] + \sum_{\substack{k=1 \\ k\neq i}}^{N} \mathrm{Tr}_k\left(\left[\hat{H}_{ik}, \hat{\mathscr{A}}_i\hat{\mathscr{A}}_k\right] + \left[\hat{H}_{ik}, \hat{\mathscr{C}}_{ik}\right]\right). \tag{2.67}$$

From the time evolution of the second order phase-point operator in equation (2.64), a time evolution for the correlation operator $\hat{\mathscr{C}}_{ij}$ can be derived,

$$\begin{aligned}
i\hbar\dot{\hat{\mathscr{A}}}_{ij} &= \left[\hat{H}_i + \hat{H}_j + \hat{H}_{ij}, \hat{\mathscr{A}}_{ij}\right] + \sum_{\substack{k=1 \\ k\neq i,j}}^{N} \mathrm{Tr}_k\left(\left[\hat{H}_{ik} + \hat{H}_{jk}, \hat{\mathscr{A}}_{ijk}\right]\right) \\
&= \left[\hat{H}_i + \hat{H}_j + \hat{H}_{ij}, \hat{\mathscr{A}}_i\hat{\mathscr{A}}_j + \hat{\mathscr{C}}_{ij}\right] \\
&\quad + \sum_{\substack{k=1 \\ k\neq i,j}}^{N} \mathrm{Tr}_k\left(\left[\hat{H}_{ik} + \hat{H}_{jk}, \hat{\mathscr{A}}_i\hat{\mathscr{A}}_j\hat{\mathscr{A}}_k + \hat{\mathscr{A}}_i\hat{\mathscr{C}}_{jk} + \hat{\mathscr{A}}_j\hat{\mathscr{C}}_{ik} + \hat{\mathscr{A}}_k\hat{\mathscr{C}}_{ij} + \hat{\mathscr{C}}_{ijk}\right]\right) \\
&= i\hbar\partial_t\left(\hat{\mathscr{A}}_i\hat{\mathscr{A}}_j\right) + i\hbar\partial_t\hat{\mathscr{C}}_{ij},
\end{aligned} \tag{2.68}$$

where the product rule is used in equation (2.68). Considering the terms individually, a differential equation for the correlation operator $\hat{\mathscr{C}}_{ij}$ can be derived,

$$\begin{aligned} i\hbar\partial_t\hat{\mathscr{C}}_{ij} = &\left[\hat{H}_i + \hat{H}_j, \hat{\mathscr{C}}_{ij}\right] + \left[\hat{H}_{ij}, \hat{\mathscr{A}}_i\hat{\mathscr{A}}_j + \hat{\mathscr{C}}_{ij}\right] + \sum_{\substack{k=1\\k\neq i,j}}^{N} \mathrm{Tr}_k\left(\left[\hat{H}_{ik}, \hat{\mathscr{A}}_i\hat{\mathscr{C}}_{jk}\right]\right) \\ &+ \sum_{\substack{k=1\\k\neq i,j}}^{N} \mathrm{Tr}_k\left(\left[\hat{H}_{jk}, \hat{\mathscr{A}}_j\hat{\mathscr{C}}_{ik}\right]\right) + \sum_{\substack{k=1\\k\neq i,j}}^{N} \mathrm{Tr}_k\left(\left[\hat{H}_{ik} + \hat{H}_{jk}, \hat{\mathscr{A}}_k\hat{\mathscr{C}}_{ij}\right]\right) \\ &- \hat{\mathscr{A}}_j\mathrm{Tr}_j\left(\left[\hat{H}_{ij}, \hat{\mathscr{A}}_i\hat{\mathscr{A}}_j + \hat{\mathscr{C}}_{ij}\right]\right) - \hat{\mathscr{A}}_i\mathrm{Tr}_i\left(\left[\hat{H}_{ji}, \hat{\mathscr{A}}_j\hat{\mathscr{A}}_i + \hat{\mathscr{C}}_{ji}\right]\right). \end{aligned} \tag{2.69}$$

The derivation of the equation of motion of the correlation operators is shown in detail in appendix A.5.

One can now truncate the hierarchy at second order by setting $\hat{\mathscr{C}}_{ijk}$ to zero [16]. In this case, the time evolution of the phase point operator of particle i, as given in equation (2.67), can be calculated by using equation (2.69) for the correlation operator $\hat{\mathscr{C}}_{ij}$. This gives the second order approximation of the dynamics of the quantum mechanical system, where quantum effects are included into the time evolution by the correlation operators $\hat{\mathscr{C}}_{ij}$ [16].

If the hierarchy is truncated at first order, also the second order correlation operators $\hat{\mathscr{C}}_{ij}$ are set to zero. Then the time evolution is completely classical again and it will be easily seen in section 3.2 that it results in the same equations of motion as the ansatz in section 2.3.

To get higher order approximations, the time evolution of the third order correlation operators $\hat{\mathscr{C}}_{ijk}$ needs to be calculated, which will then depend on the fourth order correlation operators $\hat{\mathscr{C}}_{ijkl}$ and so on. This way, higher order approximations can be acchieved. In the limit of an infinitely large order, the full hierarchy equals the exact solution, but is practically not possible to calculate. In this thesis only approximations up to second order will be used.

2.5 Process of the Discrete Truncated Wigner Approximation

After the discrete quantum mechanical phase space has been defined in section 2.2 and two ways to calculate the truncated equations of motion of the system in phase space have been derived in sections 2.3 and 2.4, all ingredients for the discrete truncated Wigner approximation are given and the process can be completely derived.

The approximation is based on the idea that an initial state is sampled from the discrete phase space using the Wigner distribution. This initial state is then evolved in time using truncated time evolutions. Up to now the approximation is classical. A quantum mechanical system can not be considered to be in one state, but in a

superposition of all possible states where only a probability of the individual system states is known. This leads to quantum uncertainties appearing in the dynamics. To get these quantum fluctuations into the classical approximation, a large number of time evolutions is created from different initial states sampled from the Wigner function and the resulting observables are ultimately averaged to obtain the final approximating trajectory.

Hence, first the Wigner function $W_{\boldsymbol{\alpha}}$ needs to be calculated. Since in both, the Heisenberg and the Schrödinger picture, the Wigner function does not depend on time, only the initial Wigner function needs to be calculated, given some initial density operator $\hat{\rho}_0$. The Wigner function is then calculated using equation (2.28), where the phase-point operators $\hat{A}_{\boldsymbol{\alpha}}$ are calculated using for example equation (2.26).

As explained in section 2.1, the Wigner function is a quasi-probability-distribution, which means that it has properties of a probability distribution, but it might have negative values. If the Wigner function does not have negative entries, which will appear to be the case in the systems considered in this thesis, it yields a probability for each variable associated with the points $\boldsymbol{\alpha}$ in phase space, where the variables are different in the Heisenberg and the Schrödinger picture. These associated variables can thus be sampled from the Wigner function. In the Heisenberg picture, an operator is associated with each phase space point $\boldsymbol{\alpha}$ whose Weyl symbol is classically evolved in time. Thus, an initial classical variable is sampled from the Wigner function and then evolved in time. In the Schrödinger picture, the variable sampled from the Wigner function is the initial phase-point operator $\hat{A}_{\boldsymbol{\alpha}}(0)$, which is then evolved in time using the BBGKY hierarchy of the reduced phase-point operators.

Using the first order truncated time evolution for the initial variable or the second order truncated time evolution for the initial phase-point operator from the BBGKY hierarchy, a trajectory in time can be calculated. This way, a large number R of trajectories can be created, where the initial values are sampled individually from the Wigner distribution for each trajectory. By averaging the R calculated trajectories, quantum fluctuations are brought into the system, as has been discussed earlier.

In the Heisenberg picture, averaging R time evolved observables with initial values sampled from the Wigner distribution results in an approximation of the time evolved average of an operator, as stated in equation (2.42).

In the Schrödinger picture, the averaging equals equation (2.46) and thus results in an approximation of the time evolution of the state described by the density operator $\hat{\rho}(t)$.

In summary, the discrete truncated Wigner approximation consists of the following steps:

1. Calculate the Wigner function $W_{\boldsymbol{\alpha}}$ depending on the initial density operator

$\hat{\rho}_0$ and on the initial phase-point operators $\hat{A}_{\boldsymbol{\alpha}}$,

$$
\begin{aligned}
W_{\boldsymbol{\alpha}} &= \frac{1}{N}\mathrm{Tr}\left(\hat{\rho}_0 \hat{A}_{\boldsymbol{\alpha}}\right), \\
\hat{A}_{\boldsymbol{\alpha}} &= \frac{1}{2}\left[(-1)^{a_1}\,\hat{\sigma}_x + (-1)^{a_1+a_2}\,\hat{\sigma}_y + (-1)^{a_2}\,\hat{\sigma}_z + \hat{\mathrm{I}}\right] && \text{for } N = 2, \\
\left(\hat{A}_{\boldsymbol{\alpha}}\right)_{kl} &= \delta_{2a_1,k+l}\exp\left(\left(\frac{2\pi i}{N}\right) a_2\,(k-l)\right) && \text{for prime } N \neq 2.
\end{aligned}
$$

2. Sample a variable associated with a point $\boldsymbol{\alpha}$ in phase space from the Wigner function $W_{\boldsymbol{\alpha}}$ giving a probability for all phase-space points. The sampled variable is
   a) either the Weyl symbol of an operator associated with a point $\boldsymbol{\alpha}$ in the Heisenberg picture,
   b) or the phase-point operator $\hat{A}_{\boldsymbol{\alpha}}$ associated with a point in phase space in the Schrödinger picture.

3. Calculate a trajectory in time of
   a) either the sampled Weyl symbol using the classical time evolution in the Heisenberg picture,

$$\dot{\Omega}_{\mathrm{W}}\left(\boldsymbol{\alpha}\right) = \left\{\Omega_{\mathrm{W}}\left(\boldsymbol{\alpha}\right), H_{\mathrm{W}}\left(\boldsymbol{\alpha}\right)\right\} + \mathcal{O}\left(\hbar^2\right),$$

   b) or the sampled phase-point operator using the time evolution derived with the BBGKY hierarchy of reduced phase-point operators,

$$i\hbar\dot{\hat{\mathscr{A}}}_i = \left[\hat{H}_i, \hat{\mathscr{A}}_i\right] + \sum_{\substack{k=1 \\ k\neq i}}^{N} \mathrm{Tr}_k\left(\left[\hat{H}_{ik}, \hat{\mathscr{A}}_i\hat{\mathscr{A}}_k\right] + \left[\hat{H}_{ik}, \hat{\mathscr{C}}_{ik}\right]\right),$$

   combined with equation (2.69).

4. Calculate R trajectories and average the resulting observables to obtain
   a) either the time evolution of the expectation value of the considered operator,

$$\left\langle\hat{\Omega}\right\rangle(t) = \sum_{\boldsymbol{\alpha}} \Omega_{\mathrm{W}}\left(\boldsymbol{\alpha}_{\mathrm{cl}}\left(t\right)\right) W\left(\boldsymbol{\alpha}_0\right),$$

   b) or the time evolution of the sampled state described by the density operator,

$$\hat{\rho}\left(t\right) = \sum_{\boldsymbol{\alpha}} W\left(\boldsymbol{\alpha}_0\right) \hat{A}_{\boldsymbol{\alpha}}\left(t\right).$$

3 Spin-$\frac{1}{2}$ Systems and Sampling Schemes

The general setup for a discrete quantum mechanical phase space has been discussed in section 2.2. In this chapter, it will be applied to a spin-$\frac{1}{2}$ system according to [35, 36].The corresponding discrete quantum mechanical phase space will be introduced in section 3.1. Therefore, the size of the finite mathematical field and the operators associated with the different sets of parallel lines will be derived and the general definition for the phase-point operators as stated in equation (2.26) will be used to calculate the corresponding Wigner function. From this Wigner function an initial state for a spin-$\frac{1}{2}$ particle can be sampled and evolved in time using the classical time evolution from equation (2.41) or the second order approximation in equations (2.67) and (2.69). The corresponding equations of motion will be derived according to [16, 26, 27] in section 3.2 for a general Hamiltonian. In section 3.3, other possible choices for phase-point operators will be introduced which will lead to various possible initial states which can be sampled from the Wigner function. This variety in sampling schemes for the initial states will then give different results in the simulation process and it will be discussed how to interpret this apparent ambiguity. The so derived approximations will be benchmarked in section 3.4. There, the simulations are calculated for the exactly solvable Ising chain and the results for the different sampling schemes are compared to the exact solutions, which will be derived in section 3.4 according to [27], to benchmark the approximation and the sampling schemes.

3.1 The Discrete Phase Space of a Spin-$\frac{1}{2}$ System

In a system of spin-$\frac{1}{2}$ particles, the spin operators are the Pauli matrices $\hat{\sigma}_x$, $\hat{\sigma}_y$ and $\hat{\sigma}_z$,

$$\hat{\sigma}_x = \begin{pmatrix} 0 & 1 \\ 1 & 0 \end{pmatrix}, \qquad \begin{aligned} &\text{eigenstates}: \quad |x_0\rangle = \begin{pmatrix} 1 \\ 1 \end{pmatrix}, \quad |x_1\rangle = \begin{pmatrix} 1 \\ -1 \end{pmatrix}, \\ &\text{eigenvalues}: \qquad x_0 = 1, \qquad\quad x_1 = -1, \end{aligned}$$

$$\hat{\sigma}_y = \begin{pmatrix} 0 & -\mathrm{i} \\ \mathrm{i} & 0 \end{pmatrix}, \qquad \begin{aligned} &\text{eigenstates}: \quad |y_0\rangle = \begin{pmatrix} 1 \\ \mathrm{i} \end{pmatrix}, \quad |y_1\rangle = \begin{pmatrix} 1 \\ -\mathrm{i} \end{pmatrix}, \\ &\text{eigenvalues}: \qquad y_0 = 1, \qquad\quad y_1 = -1, \end{aligned}$$

$$\hat{\sigma}_z = \begin{pmatrix} 1 & 0 \\ 0 & -1 \end{pmatrix}, \qquad \begin{aligned} &\text{eigenstates}: \quad |z_0\rangle = \begin{pmatrix} 1 \\ 0 \end{pmatrix}, \quad |z_1\rangle = \begin{pmatrix} 0 \\ 1 \end{pmatrix}, \\ &\text{eigenvalues}: \qquad z_0 = 1, \qquad\quad z_1 = -1. \end{aligned}$$

These matrices have the following properties, which can be proven easily,

$$\hat{\sigma}_i \hat{\sigma}_j = \delta_{ij} + i \sum_{\substack{k \\ =x,y,z}} \epsilon_{ijk} \hat{\sigma}_k, \tag{3.1}$$

$$[\hat{\sigma}_i, \hat{\sigma}_j] = 2i \sum_{\substack{k \\ =x,y,z}} \epsilon_{ijk} \hat{\sigma}_k, \tag{3.2}$$

$$\mathrm{Tr}\,(\hat{\sigma}_i) = 0, \tag{3.3}$$

$$\mathrm{Det}\,(\hat{\sigma}_i) = 1, \tag{3.4}$$

with $i, j \in \{x, y, z\}$. ϵ_{ijk} is the antisymmetric Levi-Civita symbol with $\epsilon_{xyz} = 1$. Here and in the following, $\hbar$ is set to one. The Pauli matrices have each two eigenvalues, namely 1 and -1. Thus, the spins have two orthogonal states in each direction. Since the discrete phase space is an $N \times N$ array of points where N is the number of orthogonal states as explained in section 2.2, it is a 2×2 finite mathematical field for a spin-$\frac{1}{2}$ system. Therefore, all calculations are done modulo 2, see also [35, 36]. A 2×2 mathematical field consists of three sets of two parallel lines each, as can be shown using the definitions of lines and parallel lines in section 2.2. An illustration of the lines in the 2×2 mathematical field is shown in figure 3.1, where also the eigenvalues associated with the different lines are denoted. These associations will be derived in the following.

One vertical line is defined by the equation $a_1 = 0$, it consists of the points $(0, 0)$ and $(0, 1)$. The other vertical line is given by $a_1 = 1$ and contains the points $(1, 0)$

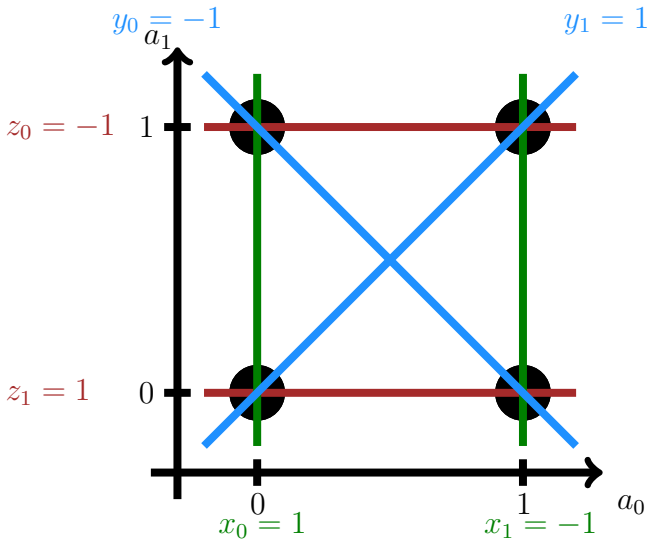

Figure 3.1: Phase space of a spin-$\frac{1}{2}$ system with sets of parallel lines and associated observables. Each set of parallel lines and the associated observables are drawn in one colour. The eigenvalues corresponding to the eigenstates associated with each line are denoted next to the corresponding lines.

and $(1, 1)$. Since their equations only differ in the right-hand side, the two lines are parallel. The lower horizontal line is defined by the equation $a_2 = 0$ and includes the points $(0, 0)$ and $(1, 0)$, while the upper horizontal line is defined by $a_2 = 1$ with the points $(0, 1)$ and $(1, 1)$. Also these two equations only differ in the right-hand side, so the two horizontal lines are parallel. Further, there exist two diagonal lines, one of them is defined by the equation $a_1 + a_2 = 0$ and contains the points $(0, 0)$ and $(1, 1)$, while the second one is defined by $a_1 + a_2 = 1$ and consists of the points $(0, 1)$ and $(1, 0)$. Also these two equations differ only in the right-hand side, therefore this is the third pair of parallel lines. In the end, the phase space of a spin-$\frac{1}{2}$ system consists of two horizontal, two vertical and two diagonal parallel lines with which operators and eigenstates need to be associated as explained in section 2.2, see also [26, 27, 35, 36].

One can easily show that the spin operators constitute mutually unbiased observables, given by the Pauli basis. In section 2.2, two bases are defined to be mutually unbiased if the quantity $|\langle v_i|\, w_j\rangle|^2$, with the sets of eigenstates $\{|v_i\rangle\}$ and $\{|w_j\rangle\}$ of the two operators, is independent of i and j. This can be easily verified by direct evaluation in the eigenstate basis of the Pauli operators, see appendix B.1. Thus, the Pauli matrices can be associated with the three sets of parallel lines in the discrete phase space of a spin-$\frac{1}{2}$ system. In the following the vertical lines will be associated with $\hat{\sigma}_x$ and the horizontal lines with $\hat{\sigma}_z$ [35].

In this configuration $\hat{\sigma}_x$ and $\hat{\sigma}_z$ are translation operators in phase space, since each line is associated with an eigenstate of the operator associated with the corre-

sponding axis and $\hat{\sigma}_x$ translates one eigenstate of $\hat{\sigma}_z$ into the other and vice versa,

$$\begin{aligned}
\hat{\sigma}_x |z_0\rangle &= \begin{pmatrix} 0 & 1 \\ 1 & 0 \end{pmatrix} \begin{pmatrix} 1 \\ 0 \end{pmatrix} = \begin{pmatrix} 0 \\ 1 \end{pmatrix} = |z_1\rangle , \\
\hat{\sigma}_x |z_1\rangle &= \begin{pmatrix} 0 & 1 \\ 1 & 0 \end{pmatrix} \begin{pmatrix} 0 \\ 1 \end{pmatrix} = \begin{pmatrix} 1 \\ 0 \end{pmatrix} = |z_0\rangle , \\
\hat{\sigma}_z |x_0\rangle &= \begin{pmatrix} 1 & 0 \\ 0 & -1 \end{pmatrix} \begin{pmatrix} 1 \\ 1 \end{pmatrix} = \begin{pmatrix} 1 \\ -1 \end{pmatrix} = |x_1\rangle , \\
\hat{\sigma}_z |x_1\rangle &= \begin{pmatrix} 1 & 0 \\ 0 & -1 \end{pmatrix} \begin{pmatrix} 1 \\ -1 \end{pmatrix} = \begin{pmatrix} 1 \\ 1 \end{pmatrix} = |x_0\rangle .
\end{aligned} \tag{3.5}$$

This means that $\hat{\sigma}_z$ interchanges the two vertical lines and $\hat{\sigma}_x$ interchanges the two horizontal lines in the phase space.

One property of the Wigner function is that it is translationally covariant on the phase space, analogously to the continuous Wigner function, see [35, 36]. Thus, if W is the Wigner function of a density operator $\hat{\rho}$ and a horizontal translation operator $\hat{H}_\mathrm{t}$ is applied on $\hat{\rho}$, W changes by a horizontal translation. A horizontal translation by one unit on the discrete phase space is given by interchanging the two vertical lines, since all calculations are done modulo two. As already discussed, this interchange of the two vertical lines is mathematically given by applying the Pauli operator $\hat{\sigma}_z$ if the eigenstates of $\hat{\sigma}_z$ and $\hat{\sigma}_x$ are associated with the horizontal and vertical lines. This shows that the translational covariance of the Wigner function is given by the association of the eigenstates of the horizontal translation operator $\hat{H}_\mathrm{t} = \hat{\sigma}_z$ with the horizontal lines. In an analogous way a vertical translation operator $\hat{V}_\mathrm{t} = \hat{\sigma}_x$ can be defined, which interchanges the two horizontal lines of the phase space if applied on a density operator $\hat{\rho}$. The translational covariance of the Wigner function is thus given if the two vertical lines are associated with the eigenstates of the vertical translation operator and analogously the two horizontal lines are associated with the eigenstates of the horizontal translation operator.

The Wigner function then also needs to be translationally covariant under a one unit translation in the diagonal direction, which corresponds to interchanging the horizontal and the vertical lines. Thus, a diagonal translation operator is given by the combination of the vertical and the horizontal translation operator, $\hat{V}_\mathrm{t}\hat{H}_\mathrm{t} = \hat{\sigma}_x\hat{\sigma}_z = \mathrm{i}\hat{\sigma}_y$, using equation (3.1). Analogoulsy to the horizontal and the vertical cases, the diagonal lines need to be associated with the basis of the eigenstates of the diagonal translation operator to ensure the translational covariance of the discrete Wigner function.

Thus, all three spin operators are associated with the three orthogonal directions in the discrete phase space of a spin-$\frac{1}{2}$ system [35, 36].

When the Pauli matrices are associated with the three sets of parallel lines, then each line needs to be associated with an eigenstate of the corresponding operator.

Thus, there are two choices for each set of parallel lines to associate the two eigenstates with the two lines. To find a consistent definition, the Wigner function is considered, because it requires the sum over each line λ in phase space to equal the probability of the measurement outcome which is associated with said line, as stated in equation (2.30). Hence, one can calculate the Wigner function with the initial condition that the system is prepared in an eigenstate of the Pauli matrices to see which line is associated with this eigenstate, since the sum of the Wigner function over this line needs to be one [35, 36].

To calculate the Wigner function, first the phase-point operators $\hat{A}_{\boldsymbol{\alpha}}$ need to be calculated using equation (2.11) for $N = 2$,

$$\hat{A}_{\boldsymbol{\alpha}} = \frac{1}{2}\left[(-1)^{a_1}\,\hat{\sigma}_x + (-1)^{a_1+a_2}\,\hat{\sigma}_y + (-1)^{a_2}\,\hat{\sigma}_z + \hat{\mathrm{I}}\right] \tag{3.6}$$

$$\Rightarrow\ \hat{A}_{(0,1)} = \begin{pmatrix} 0 & \frac{1}{2}(1+i) \\ \frac{1}{2}(1-i) & 1 \end{pmatrix}, \qquad \hat{A}_{(1,1)} = \begin{pmatrix} 0 & \frac{1}{2}(-1-i) \\ \frac{1}{2}(-1+i) & 1 \end{pmatrix},$$

$$\hat{A}_{(0,0)} = \begin{pmatrix} 1 & \frac{1}{2}(1-i) \\ \frac{1}{2}(1+i) & 0 \end{pmatrix}, \qquad \hat{A}_{(1,0)} = \begin{pmatrix} 1 & \frac{1}{2}(-1+i) \\ \frac{1}{2}(-1-i) & 0 \end{pmatrix}.$$

The density operator of a spin-$\frac{1}{2}$ system is given by the general form [26, 27, 35]

$$\hat{\rho} = \frac{1}{2}\left[\langle\hat{\sigma}_x\rangle\,\hat{\sigma}_x + \langle\hat{\sigma}_y\rangle\,\hat{\sigma}_y + \langle\hat{\sigma}_z\rangle\,\hat{\sigma}_z + \hat{\mathrm{I}}\right]. \tag{3.7}$$

If one initially prepares the system in the $+1$ eigenstate of an operator $\hat{\sigma}_i$ without any other conditions on $\hat{\sigma}_j$ for $j \neq i$, the expectation values become $\langle\hat{\sigma}_i\rangle = 1$ and $\langle\hat{\sigma}_j\rangle = 0$. This way, one can calculate the initial density operators $\hat{\rho}_x$, $\hat{\rho}_y$ and $\hat{\rho}_z$, where the system is prepared in the $+1$ eigenstate of the x-, y- and z-Pauli matrix respectively,

$$\begin{aligned}
\hat{\rho}_x &= \frac{1}{2}\left[\hat{\sigma}_x + \hat{\mathrm{I}}\right] = \frac{1}{2}\begin{pmatrix} 1 & 1 \\ 1 & 1 \end{pmatrix}, \\
\hat{\rho}_y &= \frac{1}{2}\left[\hat{\sigma}_y + \hat{\mathrm{I}}\right] = \frac{1}{2}\begin{pmatrix} 1 & -i \\ i & 1 \end{pmatrix}, \\
\hat{\rho}_z &= \frac{1}{2}\left[\hat{\sigma}_z + \hat{\mathrm{I}}\right] = \frac{1}{2}\begin{pmatrix} 1 & 0 \\ 0 & 0 \end{pmatrix}.
\end{aligned} \tag{3.8}$$

The Wigner function can now be calculated using equation (2.28). Given the phase-point operators and that the three density operators for the system are prepared in the $+1$ eigenstate of each Pauli operator, the corresponding Wigner functions are

given by plugging these into equation (2.28) [26, 27, 35, 36],

$$W_{(a_1,a_2)} = \frac{1}{2}\mathrm{Tr}\left(\hat{\rho}\hat{A}_{(a_1,a_2)}\right), \tag{3.9}$$

$\langle\hat{\sigma}_x\rangle = 1:$		$\langle\hat{\sigma}_y\rangle = 1:$		$\langle\hat{\sigma}_z\rangle = 1:$	
$W_{(0,1)} = \frac{1}{2},$	$W_{(1,1)} = 0,$	$W_{(0,1)} = 0,$	$W_{(1,1)} = \frac{1}{2},$	$W_{(0,1)} = 0,$	$W_{(1,1)} = 0,$
$W_{(0,0)} = \frac{1}{2},$	$W_{(1,0)} = 0,$	$W_{(0,0)} = \frac{1}{2},$	$W_{(1,0)} = 0,$	$W_{(0,0)} = \frac{1}{2},$	$W_{(1,0)} = \frac{1}{2}.$

The Wigner functions are indexed in the same order as the corresponding entries in the phase space.

This result shows that the vertical line consisting of the points $(0,0)$ and $(0,1)$ is associated with the $+1$ eigenstate of $\hat{\sigma}_x$, and the second vertical line is associated with the -1 eigenstate of $\hat{\sigma}_x$. The lower horizontal line is now associated with the $+1$ eigenstate of $\hat{\sigma}_z$, while the upper horizontal line is associated with the -1 eigenstate of $\hat{\sigma}_z$. The diagonal line going through the points $(0,0)$ and $(1,1)$ is associated with the $+1$ eigenstate of $\hat{\sigma}_y$ and the second diagonal line is associated with the -1 eigenstate of $\hat{\sigma}_y$. This has been visualised in figure 3.1, where the associations are represented by the corresponding eigenvalues. The value of the spin in each direction is given by the eigenvalue of the corresponding Pauli matrix and is thus also associated with one of the lines. In summary each point in phase space describes a spin state with one spin value for each direction. This is how an initial spin state is given by sampling a point in phase space from the Wigner function [26, 27, 35, 36]. An initial phase-point operator for calculations in the Schrödinger picture is given by calculating the phase-point operators associated with the points in phase space using equation (2.26) and sampling one of them from the Wigner function [16].

The derived association of the eigenstates with the different lines can already be seen in the definition of the phase-point operators in equation (2.26). The prefactors of the Pauli matrices turn out to be the associated eigenvalues. Considering for example the phase space point $(0,0)$, all prefactors in the phase-point operator $\hat{A}_{(0,0)}$ are one, which is also the case for the eigenvalues associated with the three lines meeting in this point. The same can be seen considering the other points in phase space. Hence, already the definition of the phase-point operators defines the associations of the states in phase space and since the phase-point operators are not uniquely defined, as already discussed in section 2.2, also the association of spin states and lines in phase space is not uniquely defined [16, 35, 36]. Thus, by unique transformations of the phase-point operators, different sampling schemes can be realised describing the same physics. In section 3.3 five possible sampling schemes will be introduced which will show different approximation results. The quality of the resulting approximations will be shown to depend on the approximated system.

3.2 Time Evolution of a Spin-$\frac{1}{2}$ system

After sampling an initial state of a spin-$\frac{1}{2}$ system from the Wigner function as explained in section 3.1, where the sampling process itself will be further analysed in section 3.3, the truncated time evolution of this state needs to be calculated to get an approximation of the dynamics of the system. This can either be done using the classical time evolution as derived in section 2.3 according to [26, 27] or the second order truncated time evolution derived in section 2.4 according to [16] using the BBGKY hierarchy of the reduced phase-point operators.

A general Hamiltonian for a spin-$\frac{1}{2}$ system of N spins with spin-spin interactions $\boldsymbol{J}_{ij}$ and an external field $\boldsymbol{h}_i$ is given by

$$H = -\sum_{\substack{k,l=0 \\ k\neq l}}^{N-1} \sum_{\substack{\beta \\ =x,y,z}} J_{kl}^{\beta} \hat{\sigma}_k^{\beta} \hat{\sigma}_l^{\beta} - \sum_{k=0}^{N-1} \boldsymbol{h}_k \hat{\boldsymbol{\sigma}}_k. \tag{3.10}$$

Here $\boldsymbol{J}_{ij} = \left(J_{ij}^x, J_{ij}^y, J_{ij}^z\right)$ is a vector containing the interaction strengths between the spins at sites i and j in x-, y- and z-direction, $\boldsymbol{h}_i = (h_i^x, h_i^y, h_i^z)$ is a vector containing the external field acting on the spin at site i in each direction, and $\hat{\boldsymbol{\sigma}}_i$ is the vector of spin operators at site i. The condition $k \neq l$ in the sum is chosen since the spins do not interact with themselves. From this general Hamiltonian the systems which are approximated in section 3.4 and chapter 4 can be derived by choosing different interaction strengths and external fields. Thus, the time evolution for the general spin Hamiltonian in equation (3.10) can be calculated and then adapted for different systems [16, 26, 27].

In the Heisenberg picture one spin component s^{α} is sampled from the Wigner function for each direction $\alpha \in \{x, y, z\}$ of the initial state as explained in section 3.1. Instead of evolving the Weyl symbol in time using equation (2.41), it can be replaced by the spin component which can then be classically evolved in time according to [26, 27]. The Hamiltonian in equation (3.10) can also be translated into a classical Hamiltonian, where the vectors of Pauli matrices are replaced by vectors of the spin components $\boldsymbol{s}_i$ [26, 27],

$$H_{\mathrm{c}} = -\sum_{\substack{k,l=0 \\ k\neq l}}^{N-1} \sum_{\substack{\beta \\ =x,y,z}} J_{kl}^{\beta} s_k^{\beta} s_l^{\beta} - \sum_{k=0}^{N-1} \boldsymbol{h}_k \boldsymbol{s}_k. \tag{3.11}$$

The classical time evolution of the spin component s_n^{α} of direction α at site n is then given by the Poisson bracket of the spin component s^{α} and the classical Hamiltonian as derived in equation (2.3),

$$\begin{aligned} \dot{s_i^{\alpha}} &= \{s_i^{\alpha}, H_{\mathrm{c}}\} \\ &= -\sum_{\substack{k,l=0 \\ k\neq l}}^{N-1} \sum_{\substack{\beta \\ =x,y,z}} \left(J_{kl}^{\beta} \left\{ s_i^{\alpha}, s_k^{\beta} \right\} s_l^{\beta} + J_{kl}^{\beta} s_k^{\beta} \left\{ s_i^{\alpha}, s_l^{\beta} \right\} \right) - \sum_{k=0}^{N-1} \sum_{\substack{\beta \\ =x,y,z}} \left(h_k^{\beta} \left\{ s_i^{\alpha}, s_k^{\beta} \right\} \right). \end{aligned} \tag{3.12}$$

The Poisson bracket of two spin components can now be derived by comparison with the commutator of the quantum spin operators. For spins at different sites i and j, the commutator is zero, since these spins do not effect each other and can be exchanged. The commutator of two spin operators at the same site is given by the commutator of the Pauli matrices which is stated in equation (3.2). The classical Poisson bracket is related to the commutator by [26, 27]

$$\begin{aligned} \frac{1}{i}\left[.,.\right] &\to \left\{.,.\right\}, \\ \left[\sigma_i^\alpha, \sigma_j^\beta\right] &= 2i\delta_{ij} \sum_{\substack{\gamma \\ =x,y,z}} \epsilon^{\alpha\beta\gamma}\sigma_i^\gamma \\ \Rightarrow \left\{s_i^\alpha, s_j^\beta\right\} &= 2\delta_{ij} \sum_{\substack{\gamma \\ =x,y,z}} \epsilon^{\alpha\beta\gamma} s_i^\gamma. \end{aligned} \tag{3.13}$$

Given the Poisson bracket of two spin components, equation (3.12) can be written down explicitly,

$$\begin{aligned} \dot{s}_i^\alpha = &- \sum_{\substack{k,l=0 \\ k\neq l}}^{N-1} \sum_{\substack{\beta,\gamma \\ =x,y,z}} \left(2J_{kl}^\beta \delta_{ik}\epsilon^{\alpha\beta\gamma} s_i^\gamma s_l^\beta + 2J_{kl}^\beta \delta_{il}\epsilon^{\alpha\beta\gamma} s_k^\beta s_i^\gamma\right) \\ &- \sum_{k=0}^{N-1} \sum_{\substack{\beta,\gamma \\ =x,y,z}} \left(2h_k^\beta \delta_{ik}\epsilon^{\alpha\beta\gamma} s_i^\gamma\right) \\ = &-2 \sum_{\substack{\beta,\gamma \\ =x,y,z}} \epsilon^{\alpha\beta\gamma} \left(\sum_{\substack{k=0 \\ k\neq i}}^{N-1} \left(J_{ik}^\beta s_i^\gamma s_k^\beta\right) + h_i^\beta s_i^\gamma \right). \end{aligned} \tag{3.14}$$

This is the classical time evolution for a general Hamiltonian of a spin-$\frac{1}{2}$ system. The expectation value of a spin component $\langle s_n^\alpha \rangle$, as defined in equation (2.42), can be calculated by averaging R time evolved spin components given initial states sampled from the Wigner function [26, 27],

$$\langle s_i^\alpha \rangle (t) = \frac{1}{R} \sum_{r=0}^{R-1} s_{i,r}^\alpha (t). \tag{3.15}$$

To calculate the second order truncated time evolution of the spin system according to [16] using the BBGKY hierarchy of reduced phase-point operators, equations (2.67) and (2.69) can be used. To study the spin-$\frac{1}{2}$ system, the first order reduced phase-point operators $\hat{\mathscr{A}}_i$ and the correlation operators $\hat{\mathscr{C}}_{ij}$ are represented in the basis of Pauli operators using expansion coefficients $\boldsymbol{a}_i$ and $\boldsymbol{c}_{ij}$ [16],

$$\hat{\mathscr{A}}_i = \frac{1}{2}\left(\mathrm{I}_i + \boldsymbol{a}_i \hat{\boldsymbol{\sigma}}_i\right), \tag{3.16}$$

$$\hat{\mathscr{C}}_{ij} = \frac{1}{4} \sum_{\substack{\mu,\nu \\ =x,y,z}} c_{ij}^{\mu\nu} \hat{\sigma}_i^\mu \hat{\sigma}_j^\nu. \tag{3.17}$$

The general Hamiltonian in equation (3.10) can be split into two parts analogously to equation (2.50) with

$$\begin{aligned} H_i &= \boldsymbol{h}_i \hat{\boldsymbol{\sigma}}_i, \\ H_{ij} &= \sum_{\substack{\beta \\ =x,y,z}} J_{ij}^{\beta} \hat{\sigma}_i^{\beta} \hat{\sigma}_j^{\beta}. \end{aligned} \tag{3.18}$$

By plugging these definitions into the time evolution equation (2.67), differential equations for the expansion coefficients $\boldsymbol{a}_i$ can be derived,

$$\begin{aligned} \dot{\hat{\mathscr{A}}}_i &= \frac{\partial}{\partial t}\left(\frac{1}{2}\left(\hat{\mathrm{I}}_i + \boldsymbol{a}_i \hat{\boldsymbol{\sigma}}_i\right)\right) \\ &= \frac{1}{2}\dot{\boldsymbol{a}}_i \hat{\boldsymbol{\sigma}}_i \\ &= \frac{1}{i}\left[-\boldsymbol{h}_i \hat{\boldsymbol{\sigma}}_i, \frac{1}{2}\left(\hat{\mathrm{I}}_i + \boldsymbol{a}_i \hat{\boldsymbol{\sigma}}_i\right)\right] + \frac{1}{i}\sum_{\substack{k=0 \\ k\neq i}}^{N-1} \sum_{\substack{\beta \\ =x,y,z}} \mathrm{Tr}_k \left(\left[-J_{ik}^{\beta} \hat{\sigma}_i^{\beta} \hat{\sigma}_k^{\beta}, \frac{1}{4} \sum_{\substack{\mu,\nu \\ =x,y,z}} c_{ik}^{\mu\nu} \hat{\sigma}_i^{\mu} \hat{\sigma}_k^{\nu}\right] \right. \\ &\quad \left. + \left[-J_{ik}^{\beta} \hat{\sigma}_i^{\beta} \hat{\sigma}_k^{\beta}, \frac{1}{4}\left(\hat{\mathrm{I}}_i + \boldsymbol{a}_i \hat{\boldsymbol{\sigma}}_i\right)\left(\hat{\mathrm{I}}_k + \boldsymbol{a}_k \hat{\boldsymbol{\sigma}}_k\right)\right] \right). \end{aligned} \tag{3.19}$$

Detailed calculation of this expression is carried out in appendix B.2 and returns the result for the time evolution of $\boldsymbol{a}_i$ [16],

$$\dot{a}_i^{\mu} = -2 \sum_{\substack{\gamma,\delta \\ =x,y,z}} \left[h_i^{\gamma} a_i^{\delta} \epsilon^{\mu\gamma\delta} + \sum_{\substack{k=0 \\ k\neq i}}^{N-1} J_{ik}^{\gamma} c_{ik}^{\delta\gamma} \epsilon^{\mu\gamma\delta} + \sum_{\substack{k=0 \\ k\neq i}}^{N-1} J_{ik}^{\gamma} a_i^{\delta} a_k^{\gamma} \epsilon^{\mu\gamma\delta} \right]. \tag{3.20}$$

If the BBGKY hierarchy is truncated at first order, all correlation operators $\hat{\mathscr{C}}_{ij}$ are set to zero, which means that also the expansion coefficients $\boldsymbol{c}_{ij}$ are zero. Then, the time evolution of the expansion coefficient a_i^{μ} in equation (3.20) reduces to

$$\dot{a}_{i,\mathrm{f}}^{\mu} = -2 \sum_{\substack{\gamma,\delta \\ =x,y,z}} \left[h_i^{\gamma} a_i^{\delta} \epsilon^{\mu\gamma\delta} + \sum_{\substack{k=0 \\ k\neq i}}^{N-1} J_{ik}^{\gamma} a_i^{\delta} a_k^{\gamma} \epsilon^{\mu\gamma\delta} \right]. \tag{3.21}$$

Here the index f denotes the truncation at first order. This equation of motion has the same form as equation (3.14) and shows that truncating the BBGKY hierarchy of the reduced phase-point operators at first order gives the classical time evolution, as already stated in section (2.4).

In the same way as the time evolution of the expansion coefficient a_i^{μ} is derived, the time evolution of the expansion coefficients $\boldsymbol{c}_{ij}$ can be calculated by plugging

equations (3.17) and (3.18) into equation (2.69),

$$
\begin{aligned}
\dot{\mathscr{C}}_{ij} &= \frac{\partial}{\partial t}\left(\frac{1}{4}\sum_{\substack{\mu,\nu\\ =x,y,z}} c_{ij}^{\mu\nu}\hat{\sigma}_i^{\mu}\hat{\sigma}_j^{\nu}\right)\\
&= \frac{1}{4}\sum_{\substack{\mu,\nu\\ =x,y,z}} \dot{c}_{ij}^{\mu\nu}\hat{\sigma}_i^{\mu}\hat{\sigma}_j^{\nu}\\
&= \frac{1}{i}\left[-\boldsymbol{h}_i\hat{\boldsymbol{\sigma}}_i - \boldsymbol{h}_j\hat{\boldsymbol{\sigma}}_j, \frac{1}{4}\sum_{\substack{\mu,\nu\\ =x,y,z}} c_{ij}^{\mu\nu}\hat{\sigma}_i^{\mu}\hat{\sigma}_j^{\nu}\right]\\
&\quad + \frac{1}{i}\sum_{\substack{\beta\\ =x,y,z}}\left[-J_{ij}^{\beta}\hat{\sigma}_i^{\beta}\hat{\sigma}_j^{\beta}, \frac{1}{4}\left(\hat{\mathrm{I}}_i + \boldsymbol{a}_i\hat{\boldsymbol{\sigma}}_i\right)\left(\hat{\mathrm{I}}_j + \boldsymbol{a}_j\hat{\boldsymbol{\sigma}}_j\right) + \frac{1}{4}\sum_{\substack{\mu,\nu\\ =x,y,z}} c_{ij}^{\mu\nu}\hat{\sigma}_i^{\mu}\hat{\sigma}_j^{\nu}\right]\\
&\quad + \frac{1}{i}\sum_{\substack{k=0\\ k\neq i,j}}^{N-1}\sum_{\substack{\beta\\ =x,y,z}} \mathrm{Tr}_k\left(\left[-J_{ik}^{\beta}\hat{\sigma}_i^{\beta}\hat{\sigma}_k^{\beta}, \frac{1}{8}\left(\hat{\mathrm{I}}_i + \boldsymbol{a}_i\hat{\boldsymbol{\sigma}}_i\right)\sum_{\substack{\mu,\nu\\ =x,y,z}} c_{jk}^{\mu\nu}\hat{\sigma}_j^{\mu}\hat{\sigma}_k^{\nu}\right]\right)\\
&\quad + \frac{1}{i}\sum_{\substack{k=0\\ k\neq i,j}}^{N-1}\sum_{\substack{\beta\\ =x,y,z}} \mathrm{Tr}_k\left(\left[-J_{jk}^{\beta}\hat{\sigma}_j^{\beta}\hat{\sigma}_k^{\beta}, \frac{1}{8}\left(\hat{\mathrm{I}}_j + \boldsymbol{a}_j\hat{\boldsymbol{\sigma}}_j\right)\sum_{\substack{\mu,\nu\\ =x,y,z}} c_{ik}^{\mu\nu}\hat{\sigma}_i^{\mu}\hat{\sigma}_k^{\nu}\right]\right)\\
&\quad + \frac{1}{i}\sum_{\substack{k=0\\ k\neq i,j}}^{N-1}\sum_{\substack{\beta\\ =x,y,z}} \mathrm{Tr}_k\left(\left[-J_{ik}^{\beta}\hat{\sigma}_i^{\beta}\hat{\sigma}_k^{\beta} - J_{jk}^{\beta}\hat{\sigma}_j^{\beta}\hat{\sigma}_k^{\beta}, \frac{1}{8}\left(\hat{\mathrm{I}}_k + \boldsymbol{a}_k\hat{\boldsymbol{\sigma}}_k\right)\sum_{\substack{\mu,\nu\\ =x,y,z}} c_{ij}^{\mu\nu}\hat{\sigma}_i^{\mu}\hat{\sigma}_j^{\nu}\right]\right)\\
&\quad - \frac{1}{2i}\left(\hat{\mathrm{I}}_j + \boldsymbol{a}_j\hat{\boldsymbol{\sigma}}_j\right)\sum_{\substack{\beta\\ =x,y,z}} \mathrm{Tr}_j\left(\left[-J_{ij}^{\beta}\hat{\sigma}_i^{\beta}\hat{\sigma}_j^{\beta}, \frac{1}{4}\left(\hat{\mathrm{I}}_i + \boldsymbol{a}_i\hat{\boldsymbol{\sigma}}_i\right)\left(\hat{\mathrm{I}}_j + \boldsymbol{a}_j\hat{\boldsymbol{\sigma}}_j\right)\right.\right.\\
&\quad \left.\left. + \frac{1}{4}\sum_{\substack{\mu,\nu\\ =x,y,z}} c_{ij}^{\mu\nu}\hat{\sigma}_i^{\mu}\hat{\sigma}_j^{\nu}\right]\right)\\
&\quad - \frac{1}{2i}\left(\hat{\mathrm{I}}_i + \boldsymbol{a}_i\hat{\boldsymbol{\sigma}}_i\right)\sum_{\substack{\beta\\ =x,y,z}} \mathrm{Tr}_i\left(\left[-J_{ij}^{\beta}\hat{\sigma}_i^{\beta}\hat{\sigma}_j^{\beta}, \frac{1}{4}\sum_{\substack{\mu,\nu\\ =x,y,z}} c_{ij}^{\mu\nu}\hat{\sigma}_i^{\mu}\hat{\sigma}_j^{\nu}\right.\right.\\
&\quad \left.\left. + \frac{1}{4}\left(\hat{\mathrm{I}}_i + \boldsymbol{a}_i\hat{\boldsymbol{\sigma}}_i\right)\left(\hat{\mathrm{I}}_j + \boldsymbol{a}_j\hat{\boldsymbol{\sigma}}_j\right)\right]\right). \qquad (3.22)
\end{aligned}
$$

From this expression, one obtains the time evolution of the expansion coefficients

$\boldsymbol{c}_{ij}$. Detailed calculation is carried out in appendix B.3 and gives the result [16]

$$\begin{aligned}\dot{c}_{ij}^{\mu\nu} = 2 \Bigg[& - \sum_{\substack{\gamma \\ =x,y,z}} \left(J_{ij}^{\nu} a_i^{\gamma} - J_{ij}^{\mu} a_j^{\gamma} \right) \epsilon^{\mu\nu\gamma} \\ & - \sum_{\substack{\delta,\gamma \\ =x,y,z}} \left[\left(h_i^{\gamma} + \sum_{\substack{k=0 \\ k\neq i,j}}^{N-1} J_{ik}^{\gamma} a_k^{\gamma} \right) c_{ij}^{\delta\nu} \epsilon^{\gamma\delta\mu} + \left(h_j^{\gamma} + \sum_{\substack{k=0 \\ k\neq i,j}}^{N-1} J_{jk}^{\gamma} a_k^{\gamma} \right) c_{ij}^{\mu\delta} \epsilon^{\gamma\delta\nu} \right] \\ & - \sum_{\substack{\delta,\gamma \\ =x,y,z}} \sum_{\substack{k=0 \\ k\neq i,j}}^{N-1} \left[J_{ik}^{\gamma} a_i^{\delta} c_{jk}^{\nu\gamma} \epsilon^{\gamma\delta\mu} + J_{jk}^{\gamma} a_j^{\delta} c_{ik}^{\mu\gamma} \epsilon^{\gamma\delta\nu} \right] \\ & + \sum_{\substack{\delta,\gamma \\ =x,y,z}} J_{ij}^{\gamma} \left[a_i^{\mu} \left(c_{ij}^{\gamma\delta} + a_i^{\gamma} a_j^{\delta} \right) \epsilon^{\gamma\delta\nu} + a_j^{\nu} \left(c_{ij}^{\delta\gamma} + a_i^{\delta} a_j^{\gamma} \right) \epsilon^{\gamma\delta\mu} \right] \Bigg] . \end{aligned} \tag{3.23}$$

Given the time evolutions of the expansion coefficients $\boldsymbol{a}_i$ and $\boldsymbol{c}_{ij}$, the expectation values of the one- and two-point functions of the spins can be evolved in time by averaging R runs [16],

$$\langle \sigma_i^{\mu} \rangle = \frac{1}{R} \sum_{r=0}^{R-1} a_{i,r}^{\mu}, \tag{3.24}$$

$$\left\langle \sigma_i^{\mu} \sigma_j^{\nu} \right\rangle = \frac{1}{R} \sum_{r=0}^{R-1} c_{i,j,r}^{\mu\nu} + a_{i,r}^{\mu} a_{j,r}^{\nu}. \tag{3.25}$$

Given the equations of motion of the spin system in the first order approximation in equation (3.14) and in the second order approximation in equations (3.20) and (3.23), the time evolution of each spin in the system can be approximated using the initial states sampled from the Wigner function. By repetition, a large number R of trajectories can be calculated from many sampled initial states and, eventually, the resulting observables can be averaged to get a simulation of the quantum mechanical system. This allows to efficiently calculate the expectation value of a spin component and two-point variances using equation (3.15) for the first order approximation or equation (3.24) for the second order approximation. With this, also any other observable, which can be expanded in sums of spin correlation functions, can be approximated.

3.3 Multiple Phase-Point Operators and Sampling Schemes

As mentioned in section 2.2, the discrete phase-point operators are not unique. Unitary transformations conserve the needed properties of the phase-point operators,

as do non-singular linear transformations of the phase space coordinates. Thus, there are multiple ways to define the phase-point operators [16, 35, 36].

One definition of phase-point operators is given by equation (2.26) [35, 36],

$$\begin{aligned}\hat{A}_{\boldsymbol{\alpha}} &= \frac{1}{2}\left[(-1)^{a_1}\,\hat{\sigma}_x + (-1)^{a_1+a_2}\,\hat{\sigma}_y + (-1)^{a_2}\,\hat{\sigma}_z + \hat{\mathrm{I}}\right] \\ &= \frac{1}{2}\left[\boldsymbol{r}_{\boldsymbol{\alpha}}\hat{\boldsymbol{\sigma}} + \hat{\mathrm{I}}\right]. \end{aligned} \tag{3.26}$$

In the last line, $\hat{\boldsymbol{\sigma}}$ is the vector of Pauli matrices, while $\boldsymbol{r}_{\boldsymbol{\alpha}}$ is a vector containing the prefactors of the Pauli matrices depending on the phase space point $\boldsymbol{\alpha}$,

$$\begin{aligned}\boldsymbol{r}_{(a_1,a_2)} &= \left((-1)^{a_1}, (-1)^{a_1+a_2}, (-1)^{a_2}\right), \\ \boldsymbol{r}_{(0,0)} &= (1,1,1), \\ \boldsymbol{r}_{(0,1)} &= (1,-1,-1), \\ \boldsymbol{r}_{(1,0)} &= (-1,-1,1), \\ \boldsymbol{r}_{(1,1)} &= (-1,1,-1). \end{aligned} \tag{3.27}$$

Using a unitary transformation, the sign of the second component of all $\boldsymbol{r}_{\boldsymbol{\alpha}}$ can be changed to get a different set of possible phase-point operators [16],

$$\hat{A}'_{\boldsymbol{\alpha}} = \hat{U}\hat{A}_{\boldsymbol{\alpha}}\hat{U}^\dagger = \frac{1}{2}\left[\boldsymbol{r}'_{y,\boldsymbol{\alpha}}\hat{\boldsymbol{\sigma}} + \hat{\mathrm{I}}\right]$$

$$\begin{aligned}\Rightarrow\ \boldsymbol{r}'_{y,(0,0)} &= (1,-1,1), \\ \boldsymbol{r}'_{y,(0,1)} &= (1,1,-1), \\ \boldsymbol{r}'_{y,(1,0)} &= (-1,1,1), \\ \boldsymbol{r}'_{y,(1,1)} &= (-1,-1,-1). \end{aligned} \tag{3.28}$$

As explained in section 3.1, the prefactors of the Pauli matrices in the phase-point operators, which are the vectors $\boldsymbol{r}_{\boldsymbol{\alpha}}$ here, also define the initial spin states which are sampled from the Wigner function on the phase space. Hence, this unitary transformation changes the set of initial spin states which are then evolved in time. One can now see in both sets that there appear some correlations between different components where there is no physical reason for correlations [16]. For example, if the system is initially prepared in the $+1$ state in z-direction, only the states $\boldsymbol{r}_{(0,0)}$, $\boldsymbol{r}_{(1,0)}$, $\boldsymbol{r}'_{y,(0,0)}$ and $\boldsymbol{r}'_{y,(1,0)}$ have a nonzero probability independent of the choice of phase-point operators $\hat{A}_{\boldsymbol{\alpha}}$. This can be seen in equation (3.9), where the entries $W_{(a_1,a_2)}$ give the probabilities from which the states $\boldsymbol{r}_{(a_1,a_2)}$ are sampled.

Since the Wigner function, as defined in equation (2.28), depends on the phase-point operators, it changes if the phase-point operators change. But taking a closer look at the Wigner function, one can show that, if the system is prepared in an initial state in the x- or z-direction, the Wigner function is not influenced by changing the sign of the y-component in the $\boldsymbol{r}_{\boldsymbol{\alpha}}$. By flipping the y-component of the initial spins,

the associations of the $+1$ and -1 states in y-direction with the two diagonal lines in phase space are changed, as can be seen in the phase-point operators, while the associations of $\hat{\sigma}_x$ and $\hat{\sigma}_z$ with the vertical and the horizontal lines stay the same. Thus, the Wigner functions in equation (3.9), for the system being prepared in an x- or z-state, do not change.

If the system is prepared in the $+1$ state in z-direction, the two states of the non-primed set with non-zero probability always have the same x- and y-components, while these components are always different in the two states of the primed set with non-zero probability. There is no physical reason for these correlations to appear, hence sampling the initial states from one of the two sets will introduce unphysical correlations. These can unnecessarily worsen the quality of the discrete truncated Wigner approximation, as will be further discussed in section 3.4 and chapter 4.

There is a way of combining the two sets of initial states to remove the correlations. The initial density operator $\hat{\rho}$ can be written in the following way using the definition in equation (2.27) [16],

$$\begin{aligned}\hat{\rho} &= \frac{\hat{\rho}}{2} + \frac{\hat{\rho}}{2} \\ &= \frac{1}{2}\sum_{\boldsymbol{\alpha}} W_{\boldsymbol{\alpha}} \hat{A}_{\boldsymbol{\alpha}} + \frac{1}{2}\sum_{\boldsymbol{\alpha}} W'_{\boldsymbol{\alpha}} \hat{A}'_{\boldsymbol{\alpha}}.\end{aligned} \tag{3.29}$$

Using this relation, one can combine the primed and the non-primed set. In the example of preparing the spins in the $+1$ state in z-direction, one can then sample the initial state out of the four possibilities $\boldsymbol{r}_{(0,0)}$, $\boldsymbol{r}_{(1,0)}$, $\boldsymbol{r}'_{y,(0,0)}$ and $\boldsymbol{r}'_{y,(1,0)}$ with nonzero probability. This way the correlation, which appears in the single sets, does not appear any longer since all four combinations of the spins in x- and y-direction are possible [16].

As discussed earlier, the Wigner function is not influenced by a sign flip of the y-component of $\boldsymbol{r}_{\boldsymbol{\alpha}}$ if the system is prepared in an x- or z-state. Thus, assuming this initial condition, one can combine the two sets introduced for general $\boldsymbol{\alpha}$ [16],

$$W_{\boldsymbol{\alpha}} = W'_{\boldsymbol{\alpha}} \tag{3.30}$$

$$\begin{aligned}\Rightarrow \quad \hat{\rho} &= \frac{1}{2}\sum_{\boldsymbol{\alpha}} W_{\boldsymbol{\alpha}} \left(\hat{A}_{\boldsymbol{\alpha}} + \hat{A}'_{\boldsymbol{\alpha}}\right) \\ &= \sum_{\boldsymbol{\alpha}} W_{\boldsymbol{\alpha}} \hat{\tilde{A}}_{\boldsymbol{\alpha}} \\ &= \frac{1}{2}\sum_{\boldsymbol{\alpha}} W_{\boldsymbol{\alpha}} \left(\tilde{\boldsymbol{r}}_{\boldsymbol{\alpha}} \hat{\boldsymbol{\sigma}} + \hat{\mathrm{I}}\right)\end{aligned} \tag{3.31}$$

$$\text{with} \quad \tilde{\boldsymbol{r}}_{\boldsymbol{\alpha}} = \frac{1}{2}\left(\boldsymbol{r}_{\boldsymbol{\alpha}} + \boldsymbol{r}'_{y,\boldsymbol{\alpha}}\right). \tag{3.32}$$

This combination of the primed and non-primed sets yields four states [16],

$$\begin{aligned}
\tilde{\boldsymbol{r}}_{(0,0)} &= (1,0,1)\,, \\
\tilde{\boldsymbol{r}}_{(0,1)} &= (1,0,-1)\,, \\
\tilde{\boldsymbol{r}}_{(1,0)} &= (-1,0,1)\,, \\
\tilde{\boldsymbol{r}}_{(1,1)} &= (-1,0,-1)\,.
\end{aligned} \tag{3.33}$$

The four states in this system all have a zero y-component. Since the spins interact with each other in the system, a zero y-component influences the time evolution and there is no physical reason for it to be zero. But if the system is prepared in an initial state in z-direction, also a sign flip in the x-component of the initial spins does not effect the Wigner function for the same reasons as explained above. Hence, in the same way as the $\tilde{\boldsymbol{r}}_{\boldsymbol{\alpha}}$ is created, a second set $\tilde{\boldsymbol{r}}'_{\boldsymbol{\alpha}}$ can be set up by combining a set $\boldsymbol{r}'_{x,\boldsymbol{\alpha}}$, where the x-component of the states in $\boldsymbol{r}$ is flipped, with $\boldsymbol{r}_{\boldsymbol{\alpha}}$. This then results in [16]

$$\begin{aligned}
\tilde{\boldsymbol{r}}'_{(0,0)} &= (0,1,1)\,, \\
\tilde{\boldsymbol{r}}'_{(0,1)} &= (0,-1,-1)\,, \\
\tilde{\boldsymbol{r}}'_{(1,0)} &= (0,-1,1)\,, \\
\tilde{\boldsymbol{r}}'_{(1,1)} &= (0,1,-1)\,.
\end{aligned} \tag{3.34}$$

If there is also no restriction on the z-component, which means that the Wigner function is nonzero for all possible states, it would also not be effected by a sign flip of the z-component. In the simulations in section 3.4 and chapter 4, the z-component of the spins in the system is always initially $+1$, which is why this sign flip will not be further discussed here. In general, there is no distinguished direction, hence the directions in the combinations above and in the following can be exchanged arbitrarily.

If the system is initially prepared in the $+1$ state in z-direction, one can combine the two new sets $\tilde{\boldsymbol{r}}$ and $\tilde{\boldsymbol{r}}'$, and only the states $\tilde{\boldsymbol{r}}_{(0,0)}$, $\tilde{\boldsymbol{r}}_{(1,0)}$, $\tilde{\boldsymbol{r}}'_{(0,0)}$ and $\tilde{\boldsymbol{r}}'_{(1,0)}$ have a nonzero probability. Thus, the initial state can be sampled out of these four states with the probabilities given by the Wigner function [16]. This way the x- and y-component have the same probability to be zero, while they are nonzero in the other cases.

In summary, three different sets S_{init}, S_{mix} and $\tilde{S}_{\text{mix}}$ are derived, from which the initial states can be sampled if the system is prepared in the $+1$ state in z-direction

and for which the corresponding Wigner functions can be calculated [16],

$$
\begin{array}{lll}
S_{\text{init}} & S_{\text{mix}} & \tilde{S}_{\text{mix}} \\
\boldsymbol{r}_{(0,0)} = (1,1,1)\,, & \boldsymbol{r}_{(0,0)} = (1,1,1)\,, & \tilde{\boldsymbol{r}}_{(0,0)} = (1,0,1)\,, \\
\boldsymbol{r}_{(0,1)} = (1,-1,-1)\,, & \boldsymbol{r}_{(1,0)} = (-1,-1,1)\,, & \tilde{\boldsymbol{r}}_{(1,0)} = (-1,0,1)\,, \\
\boldsymbol{r}_{(1,0)} = (-1,-1,1)\,, & \boldsymbol{r}'_{(0,0)} = (1,-1,1)\,, & \tilde{\boldsymbol{r}}'_{y,(0,0)} = (0,1,1)\,, \\
\boldsymbol{r}_{(1,1)} = (-1,1,-1)\,, & \boldsymbol{r}'_{(1,0)} = (-1,1,1)\,, & \tilde{\boldsymbol{r}}'_{y,(1,0)} = (0,-1,1)\,, \\
\\
W_{(0,0)} = 0.5, & W_{(0,0)} = 0.25, & W_{(0,0)} = 0.25, \\
W_{(0,1)} = 0, & W_{(0,1)} = 0.25, & W_{(0,1)} = 0.25, \\
W_{(1,0)} = 0.5, & W_{(1,0)} = 0.25, & W_{(1,0)} = 0.25, \\
W_{(1,1)} = 0, & W_{(1,1)} = 0.25, & W_{(1,1)} = 0.25. \qquad (3.35)
\end{array}
$$

These states of the sets can be described as lying on a cube in the s_x-s_y-s_z space of spin components with corners at all combinations of $+1$ and -1 in all directions. Then the set S_{init} consists of four of these corners, the set S_{mix} describes the four corners with $z = 1$ and the set $\tilde{S}_{\text{mix}}$ lies on the boarders connecting the corners with $z = 1$, as illustrated in figure 3.2. By combining these sets, one can generally sample states from all corners of the cube and from the centres of all boarders.

To go further, equation (3.29) can be written in a general way,

$$
\begin{gathered}
\hat{\rho} = \alpha\hat{\rho} + \beta\hat{\rho} + \gamma\hat{\rho}, \qquad (3.36) \\
\text{with} \quad \alpha + \beta + \gamma = 1 \text{ for } \alpha, \beta, \gamma \in \{0, \dots 1\}\,.
\end{gathered}
$$

Using this general form, more points of the cube can be added to the set, from which the initial states are sampled. If one combines the initial set $\boldsymbol{r}$ with the set $\boldsymbol{r}'_y$ created by a sign flip in y-direction and the analogous set $\boldsymbol{r}'_x$ created by a sign flip in x-direction, one can create a set of states using relation (3.32) in a general way,

$$
\begin{aligned}
\boldsymbol{r}^{\text{g}} &= \alpha\boldsymbol{r} + \beta\boldsymbol{r}'_y + \gamma\boldsymbol{r}'_x \qquad (3.37) \\
\Rightarrow \boldsymbol{r}^{\text{g}}_{(0,0)} &= \begin{pmatrix} \alpha+\beta-\gamma \\ \alpha-\beta+\gamma \\ \alpha+\beta+\gamma \end{pmatrix} = \begin{pmatrix} \alpha+\beta-\gamma \\ \alpha-\beta+\gamma \\ 1 \end{pmatrix}, \\
\boldsymbol{r}^{\text{g}}_{(0,1)} &= \begin{pmatrix} \alpha+\beta-\gamma \\ -\alpha+\beta-\gamma \\ -\alpha-\beta-\gamma \end{pmatrix} = \begin{pmatrix} \alpha+\beta-\gamma \\ -\alpha+\beta-\gamma \\ -1 \end{pmatrix}, \\
\boldsymbol{r}^{\text{g}}_{(1,0)} &= \begin{pmatrix} -\alpha-\beta+\gamma \\ -\alpha+\beta-\gamma \\ \alpha+\beta+\gamma \end{pmatrix} = \begin{pmatrix} -\alpha-\beta+\gamma \\ -\alpha+\beta-\gamma \\ 1 \end{pmatrix}, \\
\boldsymbol{r}^{\text{g}}_{(1,1)} &= \begin{pmatrix} -\alpha-\beta+\gamma \\ \alpha-\beta+\gamma \\ -\alpha-\beta-\gamma \end{pmatrix} = \begin{pmatrix} -\alpha-\beta+\gamma \\ \alpha-\beta+\gamma \\ -1 \end{pmatrix}. \qquad (3.38)
\end{aligned}
$$

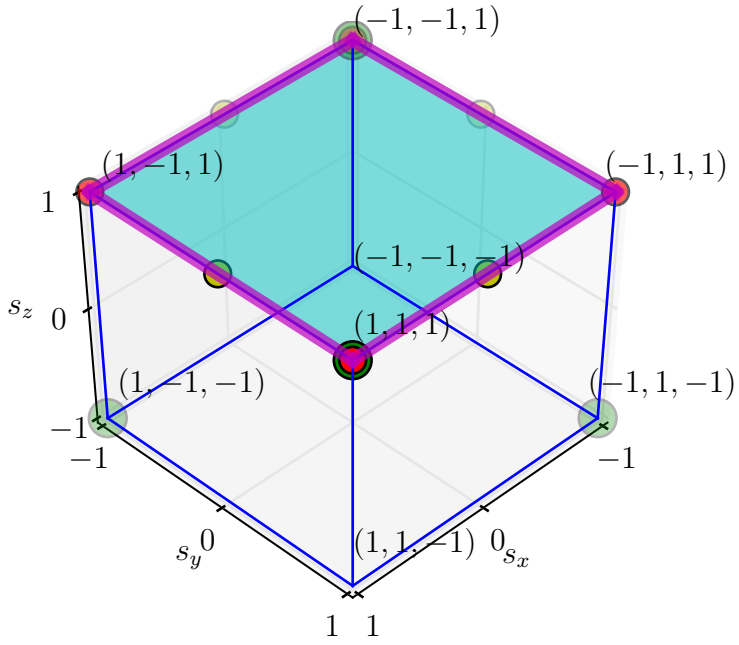

Figure 3.2: The sets from which the initial states are sampled for the different sampling schemes can be illustrated by a cube in the s_x-s_y-s_z-space. The green dots mark the states belonging to the set S_{init}, the red dots are contained in the set S_{mix} and the yellow dots show the states of the set $\tilde{S}_{\text{mix}}$. For the initial condition that the z-value of all states is $+1$, the magenta lines show the boarders from which the states are sampled in the semi-continuous sampling scheme. The continuous sampling scheme for the same initial condition samples states from the blue face of the cube.

The index g denotes the general form of the set.

Because of the initial condition on the spin value in z-direction, this component can not be modified without changing the Wigner function. Therefore, the z-component only takes the values $+1$ and -1, so that the general form includes all possible states on the upper and lower face of the cube in figure 3.2, while the Wigner function for all states with -1 in the z-component is zero. This sampling scheme is called the continuous scheme in the following since both, the x- and the y-components, are sampled continuously. If all three components of the spin states are randomly sampled from the phase space, a fourth parameter δ can be introduced to weight the states created by flipping the z-component of the states in set $\boldsymbol{r}$. The states described by the generally combined set would then be points within the entire cube in figure 3.2.

Another idea for a possible sampling scheme is to sample one spin component continuously, while the other components can only have the values $+1$ and -1,

where all components have the same probability to be continuously sampled. This sampling scheme will be called semi-continuous in the following. Considering the possible states on the cube in figure 3.2, the scheme describes the cube boarders. With the initial condition on the z-component, only the x- and y-component can be continuously sampled and the states are only sampled from the eight boarders of the cube, which have $+1$ or -1 in the z-component. Such a set of states is created by adding a condition for the parameters β and γ in equation (3.36),

$$\beta = 0 \text{ or } \gamma = 0. \tag{3.39}$$

The states weighted with β and γ in the combination for the set of general states $\boldsymbol{r}^{\mathrm{g}}$ are created by sign flips of the x- and y-component of the states weighted with α, therefore β and γ have opposite signs in all components of the combined states, as stated in equation (3.38). Thus, if $\beta = 0$, the states always lie on the boarders with $y = +1$ or $y = -1$, since the y-component of each state is either $\alpha + \gamma$ or $-\alpha - \gamma$, which is either $+1$ or -1 by condition (3.39). The same happens with the x-components for $\gamma = 0$, thus the condition forces all states to lie on the boarders of the cube in figure 3.2.

If the z-component is initially $+1$, the possible states only lie on the four upper boarders of the cube in figure 3.2. If all three components of the spin states are randomly sampled from the phase space, the states can be sampled from all boarders in an analogous way as described for the continuous sampling. For this, a fourth parameter δ needs to be introduced which, in the combination for the general set, weights the states of the set created from $\boldsymbol{r}$ by flipping the sign of the z-component. In this case, the condition in equation (3.39) changes in the way that always one of the three parameters β, γ or δ needs to be zero.

After continuous and semi-continuous sets of states have been introduced, their sampling schemes can be described in detail for the case of the initial condition on the z-component to be $+1$. For continuous sampling, two random numbers r_1 and r_2 need to be drawn from a unitary distribution, where r_1 is drawn between 0 and 1 and r_2 is drawn between 0 and $1-r_1$. This ensures that the condition $r_1+r_2+r_3 = 1$ can be fulfilled by $r_3 = 1 - r_1 - r_2$ with $0 < r_3 < 1$. There are six possibilities how to choose α, β and γ using r_1 and r_2,

$$\begin{aligned}
&\alpha = r_1, && \beta = r_2, && \gamma = 1 - r_1 - r_2,\\
&\alpha = r_1, && \beta = 1 - r_1 - r_2, && \gamma = r_2,\\
&\alpha = r_2, && \beta = r_1, && \gamma = 1 - r_1 - r_2,\\
&\alpha = r_2, && \beta = 1 - r_1 - r_2, && \gamma = r_1,\\
&\alpha = 1 - r_1 - r_2, && \beta = r_1, && \gamma = r_2,\\
&\alpha = 1 - r_1 - r_2, && \beta = r_2, && \gamma = r_1.
\end{aligned} \tag{3.40}$$

All of these possibilities are equally likely, thus one of them is drawn using a unitary probability distribution. Given values for α, β and γ, the set of initial states can be created using equation (3.38) and the initial spin state can then be sampled out of this set using the Wigner function, which has not changed during the whole procedure.

If all three components of the spin states are randomly sampled from the phase space and the continuous sampling acts on the whole cube, a third random number r_3 between 0 and $1 - r_1 - r_2$ needs to be drawn from a unitary distribution. The set of initial states is drawn out of 24 equally likely possibilities to choose α, β, γ and δ using the three random numbers. The initial state can then again be sampled using the Wigner function.

The semi-classical sampling works in an analogous way, but there, only one random number r_1 between 0 and 1 needs to be drawn from a unitary distribution, since it is always either $\beta = 0$ or $\gamma = 0$. Therefore, only four choices for α, β and γ are possible using the random variable r_1,

$$\begin{aligned} \alpha &= r_1, \quad & \beta &= 1 - r_1, \quad & \gamma &= 0, \\ \alpha &= 1 - r_1, \quad & \beta &= r_1, \quad & \gamma &= 0, \\ \alpha &= r_1, \quad & \beta &= 0, \quad & \gamma &= 1 - r_1, \\ \alpha &= 1 - r_1, \quad & \beta &= 0, \quad & \gamma &= r_1. \end{aligned} \tag{3.41}$$

Given these choices, four equally likely sets of initial states can be created. One set is then drawn out of these four using a unitary distribution and the states of the set are calculated using equation (3.38). Given the Wigner function, which has not changed, an initial state can be sampled from the boarders of the cube.

Again, if all three components of the spin states are randomly sampled from the phase space, one additional random number r_2 between 0 and $1 - r_1$ needs to be drawn from a unitary distribution. This gives 18 possible choices for α, β, γ and δ given the conditions on the four parameters as explained earlier. Out of these 18 sets of states, one is drawn using a unitary distribution and the initial state can then be sampled from the Wigner function.

In summary, five sampling schemes have been introduced in this section. Three of them are stated in equation (3.35) and the other two are the continuous and the semi-continuous sampling. All sampling schemes with their main properties are summarised in appendix B.4. In section 3.4, the effects of the different sets on the simulations will be compared and it will be analysed which sampling scheme gives the best results in comparison to the exact solution. The same will be done in chapter 4 for a different approximated system and it will become clear that the quality of the sampling schemes depends on the model which is simulated. The probabilities of the different states are given by the Wigner function, which can be directly calculated given the $\boldsymbol{r}$ vectors, since these uniquely define a corresponding phase-point operator. This also shows that the different sampling schemes work

for the Schrödinger picture in the same way, even if the derivation is done in the Heisenberg picture. The different sampling schemes also result in different phase-point operators, which can be sampled from the Wigner function on phase space for the time evolution in the Schrödinger picture.

3.4 Benchmarking the Discrete Truncated Wigner Approximation in a Spin-$\frac{1}{2}$ System

To find out whether the discrete truncated Wigner approximation is a useful simulation method for spin-$\frac{1}{2}$ systems, it can be benchmarked using an exactly solvable model and comparing it with the approximation results. The easiest exactly solvable spin-$\frac{1}{2}$ system is the N-spin Ising chain, which is given by the general Hamiltonian in equation (3.10) with $\boldsymbol{h} = 0$ and $J^y = J^z = 0$,

$$H_{\mathrm{xx}} = -\sum_{\substack{i,j=0 \\ i\neq j}}^{N-1} J_{ij}\hat{\sigma}_i^x\hat{\sigma}_j^x. \tag{3.42}$$

The exact time evolutions of the expectation values of the spin operators in this system have been calculated for example in [16, 17, 26, 27, 32] and are given by

$$\langle\hat{\sigma}_i^x\rangle(t) = \langle\hat{\sigma}_i^x\rangle(0), \tag{3.43}$$

$$\langle\hat{\sigma}_i^y\rangle(t) = \frac{1}{2^N}\sum_{\substack{m_1\ldots m_N \\ \in\{-1,+1\}}}\left[\langle\hat{\sigma}_i^y\rangle(0)\cos\left(2t\sum_{a=0}^{N-1}(J_{ia}m_a)\right)\right. \tag{3.44}$$

$$\left. + \langle\hat{\sigma}_i^z\rangle(0)\sin\left(2t\sum_{a=0}^{N-1}(J_{ia}m_a)\right)\right], \tag{3.45}$$

$$\langle\hat{\sigma}_i^z\rangle(t) = \frac{1}{2^N}\sum_{\substack{m_1\ldots m_N \\ \in\{-1,+1\}}}\left[\langle\hat{\sigma}_i^z\rangle(0)\cos\left(2t\sum_{a=0}^{N-1}(J_{ia}m_a)\right)\right. \tag{3.46}$$

$$\left. - \langle\hat{\sigma}_i^y\rangle(0)\sin\left(2t\sum_{a=0}^{N-1}(J_{ia}m_a)\right)\right]. \tag{3.47}$$

Here the sums go over all possible combinations of m_a being $+1$ or -1.

The time evolutions of the two-point variances $\left\langle\hat{\sigma}_i^\mu\hat{\sigma}_j^\nu\right\rangle$ with $\mu,\nu\in\{x,y,z\}$, have also been calculated exactly, see for example [16, 17, 26, 27, 32]. In the following, only the variance $\left\langle\hat{\sigma}_i^z\hat{\sigma}_j^z\right\rangle$ will be compared with the results of the discrete truncated Wigner approximation, since the quality of the approximation is not expected to depend on the components of the spins in the variance. All spins will initially be

chosen to be $+1$ in z-direction for the simulations. This condition also needs to be applied to the exact solution to make a comparison possible. This leads to the requirements $\langle\hat{\sigma}_i^z\rangle(0) = 1$ and $\langle\hat{\sigma}_i^y\rangle(0) = \langle\hat{\sigma}_i^x\rangle(0) = 0$ which will be used in the following. With this, the time evolution of the variance $\left\langle\hat{\sigma}_i^z\hat{\sigma}_j^z\right\rangle$ is given by [26, 27]

$$\left\langle\hat{\sigma}_i^z\hat{\sigma}_j^z\right\rangle(t) = \frac{1}{2^{N-2}} \sum_{\substack{m_1\ldots m_{i-1}m_{i+1}\ldots m_{j-1}m_{j+1}\ldots m_N \\ \in\{-1,+1\}}} \cos\left(2t\sum_{\substack{a=0 \\ a\neq i,j}}^{N-1}(J_{ia}m_a)\right) \times \cos\left(2t\sum_{\substack{b=0 \\ b\neq i,j}}^{N-1}(J_{jb}m_b)\right). \tag{3.48}$$

In the sum over all combinations of the m_a being $+1$ and -1 the two terms with m_i and m_j are not included.

Given these time evolutions, the magnetisation in z-direction and the expectation value of the total zz-variance can be evolved in time [16, 26, 27],

$$\begin{aligned}\langle\hat{\sigma}^z\rangle(t) &= \frac{1}{N}\sum_{i=0}^{N-1}\langle\hat{\sigma}_i^z\rangle(t) \\ &= \frac{1}{N}\sum_{i=0}^{N-1}\frac{1}{2^N}\sum_{\substack{m_1\ldots m_N \\ \in\{-1,+1\}}}\cos\left(2t\sum_{a=0}^{N-1}(J_{ia}m_a)\right),\end{aligned} \tag{3.49}$$

$$\begin{aligned}\left\langle(\hat{\sigma}^z)^2\right\rangle(t) &= \frac{1}{N^2}\sum_{i,j=0}^{N-1}\left\langle\hat{\sigma}_i^z\hat{\sigma}_j^z\right\rangle(t) \\ &= \frac{1}{N^2}\sum_{i,j=0}^{N-1}\frac{1}{2^N}\sum_{\substack{m_1\ldots m_{i-1}m_{i+1}\ldots m_{j-1}m_{j+1}\ldots m_N \\ \in\{-1,+1\}}} \\ &\quad\times\cos\left(2t\sum_{\substack{a=0 \\ a\neq i,j}}^{N-1}(J_{ia}m_a)\right)\cos\left(2t\sum_{\substack{b=0 \\ b\neq i,j}}^{N-1}(J_{jb}m_b)\right).\end{aligned} \tag{3.50}$$

With this, also the exact time evolution of the connected zz-correlator $\left\langle(\hat{\sigma}^z)^2\right\rangle - \langle\hat{\sigma}^z\rangle^2$ is given.

The time evolutions of these variables will be approximated using the discrete truncated Wigner approximation in the following subsections 3.4.1 and 3.4.2. In subsection 3.4.1, the classical time evolution will be compared with the exact results while in subsection 3.4.2 the second order truncated approximation will be benchmarked by comparison.

3.4.1 Analysing the First Order Approximation

First, the discrete truncated Wigner approximation will be benchmarked using the classical time evolution. The time evolutions of the spin components s_i^x, s_i^y and s_i^z can be calculated according to [27] for the classical Ising Hamiltonian H_{xx} using equation (3.14),

$$H_{\mathrm{xx}} = -\sum_{\substack{i,j=0 \\ i\neq j}}^{N-1} J_{ij} s_i^x s_j^x, \tag{3.51}$$

$$\dot{s}_i^x = 0 \Rightarrow s_i^x(t) = s_i^x(0),$$

$$\dot{s}_i^y = 2\sum_{\substack{j=0 \\ j\neq i}}^{N-1} J_{ij} s_i^z s_j^x \Rightarrow s_i^y(t) = s_i^y(0)\cos\left(2\sum_{\substack{j=0 \\ j\neq i}}^{N-1} J_{ij} s_j^x(0)\, t\right) + s_i^z(0)\sin\left(2\sum_{\substack{j=0 \\ j\neq i}}^{N-1} J_{ij} s_j^x(0)\, t\right),$$

$$\dot{s}_i^z = -2\sum_{\substack{j=0 \\ j\neq i}}^{N-1} J_{ij} s_i^y s_j^x \Rightarrow s_i^z(t) = s_i^z(0)\cos\left(2\sum_{\substack{j=0 \\ j\neq i}}^{N-1} J_{ij} s_j^x(0)\, t\right) - s_i^y(0)\sin\left(\sum_{\substack{j=0 \\ j\neq i}}^{N-1} J_{ij} s_j^x(0)\, t\right). \tag{3.52}$$

These equations of motion can be solved exactly, as stated on the right-hand side of equations (3.52) [26, 27]. Given the time evolution of the spin components, the expectation values of magnetisation and two-point variance can be evolved in time. This gives results analogous to the exact time evolutions in equations (3.49) and (3.50),

$$\begin{aligned}\langle s^z\rangle_{\mathrm{cl}}(t) &= \frac{1}{N}\sum_{i=0}^{N-1} s_i^z(t) \\ &= \frac{1}{N}\sum_{i=0}^{N-1}\cos\left(2\sum_{\substack{j=0 \\ j\neq i}}^{N-1} J_{ij} s_j^x(0)\, t\right),\end{aligned} \tag{3.53}$$

$$\left\langle (s^z)^2 \right\rangle_{\mathrm{cl}} (t) = \frac{1}{N^2} \sum_{i,j=0}^{N-1} s_i^z (t)\, s_j^z (t)$$

$$= \frac{1}{N^2} \sum_{i,j=0}^{N-1} \cos\left(2 \sum_{\substack{k=0 \\ k\neq i}}^{N-1} J_{ik} s_k^x (0) \right) \cos\left(2 \sum_{\substack{l=0 \\ l\neq j}}^{N-1} J_{jl} s_l^x (0) \right). \tag{3.54}$$

Here, the index cl denotes the classical approximation [26, 27]. It is used that all spins are initially $+1$ in z-direction by condition, thus $\langle s^z \rangle_{\mathrm{cl}} (0) = 1$ and $\langle s^x \rangle_{\mathrm{cl}} (0) = \langle s^y \rangle_{\mathrm{cl}} (0) = 0$. This cancels all the sine terms, since they are multiplied with $\langle s^y \rangle_{\mathrm{cl}} (0)$.

These equations can be compared with the exact equations of motion (3.49) and (3.50). The structure of both sets of equations is the same with the only difference that the sum over all possible combinations of the m_a being $+1$ and -1 in the exact solution is replaced by the sum over all $s_j^x (0)$ in the classical approximation. The classical approximation is calculated by averaging R runs, where for each run r the initial spin value $s_{j,r}^x (0)$ is sampled from the Wigner function, as derived in section 3.3. Thus, the classical equations of motion can be written as [26, 27]

$$\langle s^z \rangle_{\mathrm{cl}} (t) = \frac{1}{NR} \sum_{i=0}^{N-1} \sum_{r=0}^{R-1} \cos\left(2 \sum_{\substack{j=0 \\ j\neq i}}^{N-1} J_{ij} s_{j,r}^x (0)\, t \right), \tag{3.55}$$

$$\left\langle (s^z)^2 \right\rangle_{\mathrm{cl}} (t) = \frac{1}{N^2 R} \sum_{i,j=0}^{N-1} \sum_{r=0}^{R-1} \cos\left(2 \sum_{\substack{k=0 \\ k\neq i}}^{N-1} J_{ik} s_{k,r}^x (0)\, t \right) \cos\left(2 \sum_{\substack{l=0 \\ l\neq j}}^{N-1} J_{jl} s_{l,r}^x (0)\, t \right). \tag{3.56}$$

For a large number R of runs, this average over the randomly sampled initial values approximates the sum over all combinations of the initial spin values $s_i^x (0)$ being $+1$ or -1 in the sampling schemes S_{init} and S_{mix} [26, 27]. This then equals the sum over all combinations of m_a being $+1$ and -1 in the exact solution and thus gives the same equations of motion for the exact calculation and the semi-classical approximation of the magnetisation $\langle s^z \rangle$. In the variance $\left\langle (s^z)^2 \right\rangle$, there is a small difference between the exact calculation and the semi-classical approximation. While the two terms with m_i and m_j are missing in the sum of the exact calculation, $s_{i,r}^x$ and $s_{j,r}^x$ appear in the sum of the semi-classical approximation. The two time evolutions are thus related by

$$\left\langle s_i^z s_j^z \right\rangle_{\mathrm{cl}} (t) = \left\langle \hat{\sigma}_i^z \hat{\sigma}_j^z \right\rangle (t) \cos^2 (2 t J_{ij}). \tag{3.57}$$

Here it is assumed that the interaction strength between each two spins is symmetric, $J_{ij} = J_{ji}$. The detailed derivation of this relation is carried out in appendix B.5 according to [27]. Equation (3.57) is only true for the sampling schemes S_{mix} and

S_{init}, where the initial states in x- and y-direction are randomly sampled to be $+1$ or -1. For other sampling schemes the sum over all combinations of m_a being $+1$ and -1 in the exact solution can not be replaced by the sum over the $s_i^x(0)$ of the various runs, since these also take different values than $+1$ and -1. Hence, these sampling schemes do not result in the exact solution, but their approximation results will still be analysed. It will also be shown in chapter 4 that the quality of the different sampling schemes depends on the approximated system.

Given the exact time evolutions of the magnetisation $\langle s^z \rangle$ and the variance $\left\langle (s^z)^2 \right\rangle$, they can be compared with their semi-classical approximations to benchmark the discrete truncated Wigner approximation. To do so, the interaction J_{ij} between two spins at sites i and j needs to be specified. A general formulation for the interaction strength depending on the distance between two spins is given by

$$J_{ij} = \begin{cases} \frac{J}{|i-j|^\alpha} & \text{if } i \neq j \\ 0 & \text{if } i = j \end{cases}. \tag{3.58}$$

Here the variable α describes the range of the interaction. For $\alpha = 0$, the interaction range is infinitely long, all spins interact with each other with the same strength J, not depending on their distance. This all-to-all interaction will be the first case to be analysed. After this, a short-range interaction with $\alpha = 3$ will be regarded, where nearest neighbours interact with strength J, but the interaction strength decreases with a greater distance between the spins. The larger α gets, the shorter becomes the interaction range. An infinitely large α equals a nearest neighbour interaction. This case will also be benchmarked and the interaction strength will then be chosen explicitly as

$$J_{ij}^{\text{NN}} = \begin{cases} J & \text{if } |i-j| = 1 \\ 0 & \text{otherwise} \end{cases}. \tag{3.59}$$

Here the index NN denotes the nearest neighbour interaction.

Given an expression for the interaction strength $\boldsymbol{J}$, the discrete truncated Wigner approximation of the Ising model can be calculated and benchmarked. Instead of choosing a certain value for J, the time can be defined in units of J, so that the evolution of the calculated trajectories depends on tJ instead of only time t. Using this, the simulations for $\alpha = 0$, $\alpha = 3$ and the nearest neighbour interaction will be benchmarked in the following.

Figure 3.3 shows the calculations for $\alpha = 0$, which equals an all-to-all interaction. Figure 3.3a shows the magnetisation $\langle s^z \rangle (t)$, while figure 3.3b shows the correlation $\left\langle (s^z)^2 \right\rangle (t) - \langle s^z \rangle (t)^2$. In the figures the approximations for the sampling schemes S_{init}, S_{mix}, $\tilde{S}_{\text{mix}}$ as well as the semi-continuous and the continuous scheme, as defined in section 3.3, are compared to the exact solutions in equations (3.49) and (3.50). For the correlation in figure 3.3b also the modified exact solution as stated in equation (3.57) is plotted, since this can be better compared with the approximation.

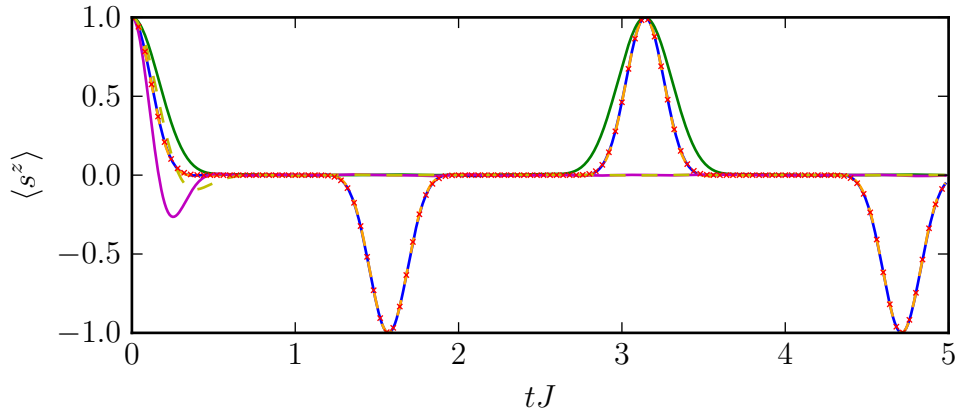

(a) Magnetisation $\langle s^z \rangle$ for $N = 20$ spins, $R = 10000$ runs and $\alpha = 0$.

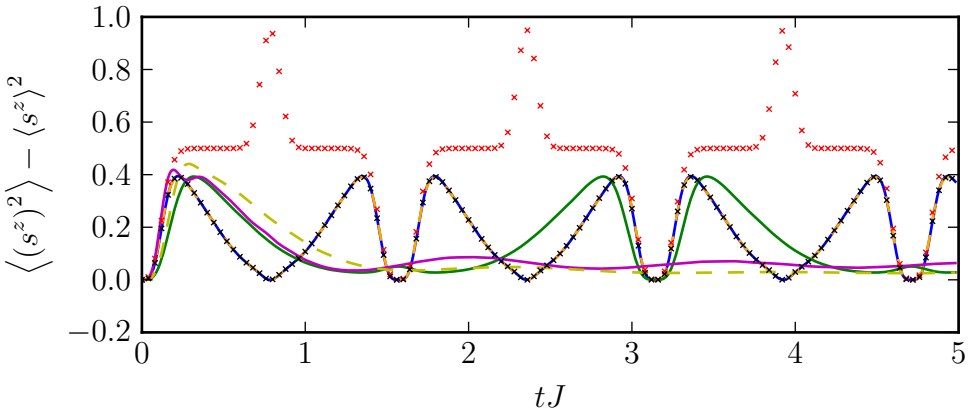

(b) Correlation $\left\langle (s^z)^2 \right\rangle - \langle s^z \rangle^2$ for $N = 20$ spins, $R = 10000$ runs and $\alpha = 0$.

Figure 3.3: Magnetisation $\langle s^z \rangle (t)$ (figure 3.3a) and correlation $\left\langle (s^z)^2 \right\rangle (t) - \langle s^z \rangle^2 (t)$ (figure 3.3b) of the Ising Hamiltonian with all-to-all interactions. First order approximations using the discrete truncated Wigner approximation with different sampling schemes are compared with the exact solution. The blue line shows the approximation using sampling scheme S_{init}, the dashed orange line shows the result for scheme S_{mix}, the green line shows the approximation using $\tilde{S}_{\text{mix}}$, the magenta line is created with the semi-continuous sampling scheme, while the dashed yellow line shows the result for the continuous sampling scheme. The red crosses show the exact result and in figure 3.3b the black crosses show the modification of the exact result as stated in equation (3.57).

In figure 3.3a one can see that the sampling schemes S_{init} and S_{mix} follow the exact time evolution of the magnetisation $\langle s^z \rangle (t)$ everywhere. They show all revivals of the exact solution at the right times and the lines lie directly on each other. The sampling scheme $\tilde{S}_{\text{mix}}$ does not follow the exact solution that closely, it only shows the positive revivals and misses the negative ones, while even the positive ones are broader than the exact solution. The continuous and the semi-continuous sampling start at the right magnetisation but fall down to zero and do not show any revivals. They only follow the exact solution for very short times.

Regarding the correlations in figure 3.3b one gets the same conclusions. None of the approximations follows the exact result, which is expected since it has been discussed before that there is some difference between the exact correlation and the semi-classical approximation. But a comparison with the modified exact solution, as stated in equation (3.57), shows again that the sampling schemes S_{init} and S_{mix} have the same behaviour as the modified solution. As in figure 3.3a, the sampling scheme $\tilde{S}_{\text{mix}}$ misses some extrema of the modified solution and is broader. The continuous and the semi-continuous sampling again only work for short times, they rise together with the modified solution, but then fall down to zero and stay there.

In figure 3.4 the discrete truncated Wigner approximation of an Ising chain with short-range interaction using $\alpha = 3$ for the different sampling schemes is compared to the exact solutions. Figure 3.4a shows the time evolution of the magnetisation $\langle s^z \rangle (t)$, while figure 3.4b shows the trajectories of the correlation $\left\langle (s^z)^2 \right\rangle (t) - \langle s^z \rangle^2 (t)$. There one can find the same conclusions as in figure 3.3 for the all-to-all interaction.

The exact magnetisation in figure 3.4a is well matched by the sampling schemes S_{init} and S_{mix}. Their evolutions follow the exact solution at all times. The approximation with sampling scheme $\tilde{S}_{\text{mix}}$ misses some revivals of the exact solution and the maxima are much broader. The continuous and the semi-continuous sampling do not follow the exact solution, they fall down to zero and show small oscillations around it. Here even the slope at short times does not match with the exact result, thus for short-range interactions these sampling schemes do not even work for small times.

In figure 3.4b no approximation matches with the exact result, which is caused by the difference in the calculations of the correlation. The modification of the exact solution in the way of equation (3.57) does not match any of the approximations at short times either, but for times $t \gtrsim 2.5tJ$ it shows the same behaviour as the approximations with the sampling schemes S_{init} and S_{mix}. For shorter times, these approximations are closer to the exact result. The trajectory calculated with the sampling scheme $\tilde{S}_{\text{mix}}$ roughly gets the behaviour of the modified and the exact solution at some times. The results for the continuous and the semi-continuous sampling scheme saturate at relatively short times and do not approximate the behaviour of the exact or the modified trajectory. While the semi-continuous sampling is close to the exact solution for the first maximum, the continuous sampling already has a different slope there.

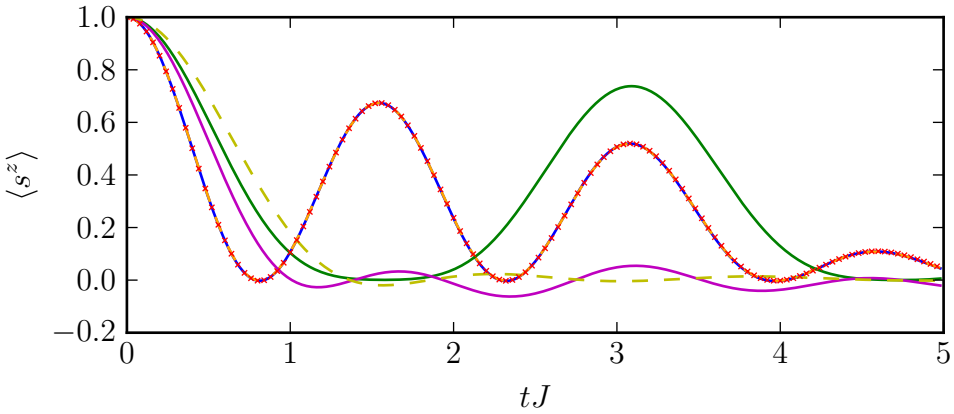

(a) Magnetisation $\langle s^z \rangle$ for $N = 20$ spins, $R = 10000$ runs and $\alpha = 3$.

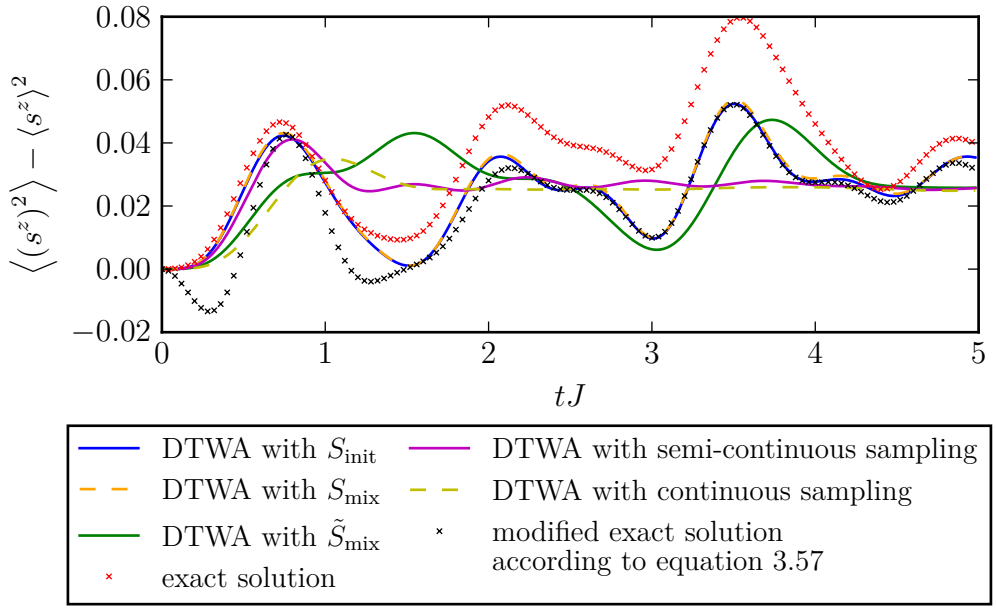

(b) Correlation $\left\langle (s^z)^2 \right\rangle - \langle s^z \rangle^2$ for $N = 20$ spins, $R = 10000$ runs and $\alpha = 3$.

Figure 3.4: Comparison of first order discrete truncated Wigner approximations of the magnetisation $\langle s^z \rangle (t)$ (figure 3.4a) and the correlation $\left\langle (s^z)^2 \right\rangle (t) - \langle s^z \rangle^2 (t)$ (figure 3.4b) in the Ising chain with the exact result using short-range interactions. The approximation using sampling scheme S_{init} is shown by the blue line, the dashed orange line describes the result for the sampling scheme S_{mix}, while the result for scheme $\tilde{S}_{\text{mix}}$ is given by the green line. The magenta and the dashed yellow lines show the approximations with the semi-continuous and the continuous sampling scheme respectively. The exact solution is given by the red crosses, while the modification of the exact solution according to equation (3.57) is shown by the black crosses in figure 3.4b.

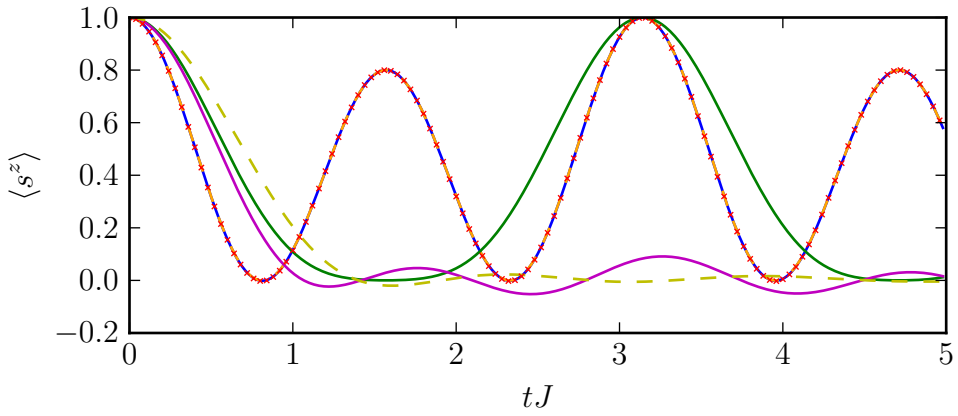

(a) Magnetisation $\langle s^z \rangle$ for $N = 20$ spins, $R = 10000$ runs and nearest neighbour interaction.

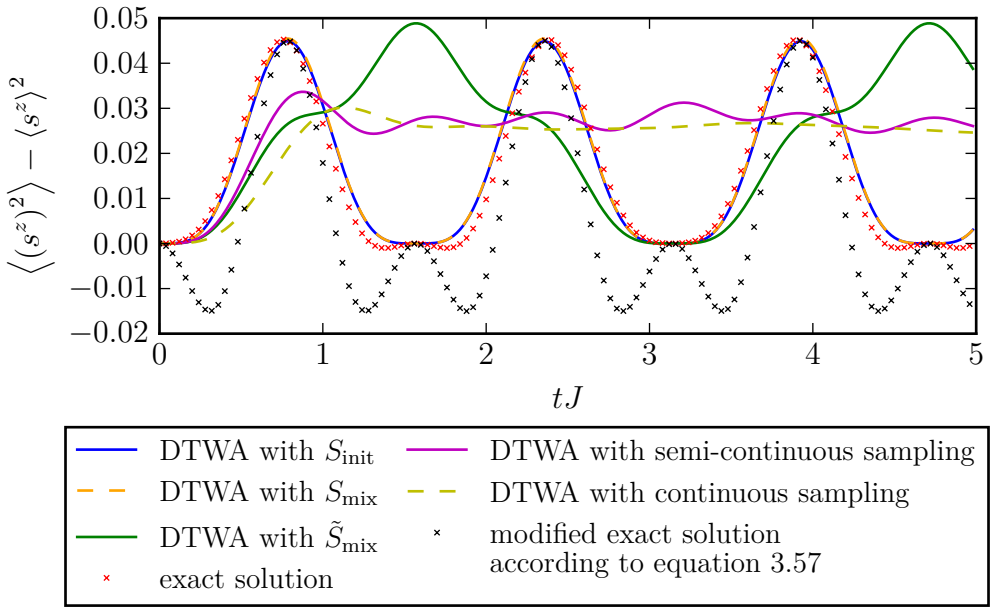

(b) Correlation $\left\langle (s^z)^2 \right\rangle - \langle s^z \rangle^2$ for $N = 20$ spins, $R = 10000$ runs and nearest neighbour interaction.

Figure 3.5: Benchmarking the first order discrete truncated Wigner approximation of magnetisation $\langle s^z \rangle (t)$ (figure 3.5a) and correlation $\left\langle (s^z)^2 \right\rangle (t) - \langle s^z \rangle^2 (t)$ (figure 3.5b) in the Ising chain with nearest neighbour interaction. The blue line shows results for S_{init}, while the dashed orange and the green line denote results using S_{mix} and $\tilde{S}_{\text{mix}}$ respectively. The magenta line is resulting from the semi-continuous sampling scheme and the dashed yellow line shows the result using the continuous sampling scheme. Red and black crosses show the exact solution and its modification according to equation (3.57) in figure 3.5b respectively.

The result for benchmarking the discrete truncated Wigner approximation of the Ising Hamiltonian with nearest neighbour interactions is shown in figure 3.5, where 3.5a shows the approximated magnetisation $\langle s^z \rangle (t)$ in comparison to the exact solution. There one can see that again the approximations using the sampling schemes S_{init} and S_{mix} closely follow the exact solution, while the approximation with $\tilde{S}_{\text{mix}}$ misses some revivals and shows broader maxima. As in figure 3.4a, the continuous and the semi-continuous sampling scheme result in trajectories, which fall down to zero after short times and then have small oscillations around it. Also here the slope of the first decrease does not match with the one of the exact solution.

Also in figure 3.5b the approximations with S_{init} and S_{mix} are close to the exact solution. Here it is peculiar that the approximations match better with the exact solution than with its modification according to equation (3.57). This does not fulfil the theoretical predictions and suggests that the two additional terms in the semi-classical approximation are suppressed compared to the modified exact solution where the two terms are taken into account. The trajectory calculated with $\tilde{S}_{\text{mix}}$ again only roughly gets the behaviour of the exact and the modified solution. Also the continuous and the semi-continuous sampling scheme do not follow the exact solution, they again saturate after short times and even the slopes for short times do not match with the exact and the modified solution.

Combining the results from figures 3.3, 3.4 and 3.5, one can conclude that the sampling schemes S_{init} and S_{mix} are in good agreement with the exact solution of the magnetisation $\langle s^z \rangle (t)$ in the Ising chain. It is peculiar that they even fit to the exact solution with nearest neighbour interactions, since it is stated in [16] and [27] that the discrete truncated Wigner approximation better works for long-range interactions. There the authors argue that for long-range interactions the deviations from mean-field are expected to be small and hence the discrete truncated Wigner approximation works well in this limit. It is proven here that the approximation also shows useful results for nearest neighbour interactions.

Considering the correlation $\left\langle (s^z)^2 \right\rangle (t) - \langle s^z \rangle^2 (t)$, S_{init} and S_{mix} give useful approximations of the modified exact solution according to equation (3.57) for all-to-all interactions. For short-range interactions, the approximations are close to the exact solution at short times and follow the modification of the exact solution at longer times. For nearest neighbour interactions, they follow the exact solution better than the modification at all times. This shows that for shorter interaction ranges, the approximations follow the exact solution for a longer time, before they match with the modification of the exact solution.

The sampling scheme $\tilde{S}_{\text{mix}}$ as well as the continuous and the semi-continuous sampling schemes do not follow the exact solution, neither for the magnetisation nor for the correlation. The continuous and the semi-continuous sampling schemes result in trajectories which are in good agreement with the exact solutions for very short times until the first maximum in the case of long interaction ranges, before they fall down to a plateau and saturate. In comparison the sampling scheme $\tilde{S}_{\text{mix}}$ always misses revivals of the magnetisation and only roughly approximates the exact

or the modified curves.

3.4.2 Analysing the Second Order Approximation

After the different sampling schemes have been benchmarked for the first order approximation of an Ising chain, the same process can be repeated to benchmark the discrete truncated Wigner approximation using the BBGKY hierarchy of the reduced phase-point operators up to second order to approximate the equations of motion. Using equation (3.20), the second order approximation of the time evolved expansion coefficients $\boldsymbol{a}_i$ can be given for the Ising Hamiltonian H_{xx} according to [16],

$$H_{\mathrm{xx}} = -\sum_{\substack{i,j=0 \\ i\neq j}}^{N-1} J_{ij} s_i^x s_j^x \tag{3.60}$$

$$\Rightarrow \dot{a}_i^x = 0, \tag{3.61}$$

$$\dot{a}_i^y = 2\sum_{\substack{k=0 \\ k\neq i}}^{N-1} J_{ik}\left(c_{ik}^{zx} + a_i^z a_k^x\right), \tag{3.62}$$

$$\dot{a}_i^z = -2\sum_{\substack{k=0 \\ k\neq i}}^{N-1} J_{ik}\left(c_{ik}^{yx} + a_i^y a_k^x\right), \tag{3.63}$$

In the same way equation (3.23) can be used to write down the approximations of the time evolved second order expansion coefficients $\boldsymbol{c}_{ij}$ according to [16],

$$\dot{c}_{ij}^{xx} = 0, \tag{3.64}$$

$$\dot{c}_{ij}^{xy} = 2\sum_{\substack{k=0 \\ k\neq i,j}}^{N-1} J_{jk}\left(a_k^x c_{ij}^{xz} + a_j^z c_{ik}^{xx}\right) - 2J_{ij}a_i^x\left(c_{ij}^{xz} + a_i^x a_j^z\right) + 2J_{ij}a_j^z, \tag{3.65}$$

$$\dot{c}_{ij}^{xz} = -2\sum_{\substack{k=0 \\ k\neq i,j}}^{N-1}\left(a_k^x c_{ij}^{xy} + a_j^y c_{ik}^{xx}\right) + 2J_{ij}a_i^x\left(c_{ij}^{xy} + a_i^x a_j^y\right) - 2J_{ij}a_j^y, \tag{3.66}$$

$$\dot{c}_{ij}^{yx} = 2\sum_{\substack{k=0 \\ k\neq i,j}}^{N-1} J_{ik}\left(a_k^x c_{ij}^{zx} + a_i^z c_{jk}^{xx}\right) - 2J_{ij}a_j^x\left(c_{ij}^{zx} + a_i^z a_j^x\right) + 2J_{ij}a_i^z, \tag{3.67}$$

$$\dot{c}_{ij}^{yy} = 2\sum_{\substack{k=0\\k\neq i,j}}^{N-1}\left[J_{ik}\left(a_k^x c_{ij}^{zy} + a_i^z c_{jk}^{yx}\right) + J_{jk}\left(a_k^x c_{ij}^{yz} + a_j^z c_{ik}^{yx}\right)\right] \tag{3.68}$$

$$- 2J_{ij}a_i^y\left(c_{ij}^{xz} + a_i^x a_j^z\right) - 2J_{ij}a_j^y\left(c_{ij}^{zx} + a_i^z a_j^x\right),$$

$$\dot{c}_{ij}^{yz} = 2\sum_{\substack{k=0\\k\neq i,j}}^{N-1}\left[J_{ik}\left(a_k^x c_{ij}^{zz} + a_i^z c_{jk}^{zx}\right) - J_{jk}\left(a_k^x c_{ij}^{yy} + a_j^y c_{ik}^{yx}\right)\right] \tag{3.69}$$

$$+ 2J_{ij}a_i^y\left(c_{ij}^{xy} + a_i^x a_j^y\right) - 2J_{ij}a_j^z\left(c_{ij}^{zx} + a_i^z a_j^x\right),$$

$$\dot{c}_{ij}^{zx} = -2\sum_{\substack{k=0\\k\neq i,j}}^{N-1}\left(a_k^x c_{ij}^{yx} + a_i^y c_{ik}^{xx}\right) + 2J_{ij}a_j^x\left(c_{ij}^{yx} + a_i^y a_j^x\right) - 2J_{ij}a_i^y, \tag{3.70}$$

$$\dot{c}_{ij}^{zy} = 2\sum_{\substack{k=0\\k\neq i,j}}^{N-1}\left[J_{jk}\left(a_k^x c_{ij}^{zz} + a_j^z c_{ik}^{zx}\right) - J_{ik}\left(a_k^x c_{ij}^{yy} + a_i^y c_{jk}^{yx}\right)\right] \tag{3.71}$$

$$+ 2J_{ij}a_j^y\left(c_{ij}^{yx} + a_i^y a_j^x\right) - 2J_{ij}a_i^z\left(c_{ij}^{xz} + a_i^x a_j^z\right),$$

$$\dot{c}_{ij}^{zz} = -2\sum_{\substack{k=0\\k\neq i,j}}^{N-1}\left[J_{ik}\left(a_k^x c_{ij}^{yz} + a_i^y c_{jk}^{zx}\right) + J_{jk}\left(a_k^x c_{ij}^{zy} + a_j^y c_{ik}^{zx}\right)\right] \tag{3.72}$$

$$+ 2J_{ij}a_i^z\left(c_{ij}^{xy} + a_i^x a_j^y\right) + 2J_{ij}a_j^z\left(c_{ij}^{yx} + a_i^y a_j^x\right).$$

Since in the approximation the initial values of all expansion coefficients $\boldsymbol{c}_{ij}$ are chosen to be zero, c_{ij}^{xx} will be zero at all times. Also the time evolutions of c_{ij}^{xy} and c_{ij}^{xz} only depend on each other and on a_i^x, hence they will also be zero at all times. The same is true for the time evolutions of c_{ij}^{yx} and c_{ij}^{zx}. With these properties, the equations of motion of the expansion coefficients become [16]

$$\begin{aligned}
\dot{a}_i^x &= 0,\\
\dot{a}_i^y &= 2\sum_{\substack{k=0\\k\neq i}}^{N-1} J_{ik}a_i^z a_k^x,\\
\dot{a}_i^z &= -2\sum_{\substack{k=0\\k\neq i}}^{N-1} J_{ik}a_i^y a_k^x,
\end{aligned} \tag{3.73}$$

$$\dot{c}_{ij}^{xx} = 0,$$

$$\dot{c}_{ij}^{xy} = 0,$$

$$\dot{c}_{ij}^{xz} = 0,$$

$$\dot{c}_{ij}^{yx} = 0,$$

$$\dot{c}_{ij}^{yy} = 2\sum_{\substack{k=0\\k\neq i,j}}^{N-1}\left(J_{ik}a_k^x c_{ij}^{zy} + J_{jk}a_k^x c_{ij}^{yz}\right) - 2J_{ij}a_i^y a_i^x a_j^z - 2J_{ij}a_j^y a_i^z a_j^x,$$

$$\dot{c}_{ij}^{yz} = 2\sum_{\substack{k=0\\k\neq i,j}}^{N-1}\left(J_{ik}a_k^x c_{ij}^{zz} - J_{jk}a_k^x c_{ij}^{yy}\right) + 2J_{ij}a_i^y a_i^x a_j^y - 2J_{ij}a_j^z a_i^z a_j^x,$$

$$\dot{c}_{ij}^{zx} = 0,$$

$$\dot{c}_{ij}^{zy} = 2\sum_{\substack{k=0\\k\neq i,j}}^{N-1}\left(J_{jk}a_k^x c_{ij}^{zz} - J_{ik}a_k^x c_{ij}^{yy}\right) + 2J_{ij}a_j^y a_j^x a_i^y - 2J_{ij}a_i^z a_j^z a_i^x,$$

$$\dot{c}_{ij}^{zz} = -2\sum_{\substack{k=0\\k\neq i,j}}^{N-1}\left(J_{ik}a_k^x c_{ij}^{yz} + J_{jk}a_k^x c_{ij}^{zy}\right) + 2J_{ij}a_i^z a_i^x a_j^y + 2J_{ij}a_j^z a_i^y a_j^x. \tag{3.74}$$

The time evolutions of the magnetisation $\langle s^z\rangle(t)$ and the variance $\left\langle (s^z)^2\right\rangle(t)$ are then given by averaging over N spins and R runs [16],

$$\langle s^z\rangle_{\mathrm{B}}(t) = \frac{1}{NR}\sum_{i=0}^{N-1}\sum_{r=0}^{R-1} a_{i,r}^z(t), \tag{3.75}$$

$$\left\langle (s^z)^2\right\rangle_{\mathrm{B}}(t) = \frac{1}{N^2R}\sum_{i,j=0}^{N-1}\sum_{r=0}^{R-1}\left(c_{ij,r}^{zz}(t) + a_{i,r}^z(t)\,a_{j,r}^z(t)\right). \tag{3.76}$$

Here the index B denotes the BBGKY-approximation. To get the time evolution of the expansion coefficients, differential equations need to be solved, which will be done numerically in the simulations. Different methods for this will be discussed in appendix C.2.

The time evolution of the magnetisation only depends on the time evolutions of the first order expansion coefficients $\boldsymbol{a}_i$. The corresponding equations of motion (3.73) are the same as the ones derived for the first order approximation in section

3.4.1, as stated in equation (3.52). Thus, also in the second order approximation the calculated time evolution of the magnetisation is the same as the exact solution. In [16] the authors have shown that for the second order approximation even the time evolution of the two-point variance is the same as in the exact solution. In this approximation there is no difference between the approximating time evolution and the exact time evolution of the variance, as it was the case for the first order approximation in subsection 3.4.1.

Given the second order approximated equations of motion using the BBGKY-hierarchy of the reduced phase-point operators, this method can be benchmarked analogously to the first order approximation in subsection 3.4.1. Also here the results using the different sampling schemes S_{init}, S_{mix}, $\tilde{S}_{\text{mix}}$ as well as the continuous and the semi-continuous scheme will be compared to the exact solution for the all-to-all interaction $\alpha = 0$, the short-range interaction $\alpha = 3$ and the nearest-neighbour interaction.

Figure 3.6 shows the approximation results for the all-to-all interaction, where 3.6a shows the magnetisation and 3.6b shows the variance $\left\langle (s^z)^2 \right\rangle$.

The approximation of the magnetisation in figure 3.6a shows the same results as in the first order approximations, which is clear since the equations of motion are the same. The only difference is that one can see deviations in the extrema appearing at longer times for all sampling schemes, which is caused by the fact that the equations of motion have been solved numerically here. This is done to benchmark the numerical method. It can be clearly seen that the quality of the numerical solution gets worse with longer times.

In figure 3.6b none of the approximations follows the exact solution. At short times all sampling schemes get the decay of the exact solution, but then deviations appear very fast for all schemes and especially for S_{init} and S_{mix} a large divergence can be seen for long times. Since it has been shown in [16] that the analytical solution of the second order equations of motion gives the exact result for the correlations, this divergence and the large deviations must be caused by the numerical solver of the differential equations. The equations of motion of the expansion coefficients $c_{ij}^{\mu\nu}$ in equation (3.74) can thus not be solved numerically in a stable way. Different solving algorithms have been tried here, but none of them gives better results, as further discussed in appendix C.2. Because of these large deviations appearing in the two-point function and the smaller deviations in the magnetisation, there is no point in regarding the correlation $\left\langle (s^z)^2 \right\rangle - \langle s^z \rangle^2$.

Figure 3.7 shows the approximations of the magnetisation (figure 3.7a) and the variance (figure 3.7b) for the short-range interaction $\alpha = 3$ and gives the same conclusions as figure 3.6. The deviations at long times in the magnetisation are much smaller here than in figure 3.6a and the quality ranking of the sampling schemes is the same as in the first order approximation.

Considering figure 3.7b, one can see that the deviations in the variance are much smaller for the short-range interactions than for the all-to-all interaction. Here no divergence appears at longer times and the schemes S_{mix} and S_{init} follow the exact

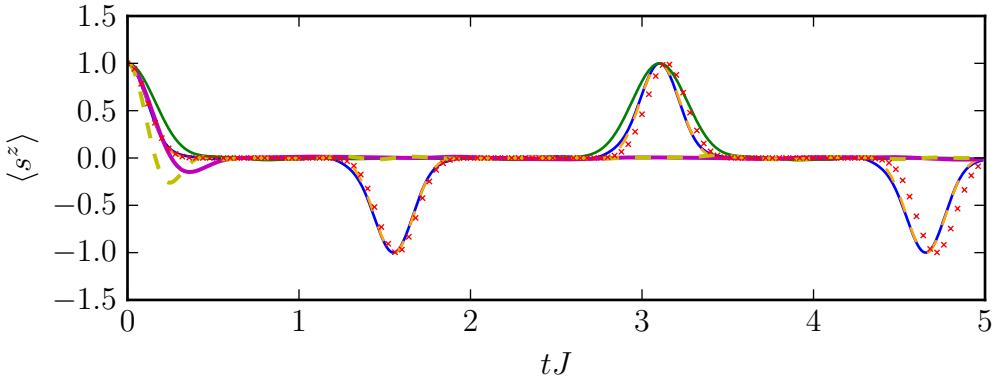

(a) Magnetisation $\langle s^z \rangle$ for $N = 20$ spins, $R = 1000$ runs and all-to-all interaction.

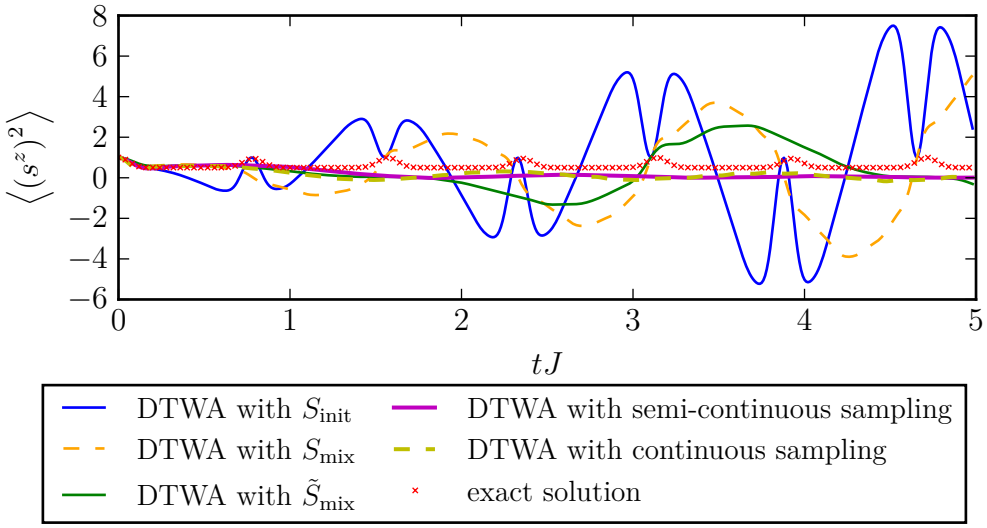

(b) Variance $\left\langle (s^z)^2 \right\rangle$ for $N = 20$ spins, $R = 1000$ runs and all-to-all interaction.

Figure 3.6: Magnetisation $\langle s^z \rangle$ (figure 3.6a) and variance $\left\langle (s^z)^2 \right\rangle$ (figure 3.6b) of the Ising chain with all-to-all interactions. Second order approximations using the sampling scheme S_{init} are shown by the blue line, while the dashed orange and the green line show the results for S_{mix} and $\tilde{S}_{\text{mix}}$ respectively. The semi-continuous sampling scheme results in the magenta line and the continuous sampling scheme gives the dashed yellow line. The exact solution is shown by the red crosses.

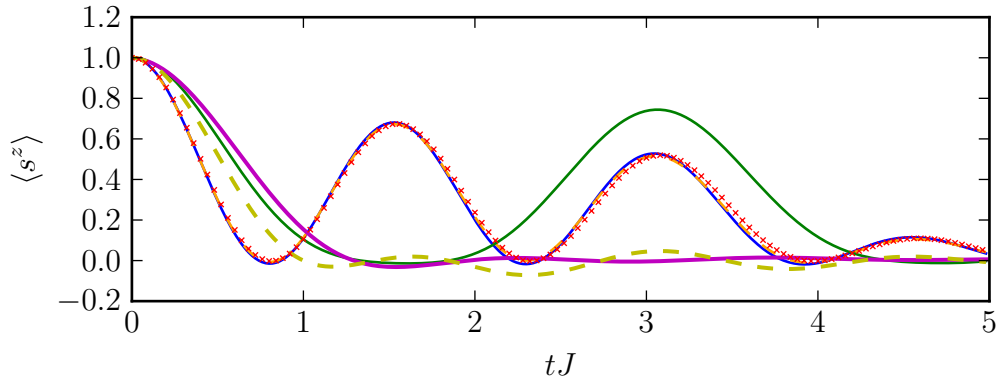

(a) Magnetisation $\langle s^z \rangle$ for $N = 20$ spins, $R = 1000$ runs and $\alpha = 3$.

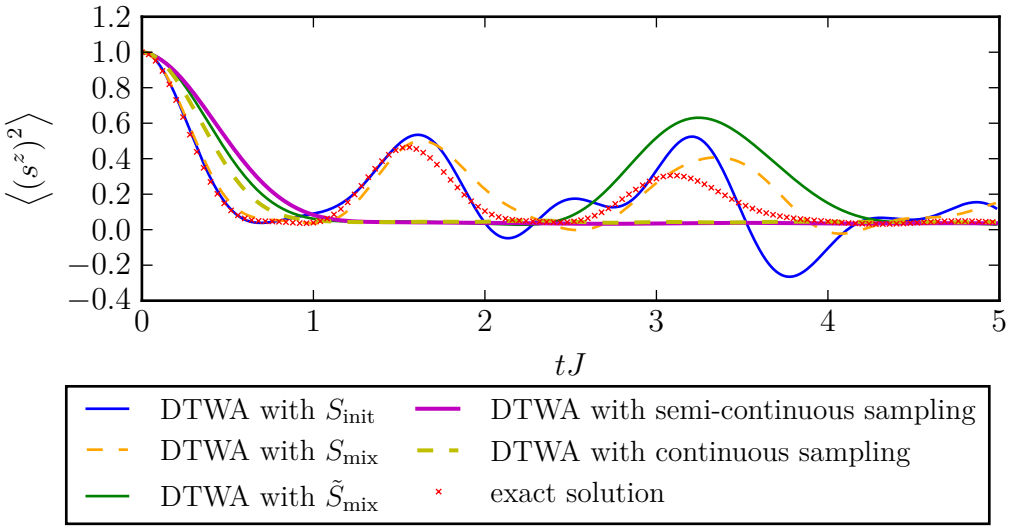

(b) Two-point variance $\left\langle (s^z)^2 \right\rangle$ for $N = 20$ spins, $R = 1000$ runs and $\alpha = 3$.

Figure 3.7: Second order approximations of the magnetisation $\langle s^z \rangle$ (figure 3.7a) and the variance $\left\langle (s^z)^2 \right\rangle$ (figure 3.7b) of the Ising Hamiltonian with short-range interactions. The sampling scheme S_{init} is described by the blue line, the dashed orange line shows the results of S_{mix} and the green line shows the behaviour of the approximation using $\tilde{S}_{\text{mix}}$. The semi-continuous and the continuous sampling scheme result in the magenta and the dashed yellow line respectively. The exact solution is shown by the red crosses.

solution until the first maximum, which is slightly shifted. After this maximum, S_{init} shows a different behaviour, while S_{mix} still gets the maxima of the exact solution. $\tilde{S}_{\text{mix}}$ misses some of the maxima, which is analogous to the behaviour in the first order approximations and also the semi-continuous and the continuous sampling scheme show the same behaviour as in the first order approximations, they decay and then stay at a plateau.

Figure 3.8 shows the approximations of the magnetisation in 3.8a and of the variance in 3.8b for nearest neighbour interactions. Here one can again find the same behaviour as in the approximations before. For the magnetisation in figure 3.8a the different sampling schemes show the same qualities as in the first order approximation and one can see deviations appearing at longer times, which are caused by the numerical solution of the equations of motion.

The approximation of the variance in figure 3.8b is much better than for the other two interactions regarded above, the calculations with S_{init} only show small deviations from the exact solution even for longer times. The deviations in the calculations with S_{mix} are larger at later times, but it still does not diverge. The behaviour of the calculations with $\tilde{S}_{\text{mix}}$ and with the semi-continuous and the continuous scheme is the same as in all other approximations discussed before.

In the end one can summarise that the numerical solving scheme does not work for very long times, but starts to show deviations, especially in the numerical calculation of the variance. Hence, the equations of motion can not be solved numerically in a stable way, while even here the analytical solutions result in the exact trajectories [16]. Different numerical solving schemes have been tried here and in [16] and also the parameters within the schemes have been changed, but so far it was not possible to find a better result. This will be further discussed in appendix C.2. Even if the second order approximation only works for short times, it will be regarded in the simulations in chapter 4, since it is not yet clear why the divergences appear. Therefore, it will be analysed at which times the divergences appear in different models and, as already stated, how the strength of the divergences changes for the different interaction ranges. It is expected that the strength of the divergences also depends on the approximated model.

By comparing the different interactions, one can see that the approximation of the correlation is qualitatively better the shorter the interaction range is. This is a peculiar result since, as already mentioned before, the discrete truncated Wigner approximation is expected to work better for long-range interactions in both, the first and second order approximations [16, 26, 27].

Also for the approximations using the second order BBGKY-hierarchy of the reduced phase-point operators one can conclude that the sampling schemes S_{init} and S_{mix} give the best approximations for the Ising chain, while the calculation with $\tilde{S}_{\text{mix}}$ misses some extrema and the semi-continuous as well as the continuous sampling scheme saturate quickly. This is again not surprising, since the exact result of the Ising chain is given by summing over all possible combinations of the spins being $+1$ and -1. This is also given by S_{init} and S_{mix}, while the spins in $\tilde{S}_{\text{mix}}$ and the semi-continuous and continuous sampling scheme can also take different values.

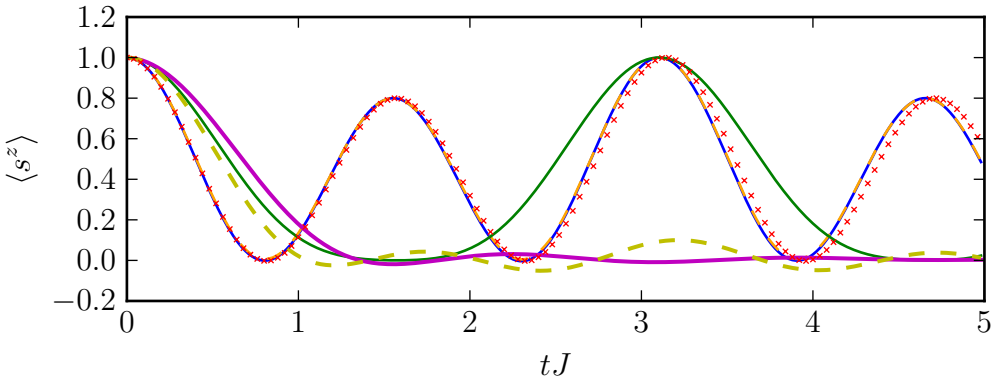

(a) Magnetisation $\langle s^z \rangle$ for $N = 20$ spins, $R = 1000$ runs and nearest neighbour interaction.

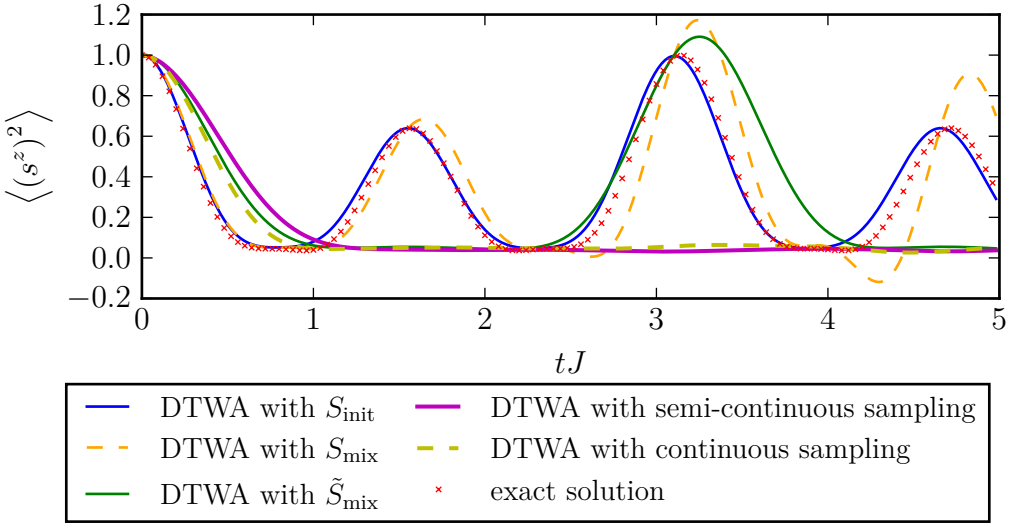

(b) Two-point variance $\left\langle (s^z)^2 \right\rangle$ for $N = 20$ spins, $R = 1000$ runs and nearest neighbour interaction.

Figure 3.8: Benchmarking the second order approximations of the magnetisation $\langle s^z \rangle$ in figure 3.8a and the variance $\left\langle (s^z)^2 \right\rangle$ in figure 3.8b of an Ising chain with nearest neighbour interactions. The five different sampling schemes are used for the approximations, where the blue line shows the results for S_{init}, the dashed orange line corresponds to S_{mix}, the green line shows $\tilde{S}_{\text{mix}}$ and the magenta and the yellow dashed line show the semi-continuous and the continuous sampling scheme respectively. For comparison the red crosses show the exact solution.

As will be shown in chapter 4, the quality of the sampling schemes depends on the approximated model. Therefore, also in the following simulations all introduced sampling schemes will be considered.

4 Sudden Quenches in the Transverse Field Ising Model

In chapter 3, the first and second order discrete truncated Wigner approximations for a spin-$\frac{1}{2}$ system have been introduced and benchmarked on an Ising chain. Going further, the method will be applied on an Ising chain with an additional transverse field within this chapter.

While the Ising model is a non-interacting system without many differences between classical and quantum-statistical fluctuations, as can be seen in section 3.4, the additional transverse field turns the model into a more complex system including a quantum phase transition. Hence, the transverse field Ising model can be used to analyse the semi-classical discrete truncated Wigner approximation in the vicinity of the quantum critical point. Since the model is exactly solvable, this analysation can be done by comparison with the exact solution. This way it can be observed whether a quantum mechanical system can be described semi-classically in the vicinity of a quantum phase transition and hence the appearance of quantum effects can be analysed.

Therefore, the model itself and the analytical calculations of the exact solution will be further introduced in section 4.1 according to [18, 22, 6, 7]. In the following section 4.2, the first order discrete truncated Wigner approximation will be applied on sudden quenches from the ground state of an infinitely large transverse field to different distances from the quantum critical point. The same procedure will be repeated for the second order discrete truncated Wigner approximation in section 4.3.

4.1 Analytical Calculations for Sudden Quenches in the Transverse Field Ising Model

The transverse field Ising chain is given by the Ising Hamiltonian in equation (3.42) in combination with a transverse field $h_i^z = h$, $h_i^x = h_i^y = 0$ which has the same value h for all sites i,

$$H_{\text{Ising}} = -\sum_{\substack{i,j=0 \\ i\neq j}}^{N-1} J_{ij}\hat{\sigma}_i^x\hat{\sigma}_j^x - h\sum_{i=0}^{N-1}\hat{\sigma}_i^z. \tag{4.1}$$

In the following, nearest neighbour interactions having the same strength J at all sites and periodic boundary conditions will be used, so that one can write the

Hamiltonian in the form

$$H_{\text{Ising}} = -\sum_{i=0}^{N-1} \left(J\hat{\sigma}_i^x \hat{\sigma}_{(i+1) \bmod N}^x + h\hat{\sigma}_i^z \right). \tag{4.2}$$

Here mod N denotes a modulo N calculation.

This quantum transverse field Ising chain is an exactly solvable model with a quantum phase transition. In particular, it is a second order phase transition at zero temperature, where a non-analyticity in the ground state energy is found [24]. This quantum critical point describes a crossover from a ferro- to a paramagnetic region. The transverse field Ising model can be diagonalised completely analytical at any finite temperature as shown in [18, 22]. See also [24, 25, 5] for a review. For this analytical diagonalisation, the Ising Hamiltonian is first fermionised by a Jordan-Wigner transformation. This means, that the Pauli operators are replaced by fermionic Jordan-Wigner operators a_j satisfying the canonical commutation relations,

$$a_j := \exp\left(\mathrm{i}\pi \sum_{k=0}^{j-1} \hat{\sigma}_k^\dagger \hat{\sigma}_k \right) \hat{\sigma}_j \text{ with } \hat{\sigma}_j = \hat{\sigma}_j^x + \mathrm{i}\hat{\sigma}_j^y \tag{4.3}$$

$$\Rightarrow \hat{\sigma}_j^x = \exp\left(\mathrm{i}\pi \sum_{k=0}^{j-1} a_k^\dagger a_k \right) \left(a_j^\dagger + a_j \right), \tag{4.4}$$

$$\hat{\sigma}_j^y = \mathrm{i}\exp\left(\mathrm{i}\pi \sum_{k=0}^{j-1} a_k^\dagger a_k \right) \left(a_j^\dagger - a_j \right), \tag{4.5}$$

$$\hat{\sigma}_j^z = \mathrm{I} - 2a_j^\dagger a_j. \tag{4.6}$$

On these Jordan-Wigner operators, a discrete Fourier transformation is applied to get the corresponding momentum degrees of freedom,

$$b_p = \frac{1}{\sqrt{N}} \sum_{j=0}^{N-1} a_j \exp\left(-\mathrm{i}pj\right) \text{ for } p \in \frac{\pi}{N}\mathbb{Z}. \tag{4.7}$$

The Ising Hamiltonian can then be expressed in terms of the Fourier transformed Jordan-Wigner operators. By applying a Bogoliubov transformation on these Fourier transformed Jordan-Wigner operators, again fermionic operators c_p are created. The expression of the operators depends on the relation between J and h. Here only the expression for $J \neq h$ will be given, since only this case will be considered in the simulations,

$$c_p = u_p b_b + v_p b_{-p}^\dagger \tag{4.8}$$

$$\text{with } u_p = \begin{cases} 0 \text{ if } p \in 2\pi\left(\mathbb{Z} + \frac{1}{2}\right) \\ 1 \text{ if } p \in 2\pi\mathbb{Z} \end{cases}, \tag{4.9}$$

$$v_p = \begin{cases} -\mathrm{i} \text{ if } p \in 2\pi\left(\mathbb{Z} + \frac{1}{2}\right) \\ 0 \text{ if } p \in 2\pi\mathbb{Z} \end{cases}. \tag{4.10}$$

The Ising Hamiltonian can then be expressed in terms of the Bogoliubov operators,

$$H = \sum_p \omega_p \left(c_p^\dagger c_p - \frac{1}{2} \right) \tag{4.11}$$

$$\text{with } \omega_p = 2\sqrt{J^2 + h^2 - 2Jh\cos(p)}. \tag{4.12}$$

Here ω_p is the single particle energy. At the quantum critical point, the ground state energy density shows a non-analycity in the thermodynamic limit, as discussed earlier. The ground state energy density can be written down in terms of the transverse field $h > 0$ in the case of $J > 0$,

$$\epsilon_0(h) = -\frac{2}{\pi}(J+h)\, E\left(\sqrt{\frac{4Jh}{(J+h)^2}} \right) \tag{4.13}$$

$$\text{with } E(k) = \int_0^{\frac{\pi}{2}} \sqrt{1 - k^2 \sin^2(p)}\mathrm{d}p. \tag{4.14}$$

It can be shown that this function has a point of non-analycity at $J = h$ [24, 25].

Given this analytic diagonalisation of the transverse field Ising model, it has been shown in [18, 22] and reviewed in [24, 5] that the model has a quantum critical point at $T = 0$ and $J = h$. At this point, a quantum phase transition between a paramagnetic and a ferromagnetic phase happens, where the system is paramagnetic for $J < h$ and ferromagnetic for $J > h$. The order parameter of the quantum phase transition is given by the expectation value of $\hat{\sigma}_i^x$ with respect to the ground state of the transverse field Ising model [24]. In the following calculations, J will be chosen to equal one, which can also be generally considered as using the ratio $\frac{h}{J}$ for the strength of the transverse field.

In the approximations of the transverse field Ising chain, the initial state will be chosen such that all spins are $+1$ in z-direction, as it was also the case in section 3.4. This configuration can be shown to equal the ground state of the transverse field Ising chain for the case of an infinitely large transverse field h. In this limit $h \to \infty$, the interaction term in the Ising Hamiltonian H_{Ising} in equation (4.2) can be neglected and the average energy of the two states $|z_0\rangle$ and $|z_1\rangle$ can be calculated explicitly,

$$H_{\text{Ising}} \approx -h \sum_{i=0}^{N-1} \hat{\sigma}_i^z \text{ for } h \to \infty, \tag{4.15}$$

$$\langle z_0 | \hat{\sigma}^z | z_0 \rangle = \begin{pmatrix} 1 \\ 0 \end{pmatrix} \begin{pmatrix} 1 & 0 \\ 0 & -1 \end{pmatrix} \begin{pmatrix} 1 \\ 0 \end{pmatrix} = 1, \tag{4.16}$$

$$\langle z_1 | \hat{\sigma}^z | z_1 \rangle = \begin{pmatrix} 0 \\ 1 \end{pmatrix} \begin{pmatrix} 1 & 0 \\ 0 & -1 \end{pmatrix} \begin{pmatrix} 0 \\ 1 \end{pmatrix} = -1. \tag{4.17}$$

Analogously it can be shown that the average energies are equal for both possible states in x- and y-direction. Hence, the lowest average energy is reached if all spins

are in $|z_0\rangle$, while there is no distinguished state in x- or y-direction. This state minimising the average energy is the ground state of the system.

In the simulations, sudden quenches will be considered, which are created by preparing the system in the ground state of an infinitely large transverse field h_i and then changing the field infinitely fast to a different value h_f. This is equivalent to computing the time evolution from the Hamiltonian $H_\mathrm{Ising}(h_\mathrm{f})$. Here the indices of h_i and h_f denote the initial and the final transverse field respectively. In the calculations, the time $t = 0$ will be chosen as the moment of the sudden quench. This way, quenches within the paramagnetic region $h > J$ can be calculated, as well as quenches across the quantum critical point into the ferromagnetic region $h < J$. In this thesis, only quenches within the paramagnetic region will be considered and compared to analytical results in [5].

The leading order behaviour of the longitudinal correlation function in the limit $d \to \infty$ and in thermodynamic limit $N \to \infty$,

$$\begin{aligned} C_d^{xx}(t, h_\mathrm{f}, h_\mathrm{i}) =& \frac{1}{N} \sum_{i=0}^{N} \left[\hat{\sigma}_i^x(t, h_\mathrm{f}, h_\mathrm{i}) \, \hat{\sigma}_{(i+d) \bmod N}^x(t, h_\mathrm{f}, h_\mathrm{i}) \right] \\ & - \frac{1}{N^2} \sum_{i=0}^{N} \hat{\sigma}_i^x(t, h_\mathrm{f}, h_\mathrm{i}) \sum_{i=0}^{N} \hat{\sigma}_{(i+d) \bmod N}^x(t, h_\mathrm{f}, h_\mathrm{i}), \end{aligned} \tag{4.18}$$

depending on time t, on the distance d between the spins and on the initial and final transverse field, has been derived and a review is given in [6, 7, 5]. The exact expression is denoted in equation 4.55 in [5] and the author also numerically evaluated it. These numerical results can now be compared with the results of the discrete truncated Wigner approximation applied on the transverse field Ising model to analyse the quality of the approximation depending on the distance of the final transverse field from the critical point.

In [6] and [7] the correlation functions in the transverse field Ising model have been calculated in the thermodynamic limit, which here means large system sizes N. There it is shown that in the thermodynamic limit the correlation functions get stationary. In this stationary state, correlation functions can be described by a generalised Gibbs ensemble, as defined in [12, 13].

The generalised Gibbs ensemble is a generalisation of the usual canonical ensemble, which describes a system in thermal equilibrium. In classical statistical physics, the Gibbs ensemble represents the states of a system with constant particle number in a fixed volume in a heat-bath. In thermal equilibrium, the statistical entropy $S(\rho)$ of a canonical state ρ is maximised. This statistical entropy can be translated into the von Neumann entropy $S(\hat{\rho})$ of a density matrix $\hat{\rho}$ in quantum statistical mechanics. This way also a Gibbs ensemble describing a quantum statistical system in thermodynamic equilibrium can be defined analogously. Hence, also the von Neumann entropy needs to be maximised in thermal equilibrium under the constraint of energy conservation. It has been shown in [6, 7] that the transverse field Ising model after a quench does not relax into the usual state of thermal equilibrium. Furthermore it relaxes into a state which can be described by the so called generalised Gibbs

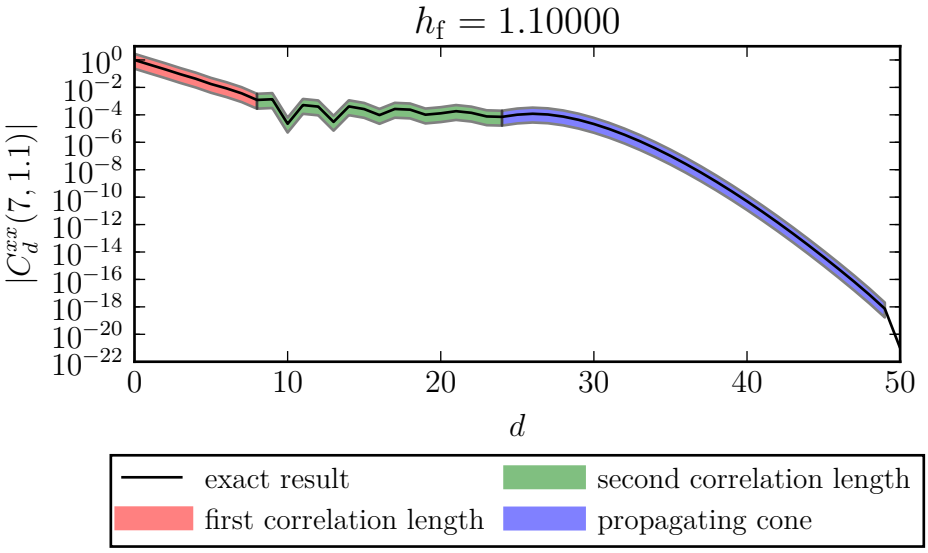

Figure 4.1: Exact correlation function in a transverse field Ising chain with $N = 100$ sites at time $t = 7$ after a sudden quench to $h_\mathrm{f} = 1.1$. The red region denotes the decay with which the first correlation length is associated and the green region shows the decay with which the second correlation length is associated. The blue region is the cone propagating through the correlation function with time.

ensemble, as introduced in [12, 13], where even more conserved quantities need to be respected in the maximisation of the von Neumann entropy.

While in [6, 7] the generalised Gibbs ensemble is found to characterise the correlation function of a transverse field Ising chain at stationarity after a quench in the scaling limit, in [5] the dynamics of the correlation functions for finite chains are evaluated numerically. There it has been observed that also for finite chains and times the correlation functions reach the stationary behaviour characterised by the generalised Gibbs ensemble.

Until the whole spin chain has reached the stationary state, a propagating cone has been observed in the correlation functions in [5] depending on the relative distance between the spins. This cone is illustrated in figure 4.1, where the exact correlation function is shown at time $t = 7$ after the quench to $h_\mathrm{f} = 1.1$. The propagating cone is found in the blue region, while the red and the green region denote correlation lengths, which will be discussed later. Inside this cone, the correlation function has been found to decay exponentially with the relative distance. These correlation functions after a sudden quench in a finite size chain can also be simulated with the discrete truncated Wigner approximation. Thus, by comparison the approximation method can be benchmarked for sudden quenches from an infinitely large initial transverse field to a final transverse field at different distances from the critical

point in the transverse field Ising model.

The infinitely large initial field is realised in the approximation by the condition that all initial states have a z-component of $+1$. In the exact calculations, a concrete value for the initial field h_i is needed. It is discussed in [5] that an initial field $h_\mathrm{i} = 1000$ can be treated as infinitely large, since it shows the same behaviour.

In [5], the author showed that in the decay of the correlation function inside the propagating cone two correlation lengths can be identified. These are illustrated in figure 4.1, where the two correlation lengths appear in the red and green region respectively. The correlation length in the red region is characterised by the generalised Gibbs ensemble and dominates for quenches close to the critical point. For quenches far away from the critical point the second correlation length dominates at short times, while the correlation length described by the generalised Gibbs ensemble is only found for short relative distances. In figure 4.1 a quench to a distance $\epsilon = 0.1$ from the critical point is considered, where it can be seen that the first correlation length is found for short relative distances, while the second correlation length dominates at larger distances. The author in [5] has shown that the correlation length described by the generalised Gibbs ensemble is already given at short times after the sudden quench in the limit of short relative distances.

This correlation length can also be calculated in the discrete truncated Wigner approximation and can thus also be used to benchmark the simulation method depending on the distance of the final transverse field from the critical point, which will be done in the following sections.

4.2 First Order Approximations of Quenches in the Transverse Field Ising Model

Given the Hamiltonian of the transverse field Ising chain in equation (4.2), the classical equations of motion of the spins s_i^μ for $\mu \in \{x, y, z\}$ can be calculated using equation (3.14),

$$\dot{s}_i^x = 2h_\mathrm{f} s_i^y, \tag{4.19}$$

$$\dot{s}_i^y = 2Js_i^z s_{(i+1) \bmod N}^x - 2h_\mathrm{f} s_i^x, \tag{4.20}$$

$$\dot{s}_i^z = -2Js_i^y s_{(i+1) \bmod N}^x. \tag{4.21}$$

These can not be solved exactly anymore, as it was the case for the Ising chain in section 3.4. Therefore, they are solved numerically in the simulations using the Runge-Kutta-Fehlberg method. More details on the numerical solving algorithm can be found in appendix C.2. With these equations of motion, the discrete truncated Wigner approximation of the spin dynamics in the transverse field Ising model can be calculated. Given the approximation of the multi-particle spin state via the ensemble of classical statistical fields $s_i^x(t)$, also the semi-classical approximation of the correlation function $C_{d,\mathrm{cl}}^{xx}(t, h_\mathrm{f})$ depending on time t, transverse field h_f after

the sudden quench from $h_\mathrm{i} \to \infty$ and relative distance d between the spins can be calculated,

$$C^{xx}_{d,\mathrm{cl}}(t, h_\mathrm{f}) = \frac{1}{NR} \sum_{i=0}^{N-1} \sum_{r=0}^{R-1} \left(s^x_{i,r}(t, h_\mathrm{f})\, s^x_{(i+d) \bmod N, r}(t, h_\mathrm{f}) \right) - \frac{1}{N^2 R^2} \sum_{i=0}^{N-1} \sum_{r=0}^{R-1} \left(s^x_{i,r}(t, h_\mathrm{f}) \right) \sum_{i=0}^{N-1} \sum_{r=0}^{R-1} \left(s^x_{(i+d) \bmod N, r}(t, h_\mathrm{f}) \right). \quad (4.22)$$

The resulting time evolved correlation function can be compared with the exact solution. In the course of this work, the exact solution is evaluated numerically from equation 4.55 in [5] using computational tools developed by the author of [5]. The dynamics of the correlation function will be calculated for different values of the final transverse field h_f in the vicinity of the quantum critical point within the paramagnetic phase. In particular, the setup is used to compare the five sampling schemes introduced in section 3.3 with the exact solution in subsection 4.2.1. In subsection 4.2.2, the correlation length will be considered for the exact solution and the approximations using the five introduced sampling schemes. This correlation length will be calculated by extending the short decay range of the correlation function from the spatial derivative at $d = 0$. Deviations between the semi-classical approximation of the transverse field Ising model and the exact quantum mechanical calculations can be found depending on the distance of the transverse field from the quantum critical point after a sudden quench from an infinitely large transverse field.

4.2.1 Correlation Functions and Numerical Precision

The calculations of the correlation function will be done using periodic boundary conditions on a chain of size N, as defined in the Hamiltonian in equation (4.2). As already explained in [5], finite size effects appear in the correlation function when the propagating cone reaches the end of the chain. For large N, these finite size effects do only appear at late times. The correlation functions build up an exponential decay within the cone of propagation, as discussed in section 4.1. Due to this, the correlation function reaches very small values. In figure 4.2, the correlation function is shown for a long chain with $N = 100$ sites. Note that due to periodic boundary conditions the correlation function is the same for distance d and $N - d$, and hence it is only plotted up to distance $d = \frac{N}{2} = 50$.

Figure 4.2 shows the exact results as well as the results of the approximations with all five sampling schemes. In figure 4.2a, the initial correlation function is plotted and figure 4.2b shows an extract thereof. One can see that the correlation function is one for distance $d = 0$ and zero for all other relative distances. While in figure 4.2a also the approximations seem to be zero for distances $d \neq 0$, it can be seen in the extract in figure 4.2b that the approximated correlation functions do not get smaller than approximately 10^{-3}, but then oscillate around zero. This oscillation has been observed in all approximations, smaller values have never been reached, even if the exact solution reaches very small values due to the exponential decay.

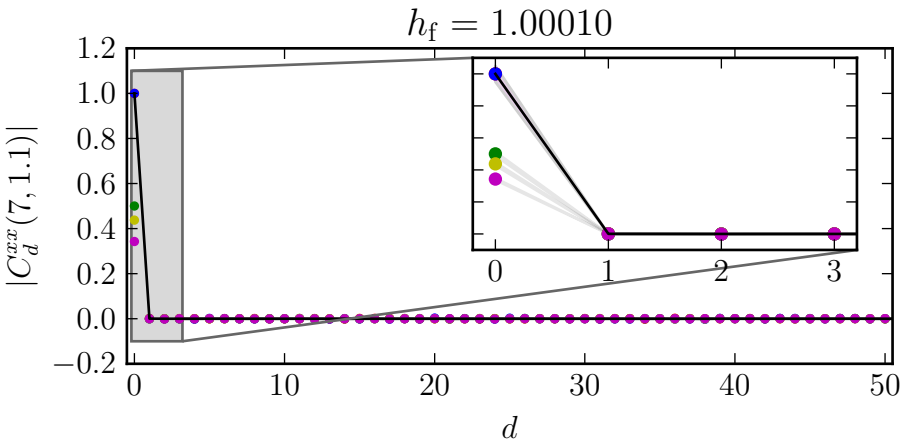

(a) Initial correlation functions

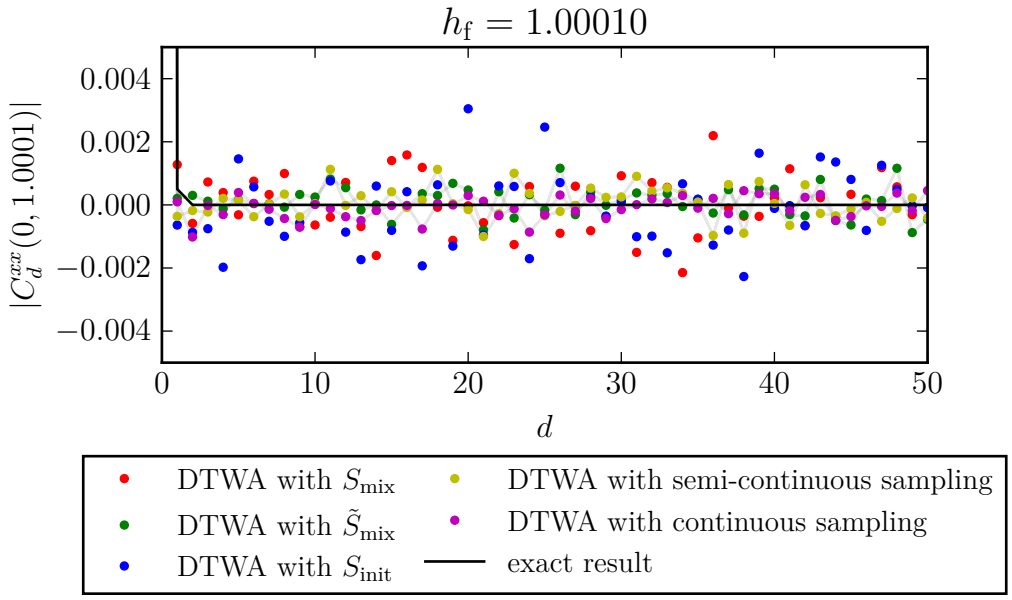

(b) Extract of figure 4.2a at small values of the correlation function

Figure 4.2: Exact results and first order approximations of the initial correlation functions in a transverse field Ising chain with $N = 100$ sites, nearest neighbour interactions and periodic boundary conditions after a sudden quench from an infinitely large transverse field to $h_\mathrm{f} = 1.0001$. Figure 4.2b shows an extract of figure 4.2a to see the approximations fluctuating around zero. The inset in figure 4.2a shows the short distance behaviour in more detail. Approximations are calculated by averaging $R = 10000$ runs and using the introduced sampling schemes. The red dots show results for S_mix, the green dots correspond to $\tilde{S}_\mathrm{mix}$ and the blue dots describe results using S_init. The semi-continuous and the continuous sampling scheme are shown by the yellow and the magenta dots respectively, while the black line shows the exact solution.

The approximated correlation functions are calculated by averaging a large number R of observables created in single runs, where the correlation functions of the individual runs have positive and negative values. For the sampling schemes S_{init} and S_{mix}, the spins in x-direction of the initial state are sampled to be $+1$ or -1 from a unique distribution. Hence, the initial correlation function for $d \neq 0$ is either $+1$ or -1, where both cases are equally likely. By averaging R runs, the initial correlation functions should average to zero, but as can be seen in figure 4.2b, they do not exactly reach zero. The existing minimal reachable value is caused by the variance of the averaging process. It is expected to get smaller if more runs are averaged. To analyse the dependence of this numerical error on R, a Monte-Carlo-integration can be considered according to [4]. This is an approximation method, which is defined for the integral of a general function $f(x)$ in a general space Ω as

$$I := \int_\Omega f(x)\,\mathrm{d}x \approx V \frac{1}{R} \sum_{i=0}^{R-1} f(x_i) =: S_R \tag{4.23}$$

$$\text{with } x_1 \dots x_R \in \Omega \text{ being uniform samples} \tag{4.24}$$

$$\text{and } V = \int_\Omega \mathrm{d}x \text{ being the volume of } \Omega. \tag{4.25}$$

By the law of large numbers, this approximation is exact for $R \to \infty$. Considering equation (2.42), one can see that such an approximation is used for the expectation values of operators in the discrete truncated Wigner approximation. The variance of S_R is then given depending on the variance of f [4],

$$\mathrm{Var}(S_R) = \frac{V^2}{R^2} \sum_{i=0}^{R-1} \mathrm{Var}(f) = V^2 \frac{\mathrm{Var}(f)}{R} = V^2 \frac{\sigma_R^2}{R}, \tag{4.26}$$

$$\mathrm{Var}(f) = \sigma_R^2 = \frac{1}{R-1} \sum_{i=0}^{R-1} \left(f(x_i) - \langle f \rangle\right)^2, \tag{4.27}$$

$$\langle f \rangle = \frac{1}{R} \sum_{i=0}^{R-1} f(x_i). \tag{4.28}$$

The estimation of the error in S_R is then given by

$$\delta S_R \approx \sqrt{\mathrm{Var}(S_R)} = V \frac{\sigma_R}{\sqrt{R}}, \tag{4.29}$$

and thus scales with $R^{-\frac{1}{2}}$ [4].

The minimal reachable value is not only caused by the variance of the averaging process, but also other numerical errors influence it. For example, the quality of the random number generator, which is further discussed in appendix C.1, also effects the minimal reachable value. Therefore, the minimal reachable value is expected to show an even worse dependence on the number of runs and to scale like R^{-b}, with $b \leq 0.5$.

To check this dependence, the initial correlation function in the transverse field Ising model has been calculated for different values of R and an average of the

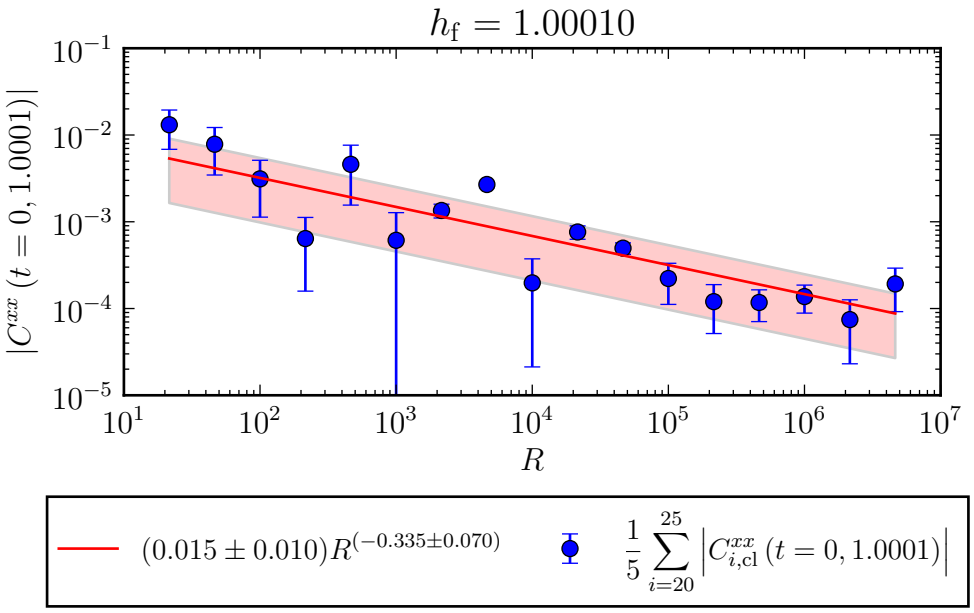

Figure 4.3: Absolute values of the initial correlation function averaged over several large distances as a function of the number R of runs. The calculations are done for a transverse field Ising chain of $N = 50$ sites with nearest neighbour interactions and periodic boundary conditions after a quench from an infinitely large transverse field to $h_\mathrm{f} = 1.0001$ close to the critical point, while $\tilde{S}_\mathrm{mix}$ is used for the first order approximations. The blue dots show the simulation results while the errorbars are the standard deviation of the averaging over the distances. A function $f(R) = aR^b$ is fitted to the data points resulting in $a = 0.015 \pm 0.010$ and $b = -0.335 \pm 0.070$, which is shown by the red line. The shaded region describes the fitting error.

absolute value over five large distances, $d = 20$ to $d = 25$, is plotted in figure 4.3, including standard deviations as errorbars. For these calculations, $\tilde{S}_\mathrm{mix}$ has been used, since this scheme will be found to give the closest results to the exact solution later in this section. This way, the minimal reachable value is plotted as a function of R and to get the dependence, a function $f(R) = aR^b$ has been fitted to the data points. This fit results in $a = 0.015 \pm 0.010$, $b = -0.335 \pm 0.070$ and is also plotted in figure 4.3 with the fit uncertainty shown as shaded region. The resulting value of b lies in the expected regime and one can conclude that the numerical errors result mainly from the finite sampling size.

In figure 4.2b it can be seen that $\tilde{S}_\mathrm{mix}$, as well as the semi-continuous and the continuous sampling scheme, show smaller minimal reachable values than S_mix and S_init. In these sampling schemes not only the values $+1$ and -1 are averaged, but also smaller values are sampled for the initial spin states. This makes the minimal reachable value smaller. Another effect of this can be seen in figure 4.2a considering

the correlation function at $d = 0$, which is one in the exact solution as well as in S_{mix} and S_{init}. In the inset in figure 4.2a, it can be clearly seen that the correlation functions show smaller values at $d = 0$ for the other three sampling schemes. Even this is caused by the fact that the spins can also take initial values other than $+1$ and -1.

Due to the dependence of the minimal reachable value on approximately $R^{-0.3}$, a large number of runs is needed to reach remarkably smaller values in the correlation function. Since the exact correlation function decays exponentially at later times, as discussed in section 4.1, it reaches very small values at large relative distances, which are not achievable in the simulations. It can be extrapolated that calculating the number of runs needed to reach that small values would take years of computation time given the setup used in this work. Therefore, $R = 10000$ will be chosen in the following calculations for first order approximations, as it was already used in figure 4.2. It has been checked that this number of runs results in small standard deviations in the approximations. For large relative distances, the approximations can then not follow the exact solution, since it reaches smaller values than the given precision of the numerical results. Thus, there is no effort in considering larger distances and the computation time can be decreased by simulating only short spin chains. In the following, chains of size $N = 20$ will be considered, where it has been checked that up to this distance the approximations can follow the exact solutions and that the short distance results are not influenced by the total chain size.

Figure 4.4 shows the absolute value of the correlation function of a transverse field Ising chain of size $N = 20$ with nearest neighbour interactions after a sudden quench to $h_{\mathrm{f}} = 1.0001$ close to the critical point for different times after the quench. The approximations are shown for the five sampling schemes introduced in section 3.3, where $R = 10000$ runs are averaged for each calculation. The simulations are compared to the exact solution. In the initial state, again the plateau of the correlation function at about 10^{-3} is found for all sampling schemes.

At time $t = 1$ one can already see the cone propagating in the exact solution at distance $d \approx 4$. The approximations also show this cone. Except for the calculations with S_{init}, they all follow the exact line very closely.

At time $t = 2$ the cone is propagated further through the chain and one can already see deviations between the exact result and the approximations for larger distances. For smaller distances, the approximations show the same decay as the exact solution, except for the trajectory calculated with S_{init}. Also S_{mix} shows a different decay than the exact solution for larger distances.

At $t = 2.5$ the exact solution shows the exponential decay for almost all distances, while the plateau can be seen for large distances in the approximations. The results calculated with $\tilde{S}_{\mathrm{mix}}$, the semi-continuous sampling scheme and the continuous scheme show the exponential decay given by the exact solution until distances of $d \approx 6$, while the other two sampling schemes still only follow the exact solution for shorter distances. The cone has now propagated through the whole chain, since the periodic boundary conditions give $C_d^{xx} = C_{N-d}^{xx}$. One can see that for $t = 3$ first finite size effects appear, since the exact solution starts to grow at large distances.

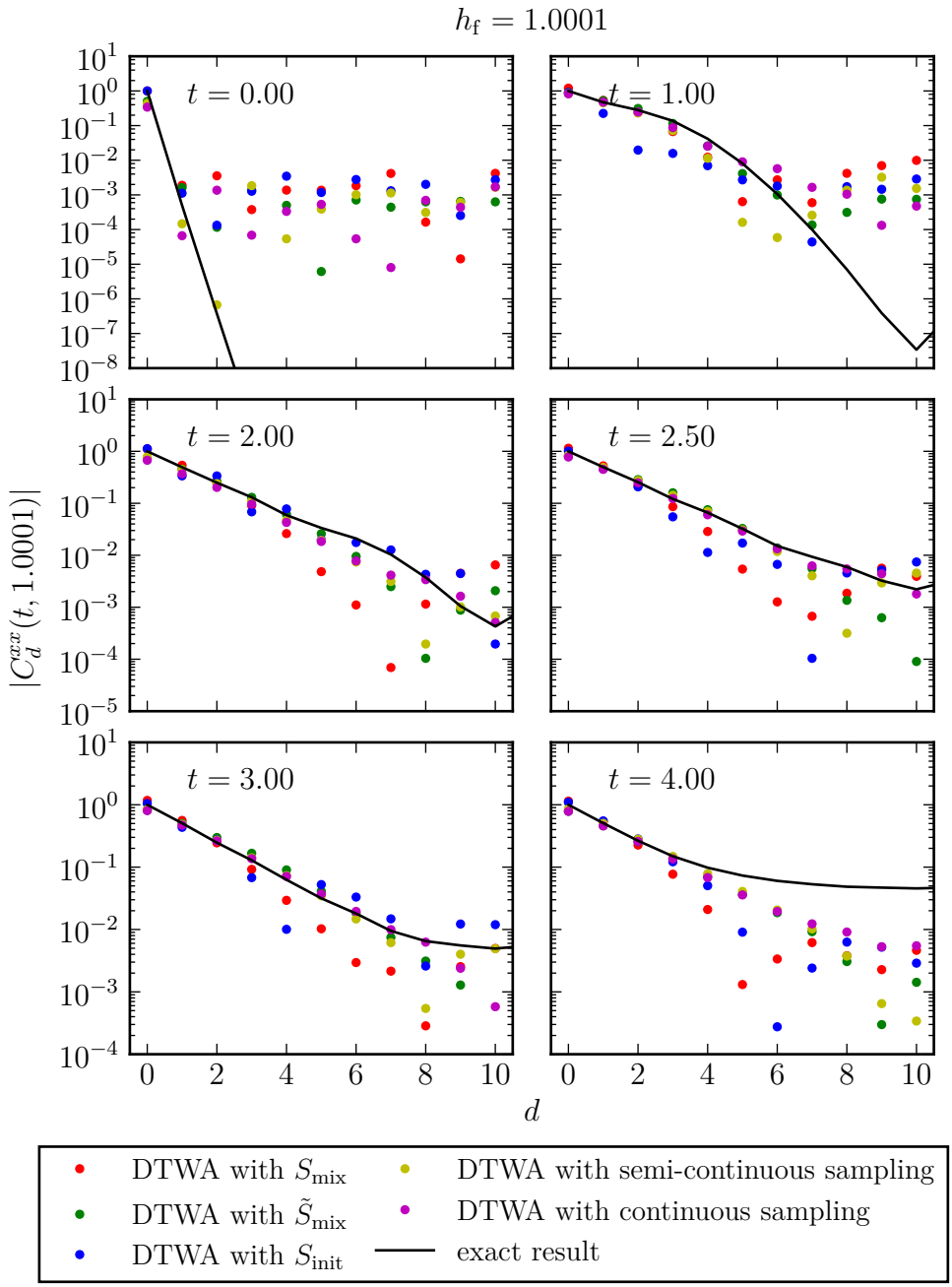

Figure 4.4: Absolute values of correlation functions in a transverse field Ising chain with $N = 20$ sites, nearest neighbour interactions and periodic boundary conditions at different times after a sudden quench from an infinite field to $h_\mathrm{f} = 1.0001$ depending on the site distance d. First order approximations are calculated by averaging $R = 10000$ runs and using S_mix (red dots), $\tilde{S}_\mathrm{mix}$ (green dots), S_init (blue dots) as well as the semi-continuous and the continuous sampling (yellow and magenta dots respectively) and compared with the exact solution (black line).

For $t = 4$ this effect is even larger and the exponential decay of the exact solution is not given anymore. onsidering the approximations, these finite size effects can not be found in the region where they appear in the exact solution, the correlation functions still show the same behaviour as for $t = 2.5$. This is peculiar, since also in the approximations periodic boundary conditions are used.

From figure 4.4 one can conclude that the exponential decay in the correlation function, which is described by a generalised Gibbs ensemble as discussed in section 4.1, is most clearly given at time $t = 2.5$, where the cone is propagated through almost the whole chain, but finite size effects do not appear yet. The comparison with the approximations shows that the semi-continuous and the continuous sampling scheme, as well as $\tilde{S}_{\mathrm{mix}}$, follow the exponential decay of the exact solution very closely until the plateau caused by numerical precision is reached. The sampling schemes S_{mix} and S_{init} only follow the exponential decay of the exact solution for very small distances and then show a different steepness.

Quenches to different distances from the critical point can now be considered at the fixed time $t = 2.5$, since this has been discussed to be the best time to analyse the correlation function inside the propagating cone. The results of the corresponding calculations are shown in figure 4.5, where the semi-classical approximations for all discussed sampling schemes are compared to the exact solutions for quenches from an infinitely large transverse field to values at different distances from the critical point, where the distances are considered in logarithmic steps.

One can see that for quenches to $h_{\mathrm{f}} = 1.001$ and $h_{\mathrm{f}} = 1.01$ the same conclusion follows from the results as for the quench to $h_{\mathrm{f}} = 1.0001$ in figure 4.4. The approximations resulting from $\tilde{S}_{\mathrm{init}}$, the semi-continuous sampling scheme and the continuous sampling scheme follow the exponential decay of the exact solution until the plateau caused by numerical precision is reached, while the calculations with S_{mix} and S_{init} only follow the exact solution for very small distances and then show a steeper decay.

These observations change for quenches to final transverse fields $h_{\mathrm{f}} \geq 1.1$. There the exact solution shows a steeper exponential decay than for quenches to smaller transverse fields, while the approximations still show roughly the same decay. Only the calculation with S_{init} follows the exact solution for very short distances considering the quenches to $h_{\mathrm{f}} = 1.1$ and $h_{\mathrm{f}} = 1.46416$ in figure 4.5. For $h_{\mathrm{f}} = 2$ also the steepness in the exponential decay of this approximation deviates from the exact solution and none of the approximations follows the exact result anymore.

One can see that for quenches to larger distances from the critical point also the exact solution builds a plateau which is at about the same height as the plateau in the approximations. In [5] the author discussed that the exact correlation functions are characterised by two correlation lengths, which are described by two decays of different steepness. There the author explains that for quenches close to the critical point, the correlation function is dominated by one correlation length, which is the one characterised by the generalised Gibbs ensemble as discussed in section 4.1. For quenches further away from the critical point both correlation lengths can be found, which is the reason for the plateau in the exact solution.

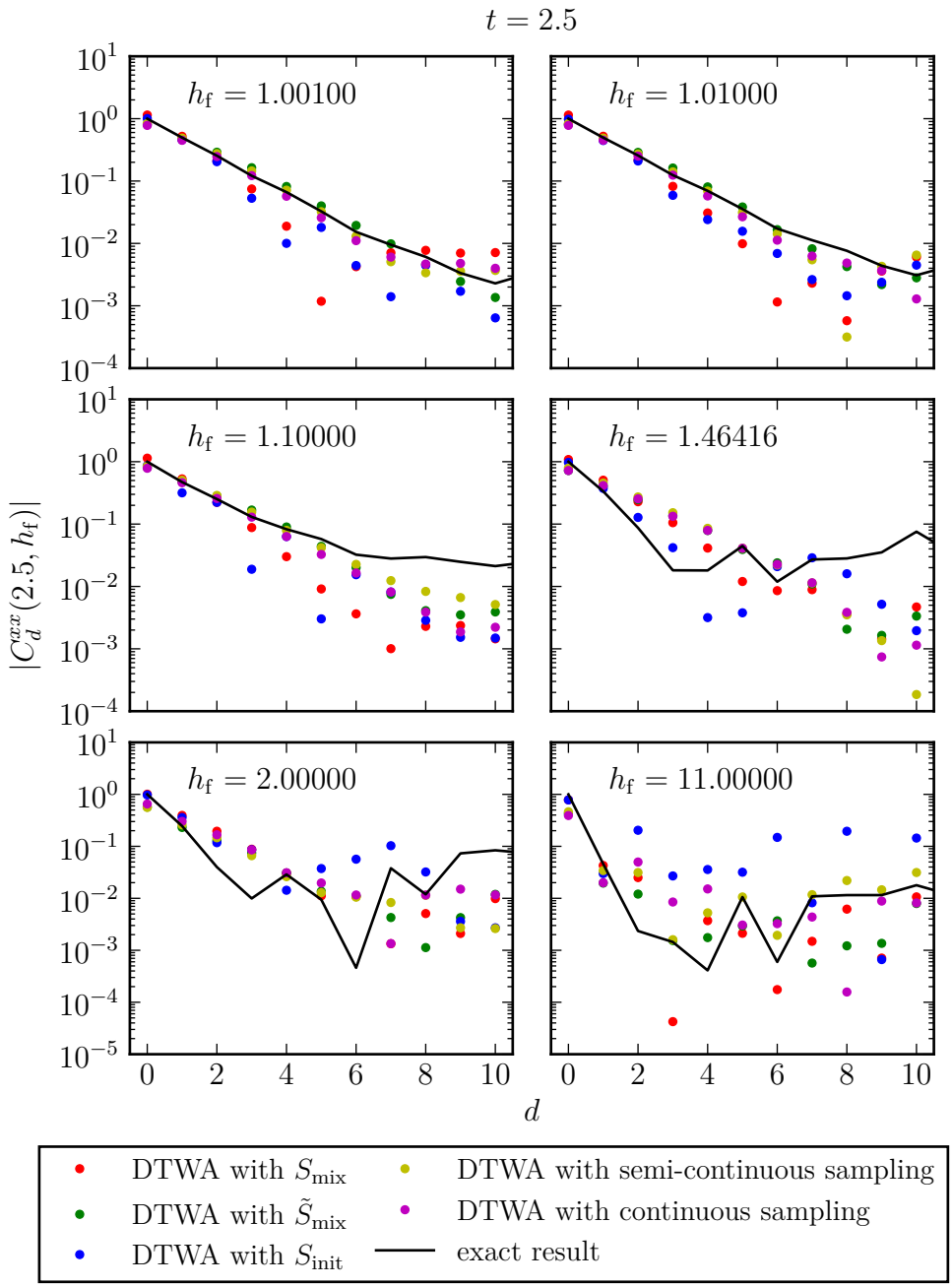

Figure 4.5: Absolute values of correlation functions in a transverse field Ising chain with $N = 20$ sites, nearest neighbour interactions and periodic boundary conditions at time $t = 2.5$ after a sudden quench from an infinite field to different distances from the critical point as a function of the site distance d. First order approximations with $R = 10000$ runs using the sampling schemes S_{mix} (red dots), $\tilde{S}_{mix}$ (green dots), S_{init} (blue dots) as well as the semi-continuous (yellow dots) and the continuous (magenta dots) scheme are compared to the exact solution (black line).

For quenches to very large distances from the critical point, the first exponential decay only appears at very small relative distances before the plateau is reached. But for $h_\mathrm{f} = 11$, the steepness of the short exponential decay is also given by the approximations again and all sampling schemes show the same behaviour. They follow the exact solution for very small relative distances until the plateau is reached.

In summary, one can conclude that for quenches to small distances from the critical point, the semi-continuous and the continuous sampling scheme as well as $\tilde{S}_\mathrm{mix}$ result in good approximations of the correlation function in the transverse field Ising chain, since they show the same exponential decay in the correlation function as the exact result. This decay equals the one described by a generalised Gibbs ensemble [5, 6, 7] and is thus an important property of the correlation function. For quenches to a transverse field between $h_\mathrm{f} \approx 1.1$ and $h_\mathrm{f} \approx 2$, none of the sampling schemes results in correlation functions with the same exponential decay as the exact solution, while all sampling schemes approximate the exact correlation function better again for quenches to even larger distances from the critical point.

In contrary to section 3.4, the sampling schemes S_init and S_mix have been found to give results which do not follow the exact solution that closely here. This shows that the quality of the sampling schemes depends on the approximated model.

4.2.2 Correlation Lengths depending on the Transverse Field

As already mentioned in subsection 4.2.1, the correlation function of the transverse field Ising model after sudden quenches gives two correlation lengths [6, 7, 5]. For quenches close to the critical point, one correlation length dominates, while the second one dominates for quenches further away from the critical point at short times. In [6, 7] the authors discussed that the first correlation length, which dominates quenches close to the critical point, is described by a generalised Gibbs ensemble, see also [5]. This correlation length will be further analysed in the approximation results.

In [6, 7, 5] it is shown that the correlation function is proportional to the exponential function of the inverse correlation length ξ^{-1} multiplied by the distance d plus an oscillating function the amplitude of which decays in time. For quenches close to the critical point, this oscillating function can be neglected. For quenches further away from the critical point, this oscillating function gives the second correlation length. Hence, to get the correlation length which will be analysed in the approximation, the short decay range is extended from the spatial derivative at $d = 0$.

In figure 4.6 the correlation length has been calculated for the approximations of the correlation functions shown in figure 4.5 using the five introduced sampling schemes and the exact solution. The correlation lengths are calculated for quenches to different distances $\epsilon = h_\mathrm{f} - 1$ from the critical point depending on the time t after the quench from an infinitely large transverse field. The shaded regions show the uncertainty in the calculation of the correlation length. In the correlation lengths retrieved from the exact correlation function, uncertainties are negligible.

One can see in all approximations that the correlation lengths for quenches to

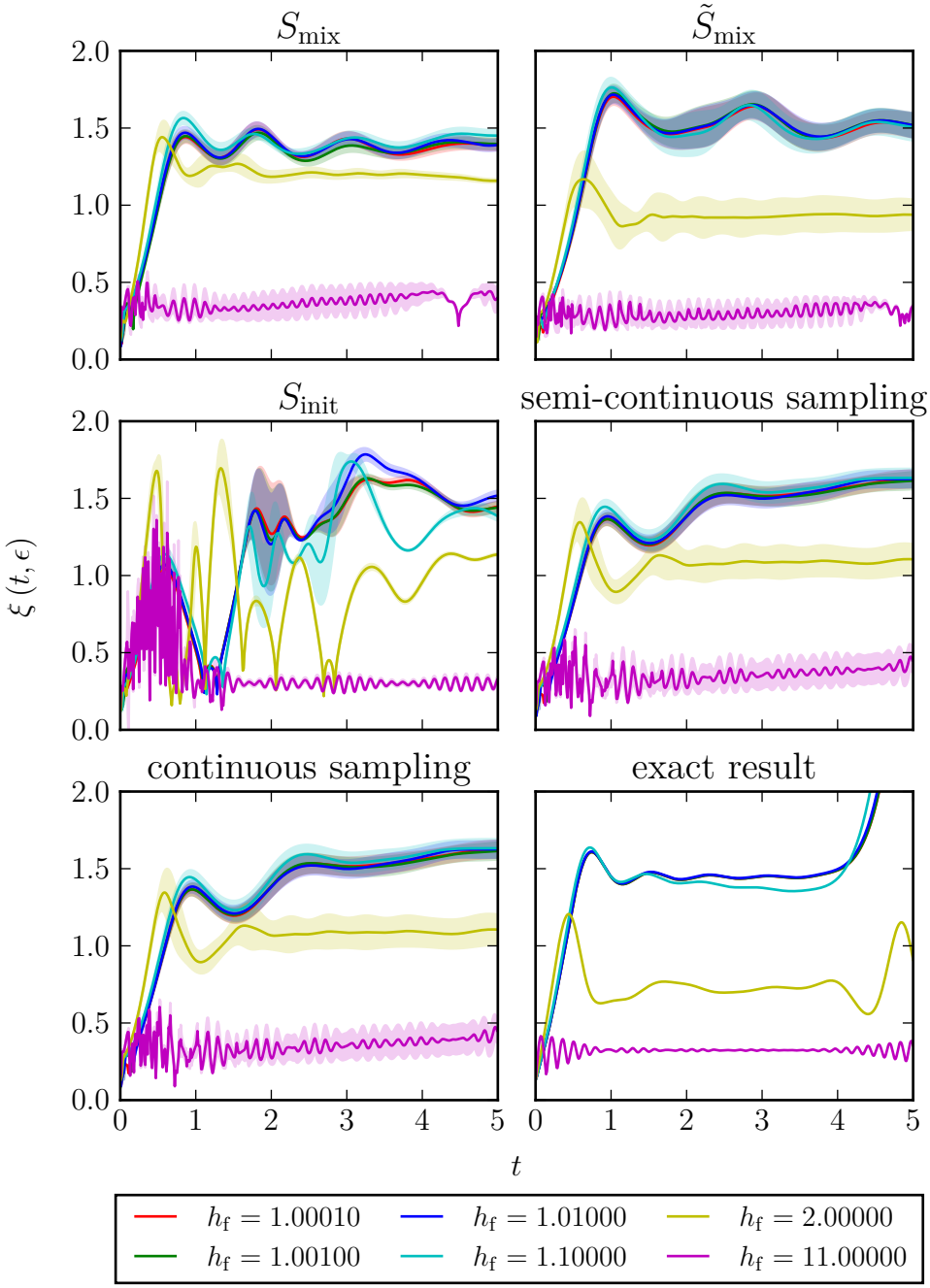

Figure 4.6: Correlation lengths $\xi(t,\epsilon)$ depending on time and distance from the critical point after a sudden quench from an infinitely large transverse field in the transverse field Ising model with $N = 20$ sites. The correlation lengths are calculated by fitting an exponential function to the correlation functions calculated using the first order discrete truncated Wigner approximations with five different sampling schemes and $R = 10000$ runs. For comparison the exact result is also shown.

$h_\mathrm{f} = 1.0001$, $h_\mathrm{f} = 1.001$, $h_\mathrm{f} = 1.01$ and $h_\mathrm{f} = 1.1$ show the same behaviour, which varies between the different sampling schemes. In all cases, as well as in the exact solution, the correlation length rises until it reaches a maximum value and then it saturates at a plateau. There one can see the propagating cone, which causes the rise in the correlation function as it propagates through the points used in the calculation of the correlation length and afterwards only small oscillations appear within the cone.

Only the approximation using S_init shows large oscillations at almost all times, which follow from the oscillations in the correlation function, as can already be seen in figure 4.5.

For the continuous and the semi-continuous sampling scheme, the plateau rises with longer times. The results for S_mix and $\tilde{S}_\mathrm{mix}$ seem to oscillate around a steady plateau, but even there a slow growth can be found at longer times.

The exact result only shows short oscillations and saturates relatively fast before the correlation length diverges at long times. This divergence is caused by finite size effects, since it appears at about $t = 4$, which is exactly where the growth in the correlation function in figure 4.4 caused by finite size effects reaches the points used for the calculation of the correlation length. For the quench to $h_\mathrm{f} = 1.1$, the correlation length calculated from the exact correlation function decays with time before it starts to diverge. This decay can not be found in any approximation, but it does not seem to saturate before the finite size effects appear.

Therefore, in figure 4.7 the correlation length for a long chain with $N = 100$ sites is calculated for long times up to $t = 20$ using the exact solution of the correlation function, as well as the approximation with $\tilde{S}_\mathrm{mix}$, which is chosen because it shows the best approximation results in figures 4.4, 4.5 and 4.6. In figure 4.7 one can see that the decay in the correlation length goes on for a much longer time before it saturates at about $t = 15$ and one can see that it only appears for the quench to $h_\mathrm{f} = 1.1$, while all other correlation lengths are stationary even for longer times. The approximated correlation length does not show any decay for all quenches, but one can see more clearly that the plateaus rise for longer times. This is peculiar and suggests that the quality of the discrete truncated Wigner approximation goes down for longer times. Figure 4.7 also confirms that it is not necessary to study approximations of longer chains for longer times, since all effects in the approximations can already be seen at short times and for short chains. The approximations get worse with longer times and are not effected by the length of the chain. Thus, one can still save computation time by only approximating short chains and times.

For quenches to $h_\mathrm{f} = 2$ one can see in all approximations, as well as in the exact solution, that the plateau is much lower than for the quenches closer to the critical point. The simulations approximate the exact solution at first maximum to a good degree, but then the plateau of the exact solution is even lower than all approximations. This is in accordance with the general expectation that the discrete truncated Wigner approximation works best at short times.

In the generalised Gibbs ensemble explained in section 4.1, the correlation length after long times can be described by a function depending on the distance $\epsilon = h_\mathrm{f} - 1$

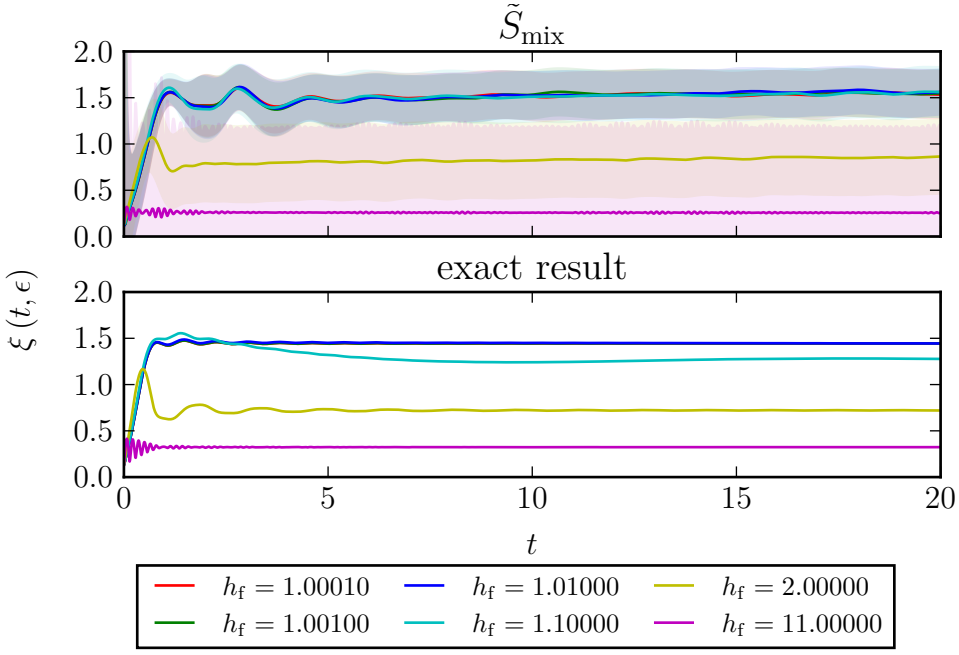

Figure 4.7: Long time calculations for sudden quenches in the transverse field Ising chain of size $N = 100$ with nearest-neighbour interactions from an infinitely large transverse field to different distances from the critical point. The first order approximations calculated with $\tilde{S}_{\mathrm{mix}}$ and $R = 10000$ runs are compared to the exact result.

of the final transverse field from the critical point in scaling limit, see [6, 7, 5],

$$f_{\mathrm{GGE}}(\epsilon) = \frac{1}{\ln(2(\epsilon+1))}. \tag{4.30}$$

In [5], the author considered the correlation length at a fixed time after quenches to different distances from the critical point and found the dependence on the distance described by the generalised Gibbs ensemble. The same can be done with the approximation results, as shown in figure 4.8. The fixed times, at which the dependence of the correlation length on ϵ is considered, can be chosen using figure 4.6. At the considered time, the correlation length should have reached the plateau at which it saturates, but the time should be at the beginning of the plateau, since it has been discussed earlier that the plateau rises with longer times. This way, the fixed times used in figure 4.6 have been chosen. For the exact solution, the fixed time has been chosen as large as possible, before the finite size effects cause the divergence of the correlation length. This is necessary since it takes a long time for the correlation length of the quench to $h_{\mathrm{f}} = 1.1$ to saturate, as analysed in the discussion of figures 4.6 and 4.7. As mentioned earlier, in the chain of size $N = 20$ this correlation length never saturates, since finite size effects appear before the saturation. Therefore, in

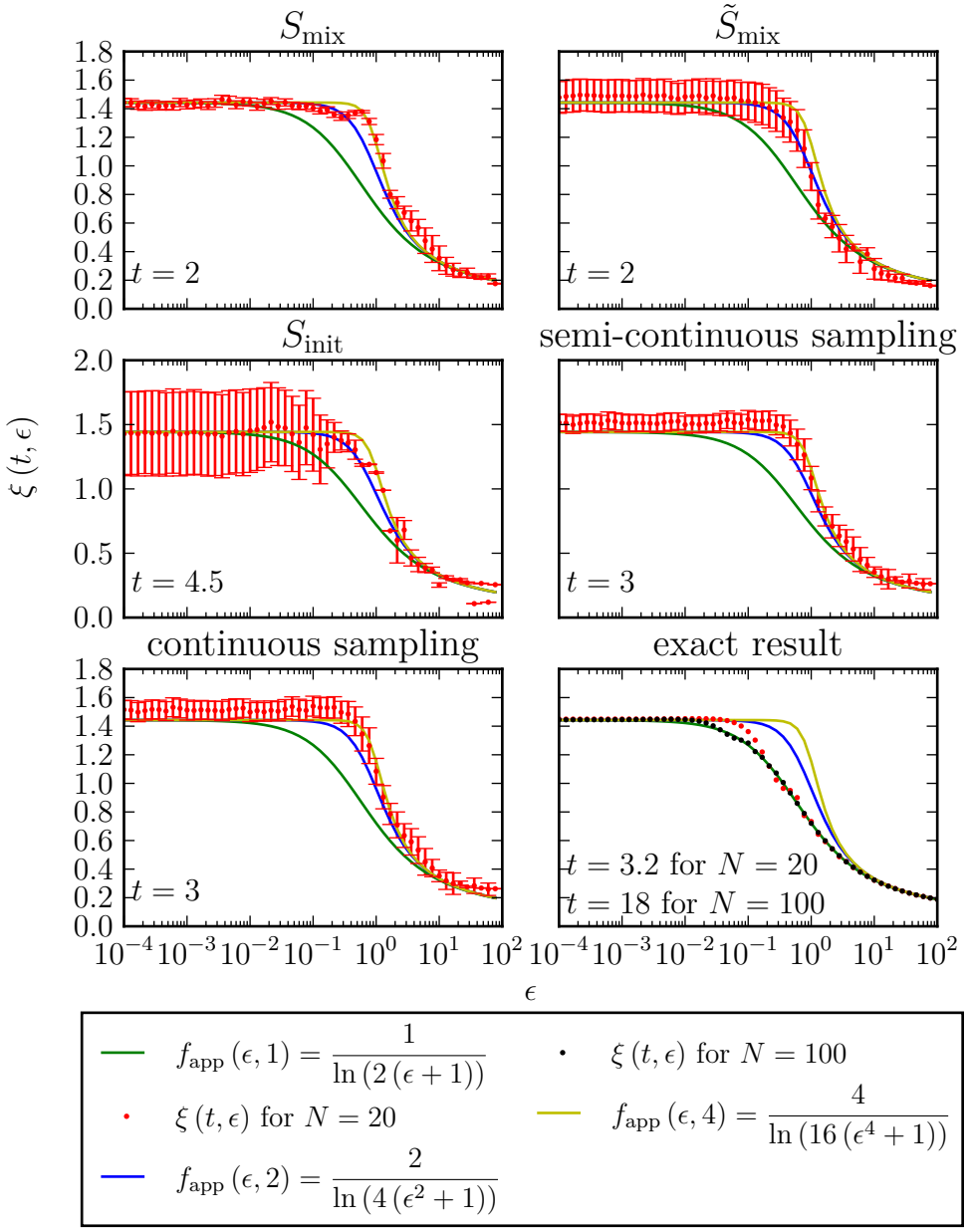

Figure 4.8: Exact and approximated correlation lengths $\xi(t, \epsilon)$ at fixed times for different sampling schemes with $R = 10000$ runs in a transverse field Ising chain with $N = 20$ sites, periodic boundary conditions and nearest-neighbour interactions depending on the distance ϵ from the critical point after a sudden quench from an infinitely large transverse field (red dots). The exact solution is also shown for $N = 100$ at later times (black dots). Three functions from equation (4.31) are added to the plots (green, blue, yellow line) to describe the dependence of the correlation length on ϵ.

figure 4.8 also the correlation length of a chain with $N = 100$ sites is considered at a fixed late time.

From the results in figure 4.8, one can conclude that the correlation length calculated from the exact correlation function shows the dependence on ϵ given by the generalised Gibbs ensemble, especially at long times after the quench. But already for short times this dependence can be found, which has also been observed in [5].

Even if the exact solution already shows the dependence of the correlation length on ϵ given by the generalised Gibbs ensemble after short times, this is not the case for the discrete truncated Wigner approximations, as can be clearly seen in figure 4.8. All sampling schemes result in approximations which show large deviations from the function $f_{\mathrm{GGE}}(\epsilon)$ at distances between $\epsilon \approx 0.1$ and $\epsilon \approx 10$, as already discussed earlier. To analyse the behaviour of the approximated correlation length at fixed times, two functions have been plotted in figure 4.8 which have the general form

$$f_{\mathrm{app}}(\epsilon, \alpha) = \frac{\alpha}{\ln\left(2^{\alpha}\left(\epsilon^{\alpha}+1\right)\right)}. \tag{4.31}$$

For $\alpha = 1$ this gives the function $f_{\mathrm{GGE}}(\epsilon)$ in equation (4.30). The function is plotted for $\alpha = 2$ and $\alpha = 4$ in figure 4.8 and one can see that, depending on the sampling scheme, the correlation lengths approximately follow one of these functions. It is hard to determine the right coefficient here, since the calculation of the correlation lengths is not very precise. For a better comparison of the approximated results with the functions f_{app}, the inverse correlation length is shown in figure 4.9, where a factor $\ln(2)$ has been subtracted, so that the results can be compared with the general functions

$$f_{\mathrm{c}}(\epsilon, \alpha) = \frac{1}{\alpha}\ln\left(\epsilon^{\alpha}+1\right). \tag{4.32}$$

These functions show large deviations in the steepness of the decay for small ϵ depending on α, thus it is easier to determine the coefficient by comparison with the approximation results. In figure 4.9 only the results with the sampling scheme $\tilde{S}_{\mathrm{mix}}$ and the semi-continuous sampling scheme are shown, since these give the best approximations compared to the exact solution in figures 4.5 and 4.8. The errorbars are left out for convenience. Since it can already be seen in figure 4.8 that the approximated correlation lengths do not exactly reach $\ln(2)$ but a higher value close to the critical point, they do not follow the decay of $f_{\mathrm{c}}(\epsilon, \alpha)$ for very small ϵ. In the semi-continuous sampling scheme this causes a plateau, while the results get negative for $\tilde{S}_{\mathrm{mix}}$ and are hence not plotted anymore. This again limits the determination of the coefficient, since the data points reach the plateau in the region where the different functions start to show large deviations depending on α. Thus, it is still not possible to determine the coefficient α exactly, but one can see in figure 4.9 that the sampling scheme $\tilde{S}_{\mathrm{mix}}$ follows the line with $\alpha = 2$, while the semi-continuous sampling scheme better fits to the behaviour of the function with coefficient $\alpha = 4$. The data allows to conclude that the coefficient matched by the approximations is about $\alpha \approx 3 \pm 1$.

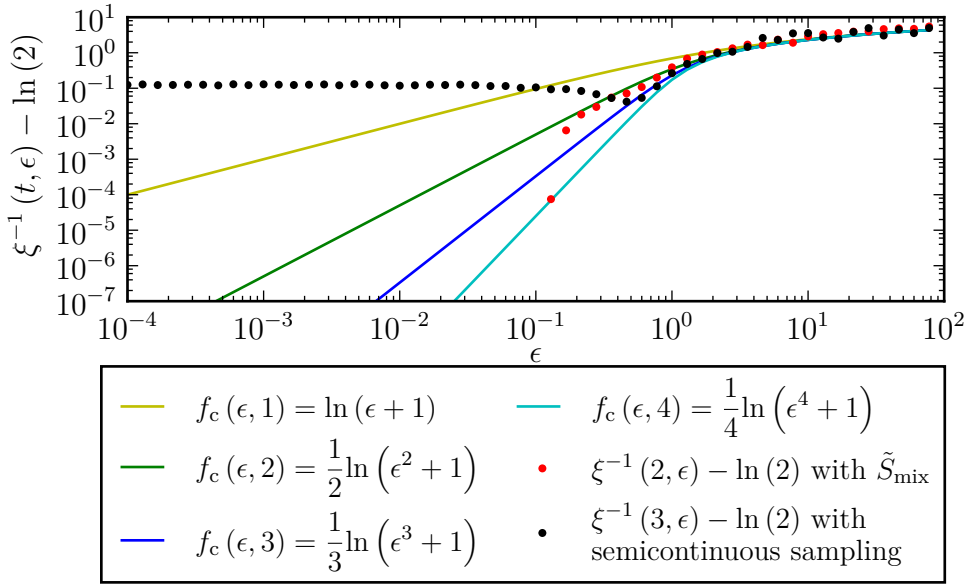

Figure 4.9: Inverse correlation length calculated from first order approximations with $\tilde{S}_{\mathrm{mix}}$ (magenta dots) and the semi-continuous sampling (black dots) of a transverse field Ising chain of size $N = 20$ with $R = 10000$ runs and nearest-neighbour interactions depending on the distance ϵ from the critical point after a sudden quench from an infinitely large transverse field. A factor $\ln(2)$ has been subtracted from the inverse correlation length which is plotted together with the function f_c for $\alpha = 1$ (red line), $\alpha = 2$ (green line), $\alpha = 3$ (dark blue line) and $\alpha = 4$ (light blue line) in a log-log-scale to determine a value for α. Negative values of $\xi^{-1}(t,\epsilon) - \ln(2)$ are left out.

In summary, the discrete truncated Wigner approximation of the transverse field Ising chain shows results close to exact calculations for sudden quenches from an infinitely large initial transverse field to small and large distances from the critical point. Only for quenches in between, around $h_f \approx 1.1$ to $h_f \approx 11$, the approximation differs from the exact solution, which can be found for all sampling schemes. It has also been shown that the quality of the semi-classical approximations goes down with longer times, which need to be considered in the exact solution.

In this section, the discrete truncated Wigner approximation has been used to simulate a non-trivial quantum mechanical system after quenches to the vicinity of a quantum critical point. It has been observed that the method shows resulting correlation functions in good agreement with exact solutions for quenches close to the critical point and far away from it, while deviations have been found for quenches to intermediate distances from the critical point.

The precision of the numerical solution has been found to be limited, so that correlation functions for large distances can not be approximated due to the ex-

act solution showing an exponential decay to very small values. Since the exact correlation length has been observed to reach stationarity at later times when the propagating cone in the correlation function has reached larger distances not capturable by the approximation, this limited precision might influence the appearing deviations.

It has also been observed that the sampling schemes, which gave results in good agreement with the exact solution of the Ising chain in section 3.4, show worse results here and vice versa. This shows that the quality of the sampling schemes depends on the simulated model. In the non-interacting Ising chain, where there is not much difference between classical and quantum-statistical fluctuations, the sampling schemes S_{init} and S_{mix} show the best results. These are the two schemes containing only the values $+1$ and -1 for the spin components. In the interacting transverse field Ising chain, the sampling schemes, where also different values can be sampled for the initial spin components, show better results. Hence, the best choice of the sampling schemes depends on the simulated model.

4.3 Second Order Approximations of Quenches in the Transverse Field Ising Model

The second order approximation of the equations of motion in the transverse field Ising model is given by plugging the Hamiltonian in equation (4.2) into the equations (3.73) and (3.74). This results in

$$\dot{a}_i^x = 2ha_i^y, \tag{4.33}$$

$$\dot{a}_i^y = 2\left[-ha_i^x + Ja^x_{(i+1) \bmod N} a_i^z + Jc^{xz}_{(i+1) \bmod N,i}\right], \tag{4.34}$$

$$\dot{a}_i^z = 2\left[-Ja^x_{(i+1) \bmod N} a_i^y - Jc^{xy}_{(i+1) \bmod N,i}\right], \tag{4.35}$$

$$\dot{c}_{ij}^{xx} = 2\left[hc_{ij}^{yx} + hc_{ij}^{xy}\right], \tag{4.36}$$

$$\begin{aligned}\dot{c}_{ij}^{xy} = 2\Big[&Ja_j^z\delta_{j,(i+1) \bmod N} + hc_{ij}^{yy} - hc_{ij}^{xx} + Ja^x_{(j+1) \bmod N} c_{ij}^{xz} + Ja_j^z c^{xx}_{i,(j+1) \bmod N} \\ &- Ja_i^x\left(c_{ij}^{xz} + a_i^x a_j^z\right)\delta_{j,(i+1) \bmod N}\Big],\end{aligned} \tag{4.37}$$

$$\begin{aligned}\dot{c}_{ij}^{xz} = 2\Big[&-Ja_j^y\delta_{j,(i+1) \bmod N} + hc_{ij}^{yz} - Ja^x_{(j+1) \bmod N} c_{ij}^{xy} - Ja_j^y c^{xx}_{i,(j+1) \bmod N} \\ &+ Ja_i^x\left(c_{ij}^{xy} + a_i^x a_j^y\right)\delta_{j,(i+1) \bmod N}\Big],\end{aligned} \tag{4.38}$$

$$\dot{c}_{ij}^{yx} = 2\Big[Ja_i^z\delta_{j,(i+1) \bmod N} - hc_{ij}^{xx} + Ja_{(i+1) \bmod N}^x c_{ij}^{zx} + hc_{ij}^{yy} + Ja_i^z c_{j,(i+1) \bmod N}^{xx} - Ja_j^x\left(c_{ij}^{zx} + a_i^z a_j^x\right)\delta_{j,(i+1) \bmod N}\Big], \tag{4.39}$$

$$\begin{aligned}\dot{c}_{ij}^{yy} = 2\Big[&-hc_{ij}^{xy} + Ja_{(i+1) \bmod N}^x c_{ij}^{zy} - hc_{ij}^{yx} + Ja_{(j+1) \bmod N}^x c_{ij}^{yz} + Ja_i^z c_{j,(i+1) \bmod N}^{yx} \\ &+ Ja_j^z c_{i,(j+1) \bmod N}^{yx} - Ja_i^y\left(c_{ij}^{zz} + a_i^x a_j^z\right)\delta_{j,(i+1) \bmod N} \\ &+ Ja_j^y\left(c_{ij}^{zx} + a_i^z a_j^x\right)\delta_{j,(i+1) \bmod N}\Big],\end{aligned} \tag{4.40}$$

$$\begin{aligned}\dot{c}_{ij}^{yz} = 2\Big[&-hc_{ij}^{xz} + Jc_{ij}^{zz} a_{(i+1) \bmod N}^x - Jc_{ij}^{yy} a_{(j+1) \bmod N}^x + Ja_i^z c_{j,(i+1) \bmod N}^{zx} \\ &- Ja_j^y c_{i,(j+1) \bmod N}^{yx} + Ja_i^y\left(c_{ij}^{xy} + a_i^x a_j^y\right)\delta_{j,(i+1) \bmod N} \\ &- Ja_j^z\left(c_{ij}^{zx} + a_i^z a_j^x\right)\delta_{j,(i+1) \bmod N}\Big],\end{aligned} \tag{4.41}$$

$$\begin{aligned}\dot{c}_{ij}^{zx} = 2\Big[&-Ja_i^y\delta_{j,(i+1) \bmod N} - Jc_{ij}^{yx} a_{(i+1) \bmod N}^x + hc_{ij}^{zy} - Ja_i^y c_{j,(i+1) \bmod N}^{xx} \\ &+ Ja_j^x\left(c_{ij}^{yx} + a_i^y a_j^x\right)\delta_{j,(i+1) \bmod N}\Big],\end{aligned} \tag{4.42}$$

$$\begin{aligned}\dot{c}_{ij}^{zy} = 2\Big[&-Jc_{ij}^{yy} a_{(i+1) \bmod N}^x - hc_{ij}^{zx} + c_{ij}^{zz} a_{(j+1) \bmod N}^x - Ja_i^y c_{j,(i+1) \bmod N}^{yx} \\ &+ Ja_j^z c_{i,(j+1) \bmod N}^{zx} - Ja_i^z\left(c_{ij}^{xz} + a_i^x a_j^z\right)\delta_{j,(i+1) \bmod N} \\ &+ Ja_j^y\left(c_{ij}^{yx} + a_i^y a_j^x\right)\delta_{j,(i+1) \bmod N}\Big],\end{aligned} \tag{4.43}$$

$$\begin{aligned}\dot{c}_{ij}^{zz} = 2\Big[&-Jc_{ij}^{yz} a_{(i+1) \bmod N}^x - Jc_{ij}^{zy} a_{(j+1) \bmod N}^x - Ja_i^y c_{j,(i+1) \bmod N}^{zx} - Ja_j^y c_{i,(j+1) \bmod N}^{zx} \\ &+ Ja_i^z\left(c_{ij}^{xy} + a_i^x a_j^y\right)\delta_{j,(i+1) \bmod N} + Ja_j^z\left(c_{ij}^{yx} + a_i^y a_j^x\right)\delta_{j,(i+1) \bmod N}\Big].\end{aligned} \tag{4.44}$$

These differential equations can also be solved numerically using the Runge-Kutta-Fehlberg method, which is introduced in appendix C.2.1. This results in a second order discrete truncated Wigner approximation of the spin dynamics $s_i^x(t)$ and independently the two-point functions $c_{ij}^{xx}(t)$ in the transverse field Ising model with nearest neighbour interactions and periodic boundary conditions. Analogously to the first order approximation, the correlation function $C_{d,\mathrm{BBGKY}}^{xx}(t, h_\mathrm{f})$ at time t after a sudden quench from an infinitely large initial transverse field to a final transverse field h_f can be approximated for a chain with N sites by averaging R runs using equations (3.75) and (3.76),

$$\begin{aligned}C_{d,\mathrm{BBGKY}}^{xx} =& \frac{1}{NR}\sum_{i=0}^{N-1}\sum_{r=0}^{R-1}\left(c_{i,(i+d) \bmod N,r}^{xx}(t, h_\mathrm{f}) + a_{i,r}^x(t, h_\mathrm{f})\, a_{(i+d) \bmod N,r}^x(t, h_\mathrm{f})\right) \\ &- \frac{1}{N^2R^2}\sum_{i=0}^{N-1}\sum_{r=0}^{R-1}\left(a_{i,r}^x(t, h_\mathrm{f})\right)\sum_{i=0}^{N-1}\sum_{r=0}^{R-1}\left(a_{(i+d) \bmod N,r}^x(t, h_\mathrm{f})\right).\end{aligned} \tag{4.45}$$

Thus, also the second order discrete truncated Wigner approximation of the time evolved correlation function after a sudden quench in the transverse field Ising model

can be compared to the exact solutions calculated with the numerical tools used in [5]. The comparison will be done analogously to the procedure for the first order approximation in section 4.2. In subsection 4.3.1, the approximated correlation functions using the different sampling schemes will be analysed, while in subsection 4.3.2 the approximated correlation lengths will be considered.

4.3.1 Correlation Functions and Divergences

As in section 4.2, the second order approximation of the correlation function is calculated using periodic boundary conditions and nearest neighbour interactions. Also here only short chains with $N = 20$ sites are calculated since it will be observed that the approximation only works for very short times, so that the correlation function inside the propagating cone can only be considered for very short distances, hence there is no need in simulating longer chains.

For the second order discrete truncated Wigner approximations only $R = 1000$ runs will be averaged, in contrast to the first order approximations in section 4.2, where $R = 10000$ runs have been used. Solving the differential equations of motion takes much more computation time in the second order approximation, since a lot more function evaluations are needed. It has been checked that the variations in the approximation results using $R = 1000$ runs are still small, so that there is no need in taking more runs. Since also here a Monte-Carlo-Integration is used to calculate the correlation function, the same numerical error as in section 4.2.1 causes a minimal reachable value. Hence, R also influences this value, but as can already be seen in figure 4.3, the difference between the minimal reachable values for $R = 10000$ and $R = 1000$ is rather small.

Analogously to figure 4.4, the absolute values of the correlation functions at several times after a sudden quench from an infinitely large transverse field to a final transverse field $h_\mathrm{f} = 1.0001$ are shown in figure 4.10 as a function of the relative distance d between the sites. The results of the second order discrete truncated Wigner approximation using the five sampling schemes introduced in section 3.3 are plotted, as well as the exact result for comparison.

The times at which the correlation function is considered in figure 4.3.1 are small compared to the times in figure 4.2.1. But one can already see at time $t = 1.1$ that the results using S_mix and S_init start to rise at all relative distances. For later times these two results are not plotted anymore, since they have diverged to infinitely large values. At time $t = 1.4$ also the result of the semi-continuous sampling scheme has diverged. This shows that the same divergences which have been found in subsection 3.4.2, where the second order discrete truncated Winger approximation has been benchmarked on the Ising chain, also appear in the transverse field Ising model. It has been checked that at time $t = 1.5$ all sampling schemes have diverged. The start of the divergence can be defined when the correlation function at zero relative distance starts to grow larger than one, which is physically impossible and hence shows where the approximation does not work anymore. Before this, the approximation still gives valid results. This shows that the divergence appears at

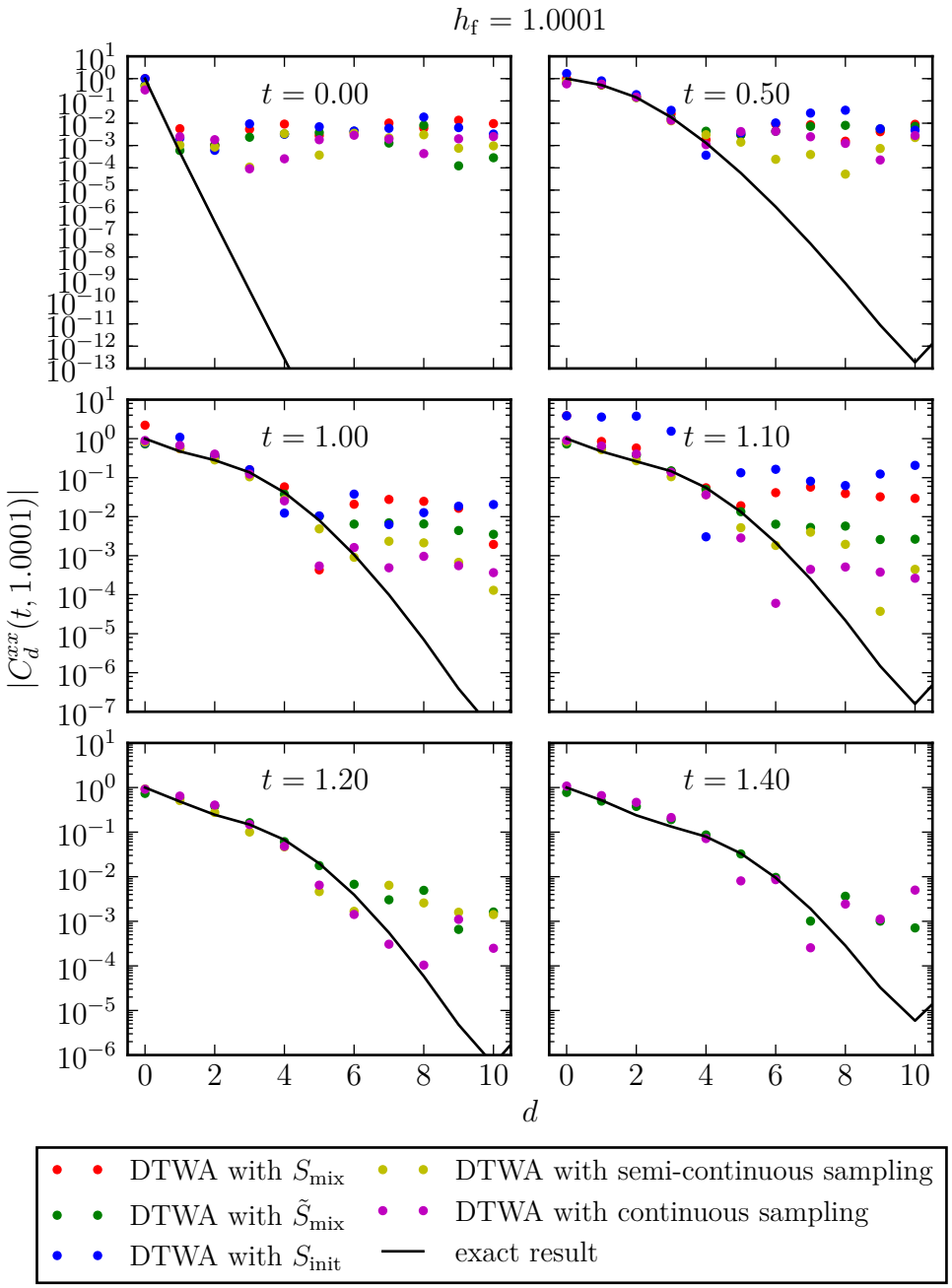

Figure 4.10: Absolute values of correlation functions in a transverse field Ising chain with $N = 20$ sites, nearest neighbour interactions and periodic boundary conditions at different times after a sudden quench from an infinitely large field to $h_\mathrm{f} = 1.0001$ depending on the spin distance d. Second order approximations are calculated by averaging $R = 1000$ runs and using S_mix (red dots), $\tilde{S}_\mathrm{mix}$ (green dots), S_init (blue dots) as well as the semi-continuous and the continuous sampling (yellow and magenta dots respectively) and are compared with the exact solution (black line).

very short times in this model and it even appears before the propagating cone has reached the end of the chain. Thus, the approximations also diverge before finite size effects appear in the exact solution and hence there is no need in studying longer spin chains and times.

For very short times one can see in figure 4.3.1 that the approximations follow the exact solution closely, except for the plateau caused by a limited numerical precision, as already discussed in section 4.2. But even the propagating cone can be seen clearly in the approximations before they start to diverge. Especially the results of $\tilde{S}_{\text{mix}}$ and the semi-continuous sampling scheme follow the exact solution very closely for short times.

Figure 4.11 shows the absolute value of the correlation functions depending on the relative distance d at a fixed time $t = 1$ after a sudden quench from an infinitely large transverse field to final transverse fields at different distances from the critical point. Again the five introduced sampling schemes are compared to the exact solution, analogously to figure 4.5 for the first order approximations. There one can conclude that especially the results using $\tilde{S}_{\text{mix}}$, the semi-continuous and the continuous sampling schemes follow the exact solution closely for very short times, while the other two sampling schemes S_{mix} and S_{init} show small differences, but all in all also match with the exact solution before the divergences appear.

A peculiar fact can be seen for quenches to $h_{\text{f}} = 1.1$ and $h_{\text{f}} = 2$, where the divergence seems to appear much earlier for the sampling schemes S_{mix} and S_{init}. This shows that the time, at which the second order approximation diverges, is influenced by the distance from the critical point after the sudden quench and it appears earlier exactly in the region where the first order approximation in section 4.2 has shown large differences from the exact solution. In this region also the results of the three sampling schemes, which have not yet diverged at $t = 1$, do not follow the exact solution that closely anymore, even for very small relative distances. Thus, even in the second order approximation the results get worse for quenches to intermediate distances from the critical point. But at this time the cone is not propagated far, as discussed in section 4.2 even the exact correlation function takes a longer time to saturate. These longer times can not be reached with the second order approximation and it can therefore not be seen whether the approximation gets better at later times.

For quenches to transverse fields further away from the critical point, like $h_{\text{f}} = 11$, one can see in figure 4.11 that the second order discrete truncated Wigner approximation shows better results again. The divergence appears at later times again and also the short distance decay of the exact solution is matched by the results of most sampling schemes, especially by $\tilde{S}_{\text{mix}}$ and the semi-continuous sampling scheme. Thus, as the first order approximation in section 4.2, the second order approximation follows the exact solution closely for quenches close to the critical point and far away from the critical point. In between the approximations show some deviations, but since only very short times can be simulated, no final conclusion is possible.

As in the first order approximation of the transverse field Ising model, also the second order approximations of the equations of motion have been solved numerically

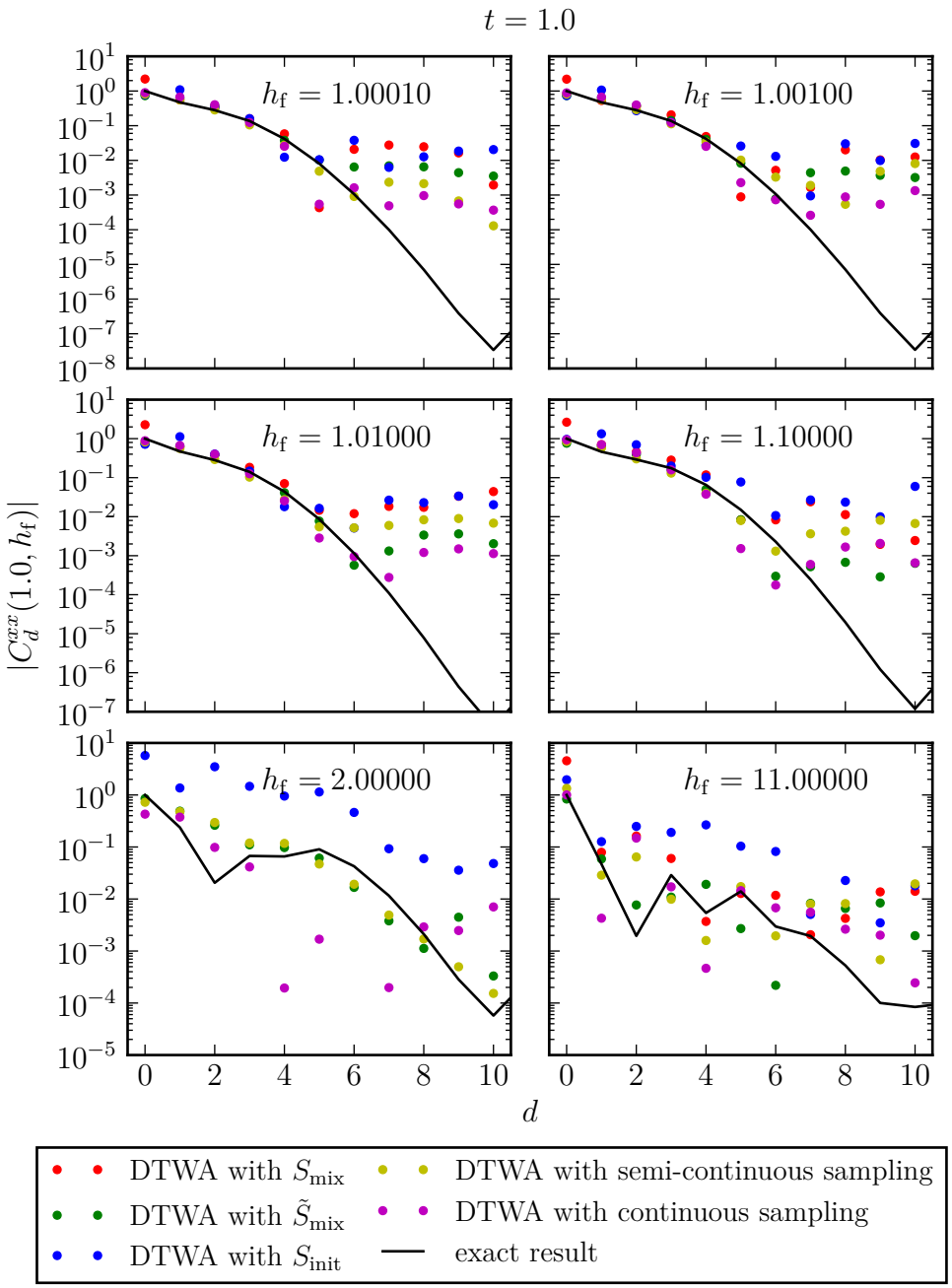

Figure 4.11: Absolute values of correlation functions in a transverse field Ising chain with $N = 20$ sites, nearest neighbour interactions and periodic boundary conditions at time $t = 1$ after a sudden quench from an infinite field to different distances from the critical point as a function of the site distance d. Second order approximations with $R = 1000$ runs using the sampling schemes S_mix (red dots), $\tilde{S}_\mathrm{mix}$ (green dots), S_init (blue dots) as well as the semi-continuous (yellow dots) and the continuous (magenta dots) scheme are compared to the exact solution (black line).

using the Runge-Kutta-Fehlberg method which is further introduced in appendix C.2.1. Also different numerical time-integration schemes have been tested, like the predictor-corrector Adams-Bahsforth-Moulton method, which is further introduced in appendix C.2.2. This way it has been checked whether the divergences can be captured with standard numerical methods. This was not found to be the case. It was not even possible to shift the divergences to later times, which would have been useful in the case of the transverse field Ising model, since most effects on the dynamics are already given at short times in the exact solution [5]. Stronger numerical methods might be useful at this point.

The divergence in the solutions might also be caused by an error in the truncation of the quantum mechanical equations of motion in section 2.4. In [8] it has been shown that the transverse field Ising model after a sudden quench has further conserved quantities next to the energy. The conservation of these quantities is not necessarily given in the truncated equations of motion, which might cause the divergences. At this point, a further analysation of the conserved quantities and an idea how to include a conservation into the truncation scheme would be helpful, but goes beyond the scope of this thesis.

4.3.2 Short Time Correlation Lengths

Analogously to subsection 4.2.2, the second order approximation of the correlation length can be analysed. But as it has already been discussed in subsection 4.3.1, a divergence in the approximated observables appears at short times after the sudden quench. When these divergences appear, the cone in the correlation function has not propagated to far distances, thus it is hard to get a correlation length here, since it is calculated by extracting the short decay range from the spatial derivative at $d = 0$, as in subsection 4.2.2.

Figure 4.12 shows the short time correlation lengths of the five introduced sampling schemes in comparison with the exact solution. Since the propagating cone in the correlation function needs to pass the short distance at which the exponential function is fitted, as discussed in section 4.1, one can see in figure 4.12 that the correlation length does not saturate before the divergences appear. Even the exact solution has not saturated yet at these short times. For most sampling schemes one can see large divergences and oscillations. At very short times, all sampling schemes follow the rise of the exact solution, before they suddenly break and diverge. Only the semi-continuous sampling scheme shows a stable solution until time $t = 1$. There one can see that the correlation length at this time still keeps on decaying, thus the approximation might get better at longer times. This suggests that the results of the second order approximation are promising. Hence, it is vital to understand the origin of the divergence. As discussed in subsection 4.3.1, either the truncation error needs to be analysed further, or a purely numerical solution to this problem needs to be found. Either way would allow to obtain a qualitatively much better approximation. Finding a solution to this problem is beyond the scope of this thesis and hence attributed to future studies.

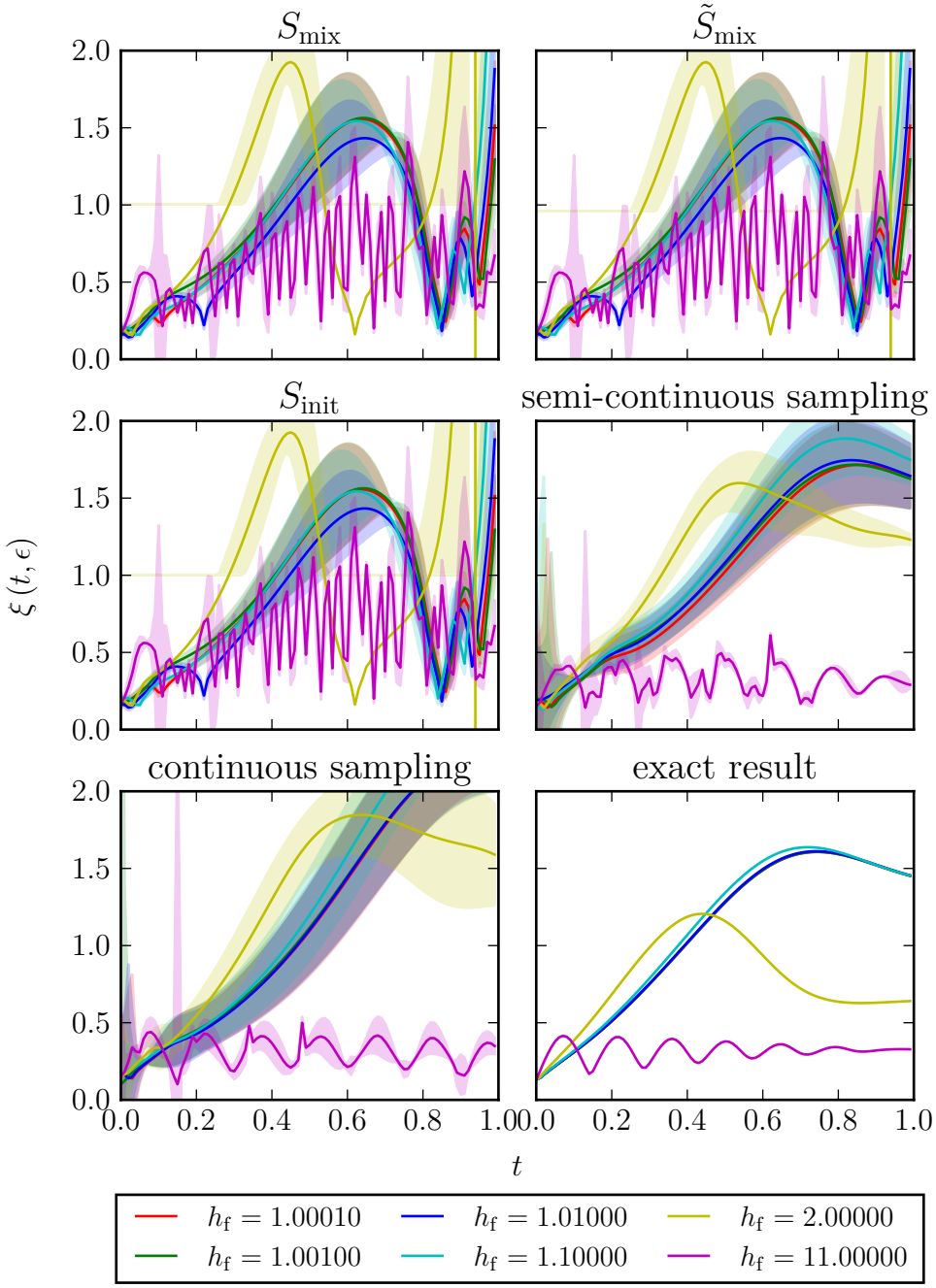

Figure 4.12: Correlation lengths $\xi(t,\epsilon)$ depending on time and distance from the critical point after a sudden quench from an infinitely large transverse field in the transverse field Ising model with $N = 20$ sites. The correlation lengths are calculated by fitting an exponential function to the short distance correlation functions which are calculated using the second order discrete truncated Wigner approximations with five different sampling schemes and $R = 1000$ runs. For comparison the exact solution is shown.

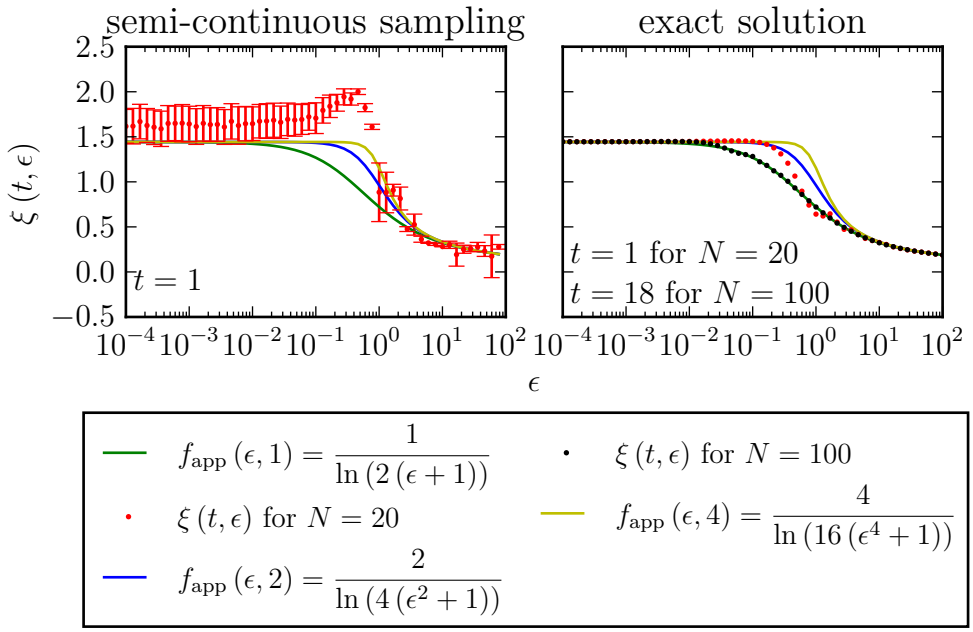

Figure 4.13: Exact and approximated correlation lengths $\xi(t,\epsilon)$ at fixed times for semi-continuous sampling with $R = 1000$ averaged runs of a transverse field Ising chain with $N = 20$ sites, periodic boundary conditions and nearest neighbour interactions depending on the distance ϵ from the critical point after a sudden quench from an infinitely large transverse field (red dots). The exact solution is also shown for $N = 100$ at later times (black dots). Three functions from equation (4.31) are added to the plots (green, blue and yellow line) to describe the dependence of the correlation length on ϵ.

Since all approximated correlation lengths in figure 4.12 diverge before they saturate, it is not possible to study the correlation lengths at a fixed time as function of the distance ϵ from the critical point, as it has been done in subsection 4.2.2 for the first order approximations. Only the semi-continuous sampling scheme gives a stable result for the correlation length up to time $t = 1$. Therefore, figure 4.13 only shows the correlation length resulting from the semi-continuous sampling scheme at fixed time $t = 1$ as a function of the distance ϵ from the critical point after the sudden quench.

One can observe in figure 4.13 that for short distances from the critical point the correlation length is larger than the exact solution. It can be seen in figure 4.12 that at time $t = 1$ the approximated correlation lengths for short distances from the critical point have not yet saturated and are still found in the decay after the first maximum. This explains why the short distance values in figure 4.13 are higher than the exact solution. Since it has been shown in figure 4.11 that for these distances the divergences appear at later times, it has been checked that the correlation length

still decays for longer times in this region and then also matches with the exact solution.

At intermediate distances from the critical point, even larger deviations from the exact solution are found than in the first order approximation. This is influenced by the divergence appearing earlier at this region, as has already been discussed. Another factor causing this large differences is the short time at which the correlation length is calculated. For comparison also the exact solution of the correlation length at time $t = 1$ is shown in figure 4.13, where one can see that also the exact solution is not yet described by a generalised Gibbs ensemble at this time. It seems to better follow the function $f_{\mathrm{app}}(\epsilon, \alpha)$ in equation (4.31) with a factor α between one and two.

For large distances from the critical point, the approximation follows the exact solution very closely, since in this region the correlation lengths saturate at earlier times and the divergences appear at later times.

One can summarise that for very short times, before the divergences appear, the second order approximation gives promising results close to the exact solution. But since the divergences appear after short times, before the stationarity of the correlation function is reached, it is hard to draw final conclusions. It has been checked that the divergences can not be captured by standard numerical methods and can also not be shifted to later times by these. Hence, either stronger numerical methods are necessary to solve the equations of motion, or the truncation scheme should be further analysed to avoid truncation errors, as discussed in subsection 4.3.1.

For quenches close to the critical point and far away from it, the second order approximation shows results in good agreement with the exact solution for short times and distances, as does the first order approximation in this region. For quenches to intermediate distances from the critical point, also the second order approximation shows deviations from the exact solution. It has already been discussed in section 4.2 that in this region even the exact solution needs a longer time to reach stationarity, thus especially there it is hard to compare the second order approximation with the exact solution.

As a conclusion of this chapter it can be said that the quantum mechanical transverse field Ising model can be described in good agreement by a semi-classical approximation for quenches close to the critical point and far away from it. Especially the good agreement close to the critical point is a result which would have not been predicted, since quantum effects not capturable by a semi-classical approximation have been expected in this region. Also the deviations between the semi-classical approximation and the quantum mechanical solution at quenches to intermediate distances from the critical point have not been expected. These differences might be a hint for quantum effects appearing in this regime. All in all, the discrete truncated Wigner approximation has been found to give semi-classical simulations of quantum mechanical systems in a better quality than expected, even for non-trivial systems including quantum phase transitions.

5 Conclusion and Outlook

In this thesis, the recently developed discrete truncated Wigner approximation has been applied on the transverse field Ising model after a sudden quench into the vicinity of a quantum phase transition. By comparison with the exact solution, it has been analysed how the quantum dynamics can be captured by a semi-classical approximation at different distances from the quantum critical point.

A derivation of the first and second order discrete truncated Wigner approximation, as introduced in [27] and [16] respectively, has been given. For this, a discrete quantum mechanical phase space, as defined in [35], has been introduced ,with a Wigner function defined on it as a quasi-probability-distribution. From this Wigner function, initial states of a discrete quantum mechanical system are sampled in the discrete truncated Wigner approximation and then evolved in time. Since the quantum mechanical time evolution can not be calculated exactly, a truncation at first and second order is used to approximate the quantum dynamics. By sampling a huge number of initial states, evolving them in time and averaging the resulting observables, the dynamics in the quantum mechanical system are approximated semi-classically.

This generally derived discrete truncated Wigner approximation has then been applied on a spin-$\frac{1}{2}$ system as an example of a discrete quantum mechanical model. The derivation of both, the first and second order truncations of the corresponding equations of motion, has been reviewed as given in [27, 16]. To sample the initial states from the discrete Wigner function, three possible sets of initial spin states associated with the discrete phase space have been introduced in [16]. In this thesis, two more possible sampling schemes have been introduced. The properties of the five introduced sampling schemes S_{init}, S_{mix}, $\tilde{S}_{\text{mix}}$, as well as the semi-continuous and the continuous sampling scheme, are summarised in appendix B.4.

These schemes have then been benchmarked on the exactly solvable Ising chain using different interaction ranges. In the benchmarking process, the magnetisation, as well as the two-point correlation resulting from the approximations, have been compared to the exact solution. There it has been observed that S_{init} and S_{mix} show the best agreements with the exact solution in both orders of truncation. The authors in [27] and [16] have predicted that the discrete truncated Wigner approximation only works for systems with long-range interactions, because the deviations from mean-field are expected to be small in this limit. Against these predictions, the method has been found to also show good agreement with the exact solution for models with short-range interactions. This shows that the deviations from mean-field do not influence the quality of the discrete truncated Wigner approximation.

In the first order approximation, an additional term has been found to appear in

the approximation of the two-point correlation compared to the exact solution. This additional term has been observed to be more important for systems with longer interaction ranges. Considering the second order approximations, huge divergences have been observed at late times, especially for systems with long-range interactions. Before these divergences appear, the second order approximation has shown the same behaviour as the first order approximation, and one can conclude that both simulations are in good agreement with the exact solution, if S_{init} and S_{mix} are used. For the other three sampling schemes, deviations from the exact solution have been observed.

After the discrete truncated Wigner approximation has been benchmarked on the non-interacting Ising chain, which shows no large differences between classical and quantum-statistical fluctuations, it has been applied on an Ising chain with an additional transverse field. As an interacting system, this model is more complex and shows a quantum phase transition. The model can be diagonalised analytically, where a review of the diagonalisation is given in [5]. The results derived therein have been compared with the discrete truncated Wigner approximation in the context of sudden quenches to the vicinity of the quantum critical point. This way, it has been analysed where the dynamics of the correlation function, as a function of the relative distance between the spins, can be captured by a semi-classical approximation. Also the simulated dynamics of a correlation length resulting from the correlation function have been analysed for a better comparison.

The first order discrete truncated Wigner approximation has been found to show results in good agreement with the exact solutions for quenches to transverse fields close to the critical point and far away from it. Differences between the approximation and the exact solution have been found for quenches to intermediate distances in the region $h_{\mathrm{f}} = 1.1$ to $h_{\mathrm{f}} = 11$. Here, the sampling scheme $\tilde{S}_{\mathrm{mix}}$, as well as the semi-continuous and the continuous scheme, have been observed to give the best agreements with the exact solution. This is peculiar, since these are exactly the schemes which showed worse results in the approximation of the Ising chain. This shows that the quality of the sampling schemes depends on the approximated model. As mentioned earlier, in the Ising chain no large differences between classical and quantum-statistical fluctuations exist. In this case, the sampling schemes, in which the initial spin states can only take the values $+1$ and -1, show better results. This is not the case in the transverse field Ising chain, where the classical and the quantum-statistical fluctuations show more differences. In this case, the sampling schemes, in which also values other than $+1$ and -1 can be chosen for the initial spin states, show better results.

For large relative distances, the exact correlation function reaches very small values due to an exponential decay in the limit of long times and large relative distances. It has been observed that these small values can not be reached in the approximation due to a limited precision in the numerical averaging process. A dependence of these limitations on the number of averaged runs has been analysed. It has been concluded that calculating the number of runs needed to reach significantly smaller values in the correlation function, is not achievable on the setup used for the calcu-

lations within this work due to exceeding computation times. But it has also been observed that in the regime, in which the first order approximation does not fit to the exact solution, a longer time is needed for the exact correlation function to reach stationarity. At these longer times, the exponential decay in the correlation function is given for large distances, so that the correlation function has reached smaller values than the minimal reachable value in the approximations. This behaviour at large distances might influence the short distance correlation functions. This would explain, why these can not be captured in the approximations, since the large distance behaviour is not given there. Hence, the deviations might be caused by the limited numerical precision. Here one could think of alternative ways to calculate the numerical results, so that the limitation can be avoided, or at least shifted to even smaller values. This goes beyond the scope of this work.

In the context of benchmarking the discrete truncated Wigner approximation on the Ising chain, it has been observed that an additional term appears in the approximation of the two-point correlation. An analogous term might be appearing in the approximation of the correlation function in the transverse field Ising model, causing the deviations at intermediate distances. Since it is not as trivial as in the case of the Ising chain to compare the exact expression with the approximation, this point has not been further analysed within this work. On the other hand, such an additional term would be expected to appear at all distances from the critical point, instead of only at intermediate distances. It has also been observed that the additional term in the correlation function of the Ising chain is more important for longer interaction ranges. Since nearest neighbour interactions are used in the simulations of the transverse field Ising model, one would not expect an analogous term to cause the deviations.

The second order approximations have been observed to show large divergences after short times. Before the divergences appear, the results have been found in good agreement with the exact solution for quenches close to the critical point and far away from it. Also in these approximations, deviations from the exact solution have been found in the region of intermediate distances from the critical point, exactly in the regime where the first order approximations do not follow the exact solutions. But since only very short times can be simulated, it can not be excluded that the approximations get better at later times. At these distances, also the divergences have been observed to appear at earlier times, while they appear at approximately the same times close to the critical point and far away from it. It has been checked that the divergences can not be captured with standard numerical methods and that they can even not be shifted to later times. Hence, stronger numerical methods would be necessary for a better analysation of the second order approximations, which seem promising in the short times before the divergences. With such stronger numerical methods, it could also be checked whether the deviations at intermediate distances in the first order approximation are caused by the numerical solution of the equations of motion.

Since the divergences have been observed to appear at earlier times in the region where the first order approximation shows deviations from the exact solution, it

has also been conjectured that both effects are caused by a truncation error. No condition on conserved quantities is included in the truncation scheme at both, first and second order. While the energy has been checked to be conserved in both cases, it has been discussed in [8] that even more conserved quantities exist for sudden quenches in the transverse field Ising model. These quantities are not necessarily conserved in the truncation process of the quantum mechanical time evolutions. Both effects, the earlier divergences and the differences from the exact solution, appearing at approximately the same distances from the critical point, suggests that they both result from an error in the truncation scheme. Since it is not trivial to find the conserved quantities and to include the conservations into the truncation scheme, this goes beyond the scope of this work, but is expected to be a promising approach.

All in all, these deviations and earlier divergences happening at intermediate distances suggest quantum effects, which can not be captured by the semi-classical approximation, appearing at this region. This is peculiar, since one would rather expect them to appear close to the critical point instead of at intermediate distances from it.

In summary, except for deviations at intermediate distances from the critical point, the discrete truncated Wigner approximation has been found to give results in good agreement with the exact solutions of sudden quenches in the transverse field Ising model. Hence, the method shows promising results for systems in the vicinity of the critical point, for which existing methods are scarce, as discussed in the beginning. The deviations found at intermediate distances suggest quantum effects appearing in this region, which can not be captured by a semi-classical approximation. Understanding these deviations in more detail might help to better understand some effects appearing in quantum mechanical systems out of equilibrium.

Appendix

A Appendix for Chapter 2

A.1 Deriving the Inner Product of the Wigner Function in Equation (2.10)

In section 2.1, the inner product of two Wigner functions $W(\boldsymbol{q},\boldsymbol{p})$ and $W'(\boldsymbol{q},\boldsymbol{p})$ is given as the trace of the product of the corresponding density operators $\hat{\rho}$ and $\hat{\rho}'$ in equation (2.10). This relation is derived according to [35] in the following using the definition of the Wigner function in the position basis as stated in equation (2.3),

$$
\begin{aligned}
&2\pi\hbar \int\int W(\boldsymbol{q},\boldsymbol{p}) W'(\boldsymbol{q},\boldsymbol{p}) \,\mathrm{d}\boldsymbol{q}\mathrm{d}\boldsymbol{p} \\
&\qquad = \frac{2}{\pi\hbar} \int\int\int\int \langle \boldsymbol{q}-\boldsymbol{x}| \,\hat{\rho}\, |\boldsymbol{q}+\boldsymbol{x}\rangle \,\langle \boldsymbol{q}-\boldsymbol{x}'| \,\hat{\rho}'\, |\boldsymbol{q}+\boldsymbol{x}'\rangle \qquad \text{(A.1)} \\
&\qquad\quad \times \exp\left(\frac{2\pi i \boldsymbol{p}\,(\boldsymbol{x}+\boldsymbol{x}')}{\hbar}\right) \mathrm{d}\boldsymbol{x}\mathrm{d}\boldsymbol{x}'\mathrm{d}\boldsymbol{q}\mathrm{d}\boldsymbol{p} \\
&\qquad = \int\int\int \langle \boldsymbol{q}-\boldsymbol{x}| \,\hat{\rho}\, |\boldsymbol{q}+\boldsymbol{x}\rangle \,\langle \boldsymbol{q}-\boldsymbol{x}'| \,\hat{\rho}'\, |\boldsymbol{q}+\boldsymbol{x}'\rangle \\
&\qquad\quad \times \delta(\boldsymbol{x}+\boldsymbol{x}')\,\mathrm{d}\boldsymbol{x}\mathrm{d}\boldsymbol{x}'\mathrm{d}\boldsymbol{q} \\
&\qquad = \int\int \langle \underbrace{\boldsymbol{q}-\boldsymbol{x}}_{:=\tilde{\boldsymbol{q}}} |\, \hat{\rho} \,|\, \underbrace{\boldsymbol{q}+\boldsymbol{x}}_{:=\tilde{\boldsymbol{x}}} \rangle \,\langle \boldsymbol{q}+\boldsymbol{x}| \,\hat{\rho}'\, |\boldsymbol{q}-\boldsymbol{x}\rangle \,\mathrm{d}\boldsymbol{x}\mathrm{d}\boldsymbol{q} \\
&\qquad = \int\int \langle \tilde{\boldsymbol{q}}| \,\hat{\rho}\, |\tilde{\boldsymbol{x}}\rangle \,\langle \tilde{\boldsymbol{x}}| \,\hat{\rho}'\, |\tilde{\boldsymbol{q}}\rangle \,\mathrm{d}\tilde{\boldsymbol{x}}\mathrm{d}\tilde{\boldsymbol{q}} \\
&\qquad = \int \langle \tilde{\boldsymbol{q}}| \,\hat{\rho}\hat{\rho}'\, |\tilde{\boldsymbol{q}}\rangle \,\mathrm{d}\tilde{\boldsymbol{q}} \\
&\qquad = \mathrm{Tr}\left(\hat{\rho}\hat{\rho}'\right). \qquad \text{(A.2)}
\end{aligned}
$$

A.2 Deriving an Expression for Phase-Point Operators in Equation (2.12)

In section 2.1, an expression for the phase-point operators $\hat{A}(\boldsymbol{q},\boldsymbol{p})$ is given in equation (2.12). This relation can be calculated according to [35] by plugging the definition of the density operator $\hat{\rho}$ in terms of the Wigner function and the phase-point operators in equation (2.11) into the definition of the Wigner function in the position basis in equation (2.3). Then the following calculation leads to an expression for the phase-point operator in the position basis,

$$W(\boldsymbol{q},\boldsymbol{p}) \stackrel{!}{=} \frac{1}{\pi\hbar}\int\int\int \langle \boldsymbol{q}-\boldsymbol{x}|\, W(\boldsymbol{q}',\boldsymbol{p}')\, \hat{A}(\boldsymbol{q}',\boldsymbol{p}')\, |\boldsymbol{q}+\boldsymbol{x}\rangle \exp\left(\frac{2i\boldsymbol{p}\boldsymbol{x}}{\hbar}\right) \mathrm{d}\boldsymbol{x}\mathrm{d}\boldsymbol{q}'\mathrm{d}\boldsymbol{p}' \tag{A.3}$$

$$\begin{aligned}
\Leftrightarrow \frac{1}{\pi\hbar}\int \langle \boldsymbol{q}-\boldsymbol{x}|\, \hat{A}(\boldsymbol{q}',\boldsymbol{p}')\, |\boldsymbol{q}+\boldsymbol{x}\rangle \exp\left(\frac{2i\boldsymbol{p}\boldsymbol{x}}{\hbar}\right) \mathrm{d}\boldsymbol{x} &= \delta(\boldsymbol{q}-\boldsymbol{q}')\,\delta(\boldsymbol{p}-\boldsymbol{p}') \\
&= 4\delta(2\boldsymbol{q}-2\boldsymbol{q}')\,\delta(2\boldsymbol{p}-2\boldsymbol{p}') \\
&= \langle \boldsymbol{q}|\, \boldsymbol{q}'\rangle \langle \boldsymbol{p}|\, \boldsymbol{p}'\rangle \\
&= \frac{1}{4\pi^2\hbar^2}\int \exp\left(\frac{i\boldsymbol{y}(\boldsymbol{q}-\boldsymbol{q}')}{\hbar}\right)\mathrm{d}\boldsymbol{y}\int \exp\left(\frac{i\boldsymbol{x}(\boldsymbol{p}-\boldsymbol{p}')}{\hbar}\right)\mathrm{d}\boldsymbol{x} \\
&= \frac{1}{\pi^2\hbar^2}\int \exp\left(\frac{2i\boldsymbol{y}(\boldsymbol{q}-\boldsymbol{q}')}{\hbar}\right)\mathrm{d}\boldsymbol{y}\int \exp\left(\frac{2i\boldsymbol{x}(\boldsymbol{p}-\boldsymbol{p}')}{\hbar}\right)\mathrm{d}\boldsymbol{x} \\
&= \frac{1}{\pi^2\hbar^2}\int\int \exp\left(\frac{2i\boldsymbol{y}(\boldsymbol{q}-\boldsymbol{q}'-\boldsymbol{x}+\boldsymbol{x})}{\hbar}\right)\exp\left(\frac{2i\boldsymbol{x}\boldsymbol{p}}{\hbar}\right) \\
&\quad \times \exp\left(-\frac{2i\boldsymbol{x}\boldsymbol{p}'}{\hbar}\right)\mathrm{d}\boldsymbol{x}\mathrm{d}\boldsymbol{y} \\
&= \frac{1}{\pi^2\hbar^2}\int\int \exp\left(\frac{i\boldsymbol{y}(-2\boldsymbol{q}'+(\boldsymbol{q}-\boldsymbol{x})+(\boldsymbol{q}+\boldsymbol{x}))}{\hbar}\right) \\
&\quad \times \exp\left(\frac{2i\boldsymbol{p}\boldsymbol{x}}{\hbar}\right)\exp\left(-\frac{2i\boldsymbol{p}'\boldsymbol{x}}{\hbar}\right)\mathrm{d}\boldsymbol{x}\mathrm{d}\boldsymbol{y} \\
&= \frac{2}{\pi\hbar}\int \delta\left(2\boldsymbol{q}'-((\underbrace{\boldsymbol{q}-\boldsymbol{x}}_{=:\tilde{\boldsymbol{q}}'})+(\underbrace{\boldsymbol{q}+\boldsymbol{x}}_{=:\tilde{\boldsymbol{q}}''}))\right)\exp\left(\frac{2i\boldsymbol{p}\boldsymbol{x}}{\hbar}\right) \\
&\quad \times \exp\left(-\frac{2i\boldsymbol{p}'\boldsymbol{x}}{\hbar}\right)\mathrm{d}\boldsymbol{x} \\
&= \frac{1}{\pi\hbar}\int \delta\left(\boldsymbol{q}'-\frac{\tilde{\boldsymbol{q}}'+\tilde{\boldsymbol{q}}''}{2}\right)\exp\left(\frac{2i\boldsymbol{p}\boldsymbol{x}}{\hbar}\right)\exp\left(-\frac{2i\boldsymbol{p}'\boldsymbol{x}}{\hbar}\right)\mathrm{d}\boldsymbol{x}.
\end{aligned} \tag{A.4}$$

Where $\delta(x)$ is the Dirac delta. Thus, an expression for the phase-point operator is given in the position basis,

$$\begin{aligned}
&\frac{1}{\pi\hbar}\int \delta\left(\boldsymbol{q}' - \frac{\tilde{\boldsymbol{q}}' + \tilde{\boldsymbol{q}}''}{2}\right)\exp\left(\frac{2i\boldsymbol{p}\boldsymbol{x}}{\hbar}\right)\exp\left(-\frac{2i\boldsymbol{p}'\boldsymbol{x}}{\hbar}\right)\mathrm{d}\boldsymbol{x} \\
&\qquad = \frac{1}{\pi\hbar}\int \langle\tilde{\boldsymbol{q}}'|\,\hat{A}\left(\boldsymbol{q}', \boldsymbol{p}'\right)|\tilde{\boldsymbol{q}}''\rangle \exp\left(\frac{2i\boldsymbol{p}\boldsymbol{x}}{\hbar}\right)\mathrm{d}\boldsymbol{x} \qquad \text{(A.5)} \\
\Leftrightarrow \langle\tilde{\boldsymbol{q}}'|\,\hat{A}\left(\boldsymbol{q}', \boldsymbol{p}'\right)|\tilde{\boldsymbol{q}}''\rangle &= \delta\left(\boldsymbol{q}' - \frac{\tilde{\boldsymbol{q}}' + \tilde{\boldsymbol{q}}''}{2}\right)\exp\left(-\frac{2i\boldsymbol{p}'\boldsymbol{x}}{\hbar}\right) \\
&= \delta\left(\boldsymbol{q}' - \frac{\tilde{\boldsymbol{q}}' + \tilde{\boldsymbol{q}}''}{2}\right)\exp\left(-\frac{i\boldsymbol{p}'\left(\boldsymbol{q} + \boldsymbol{x} - (\boldsymbol{q} - \boldsymbol{x})\right)}{\hbar}\right) \\
&= \delta\left(\boldsymbol{q}' - \frac{\tilde{\boldsymbol{q}}' + \tilde{\boldsymbol{q}}''}{2}\right)\exp\left(-\frac{i\boldsymbol{p}'\left(\tilde{\boldsymbol{q}}'' - \tilde{\boldsymbol{q}}'\right)}{\hbar}\right). \qquad \text{(A.6)}
\end{aligned}$$

An analogous expression can be derived in the momentum basis by using the definition of the Wigner function in the momentum basis, as stated in equation (2.4). This then results in the expression

$$\langle\tilde{\boldsymbol{p}}'|\,\hat{A}\left(\boldsymbol{q}', \boldsymbol{p}'\right)|\tilde{\boldsymbol{p}}''\rangle = \delta\left(\boldsymbol{p}' - \frac{\tilde{\boldsymbol{p}}' + \tilde{\boldsymbol{p}}''}{2}\right)\exp\left(-\frac{i\boldsymbol{q}'\left(\tilde{\boldsymbol{p}}'' - \tilde{\boldsymbol{p}}'\right)}{\hbar}\right). \qquad \text{(A.7)}$$

A.3 Calculation of the Trace of a Phase-Point Operator Product Given in Equation (2.18)

In section 2.1, the trace of a product of two phase-point operators $\hat{A}(\boldsymbol{q}_1, \boldsymbol{p}_1)$ and $\hat{A}(\boldsymbol{q}_2, \boldsymbol{p}_2)$ is calculated and the result is given in equation (2.18). This result can be easily calculated according to [35] by plugging the expression of the phase-point operators given in equation (2.11) into the definition of the trace,

$$\begin{aligned}
\mathrm{Tr}\left(\hat{A}(\boldsymbol{q}_1, \boldsymbol{p}_1)\,\hat{A}(\boldsymbol{q}_2, \boldsymbol{p}_2)\right) &= \int\int \langle \boldsymbol{q}'|\,\hat{A}(\boldsymbol{q}_1, \boldsymbol{p}_1)\,|\boldsymbol{q}''\rangle\,\langle \boldsymbol{q}''|\,\hat{A}(\boldsymbol{q}_2, \boldsymbol{p}_2)\,|\boldsymbol{q}'\rangle\,\mathrm{d}\boldsymbol{q}'\mathrm{d}\boldsymbol{q}'' \\
&= \int\int \delta\left(\boldsymbol{q}_1 - \frac{\boldsymbol{q}' + \boldsymbol{q}''}{2}\right)\exp\left(-\frac{i\boldsymbol{p}_1(\boldsymbol{q}'' - \boldsymbol{q}')}{\hbar}\right) \\
&\quad \times \delta\left(\boldsymbol{q}_2 - \frac{\boldsymbol{q}'' + \boldsymbol{q}'}{2}\right)\exp\left(-\frac{i\boldsymbol{p}_2(\boldsymbol{q}' - \boldsymbol{q}'')}{\hbar}\right)\mathrm{d}\boldsymbol{q}'\mathrm{d}\boldsymbol{q}'' \\
&= 2\int \exp\left(-\frac{i\boldsymbol{p}_1(2\boldsymbol{q}'' - 2\boldsymbol{q}_1)}{\hbar}\right)\delta(\boldsymbol{q}_2 - \boldsymbol{q}_1) \\
&\quad \times \exp\left(-\frac{i\boldsymbol{p}_2(2\boldsymbol{q}_1 - 2\boldsymbol{q}'')}{\hbar}\right)\mathrm{d}\boldsymbol{q}'' \\
&= 2\delta(\boldsymbol{q}_2 - \boldsymbol{q}_1)\int \exp\left(-\frac{2i\boldsymbol{q}''(\boldsymbol{p}_1 - \boldsymbol{p}_2)}{\hbar}\right) \\
&\quad \times \exp\left(-\frac{2i\boldsymbol{q}_1(\boldsymbol{p}_2 - \boldsymbol{p}_1)}{\hbar}\right)\mathrm{d}\boldsymbol{q}'' \\
&= 2\pi\hbar\delta(\boldsymbol{q}_2 - \boldsymbol{q}_1)\,\delta(\boldsymbol{p}_2 - \boldsymbol{p}_1)\exp\left(-\frac{2i\boldsymbol{q}_1(\boldsymbol{p}_2 - \boldsymbol{p}_1)}{\hbar}\right) \\
&= 2\pi\hbar\delta(\boldsymbol{q}_1 - \boldsymbol{q}_2)\,\delta(\boldsymbol{p}_1 - \boldsymbol{p}_2)\,, \qquad \text{(A.8)}
\end{aligned}$$

$$\text{using} \quad \int \exp\left(-\frac{2i\boldsymbol{q}''(\boldsymbol{p}_2 - \boldsymbol{p}_1)}{\hbar}\right)\mathrm{d}\boldsymbol{q}'' = \pi\hbar\delta(\boldsymbol{p}_2 - \boldsymbol{p}_1)\,.$$

In the last line it is used that the factor $\delta(\boldsymbol{p}_2 - \boldsymbol{p}_1)$ is only non-zero if $\boldsymbol{p}_2 = \boldsymbol{p}_1$ and in this case the exponential factor is one.

A.4 Derivation of the Weyl Symbol of a Commutator in Equation (2.33)

In section 2.3, the time evolution in the quantum mechanical phase space is calculated using the Weyl transformation of the von Neumann equation. Therefore, the Weyl symbol of a commutator of two arbitrary operators $\hat{\Omega}_1$ and $\hat{\Omega}_2$ is given in equation (2.33). This Weyl symbol of the commutator will be calculated according to [23] in the following by using the definition of the Weyl symbol in the position basis as stated in equation (2.1),

$$\begin{aligned}
[\Omega_1, \Omega_2]_{\mathrm{W}} = &\quad (\Omega_1\Omega_2)_{\mathrm{W}} - (\Omega_2\Omega_1)_{\mathrm{W}} \\
= &\quad \int \exp\left(\frac{i\boldsymbol{p}\boldsymbol{\xi}}{\hbar}\right) \left\langle \boldsymbol{q} - \frac{\boldsymbol{\xi}}{2} \middle| \hat{\Omega}_1\hat{\Omega}_2 \middle| \boldsymbol{q} + \frac{\boldsymbol{\xi}}{2} \right\rangle \mathrm{d}\boldsymbol{\xi} \\
&- \int \exp\left(\frac{i\boldsymbol{p}\boldsymbol{\xi}}{\hbar}\right) \left\langle \boldsymbol{q} - \frac{\boldsymbol{\xi}}{2} \middle| \hat{\Omega}_2\hat{\Omega}_1 \middle| \boldsymbol{q} + \frac{\boldsymbol{\xi}}{2} \right\rangle \mathrm{d}\boldsymbol{\xi} \\
= &\quad \int\int \exp\left(\frac{i\boldsymbol{p}\boldsymbol{\xi}}{\hbar}\right) \left\langle \boldsymbol{q} - \frac{\boldsymbol{\xi}}{2} \middle| \hat{\Omega}_1 \middle| \boldsymbol{q}' \right\rangle \left\langle \boldsymbol{q}' \middle| \hat{\Omega}_2 \middle| \boldsymbol{q} + \frac{\boldsymbol{\xi}}{2} \right\rangle \mathrm{d}\boldsymbol{\xi}\mathrm{d}\boldsymbol{q}' \\
&- \int\int \exp\left(\frac{i\boldsymbol{p}\boldsymbol{\xi}}{\hbar}\right) \left\langle \boldsymbol{q} - \frac{\boldsymbol{\xi}}{2} \middle| \hat{\Omega}_2 \middle| \boldsymbol{q}' \right\rangle \left\langle \boldsymbol{q}' \middle| \hat{\Omega}_1 \middle| \boldsymbol{q} + \frac{\boldsymbol{\xi}}{2} \right\rangle \mathrm{d}\boldsymbol{\xi}\mathrm{d}\boldsymbol{q}'. \qquad \text{(A.9)}
\end{aligned}$$

Here a one is introduced in the last line. To solve this, the general expression $\langle \boldsymbol{q}' | \hat{\Omega} | \boldsymbol{q}'' \rangle$ needs to be calculated. By expanding the Weyl symbol Ω_W corresponding to $\hat{\Omega}$ in a Fourier integral of a function $\omega(\boldsymbol{\sigma}, \boldsymbol{\tau})$, one gets [11]

$$\Omega_{\mathrm{W}}(\boldsymbol{q}, \boldsymbol{p}) = \int\int \omega(\boldsymbol{\sigma}, \boldsymbol{\tau}) \exp\left(i\left(\boldsymbol{\sigma}\boldsymbol{q} + \boldsymbol{\tau}\boldsymbol{p}\right)\right) \mathrm{d}\boldsymbol{\sigma}\mathrm{d}\boldsymbol{\tau}. \qquad \text{(A.10)}$$

Using this, the expectation value $\langle \boldsymbol{q} | \hat{\Omega} | \boldsymbol{q} \rangle$ can be considered to find an expression for $\hat{\Omega}$, which can then be plugged into $\langle \boldsymbol{q}' | \hat{\Omega} | \boldsymbol{q}'' \rangle$. Using the definition of the expectation

value in terms of the Wigner function $W(\boldsymbol{q},\boldsymbol{p})$ one can write [11]

$$\begin{aligned}
\langle \boldsymbol{q}|\,\hat{\Omega}\,|\boldsymbol{q}\rangle &= \mathrm{Tr}\left(\hat{\rho}\hat{\Omega}\right)\\
&= \int\int W(\boldsymbol{q},\boldsymbol{p})\,\Omega_{\mathrm{W}}(\boldsymbol{q},\boldsymbol{p})\,\mathrm{d}\boldsymbol{q}\mathrm{d}\boldsymbol{p}\\
&= \int\int\int\int W(\boldsymbol{q},\boldsymbol{p})\,\omega(\boldsymbol{\sigma},\boldsymbol{\tau})\exp\left(\frac{i\left(\boldsymbol{\sigma}\boldsymbol{q}+\boldsymbol{\tau}\boldsymbol{p}\right)}{\hbar}\right)\mathrm{d}\boldsymbol{q}\mathrm{d}\boldsymbol{p}\mathrm{d}\boldsymbol{\sigma}\mathrm{d}\boldsymbol{\tau}\\
&= \int\int\int\int\int\left\langle \boldsymbol{q}-\frac{\boldsymbol{\xi}}{2}\right|\hat{\rho}\left|\boldsymbol{q}+\frac{\boldsymbol{\xi}}{2}\right\rangle\omega(\boldsymbol{\sigma},\boldsymbol{\tau})\exp\left(\frac{i\left(\boldsymbol{\sigma}\boldsymbol{q}+\boldsymbol{\tau}\boldsymbol{p}\right)}{\hbar}\right)\\
&\quad\times\exp\left(\frac{i\boldsymbol{p}\boldsymbol{\xi}}{\hbar}\right)\mathrm{d}\boldsymbol{q}\mathrm{d}\boldsymbol{p}\mathrm{d}\boldsymbol{\sigma}\mathrm{d}\boldsymbol{\tau}\mathrm{d}\boldsymbol{\xi} \qquad (A.11)\\
&= 2\pi\hbar\int\int\int\int\left\langle \boldsymbol{q}-\frac{\boldsymbol{\xi}}{2}\right|\hat{\rho}\left|\boldsymbol{q}+\frac{\boldsymbol{\xi}}{2}\right\rangle\omega(\boldsymbol{\sigma},\boldsymbol{\tau})\\
&\quad\times\exp\left(\frac{i\boldsymbol{\sigma}\boldsymbol{q}}{\hbar}\right)\delta(\boldsymbol{\tau}+\boldsymbol{\xi})\,\mathrm{d}\boldsymbol{q}\mathrm{d}\boldsymbol{\sigma}\mathrm{d}\boldsymbol{\tau}\mathrm{d}\boldsymbol{\xi} \qquad (A.12)\\
&= 2\pi\hbar\int\int\int\left\langle \boldsymbol{q}+\frac{\boldsymbol{\tau}}{2}\right|\hat{\rho}\left|\boldsymbol{q}-\frac{\boldsymbol{\tau}}{2}\right\rangle\omega(\boldsymbol{\sigma},\boldsymbol{\tau})\exp\left(\frac{i\boldsymbol{\sigma}\boldsymbol{q}}{\hbar}\right)\mathrm{d}\boldsymbol{q}\mathrm{d}\boldsymbol{\sigma}\mathrm{d}\boldsymbol{\tau}. \qquad (A.13)
\end{aligned}$$

Here, the definitions of the Weyl symbol and the Wigner function are introduced and a Dirac delta is inserted. Now a new variable $\boldsymbol{q}' := \boldsymbol{q} - \frac{\boldsymbol{\tau}}{2}$ can be defined and substituted [11],

$$\begin{aligned}
\langle \boldsymbol{q}|\,\hat{\Omega}\,|\boldsymbol{q}\rangle &= \mathrm{Tr}\left(\hat{\rho}\hat{\Omega}\right)\\
&= 2\pi\hbar\int\int\int\langle\boldsymbol{q}'+\boldsymbol{\tau}|\,\hat{\rho}\,|\boldsymbol{q}'\rangle\,\omega(\boldsymbol{\sigma},\boldsymbol{\tau})\exp\left(\frac{i\boldsymbol{\sigma}\left(\boldsymbol{q}'+\frac{\boldsymbol{\tau}}{2}\right)}{\hbar}\right)\mathrm{d}\boldsymbol{q}'\mathrm{d}\boldsymbol{\sigma}\mathrm{d}\boldsymbol{\tau} \qquad (A.14)\\
&= 2\pi\hbar\int\int\int\left\langle \boldsymbol{q}'+\boldsymbol{\tau}\right|\hat{\rho}\exp\left(\frac{i}{\hbar}\boldsymbol{\sigma}\hat{\boldsymbol{q}}\right)\left|\boldsymbol{q}'\right\rangle\omega(\boldsymbol{\sigma},\boldsymbol{\tau})\exp\left(\frac{i\boldsymbol{\sigma}\boldsymbol{\tau}}{2\hbar}\right)\mathrm{d}\boldsymbol{q}'\mathrm{d}\boldsymbol{\sigma}\mathrm{d}\boldsymbol{\tau}\\
&= 2\pi\hbar\int\int\int\left\langle \boldsymbol{q}'\right|\exp\left(\frac{i\boldsymbol{\tau}\hat{\boldsymbol{p}}}{\hbar}\right)\hat{\rho}\exp\left(\frac{i\boldsymbol{\sigma}\hat{\boldsymbol{q}}}{\hbar}\right)\left|\boldsymbol{q}'\right\rangle\omega(\boldsymbol{\sigma},\boldsymbol{\tau})\\
&\quad\times\exp\left(\frac{i\boldsymbol{\sigma}\boldsymbol{\tau}}{2\hbar}\right)\mathrm{d}\boldsymbol{q}'\mathrm{d}\boldsymbol{\sigma}\mathrm{d}\boldsymbol{\tau}\\
&= 2\pi\hbar\mathrm{Tr}\left(\hat{\rho}\int\int\exp\left(\frac{i\boldsymbol{\tau}\hat{\boldsymbol{p}}}{\hbar}\right)\exp\left(\frac{i\boldsymbol{\sigma}\hat{\boldsymbol{q}}}{\hbar}\right)\exp\left(\frac{i\boldsymbol{\sigma}\boldsymbol{\tau}}{2\hbar}\right)\omega(\boldsymbol{\sigma},\boldsymbol{\tau})\,\mathrm{d}\boldsymbol{\sigma}\mathrm{d}\boldsymbol{\tau}\right)\\
&= 2\pi\hbar\mathrm{Tr}\left(\hat{\rho}\int\int\exp\left(\frac{i\left(\boldsymbol{\sigma}\hat{\boldsymbol{q}}+\boldsymbol{\tau}\hat{\boldsymbol{p}}\right)}{\hbar}\right)\omega(\boldsymbol{\sigma},\boldsymbol{\tau})\,\mathrm{d}\boldsymbol{\sigma}\mathrm{d}\boldsymbol{\tau}\right). \qquad (A.15)
\end{aligned}$$

In the last step the relation $\exp\left(\hat{A}+\hat{B}\right) = \exp\left(\hat{A}\right)\exp\left(\hat{B}\right)\exp\left(-\frac{\hat{D}}{2}\right)$ is used, which is true if the commutator $\hat{D}$ of two arbitrary operators $\hat{A}$, $\hat{B}$ commutes with

the operators $\hat{A}$ and $\hat{B}$. This means for the special case regarded here,

$$[\hat{\boldsymbol{p}}, \hat{\boldsymbol{q}}] = i\hbar \tag{A.16}$$

$$\Rightarrow [\hat{\boldsymbol{p}}, i\hbar] = [\hat{\boldsymbol{q}}, i\hbar] = 0 \tag{A.17}$$

$$\Rightarrow \exp\left(\frac{i\left(\boldsymbol{\sigma}\hat{\boldsymbol{q}} + \boldsymbol{\tau}\hat{\boldsymbol{p}}\right)}{\hbar}\right) = \exp\left(\frac{i\boldsymbol{\sigma}\hat{\boldsymbol{q}}}{\hbar}\right)\exp\left(\frac{i\boldsymbol{\tau}\hat{\boldsymbol{p}}}{\hbar}\right)\exp\left(\frac{i\boldsymbol{\sigma}\boldsymbol{\tau}}{2\hbar}\right). \tag{A.18}$$

From equation (A.15) one gets an expression for $\hat{\Omega}\left(\hat{\boldsymbol{q}}, \hat{\boldsymbol{p}}\right)$,

$$\mathrm{Tr}\left(\hat{\rho}\hat{\Omega}\right) = 2\pi\hbar\mathrm{Tr}\left(\hat{\rho}\int\int \exp\left(\frac{i\left(\boldsymbol{\sigma}\hat{\boldsymbol{q}} + \boldsymbol{\tau}\hat{\boldsymbol{p}}\right)}{\hbar}\right)\omega\left(\boldsymbol{\sigma}, \boldsymbol{\tau}\right)\mathrm{d}\boldsymbol{\sigma}\mathrm{d}\boldsymbol{\tau}\right) \tag{A.19}$$

$$\Rightarrow \hat{\Omega}\left(\hat{\boldsymbol{q}}, \hat{\boldsymbol{p}}\right) = 2\pi\hbar\int\int \exp\left(\frac{i\left(\boldsymbol{\sigma}\hat{\boldsymbol{q}} + \boldsymbol{\tau}\hat{\boldsymbol{p}}\right)}{\hbar}\right)\omega\left(\boldsymbol{\sigma}, \boldsymbol{\tau}\right)\mathrm{d}\boldsymbol{\sigma}\mathrm{d}\boldsymbol{\tau}. \tag{A.20}$$

This result can now be used to get an expression for $\langle \boldsymbol{q}'|\,\hat{\Omega}\,|\boldsymbol{q}''\rangle$ by simply plugging it in [11],

$$\begin{aligned}
\langle \boldsymbol{q}'|\,\hat{\Omega}\,|\boldsymbol{q}''\rangle &= 2\pi\hbar\int\int \omega\left(\boldsymbol{\sigma}, \boldsymbol{\tau}\right)\left\langle \boldsymbol{q}'\right|\exp\left(\frac{i\left(\boldsymbol{\sigma}\hat{\boldsymbol{q}} + \boldsymbol{\tau}\hat{\boldsymbol{p}}\right)}{\hbar}\right)\left|\boldsymbol{q}''\right\rangle \mathrm{d}\boldsymbol{\sigma}\mathrm{d}\boldsymbol{\tau} \\
&= 2\pi\hbar\int\int \omega\left(\boldsymbol{\sigma}, \boldsymbol{\tau}\right)\left\langle \boldsymbol{q}'\right|\exp\left(\frac{i\boldsymbol{\sigma}\hat{\boldsymbol{q}}}{\hbar}\right)\exp\left(\frac{i\boldsymbol{\tau}\hat{\boldsymbol{p}}}{\hbar}\right)\exp\left(\frac{i\boldsymbol{\sigma}\boldsymbol{\tau}}{2\hbar}\right)\left|\boldsymbol{q}''\right\rangle \mathrm{d}\boldsymbol{\sigma}\mathrm{d}\boldsymbol{\tau} \\
&= 2\pi\hbar\int\int \omega\left(\boldsymbol{\sigma}, \boldsymbol{\tau}\right)\left\langle \exp\left(-\frac{i\boldsymbol{\sigma}\boldsymbol{q}'}{\hbar}\right)\boldsymbol{q}'\right|\exp\left(\frac{i\boldsymbol{\tau}\hat{\boldsymbol{p}}}{\hbar}\right)\left|\boldsymbol{q}''\right\rangle \exp\left(\frac{i\boldsymbol{\sigma}\boldsymbol{\tau}}{2\hbar}\right)\mathrm{d}\boldsymbol{\sigma}\mathrm{d}\boldsymbol{\tau} \\
&= 2\pi\hbar\int\int \omega\left(\boldsymbol{\sigma}, \boldsymbol{\tau}\right)\exp\left(\frac{i\boldsymbol{\sigma}\boldsymbol{q}'}{\hbar}\right)\left\langle \boldsymbol{q}'\right|\exp\left(\frac{i\boldsymbol{\tau}\hat{\boldsymbol{p}}}{\hbar}\right)\left|\boldsymbol{q}''\right\rangle \exp\left(\frac{i\boldsymbol{\sigma}\boldsymbol{\tau}}{2\hbar}\right)\mathrm{d}\boldsymbol{\sigma}\mathrm{d}\boldsymbol{\tau} \\
&= 2\pi\hbar\int\int \omega\left(\boldsymbol{\sigma}, \boldsymbol{\tau}\right)\exp\left(\frac{i\boldsymbol{\sigma}\boldsymbol{q}'}{\hbar}\right)\exp\left(\frac{i\boldsymbol{\sigma}\boldsymbol{\tau}}{2\hbar}\right)\delta\left(\boldsymbol{q}' - \boldsymbol{q}'' + \boldsymbol{\tau}\right)\mathrm{d}\boldsymbol{\sigma}\mathrm{d}\boldsymbol{\tau} \\
&= 2\pi\hbar\int \omega\left(\boldsymbol{\sigma}, \boldsymbol{q}'' - \boldsymbol{q}'\right)\exp\left(\frac{i\boldsymbol{\sigma}\boldsymbol{q}'}{\hbar}\right)\exp\left(\frac{i\boldsymbol{\sigma}\left(\boldsymbol{q}'' - \boldsymbol{q}'\right)}{2\hbar}\right)\mathrm{d}\boldsymbol{\sigma} \\
&= 2\pi\hbar\int \omega\left(\boldsymbol{\sigma}, \boldsymbol{q}'' - \boldsymbol{q}'\right)\exp\left(\frac{i\boldsymbol{\sigma}\left(\boldsymbol{q}' + \boldsymbol{q}''\right)}{2\hbar}\right).
\end{aligned} \tag{A.21}$$

Here the relation

$$\begin{aligned}
\left\langle \boldsymbol{q}'\right|\exp\left(\frac{i\boldsymbol{\tau}\hat{\boldsymbol{p}}}{\hbar}\right)\left|\boldsymbol{q}''\right\rangle &= \int \langle \boldsymbol{q}'|\,\boldsymbol{p}\rangle\,\langle \boldsymbol{p}|\exp\left(\frac{i\boldsymbol{\tau}\hat{\boldsymbol{p}}}{\hbar}\right)|\boldsymbol{q}''\rangle\,\mathrm{d}\boldsymbol{p} \\
&= \int \underbrace{\langle \boldsymbol{q}'|\,\boldsymbol{p}\rangle}_{=\frac{1}{\sqrt{2\pi\hbar}}\exp\left(\frac{i\boldsymbol{p}\boldsymbol{q}'}{\hbar}\right)} \exp\left(\frac{i\boldsymbol{\tau}\boldsymbol{p}}{\hbar}\right) \underbrace{\langle \boldsymbol{p}|\,\boldsymbol{q}''\rangle}_{=\frac{1}{\sqrt{2\pi\hbar}}\exp\left(-\frac{i\boldsymbol{p}\boldsymbol{q}''}{\hbar}\right)} \mathrm{d}\boldsymbol{p} \\
&= \int \frac{1}{2\pi\hbar}\exp\left(\frac{i\left(\boldsymbol{p}\boldsymbol{q}' + \boldsymbol{\tau}\boldsymbol{p} - \boldsymbol{p}\boldsymbol{q}''\right)}{\hbar}\right)\mathrm{d}\boldsymbol{p} \\
&= \delta\left(\boldsymbol{q}' - \boldsymbol{q}'' + \boldsymbol{\tau}\right)
\end{aligned} \tag{A.22}$$

is used.

This result can now be plugged into equation (A.9) to calculate the Weyl symbol of the commutator. First, only one term is regarded for convenience, the result of the second term is calculated automatically [11],

$$\begin{aligned}(\Omega_1\Omega_2)_\mathrm{W} &= \int\int \exp\left(\frac{i\boldsymbol{p}\boldsymbol{\xi}}{\hbar}\right)\left\langle \boldsymbol{q}-\frac{\boldsymbol{\xi}}{2}\middle|\,\hat{\Omega}_1\middle|\boldsymbol{q}'\right\rangle\left\langle \boldsymbol{q}'\middle|\hat{\Omega}_2\,\middle|\boldsymbol{q}+\frac{\boldsymbol{\xi}}{2}\right\rangle \mathrm{d}\boldsymbol{\xi}\mathrm{d}\boldsymbol{q}' \\ &= 4\pi^2\hbar^2\int\int\int\int \exp\left(\frac{i\boldsymbol{p}\boldsymbol{\xi}}{\hbar}\right)\omega_1\left(\boldsymbol{\sigma},\boldsymbol{q}'-\boldsymbol{q}+\frac{\boldsymbol{\xi}}{2}\right)\exp\left(\frac{i\boldsymbol{\sigma}\left(\boldsymbol{q}'+\boldsymbol{q}-\frac{\boldsymbol{\xi}}{2}\right)}{2\hbar}\right) \\ &\quad\times\omega_2\left(\boldsymbol{\sigma}',\boldsymbol{q}+\frac{\boldsymbol{\xi}}{2}-\boldsymbol{q}'\right)\exp\left(\frac{i\boldsymbol{\sigma}'\left(\boldsymbol{q}'+\boldsymbol{q}+\frac{\boldsymbol{\xi}}{2}\right)}{2\hbar}\right)\mathrm{d}\boldsymbol{\xi}\mathrm{d}\boldsymbol{q}'\mathrm{d}\boldsymbol{\sigma}\mathrm{d}\boldsymbol{\sigma}'.\end{aligned} \tag{A.23}$$

Until now only the expression derived above is plugged in. Now two new variables can be defined and substituted:

$$\boldsymbol{\tau} := \boldsymbol{q}'-\boldsymbol{q}+\frac{\boldsymbol{\xi}}{2} \qquad \boldsymbol{\tau}' := \boldsymbol{q}-\boldsymbol{q}'+\frac{\boldsymbol{\xi}}{2} \;\Rightarrow\; \boldsymbol{\tau}+\boldsymbol{\tau}'=\boldsymbol{\xi} \tag{A.24}$$

$$\begin{aligned}\Rightarrow (\Omega_1\Omega_2)_\mathrm{W} &= 4\pi^2\hbar^2\int\int\int\int \exp\left(\frac{i\boldsymbol{p}\left(\boldsymbol{\tau}+\boldsymbol{\tau}'\right)}{\hbar}\right)\omega_1\left(\boldsymbol{\sigma},\boldsymbol{\tau}\right)\exp\left(\frac{i\boldsymbol{\sigma}\left(-\boldsymbol{\tau}'+2\boldsymbol{q}\right)}{2\hbar}\right) \\ &\quad\times\omega_2\left(\boldsymbol{\sigma}',\boldsymbol{\tau}'\right)\exp\left(\frac{i\boldsymbol{\sigma}'\left(\boldsymbol{\tau}+2\boldsymbol{q}\right)}{2\hbar}\right)\mathrm{d}\boldsymbol{\tau}\mathrm{d}\boldsymbol{\tau}'\mathrm{d}\boldsymbol{\sigma}\mathrm{d}\boldsymbol{\sigma}' \\ &= 4\pi^2\hbar^2\int\int\int\int \exp\left(\frac{i\left(\boldsymbol{\sigma}\boldsymbol{q}+\boldsymbol{\tau}\boldsymbol{p}\right)}{\hbar}\right)\omega_1\left(\boldsymbol{\sigma},\boldsymbol{\tau}\right)\underbrace{\exp\left(\frac{i\left(\boldsymbol{\tau}\boldsymbol{\sigma}'-\boldsymbol{\sigma}\boldsymbol{\tau}'\right)}{2\hbar}\right)}_{=\exp\left(\frac{\hbar\Lambda}{2i}\right)} \\ &\quad\times\exp\left(\frac{i\left(\boldsymbol{\sigma}'\boldsymbol{q}+\boldsymbol{\tau}'\boldsymbol{p}\right)}{\hbar}\right)\omega_2\left(\boldsymbol{\sigma}',\boldsymbol{\tau}'\right)\mathrm{d}\boldsymbol{\tau}\mathrm{d}\boldsymbol{\tau}'\mathrm{d}\boldsymbol{\sigma}\mathrm{d}\boldsymbol{\sigma}' \\ &= \Omega_{1,\mathrm{W}}\left(\boldsymbol{q},\boldsymbol{p}\right)\exp\left(-\frac{i\hbar\Lambda}{2}\right)\Omega_{2,\mathrm{W}}\left(\boldsymbol{q},\boldsymbol{p}\right) \qquad \text{(A.25)} \\ &= \Omega_{2,\mathrm{W}}\left(\boldsymbol{q},\boldsymbol{p}\right)\exp\left(\frac{i\hbar\Lambda}{2}\right)\Omega_{1,\mathrm{W}}\left(\boldsymbol{q},\boldsymbol{p}\right). \qquad \text{(A.26)}\end{aligned}$$

In an analogous way, the expression for the second term of the commutator can be derived,

$$\begin{aligned}(\Omega_2\Omega_1)_\mathrm{W} &= \Omega_{2,\mathrm{W}}\left(\boldsymbol{q},\boldsymbol{p}\right)\exp\left(-\frac{i\hbar\Lambda}{2}\right)\Omega_{1,\mathrm{W}}\left(\boldsymbol{q},\boldsymbol{p}\right) \\ &= \Omega_{1,\mathrm{W}}\left(\boldsymbol{q},\boldsymbol{p}\right)\exp\left(\frac{i\hbar\Lambda}{2}\right)\Omega_{2,\mathrm{W}}\left(\boldsymbol{q},\boldsymbol{p}\right).\end{aligned} \tag{A.27}$$

Given the expressions for the Weyl symbols of the two product terms of the commutator, the Weyl symbol of the commutator can be calculated by simply plugging the expressions in. The result is then stated in equation (2.33).

A.5 Derivation of the Time Evolution of the Correlation Operator in Equation (2.69)

In section 2.4, the time evolution in phase space is calculated using a BBGKY hierarchy of the reduced phase-point operators. There correlation operators $\hat{\mathscr{C}}_{ij}$ are introduced to get an expression for the second order reduced phase-point operators $\hat{\mathscr{A}}_{ij} = \hat{\mathscr{A}}_i\hat{\mathscr{A}}_j + \hat{\mathscr{C}}_{ij}$. The time evolution of the correlation operators is given in equation (2.69) and it can be derived according to [16] using equation (2.68), where the time evolution of $\hat{\mathscr{A}}_{ij}$ is already plugged in,

$$
\begin{aligned}
i\hbar\partial_t\hat{\mathscr{C}}_{ij} &= i\hbar\dot{\hat{\mathscr{A}}}_{ij} - i\hbar\partial_t\left(\hat{\mathscr{A}}_i\hat{\mathscr{A}}_j\right) \\
&= \left[\hat{H}_i + \hat{H}_j + \hat{H}_{ij}, \hat{\mathscr{A}}_i\hat{\mathscr{A}}_j + \hat{\mathscr{C}}_{ij}\right] - i\hbar\partial_t\left(\hat{\mathscr{A}}_i\hat{\mathscr{A}}_j\right) \\
&\quad + \sum_{\substack{k=1\\k\neq i,j}}^{N} \mathrm{Tr}_k\left(\left[\hat{H}_{ik} + \hat{H}_{jk}, \hat{\mathscr{A}}_i\hat{\mathscr{A}}_j\hat{\mathscr{A}}_k + \hat{\mathscr{A}}_i\hat{\mathscr{C}}_{jk} + \hat{\mathscr{A}}_j\hat{\mathscr{C}}_{ik} + \hat{\mathscr{A}}_k\hat{\mathscr{C}}_{ij} + \hat{\mathscr{C}}_{ijk}\right]\right).
\end{aligned}
\tag{A.28}
$$

The time evolution of the product $\hat{\mathscr{A}}_i\hat{\mathscr{A}}_j$ can be calculated using the product rule and the time evolution of the first order reduced phase-point operators as given in equation (2.67),

$$
\begin{aligned}
i\hbar\partial_t\left(\hat{\mathscr{A}}_i\hat{\mathscr{A}}_j\right) &= \left[\hat{H}_i, \hat{\mathscr{A}}_i\right]\hat{\mathscr{A}}_j + \sum_{\substack{k=1\\k\neq i}}^{N} \mathrm{Tr}_k\left(\left[\hat{H}_{ik}, \hat{\mathscr{A}}_i\hat{\mathscr{A}}_k\right] + \left[\hat{H}_{ik}, \hat{\mathscr{C}}_{ik}\right]\right)\hat{\mathscr{A}}_j \\
&\quad + \hat{\mathscr{A}}_i\left[\hat{H}_j, \hat{\mathscr{A}}_j\right] + \sum_{\substack{k=1\\k\neq j}}^{N} \hat{\mathscr{A}}_i\mathrm{Tr}_k\left(\left[\hat{H}_{jk}, \hat{\mathscr{A}}_j\hat{\mathscr{A}}_k\right] + \left[\hat{H}_{jk}, \hat{\mathscr{C}}_{jk}\right]\right) \\
&= \left[\hat{H}_i, \hat{\mathscr{A}}_i\right]\hat{\mathscr{A}}_j + \hat{\mathscr{A}}_i\left[\hat{H}_j, \hat{\mathscr{A}}_j\right] + \mathrm{Tr}_j\left(\left[\hat{H}_{ij}, \hat{\mathscr{A}}_i\hat{\mathscr{A}}_j\right]\right)\hat{\mathscr{A}}_j \\
&\quad + \mathrm{Tr}_j\left(\left[\hat{H}_{ij}, \hat{\mathscr{C}}_{ij}\right]\right)\hat{\mathscr{A}}_j + \hat{\mathscr{A}}_i\mathrm{Tr}_i\left(\left[\hat{H}_{ji}, \hat{\mathscr{A}}_j\hat{\mathscr{A}}_i\right]\right) \\
&\quad + \hat{\mathscr{A}}_i\mathrm{Tr}_i\left(\left[\hat{H}_{ji}, \hat{\mathscr{C}}_{ji}\right]\right) + \sum_{\substack{k=1\\k\neq i,j}}^{N} \mathrm{Tr}_k\left(\left[\hat{H}_{ik}, \hat{\mathscr{A}}_i\hat{\mathscr{A}}_k\right]\hat{\mathscr{A}}_j\right. \\
&\quad \left. + \left[\hat{H}_{ik}, \hat{\mathscr{C}}_{ik}\right]\hat{\mathscr{A}}_j + \left[\hat{H}_{jk}, \hat{\mathscr{A}}_j\hat{\mathscr{A}}_k\right]\hat{\mathscr{A}}_i + \left[\hat{H}_{jk}, \hat{\mathscr{C}}_{jk}\right]\hat{\mathscr{A}}_i\right)
\end{aligned}
$$

$$
\begin{aligned}
\Rightarrow i\hbar\partial_t\left(\hat{\mathscr{A}}_i\hat{\mathscr{A}}_j\right) = &\left[\hat{H}_i,\hat{\mathscr{A}}_i\hat{\mathscr{A}}_j\right] + \left[\hat{H}_j,\hat{\mathscr{A}}_i\hat{\mathscr{A}}_j\right] + \mathrm{Tr}_j\left(\left[\hat{H}_{ij},\hat{\mathscr{C}}_{ij}\right]\right)\hat{\mathscr{A}}_j \\
&+ \mathrm{Tr}_j\left(\left[\hat{H}_{ij},\hat{\mathscr{A}}_i\hat{\mathscr{A}}_j\right]\right)\hat{\mathscr{A}}_j + \mathrm{Tr}_i\left(\left[\hat{H}_{ji},\hat{\mathscr{C}}_{ji}\right]\right)\hat{\mathscr{A}}_i \\
&+ \mathrm{Tr}_i\left(\left[\hat{H}_{ji},\hat{\mathscr{A}}_j\hat{\mathscr{A}}_i\right]\right)\hat{\mathscr{A}}_i + \sum_{\substack{k=1\\k\neq i,j}}^{N}\mathrm{Tr}_k\left(\left[\hat{H}_{ik},\hat{\mathscr{A}}_i\hat{\mathscr{A}}_j\hat{\mathscr{A}}_k\right]\right. \\
&\left.+ \left[\hat{H}_{jk},\hat{\mathscr{A}}_i\hat{\mathscr{A}}_j\hat{\mathscr{A}}_k\right] + \left[\hat{H}_{ik},\hat{\mathscr{C}}_{ik}\hat{\mathscr{A}}_j\right] + \left[\hat{H}_{jk},\hat{\mathscr{C}}_{jk}\hat{\mathscr{A}}_i\right]\right). \qquad \text{(A.29)}
\end{aligned}
$$

Plugging equation (A.29) into equation (A.28) gives the equation of motion of the correlation operator $\hat{\mathscr{C}}_{ij}$ [16],

$$
\begin{aligned}
i\hbar\partial_t\hat{\mathscr{C}}_{ij} = &\left[\hat{H}_i+\hat{H}_j+\hat{H}_{ij},\hat{\mathscr{A}}_i\hat{\mathscr{A}}_j\right] + \left[\hat{H}_i+\hat{H}_j+\hat{H}_{ij},\hat{\mathscr{C}}_{ij}\right] \\
&+ \sum_{\substack{k=1\\k\neq i,j}}^{N}\mathrm{Tr}_k\left(\left[\hat{H}_{ik}+\hat{H}_{jk},\hat{\mathscr{A}}_i\hat{\mathscr{A}}_j\hat{\mathscr{A}}_k + \hat{\mathscr{A}}_i\hat{\mathscr{C}}_{jk} + \hat{\mathscr{A}}_j\hat{\mathscr{C}}_{ik} + \hat{\mathscr{A}}_k\hat{\mathscr{C}}_{ij} + \hat{\mathscr{C}}_{ijk}\right]\right) \\
&- \left[\hat{H}_i+\hat{H}_j,\hat{\mathscr{A}}_i\hat{\mathscr{A}}_j\right] - \mathrm{Tr}_j\left(\left[\hat{H}_{ij},\hat{\mathscr{C}}_{ij}\right]\right)\hat{\mathscr{A}}_j - \mathrm{Tr}_j\left(\left[\hat{H}_{ij},\hat{\mathscr{A}}_i\hat{\mathscr{A}}_j\right]\right)\hat{\mathscr{A}}_j \\
&- \mathrm{Tr}_i\left(\left[\hat{H}_{ji},\hat{\mathscr{C}}_{ji}\right]\right)\hat{\mathscr{A}}_i - \mathrm{Tr}_i\left(\left[\hat{H}_{ji},\hat{\mathscr{A}}_j\hat{\mathscr{A}}_i\right]\right)\hat{\mathscr{A}}_i \\
&- \sum_{\substack{k=1\\k\neq i,j}}^{N}\mathrm{Tr}_k\left(\left[\hat{H}_{ik}+\hat{H}_{jk},\hat{\mathscr{A}}_i\hat{\mathscr{A}}_j\hat{\mathscr{A}}_k\right] + \left[\hat{H}_{ik},\hat{\mathscr{C}}_{ik}\hat{\mathscr{A}}_j\right] + \left[\hat{H}_{jk},\hat{\mathscr{C}}_{jk}\hat{\mathscr{A}}_i\right]\right) \\
= &\left[\hat{H}_{ij},\hat{\mathscr{A}}_i\hat{\mathscr{A}}_j\right] + \left[\hat{H}_i+\hat{H}_j+\hat{H}_{ij},\hat{\mathscr{C}}_{ij}\right] + \sum_{\substack{k=1\\k\neq i,j}}^{N}\mathrm{Tr}_k\left(\left[\hat{H}_{ik}+\hat{H}_{jk},\hat{\mathscr{C}}_{ij}\hat{\mathscr{A}}_k\right]\right) \\
&+ \sum_{\substack{k=1\\k\neq i,j}}^{N}\mathrm{Tr}_k\left(\left[\hat{H}_{ik},\hat{\mathscr{A}}_i\hat{\mathscr{C}}_{jk}\right]\right) + \sum_{\substack{k=1\\k\neq i,j}}^{N}\mathrm{Tr}_k\left(\left[\hat{H}_{jk},\hat{\mathscr{A}}_j\hat{\mathscr{C}}_{ik}\right]\right) \\
&- \mathrm{Tr}_j\left(\left[\hat{H}_{ij},\hat{\mathscr{A}}_i\hat{\mathscr{A}}_j\right]\right)\hat{\mathscr{A}}_j - \mathrm{Tr}_j\left(\left[\hat{H}_{ij},\hat{\mathscr{C}}_{ij}\right]\right)\hat{\mathscr{A}}_j - \mathrm{Tr}_i\left(\left[\hat{H}_{ji},\hat{\mathscr{A}}_j\hat{\mathscr{A}}_i\right]\right)\hat{\mathscr{A}}_i \\
&- \mathrm{Tr}_i\left(\left[\hat{H}_{ji},\hat{\mathscr{C}}_{ji}\right]\right)\hat{\mathscr{A}}_i
\end{aligned}
$$

$$\Rightarrow i\hbar\partial_t\hat{\mathscr{C}}_{ij} = \left[\hat{H}_i + \hat{H}_j, \hat{\mathscr{C}}_{ij}\right] + \left[\hat{H}_{ij}, \hat{\mathscr{A}}_i\hat{\mathscr{A}}_j + \hat{\mathscr{C}}_{ij}\right] + \sum_{\substack{k=1\\k\neq i,j}}^{N} \mathrm{Tr}_k\left(\left[\hat{H}_{ik}, \hat{\mathscr{A}}_i\hat{\mathscr{C}}_{jk}\right]\right) \quad \text{(A.30)}$$

$$+ \sum_{\substack{k=1\\k\neq i,j}}^{N} \mathrm{Tr}_k\left(\left[\hat{H}_{jk}, \hat{\mathscr{A}}_j\hat{\mathscr{C}}_{ik}\right]\right) + \sum_{\substack{k=1\\k\neq i,j}}^{N} \mathrm{Tr}_k\left(\left[\hat{H}_{ik} + \hat{H}_{jk}, \hat{\mathscr{A}}_k\hat{\mathscr{C}}_{ij}\right]\right)$$

$$- \hat{\mathscr{A}}_j\mathrm{Tr}_j\left(\left[\hat{H}_{ij}, \hat{\mathscr{A}}_i\hat{\mathscr{A}}_j + \hat{\mathscr{C}}_{ij}\right]\right) - \hat{\mathscr{A}}_i\mathrm{Tr}_i\left(\left[\hat{H}_{ji}, \hat{\mathscr{A}}_j\hat{\mathscr{A}}_i + \hat{\mathscr{C}}_{ji}\right]\right).$$

This result is stated for the time evolution of the two-point correlation operator in equation (2.69).

B Appendix for Chapter 3

B.1 Proving the Pauli Matrices to be Mutually Unbiased

In section 3.1 it is discussed that the Pauli matrices form a mutually unbiased basis. The proof can be given easily by calculating the quantity $|\langle v_i|\, w_j\rangle|^2$, with the eigenstates $\{|v_i\rangle\}$ and $\{|w_j\rangle\}$ of two operators, and showing that the results are independent of i and j,

	$\lvert\langle x_i\rvert\, y_j\rangle\rvert^2$	$\lvert\langle x_i\rvert\, z_j\rangle\rvert^2$	$\lvert\langle y_i\rvert\, z_j\rangle\rvert^2$
$i=0$ $j=0$	$\left\lvert\begin{pmatrix}1 & 1\end{pmatrix}\begin{pmatrix}1\\ \mathrm{i}\end{pmatrix}\right\rvert^2 = 2,$	$\left\lvert\begin{pmatrix}1 & 1\end{pmatrix}\begin{pmatrix}1\\ 0\end{pmatrix}\right\rvert^2 = 1,$	$\left\lvert\begin{pmatrix}1 & \mathrm{i}\end{pmatrix}\begin{pmatrix}1\\ 0\end{pmatrix}\right\rvert^2 = 1,$
$i=0$ $j=1$	$\left\lvert\begin{pmatrix}1 & 1\end{pmatrix}\begin{pmatrix}1\\ -\mathrm{i}\end{pmatrix}\right\rvert^2 = 2,$	$\left\lvert\begin{pmatrix}1 & 1\end{pmatrix}\begin{pmatrix}0\\ 1\end{pmatrix}\right\rvert^2 = 1,$	$\left\lvert\begin{pmatrix}1 & \mathrm{i}\end{pmatrix}\begin{pmatrix}0\\ 1\end{pmatrix}\right\rvert^2 = 1,$
$i=1$ $j=0$	$\left\lvert\begin{pmatrix}1 & -1\end{pmatrix}\begin{pmatrix}1\\ \mathrm{i}\end{pmatrix}\right\rvert^2 = 2,$	$\left\lvert\begin{pmatrix}1 & -1\end{pmatrix}\begin{pmatrix}1\\ 0\end{pmatrix}\right\rvert^2 = 1,$	$\left\lvert\begin{pmatrix}1 & -\mathrm{i}\end{pmatrix}\begin{pmatrix}1\\ 0\end{pmatrix}\right\rvert^2 = 1,$
$i=1$ $j=1$	$\left\lvert\begin{pmatrix}1 & -1\end{pmatrix}\begin{pmatrix}1\\ -\mathrm{i}\end{pmatrix}\right\rvert^2 = 2,$	$\left\lvert\begin{pmatrix}1 & -1\end{pmatrix}\begin{pmatrix}0\\ 1\end{pmatrix}\right\rvert^2 = 1,$	$\left\lvert\begin{pmatrix}1 & -\mathrm{i}\end{pmatrix}\begin{pmatrix}0\\ 1\end{pmatrix}\right\rvert^2 = 1.$

Each row shows all possible combinations of eigenstate products of two operators and they all give the same result. Thus, the Pauli matrices are mutually unbiased.

B.2 Deriving the Time Evolution of the Expansion Coefficients a_i in Equation (3.19)

In section 3.2, the first order reduced phase point operator $\hat{\mathscr{A}_i}$ is represented in terms of the Pauli operators using the expansion coefficients $\boldsymbol{a}_i$,

$$\hat{\mathscr{A}_i} = \frac{1}{2}\left(\hat{\mathrm{I}}_i + \boldsymbol{a}_i\hat{\boldsymbol{\sigma}}_i\right).$$

The time evolution of these expansion coefficients is calculated in equation (3.19) and gives the result in equation (3.20) by the following calculation according to [16],

$$\begin{aligned}
\frac{1}{2}\dot{\boldsymbol{a}}_i\hat{\boldsymbol{\sigma}}_i = &\sum_{\substack{\beta,\gamma\\=x,y,z}}\left(-\frac{h_i^\beta a_i^\gamma}{2i}\left[\hat{\sigma}_i^\beta,\hat{\sigma}_i^\gamma\right]\right) + \sum_{\substack{k=0\\k\neq i}}^{N-1}\sum_{\substack{\beta,\mu,\nu\\=x,y,z}}\left(-\frac{J_{ik}^\beta c_{ik}^{\mu\nu}}{4i}\mathrm{Tr}_k\left(\left[\hat{\sigma}_i^\beta\hat{\sigma}_k^\beta,\ \hat{\sigma}_i^\mu\hat{\sigma}_k^\nu\right]\right)\right)\\
&+\sum_{\substack{k=0\\k\neq i}}^{N-1}\sum_{\substack{\beta,\gamma\\=x,y,z}}\left(-\frac{J_{ik}^\beta a_i^\gamma}{4i}\mathrm{Tr}_k\left(\left[\hat{\sigma}_i^\beta\hat{\sigma}_k^\beta,\ \hat{\sigma}_i^\gamma\right]\right) - \frac{J_{ik}^\beta a_k^\gamma}{4i}\mathrm{Tr}_k\left(\left[\hat{\sigma}_i^\beta\hat{\sigma}_k^\beta,\ \hat{\sigma}_k^\gamma\right]\right)\right)\\
&+\sum_{\substack{k=0\\k\neq i}}^{N-1}\sum_{\substack{\beta,\gamma,\delta\\=x,y,z}}\left(-\frac{J_{ik}^\beta a_i^\gamma a_k^\delta}{4i}\mathrm{Tr}_k\left(\left[\hat{\sigma}_i^\beta\hat{\sigma}_k^\beta,\ \hat{\sigma}_i^\gamma\hat{\sigma}_k^\delta\right]\right)\right)\\
= &\sum_{\substack{\beta,\gamma\\=x,y,z}}\left(-\frac{h_i^\beta a_i^\gamma}{2i}\left[\hat{\sigma}_i^\beta,\ \hat{\sigma}_i^\gamma\right]\right)\\
&+\sum_{\substack{k=0\\k\neq i}}^{N-1}\sum_{\substack{\beta,\mu,\nu\\=x,y,z}}\left(-\frac{J_{ik}^\beta c_{ik}^{\mu\nu}}{4i}\hat{\sigma}_i^\beta\hat{\sigma}_i^\mu\mathrm{Tr}_k\left(\left[\hat{\sigma}_k^\beta,\ \hat{\sigma}_k^\nu\right]\right) - \frac{J_{ik}^\beta c_{ik}^{\mu\nu}}{4i}\mathrm{Tr}_k\left(\hat{\sigma}_k^\beta\hat{\sigma}_k^\nu\right)\left[\hat{\sigma}_i^\beta,\ \hat{\sigma}_i^\mu\right]\right)\\
&+\sum_{\substack{k=0\\k\neq i}}^{N-1}\sum_{\substack{\beta,\gamma\\=x,y,z}}\left(-\frac{J_{ik}^\beta a_i^\gamma}{4i}\mathrm{Tr}_k\left(\hat{\sigma}_k^\beta\right)\left[\hat{\sigma}_i^\beta,\ \hat{\sigma}_i^\gamma\right] - \frac{J_{ik}^\beta a_k^\gamma}{4i}\hat{\sigma}_i^\beta\mathrm{Tr}_k\left(\left[\hat{\sigma}_k^\beta,\ \hat{\sigma}_k^\gamma\right]\right)\right)\\
&+\sum_{\substack{k=0\\k\neq i}}^{N-1}\sum_{\substack{\beta,\gamma,\delta\\=x,y,z}}\left(-\frac{J_{ik}^\beta a_i^\gamma a_k^\delta}{4i}\left[\hat{\sigma}_i^\beta,\ \hat{\sigma}_i^\gamma\right]\mathrm{Tr}_k\left(\hat{\sigma}_k^\beta\hat{\sigma}_k^\delta\right)\right.\\
&\left.-\frac{J_{ik}^\beta a_i^\gamma a_k^\delta}{4i}\hat{\sigma}_i^\beta\hat{\sigma}_i^\gamma\mathrm{Tr}_k\left(\left[\hat{\sigma}_k^\beta,\ \hat{\sigma}_k^\delta\right]\right)\right)
\end{aligned}$$

$$
\begin{aligned}
\Rightarrow \frac{1}{2}\dot{\boldsymbol{a}}_i\hat{\boldsymbol{\sigma}}_i = & \sum_{\substack{\beta,\gamma,\delta \\ =x,y,z}} \left(-h_i^\beta a_i^\gamma \epsilon^{\beta\gamma\delta}\hat{\sigma}_i^\delta\right) \\
& + \sum_{\substack{k=0 \\ k\neq i}}^{N-1} \sum_{\substack{\beta,\mu,\nu,\delta \\ =x,y,z}} \left(-\frac{J_{ik}^\beta c_{ik}^{\mu\nu}}{2} \left(\delta_{\beta\mu}\hat{\mathrm{I}}_i + i \sum_{\substack{\gamma \\ =x,y,z}} \epsilon^{\beta\mu\gamma}\hat{\sigma}_i^\gamma \right) \epsilon^{\beta\nu\delta}\mathrm{Tr}_k\left(\hat{\sigma}_k^\delta\right) \right. \\
& \left. -\frac{J_{ik}^\beta c_{ik}^{\mu\nu}}{2} \left(\delta_{\beta\nu}\mathrm{Tr}_k\left(\hat{\mathrm{I}}_k\right) + i \sum_{\substack{\gamma \\ =x,y,z}} \epsilon^{\beta\mu\gamma}\mathrm{Tr}_k\left(\hat{\sigma}_k^\gamma\right) \right) \epsilon^{\beta\mu\delta}\hat{\sigma}_i^\delta \right) \\
& + \sum_{\substack{k=0 \\ k\neq i}}^{N-1} \sum_{\substack{\beta,\gamma,\delta \\ =x,y,z}} \left(-\frac{J_{ik}^\beta a_i^\gamma}{2}\mathrm{Tr}_k\left(\hat{\sigma}_k^\beta\right)\epsilon^{\beta\gamma\delta}\hat{\sigma}_i^\delta - \frac{J_{ik}^\beta a_k^\gamma}{2}\hat{\sigma}_i^\beta\epsilon^{\beta\gamma\delta}\mathrm{Tr}_k\left(\hat{\sigma}_k^\delta\right) \right) \\
& + \sum_{\substack{k=0 \\ k\neq i}}^{N-1} \sum_{\substack{\beta,\gamma,\delta,\mu \\ =x,y,z}} \left(-\frac{J_{ik}^\beta a_i^\gamma a_k^\delta}{2}\epsilon^{\beta\gamma\mu}\hat{\sigma}_i^\mu \left(\delta_{\beta\delta}\mathrm{Tr}_k\left(\hat{\mathrm{I}}_k\right) + i \sum_{\substack{\nu \\ =x,y,z}} \epsilon^{\beta\delta\nu}\mathrm{Tr}_k\left(\hat{\sigma}_k^\nu\right) \right) \right. \\
& \left. -\frac{J_{ik}^\beta a_i^\gamma a_k^\delta}{2} \left(\delta_{\beta\gamma}\hat{\mathrm{I}}_i + i \sum_{\substack{\nu \\ =x,y,z}} \epsilon^{\beta\gamma\nu}\hat{\sigma}_i^\nu \right) \epsilon^{\beta\delta\mu}\mathrm{Tr}_k\left(\hat{\sigma}_k^\mu\right) \right).
\end{aligned}
$$

Using the fact that the trace of any Pauli matrix is zero as given in equation (3.3), this gives

$$
\begin{aligned}
\frac{1}{2}\dot{\boldsymbol{a}}_i\hat{\boldsymbol{\sigma}}_i = & \sum_{\substack{\beta,\gamma,\mu \\ =x,y,z}} \left(-h_i^\beta a_i^\gamma \epsilon^{\beta\gamma\mu}\hat{\sigma}_i^\mu\right) + \sum_{\substack{k=0 \\ k\neq i}}^{N-1} \sum_{\substack{\mu,\nu,\delta \\ =x,y,z}} \left(-J_{ik}^\nu c_{ik}^{\delta\nu}\epsilon^{\nu\delta\mu}\hat{\sigma}_i^\mu\right) \\
& + \sum_{\substack{k=0 \\ k\neq i}}^{N-1} \sum_{\substack{\gamma,\delta,\mu \\ =x,y,z}} \left(-J_{ik}^\delta a_i^\gamma a_k^\delta \epsilon^{\delta\gamma\mu}\hat{\sigma}_i^\mu\right) \\
= & \frac{1}{2} \sum_{\substack{\mu \\ =x,y,z}} \dot{a}_i^\mu \hat{\sigma}_i^\mu
\end{aligned}
$$

By eliminating $\hat{\sigma}_i^\mu$ on both sides, one gets an expression for $\dot{a}_i^\mu$:

$$
\frac{1}{2}\dot{a}_i^\mu = - \sum_{\substack{\gamma,\delta \\ =x,y,z}} \left[h_i^\gamma a_i^\delta \epsilon^{\mu\gamma\delta} + \sum_{\substack{k=0 \\ k\neq i}}^{N-1} J_{ik}^\gamma c_{ik}^{\delta\gamma}\epsilon^{\mu\gamma\delta} + \sum_{\substack{k=0 \\ k\neq i}}^{N-1} J_{ik}^\gamma a_i^\delta a_k^\gamma \epsilon^{\mu\gamma\delta} \right]
$$

B.3 Deriving the Time Evolution of the Expansion Coefficients c_{ij} in Equation (3.22)

The correlation operator $\hat{\mathscr{C}}_{ij}$ is represented in terms of the Pauli operators in equation (3.17) in section 3.2. Given this representation, the truncated time evolution of the expansion coefficients $\boldsymbol{c}_{ij}$ can be calculated using equation (3.22), which gives the result stated in equation (3.23). This result can be calculated according to [16] regarding the terms of equation (3.22) individually,

$$\begin{aligned}
\frac{1}{i}\Bigg[&- \boldsymbol{h}_i\hat{\boldsymbol{\sigma}}_i - \boldsymbol{h}_j\hat{\boldsymbol{\sigma}}_j,\ \ \frac{1}{4}\sum_{\substack{\mu,\nu\\=x,y,z}} c_{ij}^{\mu\nu}\hat{\sigma}_i^{\mu}\hat{\sigma}_j^{\nu}\Bigg] \\
&= \frac{1}{i}\sum_{\substack{\mu,\nu,\gamma\\=x,y,z}}\left(-\frac{h_i^{\gamma}c_{ij}^{\mu\nu}}{4}\left[\hat{\sigma}_i^{\gamma},\ \hat{\sigma}_i^{\mu}\hat{\sigma}_j^{\nu}\right] - \frac{h_j^{\gamma}c_{ij}^{\mu\nu}}{4}\left[\hat{\sigma}_j^{\gamma},\ \hat{\sigma}_i^{\mu}\hat{\sigma}_j^{\nu}\right]\right) \\
&= \sum_{\substack{\mu,\nu,\gamma,\delta\\=x,y,z}}\left(-\frac{h_i^{\gamma}c_{ij}^{\mu\nu}}{2}\epsilon^{\gamma\mu\delta}\hat{\sigma}_i^{\delta}\hat{\sigma}_j^{\nu} - \frac{h_j^{\gamma}c_{ij}^{\mu\nu}}{2}\epsilon^{\gamma\nu\delta}\hat{\sigma}_i^{\mu}\hat{\sigma}_j^{\delta}\right),
\end{aligned}$$

$$\begin{aligned}
\frac{1}{i}\sum_{\substack{\beta,\mu,\nu\\=x,y,z}}\Bigg[&- J_{ij}^{\beta}\hat{\sigma}_i^{\beta}\hat{\sigma}_j^{\beta},\ \ \frac{1}{4}c_{ij}^{\mu\nu}\hat{\sigma}_i^{\mu}\hat{\sigma}_j^{\nu}\Bigg] \\
&= -\frac{1}{i}\sum_{\substack{\beta,\mu,\nu\\=x,y,z}}\frac{J_{ij}^{\beta}c_{ij}^{\mu\nu}}{4}\left[\hat{\sigma}_i^{\beta}\hat{\sigma}_j^{\beta},\ \hat{\sigma}_i^{\mu}\hat{\sigma}_j^{\nu}\right] \\
&= -\sum_{\substack{\beta,\mu,\nu,\delta\\=x,y,z}}\frac{J_{ij}^{\beta}c_{ij}^{\mu\nu}}{2}\left(\delta_{\beta\nu}\epsilon^{\beta\mu\delta}\hat{\sigma}_i^{\delta} + \delta_{\beta\mu}\epsilon^{\beta\nu\delta}\hat{\sigma}_j^{\delta}\right) \\
&= -\sum_{\substack{\beta,\mu,\nu\\=x,y,z}}\left(\frac{J_{ij}^{\beta}c_{ij}^{\mu\beta}}{2}\epsilon^{\beta\mu\nu}\hat{\sigma}_i^{\nu} + \frac{J_{ij}^{\beta}c_{ij}^{\beta\nu}}{2}\epsilon^{\beta\nu\mu}\hat{\sigma}_j^{\mu}\right),
\end{aligned}$$

$$\frac{1}{i}\sum_{\substack{\beta\\=x,y,z}}\Big[-J_{ij}^{\beta}\hat{\sigma}_i^{\beta}\hat{\sigma}_j^{\beta},\quad \frac{1}{4}\left(\hat{\mathrm{I}}_i+\boldsymbol{a}_i\hat{\boldsymbol{\sigma}}_i\right)\left(\hat{\mathrm{I}}_j+\boldsymbol{a}_j\hat{\boldsymbol{\sigma}}_j\right)\Big]$$

$$=\frac{1}{i}\sum_{\substack{\beta,\delta\\=x,y,z}}\left(-\frac{J_{ij}^{\beta}a_i^{\delta}}{4}\left[\hat{\sigma}_i^{\beta}\hat{\sigma}_j^{\beta},\ \hat{\sigma}_i^{\delta}\right]-\frac{J_{ij}^{\beta}a_j^{\delta}}{4}\left[\hat{\sigma}_i^{\beta}\hat{\sigma}_j^{\beta},\ \hat{\sigma}_j^{\delta}\right]\right)$$

$$+\frac{1}{i}\sum_{\substack{\beta,\delta,\gamma\\=x,y,z}}\left(-\frac{J_{ij}^{\beta}a_i^{\delta}a_j^{\gamma}}{4}\left[\hat{\sigma}_i^{\beta}\hat{\sigma}_j^{\beta},\ \hat{\sigma}_i^{\delta}\hat{\sigma}_j^{\gamma}\right]\right)$$

$$=\sum_{\substack{\beta,\delta,\gamma\\=x,y,z}}\left(-\frac{J_{ij}^{\beta}a_i^{\delta}}{2}\epsilon^{\beta\delta\gamma}\hat{\sigma}_i^{\gamma}\hat{\sigma}_j^{\beta}-\frac{J_{ij}^{\beta}a_j^{\delta}}{2}\epsilon^{\beta\delta\gamma}\hat{\sigma}_i^{\beta}\hat{\sigma}_j^{\gamma}\right)$$

$$-\sum_{\substack{\beta,\delta,\gamma,\mu\\=x,y,z}}\frac{J_{ij}^{\beta}a_i^{\delta}a_j^{\gamma}}{2}\left(\delta_{\beta\gamma}\epsilon^{\beta\delta\mu}\hat{\sigma}_i^{\mu}+\delta_{\beta\delta}\epsilon^{\beta\gamma\mu}\hat{\sigma}_j^{\mu}\right)$$

$$=\sum_{\substack{\beta,\delta,\gamma\\=x,y,z}}\left(-\frac{J_{ij}^{\beta}a_i^{\delta}}{2}\epsilon^{\beta\delta\gamma}\hat{\sigma}_i^{\gamma}\hat{\sigma}_j^{\beta}-\frac{J_{ij}^{\beta}a_j^{\delta}}{2}\epsilon^{\beta\delta\gamma}\hat{\sigma}_i^{\beta}\hat{\sigma}_j^{\gamma}\right.$$

$$\left.-\frac{J_{ij}^{\beta}a_i^{\delta}a_j^{\beta}}{2}\epsilon^{\beta\delta\gamma}\hat{\sigma}_i^{\gamma}-\frac{J_{ij}^{\beta}a_i^{\beta}a_j^{\gamma}}{2}\epsilon^{\beta\gamma\delta}\hat{\sigma}_j^{\delta}\right),$$

using $\left[\hat{\sigma}_i^{\beta}\hat{\sigma}_j^{\beta},\hat{\sigma}_i^{\delta}\hat{\sigma}_j^{\gamma}\right]=2i\sum_{\substack{\mu\\=x,y,z}}\left(\delta_{\beta\gamma}\epsilon^{\beta\delta\mu}\hat{\sigma}_i^{\mu}+\delta_{\beta\delta}\epsilon^{\beta\gamma\mu}\hat{\sigma}_j^{\mu}\right),$

$$\frac{1}{i}\sum_{\substack{k=0\\k\neq i,j}}^{N-1}\mathrm{Tr}_k\left(\sum_{\substack{\beta,\delta,\mu,\nu\\=x,y,z}}\left[-J_{jk}^{\beta}\hat{\sigma}_j^{\beta}\hat{\sigma}_k^{\beta},\quad\frac{1}{8}\left(\hat{\mathrm{I}}_j+a_j^{\delta}\hat{\sigma}_j^{\delta}\right)c_{ik}^{\mu\nu}\hat{\sigma}_i^{\mu}\hat{\sigma}_k^{\nu}\right]\right)$$

$$=-\frac{1}{i}\sum_{\substack{k=0\\k\neq i,j}}^{N-1}\sum_{\substack{\beta,\delta,\mu,\nu\\=x,y,z}}\frac{J_{jk}^{\beta}c_{ik}^{\mu\nu}}{8}\mathrm{Tr}_k\left(\left[\hat{\sigma}_j^{\beta}\hat{\sigma}_k^{\beta},\ \hat{\sigma}_i^{\mu}\hat{\sigma}_k^{\nu}\right]\right.$$

$$\left.+a_j^{\delta}\left[\hat{\sigma}_j^{\beta}\hat{\sigma}_k^{\beta},\ \hat{\sigma}_i^{\mu}\hat{\sigma}_j^{\delta}\hat{\sigma}_k^{\nu}\right]\right)$$

$$=-\sum_{\substack{k=0\\k\neq i,j}}^{N-1}\sum_{\substack{\beta,\delta,\gamma,\mu\\=x,y,z}}\frac{J_{jk}^{\beta}c_{ik}^{\mu\beta}a_j^{\delta}}{2}\epsilon^{\beta\delta\gamma}\hat{\sigma}_i^{\mu}\hat{\sigma}_j^{\gamma},$$

$$\frac{1}{i}\sum_{\substack{k=0\\k\neq i,j}}^{N-1}\mathrm{Tr}_k\left(\sum_{\substack{\beta,\delta,\mu,\nu\\=x,y,z}}\left[-J_{ik}^{\beta}\hat{\sigma}_i^{\beta}\hat{\sigma}_k^{\beta},\quad\frac{1}{8}\left(\hat{\mathrm{I}}_i+a_i^{\delta}\hat{\sigma}_i^{\delta}\right)c_{jk}^{\mu\nu}\hat{\sigma}_j^{\mu}\hat{\sigma}_k^{\nu}\right]\right)$$

$$=-\frac{1}{i}\sum_{\substack{k=0\\k\neq i,j}}^{N-1}\sum_{\substack{\beta,\delta,\mu,\nu\\=x,y,z}}\frac{J_{ik}^{\beta}c_{jk}^{\mu\nu}}{8}\mathrm{Tr}_k\left(\left[\hat{\sigma}_i^{\beta}\hat{\sigma}_k^{\beta},\ \hat{\sigma}_j^{\mu}\hat{\sigma}_k^{\nu}\right]\right.$$

$$\left.+a_i^{\delta}\left[\hat{\sigma}_i^{\beta}\hat{\sigma}_k^{\beta},\ \hat{\sigma}_i^{\delta}\hat{\sigma}_j^{\mu}\hat{\sigma}_k^{\nu}\right]\right)$$

$$=-\sum_{\substack{k=0\\k\neq i,j}}^{N-1}\sum_{\substack{\beta,\delta,\gamma,\mu,\nu\\=x,y,z}}\frac{J_{ik}^{\beta}c_{jk}^{\mu\nu}}{4}\left(\epsilon^{\beta\nu\gamma}\hat{\sigma}_i^{\beta}\hat{\sigma}_j^{\mu}\mathrm{Tr}_k\left(\hat{\sigma}_k^{\gamma}\right)\right.$$

$$+a_i^{\delta}\delta_{\beta\delta}\epsilon^{\beta\nu\gamma}\hat{\sigma}_j^{\mu}\mathrm{Tr}_k\left(\hat{\sigma}_k^{\gamma}\right)$$

$$\left.+a_i^{\delta}\delta_{\beta\nu}\epsilon^{\beta\delta\gamma}\hat{\sigma}_i^{\gamma}\hat{\sigma}_j^{\mu}\mathrm{Tr}_k\left(\hat{\mathrm{I}}_k\right)\right)$$

$$=-\sum_{\substack{k=0\\k\neq i,j}}^{N-1}\sum_{\substack{\beta,\delta,\gamma,\mu\\=x,y,z}}\frac{J_{ik}^{\beta}c_{jk}^{\mu\beta}a_i^{\delta}}{2}\epsilon^{\beta\delta\gamma}\hat{\sigma}_i^{\gamma}\hat{\sigma}_j^{\mu},$$

$$\frac{1}{i}\sum_{\substack{k=0\\k\neq i,j}}^{N-1}\sum_{\substack{\beta,\mu,\nu,\delta\\=x,y,z}}\mathrm{Tr}_k\left(\left[-J_{ik}^{\beta}\hat{\sigma}_i^{\beta}\hat{\sigma}_k^{\beta},\ \frac{1}{8}c_{ij}^{\mu\nu}\hat{\sigma}_i^{\mu}\hat{\sigma}_j^{\nu}+\frac{1}{8}a_k^{\delta}c_{ij}^{\mu\nu}\hat{\sigma}_i^{\mu}\hat{\sigma}_j^{\nu}\hat{\sigma}_k^{\delta}\right]\right)$$

$$=\frac{1}{i}\sum_{\substack{k=0\\k\neq i,j}}^{N-1}\sum_{\substack{\beta,\delta,\mu,\nu\\=x,y,z}}\frac{J_{ik}^{\beta}c_{ij}^{\mu\nu}}{8}\mathrm{Tr}_k\left(\left[\hat{\sigma}_i^{\beta}\hat{\sigma}_k^{\beta},\ \hat{\sigma}_i^{\mu}\hat{\sigma}_j^{\nu}\right]\right.$$

$$\left.+a_k^{\delta}\left[\hat{\sigma}_i^{\beta}\hat{\sigma}_k^{\beta},\ \hat{\sigma}_i^{\mu}\hat{\sigma}_j^{\nu}\hat{\sigma}_k^{\delta}\right]\right)$$

$$=-\sum_{\substack{k=0\\k\neq i,j}}^{N-1}\sum_{\substack{\beta,\nu,\gamma,\mu\\=x,y,z}}\frac{J_{ik}^{\beta}c_{ij}^{\mu\nu}a_k^{\beta}}{2}\epsilon^{\beta\mu\gamma}\hat{\sigma}_i^{\gamma}\hat{\sigma}_j^{\nu},$$

$$\frac{1}{i}\sum_{\substack{k=0\\k\neq i,j}}^{N-1}\sum_{\substack{\beta,\mu,\nu,\delta\\=x,y,z}}\mathrm{Tr}_k\left(\Big[-J_{jk}^{\beta}\hat{\sigma}_j^{\beta}\hat{\sigma}_k^{\beta},\quad \frac{1}{8}c_{ij}^{\mu\nu}\hat{\sigma}_i^{\mu}\hat{\sigma}_j^{\nu}+\frac{1}{8}a_k^{\delta}c_{ij}^{\mu\nu}\hat{\sigma}_i^{\mu}\hat{\sigma}_j^{\nu}\hat{\sigma}_k^{\delta}\Big]\right)$$

$$=\frac{1}{i}\sum_{\substack{k=0\\k\neq i,j}}^{N-1}\sum_{\substack{\beta,\delta,\mu,\nu\\=x,y,z}}\frac{J_{jk}^{\beta}c_{ij}^{\mu\nu}}{8}\mathrm{Tr}_k\left(\left[\hat{\sigma}_j^{\beta}\hat{\sigma}_k^{\beta},\ \hat{\sigma}_i^{\mu}\hat{\sigma}_j^{\nu}\right]\right.$$

$$\left.+a_k^{\delta}\left[\hat{\sigma}_j^{\beta}\hat{\sigma}_k^{\beta},\ \hat{\sigma}_i^{\mu}\hat{\sigma}_j^{\nu}\hat{\sigma}_k^{\delta}\right]\right)$$

$$=-\sum_{\substack{k=0\\k\neq i,j}}^{N-1}\sum_{\substack{\beta,\nu,\gamma,\mu\\=x,y,z}}\frac{J_{jk}^{\beta}c_{ij}^{\mu\nu}a_k^{\beta}}{2}\epsilon^{\beta\nu\gamma}\hat{\sigma}_i^{\mu}\hat{\sigma}_j^{\gamma},$$

$$-\frac{1}{2i}\left(\hat{\mathrm{I}}_j+\boldsymbol{a}_j\hat{\boldsymbol{\sigma}}_j\right)$$

$$\times\mathrm{Tr}_j\left(\left[-\sum_{\substack{\beta\\=x,y,z}}J_{ij}^{\beta}\hat{\sigma}_i^{\beta}\hat{\sigma}_j^{\beta},\frac{1}{4}\left(\hat{\mathrm{I}}_i+\boldsymbol{a}_i\hat{\boldsymbol{\sigma}}_i\right)\left(\hat{\mathrm{I}}_j+\boldsymbol{a}_j\hat{\boldsymbol{\sigma}}_j\right)+\frac{1}{4}\sum_{\substack{\mu,\nu\\=x,y,z}}c_{ij}^{\mu\nu}\hat{\sigma}_i^{\mu}\hat{\sigma}_j^{\nu}\right]\right)$$

$$=-\frac{1}{2}\left(\hat{\mathrm{I}}_j+\boldsymbol{a}_j\hat{\boldsymbol{\sigma}}_j\right)\mathrm{Tr}_j\left(\sum_{\substack{\beta,\mu,\nu\\=x,y,z}}\left(-\frac{J_{ij}^{\beta}a_i^{\mu}}{2}\epsilon^{\beta\mu\nu}\hat{\sigma}_i^{\nu}\hat{\sigma}_j^{\beta}-\frac{J_{ij}^{\beta}a_j^{\mu}}{2}\epsilon^{\beta\mu\nu}\hat{\sigma}_i^{\beta}\hat{\sigma}_j^{\nu}\right.\right.$$

$$\left.\left.-\frac{J_{ij}^{\beta}a_i^{\mu}a_j^{\beta}}{2}\epsilon^{\beta\mu\nu}\hat{\sigma}_i^{\nu}-\frac{J_{ij}^{\beta}a_i^{\beta}a_j^{\mu}}{2}\epsilon^{\beta\mu\nu}\hat{\sigma}_j^{\nu}-\frac{J_{ij}^{\beta}c_{ij}^{\mu\beta}}{2}\epsilon^{\beta\mu\nu}\hat{\sigma}_i^{\nu}+\frac{J_{ij}^{\beta}c_{ij}^{\beta\nu}}{2}\epsilon^{\beta\nu\mu}\hat{\sigma}_j^{\mu}\right)\right)$$

$$=-\frac{1}{2}\left(\hat{\mathrm{I}}_j+\boldsymbol{a}_j\hat{\boldsymbol{\sigma}}_j\right)\sum_{\substack{\beta,\mu,\nu\\=x,y,z}}\left(-J_{ij}^{\beta}a_i^{\mu}a_j^{\beta}\epsilon^{\beta\mu\nu}\hat{\sigma}_i^{\nu}-J_{ij}^{\beta}c_{ij}^{\mu\beta}\epsilon^{\beta\mu\nu}\hat{\sigma}_i^{\nu}\right)$$

$$=-\frac{1}{2}\sum_{\substack{\beta,\mu,\nu\\=x,y,z}}\left(-J_{ij}^{\beta}a_i^{\mu}a_j^{\beta}\epsilon^{\beta\mu\nu}\hat{\sigma}_i^{\nu}-J_{ij}^{\beta}c_{ij}^{\mu\beta}\epsilon^{\beta\mu\nu}\hat{\sigma}_i^{\nu}\right)$$

$$-\frac{1}{2}\sum_{\substack{\beta,\mu,\nu,\gamma\\=x,y,z}}\left(-J_{ij}^{\beta}a_i^{\mu}a_j^{\beta}a_j^{\gamma}\epsilon^{\beta\mu\nu}\hat{\sigma}_i^{\nu}\hat{\sigma}_j^{\gamma}-J_{ij}^{\beta}a_j^{\gamma}c_{ij}^{\mu\beta}\epsilon^{\beta\mu\nu}\hat{\sigma}_i^{\nu}\hat{\sigma}_j^{\gamma}\right),$$

$$
\begin{aligned}
&-\frac{1}{2i}\left(\hat{\mathrm{I}}_i + \boldsymbol{a}_i\hat{\boldsymbol{\sigma}}_i\right) \\
&\quad \mathrm{Tr}_i\left(\left[-\sum_{\substack{\beta \\ =x,y,z}} J_{ij}^{\beta}\hat{\sigma}_i^{\beta}\hat{\sigma}_j^{\beta},\ \frac{1}{4}\left(\hat{\mathrm{I}}_i + \boldsymbol{a}_i\hat{\boldsymbol{\sigma}}_i\right)\left(\hat{\mathrm{I}}_j + \boldsymbol{a}_j\hat{\boldsymbol{\sigma}}_j\right) + \frac{1}{4}\sum_{\substack{\mu,\nu \\ =x,y,z}} c_{ij}^{\mu\nu}\hat{\sigma}_i^{\mu}\hat{\sigma}_j^{\nu}\right]\right) \\
&= -\frac{1}{2}\left(\hat{\mathrm{I}}_i + \boldsymbol{a}_i\hat{\boldsymbol{\sigma}}_i\right)\sum_{\substack{\beta,\mu,\nu \\ =x,y,z}}\left(-J_{ij}^{\beta}a_i^{\beta}a_j^{\mu}\epsilon^{\beta\mu\nu}\hat{\sigma}_j^{\nu} - J_{ij}^{\beta}c_{ij}^{\beta\mu}\epsilon^{\beta\mu\nu}\hat{\sigma}_j^{\nu}\right) \\
&= -\frac{1}{2}\sum_{\substack{\beta,\mu,\nu \\ =x,y,z}}\left(-J_{ij}^{\beta}a_i^{\beta}a_j^{\mu}\epsilon^{\beta\mu\nu}\hat{\sigma}_j^{\nu} - J_{ij}^{\beta}c_{ij}^{\beta\mu}\epsilon^{\beta\mu\nu}\hat{\sigma}_j^{\nu}\right) \\
&\quad -\frac{1}{2}\sum_{\substack{\beta,\mu,\nu,\gamma \\ =x,y,z}}\left(-J_{ij}^{\beta}a_i^{\beta}a_i^{\gamma}a_j^{\mu}\epsilon^{\beta\mu\nu}\hat{\sigma}_i^{\gamma}\hat{\sigma}_j^{\nu} - J_{ij}^{\beta}a_i^{\gamma}c_{ij}^{\beta\mu}\epsilon^{\beta\mu\nu}\hat{\sigma}_i^{\gamma}\hat{\sigma}_j^{\nu}\right).
\end{aligned}
$$

Adding all terms together and renaming the indices results in

$$
\begin{aligned}
\frac{1}{4}\sum_{\substack{\mu,\nu \\ =x,y,z}} \dot{c}_{ij}^{\mu\nu}\hat{\sigma}_i^{\mu}\hat{\sigma}_j^{\nu} = &\sum_{\substack{\mu,\nu,\gamma,\delta \\ =x,y,z}}\left(-\frac{h_i^{\gamma}c_{ij}^{\delta\nu}}{2}\epsilon^{\gamma\delta\mu}\hat{\sigma}_i^{\mu}\hat{\sigma}_j^{\nu} - \frac{h_j^{\gamma}c_{ij}^{\mu\delta}}{2}\epsilon^{\gamma\delta\nu}\hat{\sigma}_i^{\mu}\hat{\sigma}_j^{\nu}\right) \\
&+\sum_{\substack{\mu,\nu,\gamma \\ =x,y,z}}\left(-\frac{J_{ij}^{\nu}a_i^{\gamma}}{2}\epsilon^{\nu\gamma\mu}\hat{\sigma}_i^{\mu}\hat{\sigma}_j^{\nu} - \frac{J_{ij}^{\mu}a_j^{\gamma}}{2}\epsilon^{\mu\gamma\nu}\hat{\sigma}_i^{\mu}\hat{\sigma}_j^{\nu}\right. \\
&-\frac{J_{ij}^{\gamma}a_i^{\nu}a_j^{\gamma}}{2}\epsilon^{\gamma\nu\mu}\hat{\sigma}_i^{\mu} - \frac{J_{ij}^{\gamma}a_i^{\gamma}a_j^{\mu}}{2}\epsilon^{\gamma\mu\nu}\hat{\sigma}_j^{\nu} - \frac{J_{ij}^{\gamma}c_{ij}^{\nu\gamma}}{2}\epsilon^{\gamma\nu\mu}\hat{\sigma}_i^{\mu} \\
&\left.-\frac{J_{ij}^{\gamma}c_{ij}^{\gamma\mu}}{2}\epsilon^{\gamma\mu\nu}\hat{\sigma}_j^{\nu}\right) + \sum_{\substack{k=0 \\ k\neq i,j}}^{N-1}\sum_{\substack{\mu,\nu,\gamma,\delta \\ =x,y,z}}\left(-\frac{J_{ik}^{\gamma}c_{jk}^{\nu\gamma}a_i^{\delta}}{2}\epsilon^{\gamma\delta\mu}\hat{\sigma}_i^{\mu}\hat{\sigma}_j^{\nu}\right. \\
&-\frac{J_{jk}^{\gamma}c_{ik}^{\mu\gamma}a_j^{\delta}}{2}\epsilon^{\gamma\delta\nu}\hat{\sigma}_i^{\mu}\hat{\sigma}_j^{\nu} - \frac{J_{ik}^{\gamma}c_{ij}^{\delta\nu}a_k^{\gamma}}{2}\epsilon^{\gamma\delta\mu}\hat{\sigma}_i^{\mu}\hat{\sigma}_j^{\nu} \\
&\left.-\frac{J_{jk}^{\gamma}c_{ij}^{\mu\delta}a_k^{\gamma}}{2}\epsilon^{\gamma\delta\nu}\sigma_i^{\mu}\sigma_j^{\nu}\right) - \sum_{\substack{\mu,\nu,\gamma \\ =x,y,z}}\left(-\frac{J_{ij}^{\gamma}a_i^{\nu}a_j^{\gamma}}{2}\epsilon^{\gamma\nu\mu}\hat{\sigma}_i^{\mu}\right. \\
&-\frac{J_{ij}^{\gamma}c_{ij}^{\nu\gamma}}{2}\epsilon^{\gamma\nu\mu}\hat{\sigma}_i^{\mu} - \frac{J_{ij}^{\gamma}a_i^{\gamma}a_j^{\mu}}{2}\epsilon^{\gamma\mu\nu}\hat{\sigma}_j^{\nu} - \frac{J_{ij}^{\gamma}c_{ij}^{\gamma\mu}}{2}\epsilon^{\gamma\mu\nu}\hat{\sigma}_j^{\nu}\Big) \\
&-\sum_{\substack{\mu,\nu,\gamma,\delta \\ =x,y,z}}\left(-\frac{J_{ij}^{\gamma}a_i^{\delta}a_j^{\gamma}a_j^{\nu}}{2}\epsilon^{\gamma\delta\mu}\hat{\sigma}_i^{\mu}\hat{\sigma}_j^{\nu} - \frac{J_{ij}^{\gamma}a_j^{\nu}c_{ij}^{\delta\gamma}}{2}\epsilon^{\gamma\delta\mu}\hat{\sigma}_i^{\mu}\hat{\sigma}_j^{\nu}\right. \\
&\left.-\frac{J_{ij}^{\gamma}a_i^{\gamma}a_i^{\mu}a_j^{\delta}}{2}\epsilon^{\gamma\delta\nu}\hat{\sigma}_i^{\mu}\hat{\sigma}_j^{\nu} - \frac{J_{ij}^{\gamma}a_i^{\mu}c_{ij}^{\gamma\delta}}{2}\epsilon^{\gamma\delta\nu}\hat{\sigma}_i^{\mu}\hat{\sigma}_j^{\nu}\right)
\end{aligned}
$$

$$
\begin{aligned}
= -\frac{1}{2} \sum_{\substack{\mu,\nu \\ =x,y,z}} \Bigg[& - \sum_{\substack{\delta \\ =x,y,z}} \left(J_{ij}^{\nu} a_i^{\gamma} - J_{ij}^{\mu} a_j^{\gamma} \right) \epsilon^{\mu\nu\gamma} \\
& - \sum_{\substack{\delta,\gamma \\ =x,y,z}} \left(\left(h_i^{\gamma} + \sum_{\substack{k=0 \\ k\neq i,j}}^{N-1} J_{ik}^{\gamma} a_k^{\gamma} \right) c_{ij}^{\delta\nu} \epsilon^{\gamma\delta\mu} + \left(h_j^{\gamma} + \sum_{\substack{k=0 \\ k\neq i,j}}^{N-1} J_{jk}^{\gamma} a_k^{\gamma} \right) c_{ij}^{\mu\delta} \epsilon^{\gamma\delta\nu} \right) \\
& - \sum_{\substack{\delta,\gamma \\ =x,y,z}} \sum_{\substack{k=0 \\ k\neq i,j}}^{N-1} \left(J_{ik}^{\gamma} a_i^{\delta} c_{jk}^{\nu\gamma} \epsilon^{\gamma\delta\mu} + J_{jk}^{\gamma} a_j^{\delta} c_{ik}^{\mu\gamma} \epsilon^{\gamma\delta\nu} \right) \\
& + \sum_{\substack{\delta,\gamma \\ =x,y,z}} J_{ij}^{\gamma} \left(a_i^{\mu} \left(c_{ij}^{\gamma\delta} + a_i^{\gamma} a_j^{\delta} \right) \epsilon^{\gamma\delta\nu} + a_j^{\nu} \left(c_{ij}^{\delta\gamma} + a_i^{\delta} a_j^{\gamma} \right) \epsilon^{\gamma\delta\mu} \right) \Bigg] \hat{\sigma}_i^{\mu} \hat{\sigma}_j^{\nu}.
\end{aligned}
$$

Considering only the term $\dot{c}_{ij}^{\mu\nu}$ gives the result stated in equation (3.22).

B.4 Summarising the Sampling Schemes Introduced in Section 3.3

Sampling Scheme S_{init}

- sampled from

$$\begin{aligned} \boldsymbol{r}_{(0,0)} &= (1,1,1)\,, & W_{(0,0)} &= 0.5, \\ \boldsymbol{r}_{(0,1)} &= (1,-1,-1)\,, & W_{(0,1)} &= 0, \\ \boldsymbol{r}_{(1,0)} &= (-1,-1,1)\,, & W_{(1,0)} &= 0.5, \\ \boldsymbol{r}_{(1,1)} &= (-1,1,-1)\,, & W_{(1,1)} &= 0 \end{aligned}$$

- direct result of the phase-point operators in equation (2.26)

- correlation between the x- and y-component in the two states with nonzero Wigner function

Sampling Scheme S_{mix}

- sampled from

$$\begin{aligned} \boldsymbol{r}_{(0,0)} &= (1,1,1)\,, & W_{(0,0)} &= 0.25, \\ \boldsymbol{r}_{(0,1)} &= (-1,-1,1)\,, & W_{(0,1)} &= 0.25, \\ \boldsymbol{r}_{(1,0)} &= (1,-1,1)\,, & W_{(1,0)} &= 0.25, \\ \boldsymbol{r}_{(1,1)} &= (-1,1,1)\,, & W_{(1,1)} &= 0.25 \end{aligned}$$

- taking the two states of S_{init} with non-zero Wigner function and creating two more states by flipping the y-components

- no correlation between the x- and y-component, all four possible states included

Sampling Scheme $\tilde{S}_{\text{mix}}$

- sampled from

$$\boldsymbol{r}_{(0,0)} = (1, 0, 1)\,, \qquad W_{(0,0)} = 0.25,$$

$$\boldsymbol{r}_{(0,1)} = (-1, 0, 1)\,, \qquad W_{(0,1)} = 0.25,$$

$$\boldsymbol{r}_{(1,0)} = (0, 1, 1)\,, \qquad W_{(1,0)} = 0.25,$$

$$\boldsymbol{r}_{(1,1)} = (0, -1, 1)\,, \qquad W_{(1,1)} = 0.25$$

- taking the sum of the two states of S_{init} with non-zero Wigner function and the results by flipping the x- and y-components
- no correlation between the x- and y-component, spin components can take initial value 0, which is not possible in quantum mechanics

Semi-Continuous Sampling Scheme

- sampled from the four boarders of the cube in figure 3.2 with $s_z = 1$
- general combination of the two states of S_{init} with non-zero Wigner function and the results of flipping the x- and y-components
- no correlation between the x- and y-component, but in each possible initial state either the x- or y-component of the spin can take continuous values, which is not possible in quantum mechanics

Continuous Sampling Scheme

- sampled from the side of the cube in figure 3.2 with $s_z = 1$
- general combination of the two states of S_{init} with non-zero Wigner function and the results of flipping the x- and y-components
- no correlation between the x- and y-component, but in each possible initial state the x- and y-component of the spin can take continuous values, which is not possible in quantum mechanics

B.5 Deriving the Relation Between the Exact Correlation Function and the First Order Approximation in Equation (3.57)

The relation between the exact solution and the first order approximation of the correlation function $\left\langle \hat{\sigma}_i^z \hat{\sigma}_j^z \right\rangle$ is stated in equation (3.57). This relation is derived according to [27] in the following way,

$$
\begin{aligned}
\left\langle s_i^z s_j^z \right\rangle_{\mathrm{cl}}(t) = \frac{\left\langle \hat{\sigma}_i^z \hat{\sigma}_j^z \right\rangle(0)}{2^N} \sum_{\substack{m_1 \ldots m_N \\ \in\{-1,+1\}}} & \left[\cos\left(2tJ_{ij}m_j + 2t \sum_{\substack{a=0 \\ a\neq i,j}}^{N-1} (J_{ia}m_a) \right) \right. \\
& \left. \times \cos\left(2tJ_{ji}m_i + 2t \sum_{\substack{b=0 \\ b\neq i,j}}^{N-1} (J_{jb}m_b) \right) \right] \\
= \frac{\left\langle \hat{\sigma}_i^z \hat{\sigma}_j^z \right\rangle(0)}{2^N} \sum_{\substack{m1 \ldots m_N \\ \in\{-1,+1\}}} & \left[\cos(2tJ_{ij}m_j) \cos\left(2t \sum_{\substack{a=0 \\ a\neq i,j}}^{N-1} J_{ia}m_a \right) \right. \\
& \left. - \sin(2tJ_{ij}m_j) \sin\left(2t \sum_{\substack{a=0 \\ a\neq i,j}}^{N-1} J_{ia}m_a \right) \right] \\
& \times \left[\cos(2tJ_{ji}m_i) \cos\left(2t \sum_{\substack{b=0 \\ b\neq i,j}}^{N-1} J_{jb}m_b \right) \right. \\
& \left. - \sin(2tJ_{ji}m_i) \sin\left(2t \sum_{\substack{b=0 \\ b\neq i,j}}^{N-1} J_{jb}m_b \right) \right].
\end{aligned}
$$

Writing out the sum over all possible combinations of m_i and m_j to be $+1$ or -1 gives

$$\begin{aligned}
\left\langle s_i^z s_j^z \right\rangle_{cl}(t) =& \frac{\left\langle \hat{\sigma}_i^z \hat{\sigma}_j^z \right\rangle(0)}{2^N} \sum_{\substack{m_1 \ldots m_{i-1} m_{i+1} \ldots m_{j-1} m_{j+1} \ldots m_N \\ \in \{-1,+1\}}} \\
& \times \left[\left(\cos\left(2tJ_{ij}\right) + \cos\left(-2tJ_{ij}\right)\right) \cos\left(2t \sum_{\substack{a=0 \\ a \neq i,j}}^{N-1} J_{ia} m_a \right) \right. \\
& \left. - \left(\sin\left(2tJ_{ij}\right) + \sin\left(-2tJ_{ij}\right)\right) \sin\left(2t \sum_{\substack{a=0 \\ a \neq i,j}}^{N-1} J_{ia} m_a \right) \right] \\
& \times \left[\left(\cos\left(2tJ_{ji}\right) + \cos\left(-2tJ_{ji}\right)\right) \cos\left(2t \sum_{\substack{b=0 \\ b \neq i,j}}^{N-1} J_{jb} m_b \right) \right. \\
& \left. - \left(\sin\left(2tJ_{ji}\right) + \sin\left(-2tJ_{ji}\right)\right) \sin\left(2t \sum_{\substack{b=0 \\ b \neq i,j}}^{N-1} J_{jb} m_b \right) \right] \\
= & \frac{\left\langle \hat{\sigma}_i^z \hat{\sigma}_j^z \right\rangle(0)}{2^N} \sum_{\substack{m_1 \ldots m_{i-1} m_{i+1} \ldots m_{j-1} m_{j+1} \ldots m_N \\ \in \{-1,+1\}}} \\
& \times 4 \left[\cos\left(2tJ_{ij}\right) \cos\left(2t \sum_{\substack{a=0 \\ a \neq i,j}}^{N-1} J_{ia} m_a \right) \right] \\
& \times \left[\cos\left(2tJ_{ji}\right) \cos\left(2t \sum_{\substack{b=0 \\ b \neq i,j}}^{N-1} J_{jb} m_b \right) \right] \\
= & \left\langle \hat{\sigma}_i^z \hat{\sigma}_j^z \right\rangle(t) \cos\left(2tJ_{ij}\right) \cos\left(2tJ_{ji}\right) \\
= & \left\langle \hat{\sigma}_i^z \hat{\sigma}_j^z \right\rangle(t) \cos^2\left(2tJ_{ij}\right).
\end{aligned}$$

Where the following relations are used,

$$\begin{aligned}\cos(x+y) &= \cos(x)\cos(y) - \sin(x)\sin(y),\\ \cos(x) + \cos(-x) &= 2\cos(x),\\ \sin(x) + \sin(-x) &= 0.\end{aligned}$$

In the last line, the interaction matrix $\boldsymbol{J}$ is defined to be symmetric, $J_{ij} = J_{ji}$.

C Computational Background

This thesis is based on a semi-classical numerical approximation of discrete quantum mechanical systems. The theory of this approximation scheme has been introduced in chapters 2 and 3 and the simulation results for a spin-$\frac{1}{2}$ chain are shown in chapter 4. In the following, the numerical implementation of the approximation method will be discussed. Therefore, in appendix C.1 a detailed description of the various steps in the implementation will be given.

The equations of motion of a spin-$\frac{1}{2}$ system have been derived in section 3.2 as ordinary differential equations. It has already been discussed that these differential equations need to be solved numerically and appendix C.2 will introduce two numerical solving methods. The Runge-Kutta-Fehlberg method, which will be further introduced in appendix C.2.1, has been used for all results in section 3.4 and chapter 4. Since the solutions of the non-linear equations of motion given by the second order approximation in section 3.2 show large divergences in sections 3.4.2 and 4.3, a second numerical method with higher accuracy has been tested to solve these non-linear ordinary differential equations. This way it can be analysed whether the divergences depend on the numerical solver. This Adams-Bashforth-Moulton method will be further introduced in appendix C.2.2.

C.1 General Implementation of the Discrete Truncated Wigner Approximation

The discrete truncated Wigner approximation has been implemented in C++ while the evaluations of the results are done using Python. For the discrete truncated Wigner approximation first the Wigner function needs to be calculated, which depends on the phase-point operators. To get these, two possibilities can be used. First a general way to calculate the phase-point operators depending on the initial condition has been implemented. This general calculation has also been implemented for a pair of qubits, or consistent with the previous chapters for a pair of spin-$\frac{1}{2}$ particles, which results in approximations of spin-$\frac{3}{2}$ systems [35, 36]. But since in the approximations considered in this thesis, the initial conditions are always the same, computation time can be saved by calculating the phase-point operators once, storing them and then importing them in every approximation. Given these, the calculation of the Wigner function is implemented explicitly and called once, while the resulting function is reused for every run.

After the Wigner function has been calculated, an initial spin state can be sampled for each run. The Wigner function as a quasi-probability-distribution gives a

probability for the spin being in each of the four possible states associated with the points in the discrete phase space, given it is positive definite. This is not necessarily the case, since the Wigner function may have negative values and then does not give a probability for each state. In this case one has to think of a way how to treat the negative values to sample from the Wigner function. Since for the initial conditions regarded in this thesis the Wigner function is always positive, as derived in section 3.1, the initial spin states can be directly sampled given the probabilities for the possible states. To do so, a random number is drawn from a uniform distribution, where in the implementation the random number generator in the C++ standard library is used. Therefore, an unsigned integer is drawn from a uniform distribution using `random_device` from the C++ standard library. This random number generator uses hardware random number generators if they are available and then produces non-deterministic numbers where replication is avoided, see [14]. The implementation is parallelised which causes that multiple random numbers are generated at the same time. If a hardware random number generator is used, the numbers generated at the same time are all the same. To avoid this, the resulting numbers are used as a seed for a pseudo-random number generator, which then produces uniformly distributed random numbers between zero and one. As a pseudo-random number generator, the "Mersenne Twister" from the C++ standard library is used, which produces random numbers with period $2^{19937} - 1$ from a given distribution. Here the `uniform_real_distribution` from the C++ standard library is used to draw a uniform random number between zero and one [14].

To sample the initial state $\boldsymbol{s}_i$ from the Wigner function, the following algorithm can be used given a uniform random number g between zero and one,

```
if(g < W[0,0])
{
        s = r[0,0];
}
else if(g < W[0,0] + W[0,1])
{
        s = r[0,1];
}
else if(g < W[0,0] + W[0,1] + W[1,0])
{
        s = r[1,0];
}
else
{
        s = r[1,1];
}.
```

`W[a,b]` denotes the Wigner function at point (a, b) in phase space and `r[a,b]` denotes the initial state associated with this point.

After an initial state has been sampled from the Wigner function in the explained

way, it can be evolved in time using either the classical equations of motion given in equation (3.14), or the second order time evolution stated in equations (3.20) and (3.23). These equations of motion need to be solved numerically in most cases, where the algorithms for the numerical solutions of differential equations are further discussed in appendix C.2.

The equations of motion depend on the spin-spin interaction $\boldsymbol{J}_{ij}$ between each two spins. To calculate this interaction, a two-dimensional array is created, in which for each site the distance to any other site is stored. Given the distances between each two sites, the interaction strength can be calculated, since it is proportional to the distance. For a one-dimensional spin chain with N sites, the distance array is an $N \times N$ array, while a three-dimensional $N \times N \times N$ array is needed to store the distances in a two-dimensional spin system. This has also been implemented, so that two-dimensional spin systems can be considered. Since also in [26] the authors approximated two-dimensional spin systems and benchmarked them with exact results, the calculated two-dimensional approximations can be benchmarked by comparison with the results in [26]. This has been done and the results have shown that the implementation works well, so that the code can also be used to approximate two-dimensional spin systems. In the same way, also an approximation of three-dimensional spin systems can be implemented, which has not been done yet.

Given the time evolution, the approximation of the spin dynamics is fully derived and can thus be evaluated. In chapter 4 the correlation function was needed for the comparison with the exact solution. This can be calculated straight forward by averaging all possible correlation functions for each distance. That process requires looping over the whole chain twice, since the correlation function of each spin with all other spins needs to be calculated. Looping twice over the whole chain causes a long computation time, especially for large spin chains. To increase the computation speed, a different way to compute the correlation function was chosen here, which is given by using a Fast Fourier transformation. A discrete correlation function can be calculated using a Fourier transformation $F\left(s_i^x\left(t\right)\right)$ of the spins,

$$\begin{aligned} C_d^{xx}\left(t\right) = &\sum_{i=0}^{N-1} s_i^x\left(t\right) s_{(i+d) \bmod N}^x\left(t\right) \\ =&S_d^x\left(t\right)\left(S_d^x\right)^*\left(t\right) \\ =&\mathrm{Re}\left(S_d^x\left(t\right)\right)^2 + \mathrm{Im}\left(S_d^x\left(t\right)\right)^2 \\ \text{with } S_d^x\left(t\right) =&F\left(s_i^x\left(t\right)\right). \end{aligned}$$

Thus, for each time step the Fast Fourier transformation from the C++ library `FFTW` is used to calculate the Fourier transformation of each spin in the chain, then the product of each transformed spin with its complex conjugate is calculated and transformed backwards to get the correlation function for each distance d.

These are the main points of the implementation, where all calculations are done in double precision. As it has been discussed in chapter 4, the precision of the

approximations is limited by the error appearing in the Monte-Carlo-Integration which is used to calculate the expectation value of an operator. Hence, it is not necessary to use a higher precision in the calculations, since the limitation in the calculations is higher than double precision.

C.2 Numerical Solutions of the Equations of Motion

To calculate the time evolution of the initially sampled spin states in the discrete truncated Wigner approximation, differential equations need to be solved, which is often very hard or even impossible to do analytically. Therefore, numerical methods are used to calculate the time evolution.

In the first order approximation, the equations of motion (3.14) form a set of linear ordinary differential equations, which can be solved using the Runge-Kutta method, as will be further introduced in appendix C.2.1. In the second order approximation, the equations of motion of the expansion coefficients $\boldsymbol{c}_{ij}$ in equation (3.22) form a set of non-linear ordinary differential equations and a divergence in the solution of the equations of motion has been found in sections 3.4 and 4.3. Also here the Runge-Kutta method has been used, but additionally a second method, the Adams-Bashforth-Moulton method has been implemented, which will be further introduced in appendix C.2.2. As a predictor-corrector method, this has a higher accuracy and thus the effect of the numerical approximation on the divergences can be considered.

C.2.1 The Runge-Kutta Method

The Runge-Kutta method is an iterative one-step method to solve ordinary differential equations of the general form

$$\dot{y}(t) = f(t, y), \tag{C.1}$$

$$y(t_0) = y_0. \tag{C.2}$$

The dot denotes a time derivative and t_0 is the initial time, thus equation (C.2) is the initial condition.

Numerical solving schemes of ordinary differential equations are based on calculating approximating solutions y_n of $y(t_n)$ at equidistant times $t_n = t_0 + \sum_{i=0}^{n} h_i$ with step size h_i which is generally different for each calculated step. In one-step methods, the calculation of the approximation at each step depends on the approximation of the previous step, and thus iteratively depends on the initial condition y_0. In multi-step methods, each step depends on multiple previous steps, as will be further explained in appendix C.2.2 [29, 30].

The Runge-Kutta method can be defined explicitly or implicitly. In the explicit method, the calculation of the approximation y_n only depends on y_{n-1}, while in the implicit method it also depends on y_n itself. This classification of explicit and implicit methods is generally defined [29, 30]. Here only explicit Runge-Kutta methods

0					
c_2	a_{21}				
c_3	a_{31}	a_{32}			
$\vdots$	$\vdots$	$\dots$	$\ddots$		
c_s	a_{s1}	a_{s2}	$\dots$	$a_{s,s-1}$	
	b_1	b_2	$\dots$	b_{s-1}	b_s

Table C.1: Butcher Tableau of a general Runge-Kutta method.

will be used, since implicit methods are harder to implement, especially for non-linear ordinary differential equations. But implicit methods show a higher accuracy and therefore a mixture of an explicit and an implicit method will be introduced in appendix C.2.2 and used to solve the non-linear ordinary differential equations which arise in the second order approximation of the equations of motion in section 3.2 [29, 30].

Generally, the Runge-Kutta method is given in the form [29, 30]

$$y_{n+1} = y_n + h_n \sum_{i=1}^{s} b_i k_i, \tag{C.3}$$

$$\text{with } k_i = f\left(t_n + c_i h_n, y_n + h_n \left(a_{i1}k_1 + a_{i2}k_2 + \cdots + a_{i,i-1}k_{i-1}\right)\right). \tag{C.4}$$

Here s denotes the number of stages of the method, the matrix $[a_{ij}]$ is called the Runge-Kutta matrix, the b_i are called weights and the c_i are called nodes. Using different values for these variables, various possible Runge-Kutta methods can be created, while a condition for the method to be convergent is given by $\sum_{i=1}^{s} b_i = 1$ [29, 30]. If the Runge-Kutta matrix is a lower triangular matrix, the method is explicit, while it is implicit if at least one $a_{ij} \neq 0$ for $j \geq i$. Since only explicit methods are used in this thesis, the Runge-Kutta matrix will be a lower triangular matrix in the following. The different variables of a specific Runge-Kutta method can be written in a Butcher Tableau, which is shown in table C.1 [30].

By choosing a value for the number of stages s and different variables in the Butcher Tableau, the Runge-Kutta method can be created with different orders of convergence. The convergence order p is defined by the maximum approximation error of all K steps of approximation [29, 30],

$$\max_{n=0,\dots,K} |y\left(t_n\right) - y_n| = \mathcal{O}\left(h^p\right) \text{ for } h \to 0. \tag{C.5}$$

0						
$\frac{1}{4}$	$\frac{1}{4}$					
$\frac{3}{8}$	$\frac{13}{32}$	$\frac{9}{32}$				
$\frac{12}{13}$	$\frac{1932}{2197}$	$-\frac{7200}{2197}$	$\frac{7296}{2197}$			
1	$\frac{439}{216}$	-8	$\frac{3680}{513}$	$-\frac{845}{4104}$		
$\frac{1}{2}$	$-\frac{8}{27}$	2	$-\frac{3544}{2565}$	$\frac{1859}{4104}$	$-\frac{11}{40}$	
	$\frac{25}{216}$	0	$\frac{1408}{2565}$	$\frac{2197}{4104}$	$-\frac{1}{5}$	
	$\frac{16}{135}$	0	$\frac{6656}{12825}$	$\frac{28561}{56430}$	$-\frac{9}{50}$	$\frac{2}{55}$

Table C.2: Butcher Tableau for the Runge-Kutta-Fehlberg Method.

Here a general step size h_i is used, all step sizes are considered in the limit $h \to 0$ and hence are approximately the same. The convergence order increases with the number of stages s of the method, but the higher the order, the more function evaluations are needed, which takes more computation time. Therefore, the order must not be chosen too small, but also not too high.

Also an adequate step size h needs to be chosen. If the step size is chosen too large, changes in the resulting function might be skipped, which would result in large deviations between the numerical and the exact solution. But if the step size is chosen too small, the computation time rises. Thus, in this thesis the Runge-Kutta-Fehlberg method is used, which includes an adaptive step size. This gives a small step size when the resulting function shows fast changes and a larger step size if not. The adaption is created by comparing results of a Runge-Kutta method with 4^{th} and 5^{th} order convergence, which have the same nodes and the same Runge-Kutta matrices, but different weights. Hence, their Butcher tableaux can be combined by writing the different weights in two lines, as shown in table C.2 [9].

Each step of the Runge-Kutta-Fehlberg method thus gives a result y_{n+1} of the 4^{th} order Runge-Kutta method and a result $\hat{y}_{n+1}$ of the 5^{th} order Runge-Kutta method. These two results can now be compared to adapt the step size. Therefore, an error ϵ is defined,

$$\epsilon = \|y_{n+1} - \hat{y}_{n+1}\| . \tag{C.6}$$

With this error ϵ, the step size h is adapted in the following way [9],

```
if(eps < eps_min)
{
        y[n + 1] = y4[n + 1];
        h = 2 * h;
}
else if(eps > eps_max)
{
        h = h / 2.;
}
else
{
        y[n + 1] = y4[n + 1];
}.
```

Here ϵ is denoted as `eps` and the result of the 4^{th} order Runge-Kutta method is denoted as `y4`. The result of the 4^{th} order Runge-Kutta method is then used as the result of the step, since it has been proven for this scheme that a higher order algorithm does not influence the result that much. For this algorithm a minimum error `eps_min` needs to be defined, which decides whether the step size is increased. If the calculated error is smaller than `eps_min`, the resulting function has no fast fluctuations and thus the step size can be increased. A maximum error `eps_max` is analogously needed to decide whether a smaller step size is required in case of fast changes in the resulting function. If the resulting error is larger than `eps_max`, the result of the Runge-Kutta method is not stored, but calculated again using a smaller step size. If the resulting error is between `eps_min` and `eps_max`, the step size does not need to be changed [9]. The values of `eps_min` and `eps_max` need to be chosen depending on the approximated system.

This adaptive step size method works very well given an initial value. But since already the first step size is adapted, this initial value can be chosen arbitrarily, where a first guess is known in most cases. What is more important, is a limit on the step size, so that it does not get smaller or larger than a chosen region. This is important to prevent the calculation from getting stuck in too small step sizes and on the other hand the step size must not get larger than the steps in which the results will be stored.

In the first order approximation of the quantum equations of motion, this Runge-Kutta-Fehlberg method works very well, thus it has been used for all calculations in sections 3.4, 4.2 and 4.3. For the second order approximation of the equations of motion a divergence in the spin dynamics has been found, as already discussed in section 4.3. But explicit methods do not show an accuracy as high as implicit methods. Since implicit methods are very hard to implement, especially for non-linear ordinary differential equations, a mixture of an explicit and an implicit method, the Adams-Bashforth-Moulton method, which will be further introduced in appendix C.2.2, has additionally been implemented to analyse whether these divergences can be captured by this numerical solving method of the equations of motion.

C.2.2 Adams-Bashforth-Moulton Method

The Runge-Kutta method introduced in appendix C.2.1 was defined to be an explicit one-step method. A higher accuracy in numerically solving ordinary differential equations can be reached by using implicit methods. These are hard to implement, especially for non-linear differential equations, such as the second order approximation of the equations of motion in section 3.2. Hence, the Adams-Bashforth-Moulton method, which is a multi-step predictor-corrector method, will be introduced. It uses an explicit multi-step method, the Adams-Bashforth method, to predict a value for y_{n+1}, which is then corrected by the implicit Adams-Moulton method [29]. Both methods need more than one previous point to calculate the next step, where the initial points will be calculated using the one-step Runge-Kutta method. The number of points required for the multi-step methods also defines the convergence order, which is p for a p-step method [29]. Here both methods are introduced as 4-step methods, thus the points y_{n-3}, y_{n-2}, y_{n-1} and y_n are required to calculate y_{n+1} in the explicit method.

Generally, the explicit Adams-Bashforth method can be derived by replacing an integrand by an interpolating polynomial [29],

$$\dot{y}(t) = f(t, y), \tag{C.7}$$

$$y(t_0) = y_0, \tag{C.8}$$

$$\begin{aligned} \Rightarrow y(t_{n+1}) - y(t_n) &= \int_{t_{n-1}}^{t_n} f(t', y(t'))\,\mathrm{d}t' \\ &\approx h \sum_{i=0}^{3} \beta_{i,\mathrm{AB}} f(t_{n-1}, y(t_{n-1})), \end{aligned} \tag{C.9}$$

$$\text{with } \beta_{i,\mathrm{AB}} = \int_0^1 \prod_{\substack{l=0 \\ l \neq i}}^{3} \frac{s+l}{-i+l} \mathrm{d}s, \; i = 0, 1, \ldots, n$$

$$\Rightarrow y_{n+1} = y_n + h \sum_{i=0}^{3} \beta_{i,\mathrm{AB}} f_{n-i}. \tag{C.10}$$

The index AB denotes the definition of β_i in the Adams-Bashforth method.

By calculating the values for $\beta_{3,\mathrm{AB}}$, $\beta_{2,\mathrm{AB}}$, $\beta_{1,\mathrm{AB}}$ and $\beta_{0,\mathrm{AB}}$, the 4^{th} order Adams-Bashforth method is given by

$$\begin{aligned} y_{n+1} =& y_n + \frac{h}{24} \left[55 f(t_0 + nh, y_n) - 59 f(t_0 + (n-1)h, y_{n-1}) \right. \\ &\left. + 37 f(t_0 + (n-2)h, y_{n-2}) - 9 f(t_0 + (n-3)h, y_{n-3}) \right]. \end{aligned} \tag{C.11}$$

The implicit Adams-Moulton method can be derived in the same way, where only

the definition of β_i changes and is denoted by the index AM [29],

$$\begin{aligned} y\left(t_{n+1}\right) - y\left(t_n\right) &= \int_{t_{n-1}}^{t_n} f\left(t', y\left(t'\right)\right) \mathrm{d}t' \\ &\approx h \sum_{i=0}^{3} \beta_{i,\mathrm{AM}} f\left(t_{n-1}, y\left(t_{n-1}\right)\right), \end{aligned} \tag{C.12}$$

$$\text{with } \beta_{i,\mathrm{AM}} = \int_{-1}^{0} \prod_{\substack{l=0 \\ l \neq i}}^{3} \frac{s+l}{-i+l} \mathrm{d}s, \; i = 0, 1, \ldots, n$$

$$\Rightarrow y_{n+1} = y_n + h \sum_{i=0}^{3} \beta_{i,\mathrm{AM}} f_{n-i}. \tag{C.13}$$

The 4^{th} order Adams-Moulton method can then be derived explicitly by calculating $\beta_{3,\mathrm{AM}}$, $\beta_{2,\mathrm{AM}}$, $\beta_{1,\mathrm{AM}}$ and $\beta_{0,\mathrm{AM}}$,

$$\begin{aligned} y_{n+1} =& y_n + \frac{h}{24} \left[9 f\left(t_0 + (n+1)\, h, y_{n+1}\right) + 19 f\left(t_0 + nh, y_n\right)\right. \\ & \left. -5 f\left(t_0 + (n-1)\, h, y_{n-1}\right) + f\left(t_0 + (n-2)\, h, y_{n-2}\right)\right] \end{aligned} \tag{C.14}$$

Given the definition of the Adams-Bashforth and the Adams-Moulton method, they can be combined to give the predictor-corrector Adams-Bashforth-Moulton method. Therefore, a first prediction for y_{n+1} is calculated using the explicit Adams-Bashforth method. A correction to this prediction is then calculated using the implicit Adams-Moulton method, where the prediction for y_{n+1} is plugged into the right hand side of equation (C.14). The results before and after the correction can then be compared and the correction step can be repeated until the corrections converge [29].

Since in this numerical method an implicit multi-step method is used, it shows a higher accuracy and has thus also been tested to solve the second order approximations of the equations of motion derived in section 3.2. It has been found that this numerical solution method shows the same divergences as the Runge-Kutta method at approximately the same times after the sudden quench. This leads to the conclusion that the divergences in sections 3.4 and 4.3 can not be captured with standard numerical methods and more complex methods might be needed to get rid of the divergences. On the other hand, the divergences might also be caused by the truncation of the quantum mechanical equations of motion, where the conservation of several quantities is not given anymore, as already discussed in section 4.3.

D Lists

D.1 List of Figures

D.2 List of Tables

E Bibliography

[1] R. Blatt and C. F. Roos. Quantum simulations with trapped ions. *Nat Phys*, 8(4):277–284, 2012.

[2] I. Bloch, J. Dalibard, and S. Nascimbène. Quantum simulations with ultracold quantum gases. *Nat Phys*, 8(4):267–276, 2012.

[3] M. Bonitz. *Quantum Kinetic Theory*. B. G. Teubner Stuttgart, Leipzig, 1998.

[4] R. E. Caflisch. Monte carlo and quasi-monte carlo methods. *Acta Numerica*, 7:1–49, 1998.

[5] H. Cakir. Dynamics of the transverse field ising chain after a sudden quench. Master's thesis, Ruprecht-Karls-Universität Heidelberg, 2015.

[6] P. Calabrese, F. H. L. Essler, and M. Fagotti. Quantum quench in the transverse field ising chain: I. time evolution of order parameter correlators. *Journal of Statistical Mechanics: Theory and Experiment*, 2012(07):P07016, 2012.

[7] P. Calabrese, F. H. L. Essler, and M. Fagotti. Quantum quench in the transverse field ising chain: II. stationary state properties. *Journal of Statistical Mechanics: Theory and Experiment*, 2012(07):P07022, 2012.

[8] M. Fagotti and F. H. L. Essler. Reduced density matrix after a quantum quench. *Phys. Rev. B*, 87(24):245107, 2013.

[9] E. Fehlberg. Klassische runge-kutta-formeln vierter und niedrigerer ordnung mit schrittweiten-kontrolle und ihre anwendung auf wärmeleitungsprobleme. *Computing*, 6, 1970.

[10] K. R. A. Hazzard, B. Gadway, M. Foss-Feig, B. Yan, S. A. Moses, J. P. Covey, N. Y. Yao, M. D. Lukin, J. Ye, D. S. Jin, and A. M. Rey. Many-body dynamics of dipolar molecules in an optical lattice. *Phys. Rev. Lett.*, 113(19):195302, 2014.

[11] M. Hillery, R. F. O'Connell, M. O. Scully, and E. P. Wigner. Distribution functions in physics: Fundamentals. *Physics Reports*, 106(3):121–167, 1984.

[12] E. T. Jaynes. Information theory and statistical mechanics. *Phys. Rev.*, 106(4):620–630, 1957.

[13] E. T. Jaynes. Information theory and statistical mechanics. II. *Phys. Rev.*, 108(2):171–190, 1957.

[14] N. M. Josuttis. *The C++ Standard Library - A Tutorial and Reference*. Addison-Wesley, second edition edition, 2012.

[15] P. Jurcevic, B. P. Lanyon, P. Hauke, C. Hempel, P. Zoller, R. Blatt, and C. F. Roos. Quasiparticle engineering and entanglement propagation in a quantum many-body system. *Nature*, 511(7508):202–205, 2014.

[16] M. Kastner, L. Pucci, and A. Roy. Simulation of quantum spin dynamics by phase space sampling of BBGKY trajectories. *arXiv:1510.03768v2 [cond-mat.stat-mech]*, 2015.

[17] M. Kastner and M. van den Worm. Relaxation timescales and prethermalisation in d-dimensional long-range quantum spin models. *Phys. Scripta*, 2015(T165):014039, 2015.

[18] E. Lieb, T. Schultz, and D. Mattis. Two soluble models of an antiferromagnetic chain. *Annals of Physics*, 16(3):407–466, 1961.

[19] E. Nicklas, M. Karl, M. Höfer, A. Johnson, W. Muessel, H. Strobel, J. Tomkocič, T. Gasenzer, and M. K. Oberthaler. Obsevation of scaling in the dynamics of a strongly quenched quantum gas. *Physical Review Letters*, 115(24):245301, 2015.

[20] R. F. O'Connell and E. P. Wigner. Quantum-mechanical distribution functions: Conditions for uniqueness. *Physics Letters*, 83A(4), 1981.

[21] R. Paškauskas and M. Kastner. Equilibration in long-range quantum spin systems from a BBGKY perspective. *J. Stat. Mech.*, 2012(02):P02005, 2012.

[22] P. Pfeuty. The one-dimensional ising model with a transverse field. *Annals of Physics*, 57(1):79–90, 1970.

[23] A. Polkovnikov. Phase space representation of quantum dynamics. *Annals of Physics*, 325(8):1790–1852, 2010.

[24] S. Sachdev. *Quantum Phase Transitions*. Cambridge University Press, second edition, 2011.

[25] S. Sachdev and A. P. Young. Low temperature rerelaxation dynamics of the ising chain in a transverse field. *Phys. Rev. Lett.*, 78(11):2220–2223, 1997.

[26] J. Schachenmayer, A. Pikovski, and A. M. Rey. Dynamics of correlations in two-dimensional quantum spin models with long-range interactions: a phase-space monte-carlo study. *New Journal of Physics*, 17(6):065009, 2015.

[27] J. Schachenmayer, A. Pikovski, and A. M. Rey. Many-body quantum spin dynamics with monte carlo trajectories on a discrete phase space. *Physical Review X*, 5(1):011022, 2015.

[28] P. Schauß, M. Cheneau, M. Endres, T. Fukuhara, S. Hild, A. Omran, T. Pohl, C. Gross, S. Kuhr, and I. Bloch. Observation of spatially ordered structures in a two-dimensional rydberg gas. *Nature*, 491(7422):87–91, 2012.

[29] J. Stoer and R. Bulirsch. *Numerische Mathematik 2*. 2005.

[30] K. Strehmel, R. Weiner, and H. Podhaisky. *Numerik gewöhnlicher Differentialgleichungen*. Vieweg+Teubner Verlag, 2012.

[31] S. Trotzky, L. Pollet, F. Gerbier, U. Schnorrberger, I. Bloch., N. V. Prokofév, B. Svistunov, and M. Troyer. Suppression of the critical temperature for superfluidity near the mott transition. *Nat Phys*, 6(12):998–1004, 12 2010.

[32] M. van den Worm, B. C. Sawyer, J. J. Bollinger, and M. Kastner. Relaxation timescales and decay of correlations in a long-range interacting quantum simulator. *New J. Phys.*, 15(8):083007, 2013.

[33] S. R. White and A. E. Feiguin. Real-time evolution using the density matrix renormalization group. *Phys. Rev. Lett.*, 93(7):076401, 2004.

[34] E. Wigner. On the quantum correction for thermodynamic equilibrium. *Phys. Rev.*, 40(5):749–759, 1932.

[35] W. K. Wootters. A wigner-function formulation of finite-state quantum mechanics. *Annals of Physics*, 176(1):1–21, 1987.

[36] W. K. Wootters. Picturing qubits in phase space. 2003.

Acknowledgement

First of all I would like to thank Mr. Prof. Dr. Thomas Gasenzer for supervising the work on this thesis. He was always available to answer questions appearing during my work and to discuss the results. I would also like to thank him for offering the topic of my thesis. Implementing an approximation method for a physical system gave me the opportunity to apply the knowledge I earned during my studies.

I would also like to thank Mr. Prof. Dr. Markus K. Oberthaler for discussions from a different point of view. His ideas from an experimental vantage point were a great enrichment for my research.

Next I would like to thank the people of the group for interesting discussions. A special thank goes to Mr. Markus Karl for supporting me during my work on this thesis with many ideas and discussions from which I learned a lot.

In the end I would like to thank my family as well as my boyfriend, his family and all of my friends for always supporting me during my whole studies and making the busy times easier.

Erklärung:

Ich versichere, dass ich diese Arbeit selbstständig verfasst habe und keine anderen als die angegebenen Quellen und Hilfsmittel benutzt habe.

Heidelberg, den 29. März 2016 .....